University of Southampton

University of Southampton Research Repository

Copyright © and Moral Rights for this thesis and, where applicable, any accompanying data are retained by the author and/or other copyright owners. A copy can be downloaded for personal non-commercial research or study, without prior permission or charge. This thesis and the accompanying data cannot be reproduced or quoted extensively from without first obtaining permission in writing from the copyright holder/s. The content of the thesis and accompanying research data (where applicable) must not be changed in any way or sold commercially in any format or medium without the formal permission of the copyright holder/s.

When referring to this thesis and any accompanying data, full bibliographic details must be given, e.g.

Thesis: Author (Year of Submission) "Full thesis title", University of Southampton, name of the University Faculty or School or Department, PhD Thesis, pagination.

Data: Author (Year) Title. URI [dataset]

University of Southampton

Faculty of Engineering and Physical Science

School of Engineering

A Detailed Chemistry Solver on Adaptive Curvilinear Meshes and Its Application to Rotating Detonation Simulations

by

Han Peng

ORCID ID https://orcid.org/0000-0003-4503-360X

Thesis for the degree of Doctor of Philosophy

January 2024

University of Southampton

Abstract

Faculty of Engineering and Physical Science

School of Engineering

Doctor of Philosophy

A Detailed Chemistry Solver on Adaptive Curvilinear Meshes and Its Application to Rotating Detonation Simulations

by

Han Peng

The rotating detonation engine (RDE) has drawn increasing interest in recent years due to its potential for high thermal efficiency and pressure-gain properties. The simulations of RDE have primarily focused on premixed injection and its wave structure, as the premixing assumption allows for the use of simplified chemistry models. However, a fully premixed RDE may lead to potential flashback issues during actual experiments. Another common simplification present in the simulation of RDEs is the adiabatic wall boundary condition. As the duration of operation increases to hundreds of seconds, the need of a cooling system has become more urgent. Simulations addressing these challenges require a three-dimensional solver capable of accurately and efficiently handling detailed chemistry and boundary flows.

In this work, a three-dimensional solver is developed based on the Adaptive Mesh Refinement in Object-oriented C++ (AMROC) framework. The adaptive mesh refinement technique enables dynamic mesh refinement based on a user-defined threshold. Initially proposed for Cartesian meshes, the adaptive mesh technique is extended and implemented on curvilinear meshes in this study. This novel combination of a stretched body-fitted mesh and the dynamic adaptive mesh reduces the total number of meshes required for an RDE simulation. The developed solver is verified and validated with different benchmark tests. The results show that the present solver achieves second-order accuracy and ensures conservation across the multi-level hierarchy. In addition, the solver demonstrates the capability for robust and accurate simulation of high-speed reacting flows, including unsteady shock-induced combustion and curved cellular detonation.

Finally, the solver is applied to investigate the effects of partial premixing on RDE performance. Hydrogen fuel is blended into the air stream at different bypass flow rates. An increase in bypass flow rate results in improved RDE performance, as indicated by higher detonation velocity, thrust, and specific impulse. The effects of cooling walls are also studied, and the results confirm that introducing a cooling wall during the operation process still preserves the number of detonation heads and the macro structure on the middle plane. The adiabatic case overestimates the detonation velocity without considering the heat loss on detonation. The cooling walls play a crucial role in suppressing parasitic and commensal combustion waves near the walls, leading to a reduction in low-pressure heat release. Moreover, the walls experienced unequal heat loads, primarily influenced by the internal combustion zones and the channel width. These findings enhance the understanding of partial premixing and cooling walls on RDE from the numerical aspect.

Table of Contents

Table of Tables

Table of Figures

Table of Figures

Table of Figures

Table of Figures

Research Thesis: Declaration of Authorship

Print name: Han Peng

Title of thesis: A Detailed Chemistry Solver on Adaptive Curvilinear Meshes and Its Application to Rotating Detonation Simulations

I declare that this thesis and the work presented in it are my own and has been generated by me as the result of my own original research.

I confirm that:

1. This work was done wholly or mainly while in candidature for a research degree at this University;
2. Where any part of this thesis has previously been submitted for a degree or any other qualification at this University or any other institution, this has been clearly stated;
3. Where I have consulted the published work of others, this is always clearly attributed;
4. Where I have quoted from the work of others, the source is always given. With the exception of such quotations, this thesis is entirely my own work;
5. I have acknowledged all main sources of help;
6. Where the thesis is based on work done by myself jointly with others, I have made clear exactly what was done by others and what I have contributed myself;
7. Parts of this work have been published as:

Peng, H. and Deiterding, R., 2023. A three-dimensional solver for simulating detonation on curvilinear adaptive meshes. Computer Physics Communications, 288, p.108752.

Peng, H., Atkins, C.W. and Deiterding, R., 2022. A solver for simulating shock-induced combustion on curvilinear adaptive meshes. Computers & Fluids, 232, p.105188.

Peng, H. and Deiterding, R., 2023. Adaptive three-dimensional simulations of rotating detonation with cooling walls. In 29th International Colloquium on the Dynamics of Explosion and Reactive Systems, p. 190.

Peng, H. and Deiterding, R., 2022. Simulations of ethylene-oxygen rotating detonation waves under different local equivalence ratio. In 28th International Colloquium on the Dynamics of Explosion and Reactive Systems, p. 85.

Peng, H. and Deiterding, R., 2022. Parallel adaptive simulation of rotating detonation engines. In 11th International Conference on Engineering Computational Technology, p. 165.

Peng, H. and Deiterding, R., 2022. A three-dimensional solver for simulating reactive flow on curvilinear parallel adaptive meshes. In 33rd Parallel CFD International Conference, p. 34.

Signature: ..... Date:.....

Acknowledgements

First, I would like to thank my supervisor, Prof. Ralf Deiterding, for his patient guidance, support and encouragement over the last four years. I would like to thank Prof. Edward Richardson and Dr. Zhiwei Hu for their constructive suggestions and insights at each review stage throughout my PhD studies.

I would like to express my appreciation for the financial support from the China Scholarship Council (CSC) and the University of Southampton. I also acknowledge the use of the IRIDIS High Performance Computing Facility, and associated support services at the University of Southampton. I would like to thank the use of the ARCHER2 UK National Supercomputing Service.

I would like to acknowledge Dr. Chay Atkins for his support and discussions in using AMROC. I want to express my gratitude to Dr. Mikael Grondeau for his help in using ARCHER2. I would like to thank Dr. Pushpender Sharma and Keertan Maskey for their useful comments.

I would like to thank Prof. Yue Huang and Dr. Zhenye Luan for their insightful discussions on detonation problems. I would also like to thank all my friends back in China for their support and encouragement during the pandemic.

Finally, I would like to thank my family for their support throughout my studies.

Nomenclature

Abbreviations

AFRL ..... Air Force Research Laboratory

AMR ..... Adaptive Mesh Refinement

AMROC ..... Adaptive Mesh Refinement in Object-oriented C++

AUSM ..... Advective Upstream Splitting Method

CFD ..... Computational Fluid Dynamics

CFL ..... Courant–Friedrichs–Lewy

C-J ..... Chapman-Jouguet

CNRS ..... French National Centre for Scientific Research

DDT ..... Deflagration to Detonation Transition

DF ..... Double-Flux scheme

DG ..... Discontinuous Galerkin

DWBLI ..... Detonation Wave/Boundary Layer Interactions

ER ..... Equivalence Ratio

ERD ..... Equivalence Ratio Difference

FC ..... Fully Conservative scheme

FDM ..... Finite Difference Method

FFT ..... Fast Fourier Transform

FVM ..... Finite Volume Method

GFM ..... Ghost Fluid Method

GRK4A ..... Semi-implicit generalized Runge–Kutta method of fourth order

HF ..... Hybrid-Flux scheme

HLL ..... Harten-Lax-Van Leer

HLLC ..... Harten-Lax-Van Leer Contact

HRR ..... Heat release rate

IDDES ..... Improved Delayed Detached Eddy Simulation

ISAS ..... Institute of Space and Astronautical Science

JAXA ..... Japan Aerospace Exploration Agency

KH ..... Kelvin–Helmholtz

LCD ..... Laboratory of Combustion and Detonation

LES ..... Large Eddy Simulation

MMS ..... Method of Manufactured Solutions

MSID ..... Mach Stem-Induced Detonation

MUSCL ..... Monotonic Upstream-centered Scheme for Conservation Laws

NFI ..... Normalised Flame Index

N-S ..... Navier-Stokes

ODWE ..... Oblique Detonation Wave Engine

OSIC ..... Oblique Shock-Induced Combustion

PDE ..... Pulse Detonation Engine

PGC ..... Pressure-Gain Combustion

PPM ..... Piecewise Parabolic Method

PVRS ..... Primitive Variable Riemann Solver

RANS ..... Reynolds-averaged Navier-Stokes

RDE ..... Rotating Detonation Engine

SAMR ..... block-Structured Adaptive Mesh Refinement

SIC ..... Shock-Induced Combustion

UCSD ..... University of California San Diego

UoS ..... University of Southampton

URANS ..... Unsteady Reynolds-averaged Navier-Stokes

WENO ..... Weighted Essentially Non-Oscillatory

ZND ..... Zel'dovich, von Neumann and Döring

Symbols

a ..... Speed of sound

$\hat{A}$ ..... Jacobian matrix of the flux function

A_f, A_c ..... Area of the fine mesh and the coarse mesh

$A_j^{\mathrm{f/r}}$ ..... Pre-exponential factor of reaction j

a_X, b_X, z_X ..... Unit vectors in the transformation matrix

$a_{\phi_x}, a_{\phi_y}, a_{\phi_z}$ ..... Constant used in manufactured solutions

C_{P_i} ..... Specific heat at constant pressure of species i

C_{v} ..... Specific heat at constant volume

$\mathbb{C}$ ..... Constant in Richardson extrapolation

D_{i} ..... Mixture-averaged diffusion coefficient of species i

D_i^T ..... Mixture-averaged thermal diffusion coefficient of species i

E ..... Total specific energy

$E_j^{\mathrm{f/r}}$ ..... Activation energy for the reaction j

$f_{s,x}, f_{s,y}, f_{s,z}$ ..... Function used in manufactured solutions

F, G, H ..... Inviscid fluxes in the x-direction, y-direction, z-direction

F_{V}, G_{V}, H_{V} ..... Viscous fluxes in the x-direction, y-direction, z-direction

H ..... Axisymmetric source term

H_{det} ..... Detonation head height in rotating detonation

h_{i} ..... Specific enthalpy of species i

h_{ref}^0 ..... Heat of formation at the reference temperature

$H^{\Delta t}$ ..... One-step explicit difference operator with time step Δt

I_{sp} ..... Specific impulse

$\boldsymbol{J}$ ..... Jacobian determinant of the grid

$J_{x,i}$, $J_{y,\mathrm{i}}$, $J_{z,i}$ ..... Diffusion fluxes of species i in the x-, y- and z-direction

k ..... Thermal conductivity

$k_j^{\mathrm{f/r}}$ ..... Rate constant of forward or reverse chemical reaction

l ..... Mesh refinement level

$L_{i,j}$ ..... Interval length between adjacent cells

L_{in} ..... Induction length for reactions

L_{x}, L_{y}, L_{z} ..... Domain length in x-, y- and z-direction

Nomenclature

M ..... Mach number

$\dot{m}_f, \dot{m}_b$ ..... Total fuel mass flow rate and the fuel mass flow rate in bypass flow

n ..... Refinement factor for adjacent levels

n_{det} ..... Number of detonation heads in rotating detonation

$N_{\max}$ ..... Total number of meshes

N_{sp} ..... Total number of reaction species

n_{x}, n_{y} ..... Unit normal vectors of the physical edges

o ..... Order of accuracy

$O(n)$ ..... Magnitude of number n

p ..... Pressure

Q ..... State vector for conservative variables

$\boldsymbol{Q}$ ..... Variables in physical space

$\mathbb{Q}$ ..... Discrete solutions in Richardson extrapolation

$\breve{Q}$ ..... State vector after flux correction

r_{d} ..... Factor used in stretched mesh generation

r_m ..... Right eigenvectors of Jacobian matrix $\hat{A}$

$\mathrm{R_u}$ ..... Ideal gas constant

S ..... Source terms

S_X ..... Scaling factor used in distorted mesh generation

s ..... Wave speed in Riemann problem

S_w ..... Scaling factor for relative error of quantity w

T ..... Temperature

T_{s} ..... Transformation matrix

T_{ref} ..... Reference temperature

u, v, w ..... Velocity components in each direction

U_{D}, $U_{\mathrm{C\text{-}J}}$ ..... Detonation velocity and C-J velocity

$\hat{U}^2$ ..... Sum of the square of the Roe average velocities

V_{f}, V_{c} ..... Volume of the fine mesh and the coarse mesh

ν_{ji}^{r}, ν_{ji}^{f} ..... Stoichiometric coefficients of species i in j th reaction

w ..... Scalar quantity used for refinement criteria

W_{i}, $\overline{W}$ ..... Molar mass of species i or mixture

W_m ..... Wave in Riemann problem for m th equation

X ..... Vector of coordinates in the physical space

x, y, z ..... Coordinates in the physical space

X_i ..... Molar fraction of species i

Y_{i} ..... Mass fraction of species i

α_m ..... Wave strength in Riemann problem for m th equation

β ..... Clustering factor used in stretched mesh generation

$\beta_j^{\mathrm{f/r}}$ ..... Exponent of reaction j

γ ..... Specific heat ratio

δ ..... Slope in MUSCL reconstruction

δF ..... Flux difference used for flux correction

$\Delta_{\min}$ ..... Minimum mesh size

ε ..... Adaptive mesh refinement threshold value

ε_i ..... Slope limiter in MUSCL reconstruction

$\hat{\lambda}_m$ ..... Eigenvalues for Jacobian matrix $\hat{A}$

μ ..... Mixture dynamic viscosity

ν ..... The specific volume

ξ, η, ζ ..... Coordinates in the computational space

ρ ..... Density

ρ_i ..... Density of species i

$\dot{\sigma}$ ..... Total thermicity in a cell

τ ..... Viscosity stress

τ^w ..... Error estimation for quantity w

φ ..... Fluid variables used in derivatives of diffusion terms

$\hat{\phi}_i$ ..... Roe average partial derivative of p with respect to Y_i

ϕ_x, ϕ_y, ϕ_z ..... Constant used in manufactured solutions

$\dot{\omega}_i$ ..... Mass generation rate of component *i*

Chapter 1 Introduction

1.1 Motivation

Conventional gas turbines use fossil fuel, whereas the sources of fossil fuel energy are limited and using these resources causes environmental pollution. Also, there is a requirement to limit the dependency on fossil fuels in propulsion systems for the next-generation aircraft [1]. The study of clean gases, like natural gas and hydrogen, as alternative energy carriers, has attracted the attention of many researchers. The use of hydrogen has high combustion efficiency and produces low concentrations of harmful substances in the exhaust gas. Low emission, high specific energy, and a wide range of flammability limits are the unique characteristics of those fuels [2,3].

In addition to using clean fuels, increasing the thermal efficiency in propulsion systems is another eco-friendly way by decreasing the energy consumption. Subsonic pressure-constant combustion is the most common type of reacting flows observed in propulsion and power generation systems. The burning of the reactants relies primarily on thermal diffusion of the products and mass transport. The pressure remains essentially constant across the flame reaction zone [4]. In conventional propulsion systems, the thermal efficiency in combustion processes has reached a bottleneck, and achieving even a small improvement in thermal efficiency requires significant investment. Hence, novel engines using different thermodynamic cycles have received increased attention in recent years [5].

Detonation is a type of reactive phenomenon where a supersonic combustion wave drives a leading shock wave, resulting in the coupled propagation of both waves. The thermodynamic states change sharply across a detonation, which is accompanied by fast energy release [6]. A detonation is also considered a pressure-gain and self-sustaining chemical reaction and is hence essentially different from subsonic combustion. The highly efficient detonation-based engines, which employ pressure-gain combustion (PGC), have been considered as one of the viable replacements for current propulsion and land-based power generation systems that employ pressure-constant combustion [7,8].

The rotating detonation engine (RDE) is a type of engine that uses one or multiple detonations to compress and burn fuel in a disk- or cylindrical-shaped device [8]. The RDE can operate with limited or no mechanical compression, leading to reduced weight and fewer manufacturing difficulties. The detonation wave rapidly propagates in the combustor resulting in a nearly constant-volume combustion process that produces high-pressure burnt products and provides thrust. Another interesting thermodynamic feature of the RDE cycle is the increased thermal efficiency compared to the Brayton cycle [9]. This means that a greater portion of the heating value of the fuel can be converted to effective energy. It is important to emphasize that these comparisons are for idealized thermodynamic cycles, i.e., for systems operating in a steady state. However, developing gas turbines using a steady or stabilized detonation wave is difficult. There are still many challenges that need to

be addressed before RDEs can be widely used in realistic systems. Studies on the RDE operation mechanism are still ongoing in terms of the detonation multiplicity, wave mode and stability, fuel and oxidizer mixing processes, and thermal management [10,11].

As the detonation travels rapidly in the combustor, the mixing in a short period has an important influence on the detonation stable operation. The majority of RDE experimental studies [12-15] were based on non-premixing injection as the premixed reactants in experiments may lead to destructive flashbacks [16]. The severe heating and shock wave back to the plenum bring difficulties in preventing the flashbacks; hence, the fully premixed injection was rarely used in RDE experiments. A special long narrow slot feed system [17] was designed for such a purpose. Partially premixed injection [18,19] has drawn increasing research attention in recent years as a compromise between the premixing degree and the abilities in suppressing flashbacks. Despite successful attempts employing partially premixed injection, the effects of the premixing strategy on RDE internal flow fields remain poorly understood and require further studies.

Another challenge for RDE's long-time operation is thermal management. The rapid heat release associated with RDEs poses challenges for cooling of walls [8,10,20-22]. Despite the fact that laboratory RDEs typically operate for only a few seconds in experiments, making the need of a wall cooling system less urgent, cooling of the walls is necessary in the case of long duration of the combustor [23]. The carried out experimental studies with cooling systems employed dilution gas [21] or water [24-26] to cool the walls of the RDE. It is observed that the estimated high-frequency heat flux results in the temperature rises of coolant [24]. The experimental results focused on the effects of detonation on the wall heat flux. The influence on detonation itself remains unclear, especially in a multi-wave mode.

The risk of flashback when using premixing injection in an RDE experiment and its extreme thermodynamic conditions make large-scale experiments costly and challenging. The addition of a cooling system increases the difficulties of experimental observation, as no instrumentation ports are available in the water-filled walls [25]. It is promising to initially design and study these problems in a stable RDE using clean fuels for energy generation by means of Computational Fluid Dynamics (CFD).

CFD is a feasible way to predict results that cannot be obtained from experiments and theoretical analysis, especially in gas turbine research relating to supersonic combustion. The role of CFD in this field has become increasingly important [27]. Note that accurate and predictive detonation simulation is difficult in itself as a detonation is a supersonic combustion phenomenon that inherently involves a discontinuous shock wave. A high mesh resolution is necessary to resolve the chemical characteristic length; as a result, numerical simulations on supersonic reacting flow are quite expensive.

An effective approach for capturing supersonic combustion and discontinuous flow structures is adaptive mesh refinement (AMR) [28,29]. AMR enables the computation to use dynamic refined grids in the region where the flow field varies dramatically, whereas other smoother regions are solved with coarser grids to decrease the total cell numbers. The open-source mesh adaptation framework Adaptive Mesh Refinement in Object-oriented C++ (AMROC) [30] is a powerful software system for large-scale simulations. It adopts the block-structured adaptive mesh refinement technique (SAMR) after Berger and Colella [29]. This method employs a patch-wise refinement approach. The meshes are dynamically flagged by using specified refinement criteria. These flagged cells are then grouped into a region of various-sized rectangular blocks. By successively creating refined meshes from respectively coarser parents, a multi-level hierarchy of embedded grid patches is created.

AMROC is a freely available dimension independent mesh adaptation framework for time-explicit Cartesian finite volume methods on distributed memory machines and employs a locality-preserving rigorous domain decomposition technique based on space-filling curves. The solvers within AMROC have been applied extensively to simulations of combustion, reactive flows and detonation problems [31-33]. The Clawpack package [34] has been incorporated into the Cartesian AMROC framework with an extended detailed chemical-kinetic model for multi-species thermally perfect gas mixtures.

AMROC also has a generic implementation of a first-order accurate embedded boundary method that can handle complex non-Cartesian boundaries [35,36] using the ghost-fluid method [37]. States in ghost cells are set before the original numerical update to model the boundary conditions. The actual boundary is considered by employing a scalar level set function [38,39]. However, the staircase approximation of the boundary introduces considerable errors, resulting in the conservation breaking in the vicinity of the boundary. Another strategy is using a cut-cell method [40] to deal with the non-Cartesian boundaries. The cells that intersect the complex boundary are truncated to represent the shape of the boundary. As the cut cells may be arbitrarily small, additional measures are necessary to avoid extremely small time steps in these small cut-cells [41].

These problems are notable as the loss of conservation can cause numerical instabilities when simulating detonations interacting with the boundary and the explicit time integration is commonly used in such cases. In both the embedded boundary method and cut cell method, the majority of conventional numerical methods and related AMR algorithms on Cartesian mesh remain unchanged for the interior cells. The complex modification is only employed for the boundary cells to treat the non-Cartesian geometry.

A more straightforward way is the application of a quadrilateral but non-Cartesian mesh to represent the actual boundary. In this work, the mapping method is implemented with a capacity function as proposed in Ref. [34]. The curvilinear body-fitted mesh is used with the AMR technique to solve the

high-speed reacting flows efficiently. In AMROC, the implementation of the 2D mapping strategy for meshes has been accomplished for overset grids with a two-temperature model [42]. Benefiting from this, the present work focuses on employing the mapping method to the Cartesian chemistry solvers for multi-species thermally perfect gas mixtures and detailed chemistry mechanisms. Combining the mapping method and AMR enables the effective simulations of detonation on curvilinear adaptive meshes for non-Cartesian geometry, such as the annular RDE combustor.

There have been few non-Cartesian 3D AMR solvers for compressible Navier-Stokes equations with detailed chemistry both in CFD commercial software and other CFD codes so far. Development of such a solver, set-up, comprehensive verification and validation cases and its utilization for large-scale high-resolution computations will be beneficial for not only the detonation simulations community but also the more specific rotating detonation engine (RDE) research. The robust and accurate simulation of the wall boundaries in RDE also contributes to the understanding of the effects of partial premixing and cooling walls on the 3D RDE internal structure from a numerical perspective.

1.2 Research objectives and novelties

The objective of the present work is primarily the development of a second-order solver with the capability of solving reacting flows on non-Cartesian domains within AMROC on curvilinear meshes. Complex data structures and a sophisticated program architecture are required to adapt high-resolution numerical methods on a dynamically changing mesh. The cell-centred finite volume schemes with shock-capturing capability, second-order accurate reconstruction and detailed chemistry are implemented for simulations of combustion and detonation with an arbitrary number of species and arbitrary chemical reaction systems.

To achieve this aim, the present thesis firstly concentrates on adaptive structured non-Cartesian meshes and solving the Euler and Navier-Stokes equations in 2D and 3D with full chemistry reaction models. Compared to the general solvers in AMROC, the main development and features of the present solver are summarized below:

- Solving multi-component compressible reactive Euler/N-S equations on curvilinear meshes.
- Application of the mapping strategy to multi-component reacting flows with detailed chemistry.
- Geometry information of the 3D meshes, such as the normal vectors and transformation matrices.
- Grid-aligned Riemann solver, and newly implemented schemes such as AUSM and HLLC.
- Second-order MUSCL-Hancock construction on 2D/3D curvilinear meshes.
- Second-order central difference for viscous terms involving the calculation of thermal and transport properties.

- Operators for information transfer between AMR levels on curvilinear meshes.
- Flux conservation correction on the coarse-fine interface for multi-level curvilinear meshes.
- Comprehensively verified and validated by different benchmark tests.

Benchmark test cases of 2D and 3D configurations are used to verify and validate the performance of the proposed solver within the mesh adaptation framework. Then the solver is applied to simulations of high-speed reacting flows related to detonation problems. The chemistry solver itself is complex and different benchmark tests are carried out to test different aspects of the implementation. These test cases verify the order of accuracy, robustness and efficiency of the proposed numerical methods to handle multi-scale reacting flows in non-Cartesian geometry, specifically the internal flow field in an annular RDE for propulsion and power generation. Then the solver is applied to simulation cases related to rotating detonation engines.

Another main aim of this thesis is to study the specific problems including the effects of premixing and cooling walls on RDE flow field structure and performances. After verification and validation, the solver is used to simulate an annual RDE. The focuses of RDE simulations studied in this thesis are summarised below:

- Build-ups of numerically stable RDE configurations using the curvilinear adaptive mesh.
- The effects of premixed, partially premixed and non-premixed injection on RDE.
- The effects of varying wall temperature on a multi-wave non-premixed RDE in operation.
- The effects of channel widths on a non-premixed RDE with cooling walls.

The solver developed in this work can be considered a prototype solver that has applied the AMR method for reacting flows on curvilinear meshes. Some fundamental detonation simulations are used to demonstrate the accuracy and robustness of the AMR method when solving the strong discontinuities in reacting flows. Owing to the efficiency of the use of adaptive meshes, it enables accurate simulations of 3D RDE and the wall effects with detailed chemistry mechanism. On the whole, the main novelties of this thesis are:

- Development of new solvers based on the AMROC framework with the abilities to solve reacting flows, such as unsteady shock-induced combustion and detonation problems.
- Application of the adaptive curvilinear solver to 3D viscous RDE simulations with detailed chemistry.
- Numerical studies on partially premixed 3D RDE with different premixing percentages.
- Numerical studies on varying wall temperatures in an operating non-premixed RDE.

The combination of curvilinear meshes with the adaptive strategy has been rarely adopted in the rapidly increasing RDE simulation fields. The use of such solvers enables us to study the problems that have been raised in conjunction with the development of the RDE experiments. These would

enhance our knowledge about the challenges in RDE simulations, and provide a basis for further experimental design.

1.3 Organisation of thesis

In Chapter 2, an introduction of detonation theory is firstly presented. A review of the rotating detonation engine is given, along with a review of the numerical simulations in this field. Then, a review of adaptive mesh refinement techniques used in RDE simulations is presented. The challenges on simulating high-speed reacting flows are analysed. The need of state-of-the-art numerical tools, that are capable of accurately simulating walls for RDE, is demonstrated.

One strategy is applying the adaptive mesh refinement technique on curvilinear meshes. The extensions on the AMROC framework are described in Chapter 3. The numerical methods implemented are described, including but not limited to the fluxes schemes, the reconstruction, the AMR operators, fluxes correction and geometric information.

The developed solvers are then verified and validated with some benchmark tests in Chapter 4. These tests contain the order of accuracy, conservation of the solver, the ability to solve inviscid discontinuities and viscous flows. After the verification and validation, the solver is used to demonstrate its capability of simulating the high-speed reacting flows in Chapter 5. The unsteady shock-induced combustion simulations and detonation simulations are compared with published experimental results.

Chapter 6 details the numerical configurations of the 2D and 3D rotating detonation cases according to different experimental set-ups. Mesh dependency studies are given with the comparison to theoretical solutions. Some numerical baseline cases are also compared with experimental results to test the accuracy of the simplified numerical set-ups.

The numerical results of rotating detonation are presented in Chapter 7 and Chapter 8, respectively. Chapter 7 focuses on the effects of premixing on the performance of RDE. In addition, a partially premixed RDE is simulated to explore the possibilities and improvement by premixed injection. In Chapter 8, the effects of wall conditions are analysed to investigate the roles of the cooling walls and the channel width on RDE performance.

Finally, Chapter 9 summarises the findings from the research and gives recommendations for future work.

Chapter 2 Literature review

2.1 Detonation theory and detonative engines

A detonation is a kind of reactive phenomenon involving a supersonic combustion wave which drives a leading shock wave, leading to the coupled propagation of both waves. It is commonly also known as explosion. The study of detonation has a long history and there are already some classical theories in this field. One of these theories is formulated by Chapman [43] and Jouguet [44], which can be employed to predict the thermodynamic states behind the detonation wave. For the state across a reacting wave, the basic conservation equations of mass, momentum and energy are given as

$$\rho_0 u_0 = \rho_1 u_1 , \tag{2.1}$$

$$p_0 + \rho_0 u_0^2 = p_1 + \rho_1 u_1^2 , \tag{2.2}$$

$$h_0 + \sum_{i=1}^{N_0} Y_i h_i + \frac{u_0^2}{2} = h_1 + \sum_{i=1}^{N_1} Y_i h_i + \frac{u_1^2}{2} . \tag{2.3}$$

The subscript 0 and 1 denote the reactants and products, respectively. ρ is density and u is velocity. p denotes the pressure and h is the sensible enthalpy of the mixture. Y_i and h_i are the mass fraction and specific enthalpy of formation for species i, respectively. N is the total number of species. Considering the conservation equations of mass and momentum, the mass flux can be derived as

$$\dot{m} = \rho_0 u_0 = \rho_1 u_1 = \sqrt{\frac{p_1 - p_0}{v_0 - v_1}} , \tag{2.4}$$

where v is the specific volume. Equation (2.4) requires that $v_0 > v_1$ and $p_1 > p_0$ (for detonation), or $v_0 < v_1$ and $p_1 < p_0$ (for deflagration). In the x-y plane $y = \hat{p} = p_1 / p_0$ and $x = \hat{v} = v_1 / v_0$, Equation (2.4) can be written as

$$\dot{m} = \sqrt{\left(\frac{y-1}{1-x}\right)\frac{p_0}{v_0}} . \tag{2.5}$$

The speed of sound a_0 in the reactants is given as

$$a_0 = \sqrt{\gamma_0 \frac{p_0}{\rho_0}} = \sqrt{\gamma_0 p_0 v_0} . \tag{2.6}$$

The Mach number is given as $M_0 = u_0 / a_0$, and Equation (2.5) can be rewritten as

$$\gamma_0 M_0^2 = \frac{y-1}{1-x} , \tag{2.7}$$

or equivalently

$$y = -\gamma_0 M_0^2 x + 1 + \gamma_0 M_0^2 . \tag{2.8}$$

Equation (2.8) defines a straight line on the *x*–*y* plane with a slope of $-\gamma_0 M_0^2$, which is called the Rayleigh line, as shown in Figure 2.1 with dashed lines. It represents the thermodynamic path of the flow transition from the initial state (1,1) to the post-wave state.

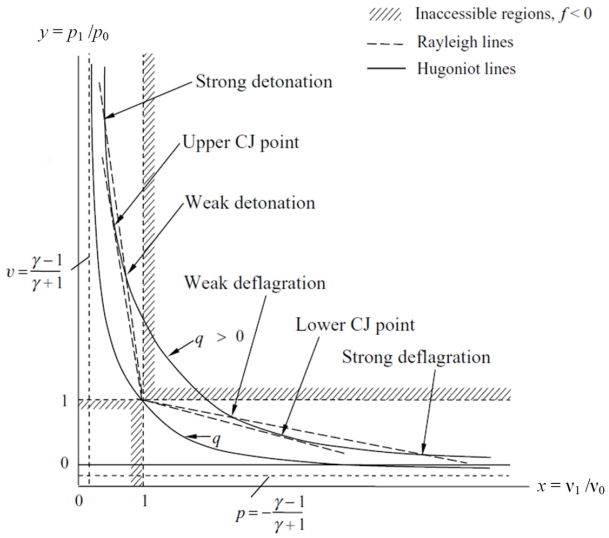

Figure 2.1 Schematic identifying the Rankine–Hugoniot solutions [45].

The difference between the enthalpies of formation of reactants and products can be calculated by

$$q = \sum_{i=1}^{N_0} Y_i h_i - \sum_{i=1}^{N_1} Y_i h_i , \tag{2.9}$$

where q indicates the chemical energy release. Replacing the velocity with the pressure and the specific volume, Equation (2.3) can be rewritten as

$$h_1 - (h_0 + q) = \frac{1}{2}(p_1 - p_0)(v_0 + v_1) . \tag{2.10}$$

This equation represents the Hugoniot curve and shows the locus of post-wave states for a given upstream state. If the calorically perfect gas assumption is introduced, the sensible enthalpy is given as

$$h = \frac{\gamma}{\gamma - 1}\frac{p}{\rho} . \tag{2.11}$$

The enthalpy in Equation (2.10) can be eliminated, and only the p and v are presented in the Hugoniot curve equation. Equation (2.10) can then be written as

$$y = \left(\frac{\gamma_0 + 1}{\gamma_0 - 1} - x + 2\frac{q}{p_0 v_0}\right) \Big/ \left(\frac{\gamma_1 + 1}{\gamma_1 - 1} x - 1\right) . \tag{2.12}$$

This equation indicates that the Hugoniot curve is in the form of a rectangular hyperbola in the *x*-*y* plane, as shown in Figure 2.1 with solid lines. The chemical energy release *q* determines the location of the Hugoniot curve.

According to the conservation laws, the solution should satisfy both the Rayleigh line and the Hugoniot curve simultaneously. Hence, for a given velocity of the reaction wave, namely the slope of the Rayleigh line, the intersections of the Rayleigh line and the Hugoniot curve are considered the post-wave state, as shown in Figure 2.1. However, the strong solution is generally unstable and the weak solution is usually not observed in practice [6]. Different states are defined by the Rankine-Hugoniot relations and Chapman-Jouguet (C-J) theory. When the Rayleigh line is tangent to the equilibrium Hugoniot curve, the intersection in the upper branch is the minimum-velocity and minimum-entropy solution, where the velocity is defined as C-J detonation velocity. This criterion is generally used to find the detonation velocity of a given explosive mixture.

The C-J theory assumes that downstream of the detonation the ideal equilibrium state can be found, which neglects the intermediate stage of reactions and is essentially a zero-dimensional analysis. Another model describing the one-dimensional detailed structure of detonation was established independently by Zel'dovich [46], von Neumann[47] and Döring [48], which is referred to as ZND model. Figure 2.2 displays the thermodynamic states along the direction of detonation propagating.

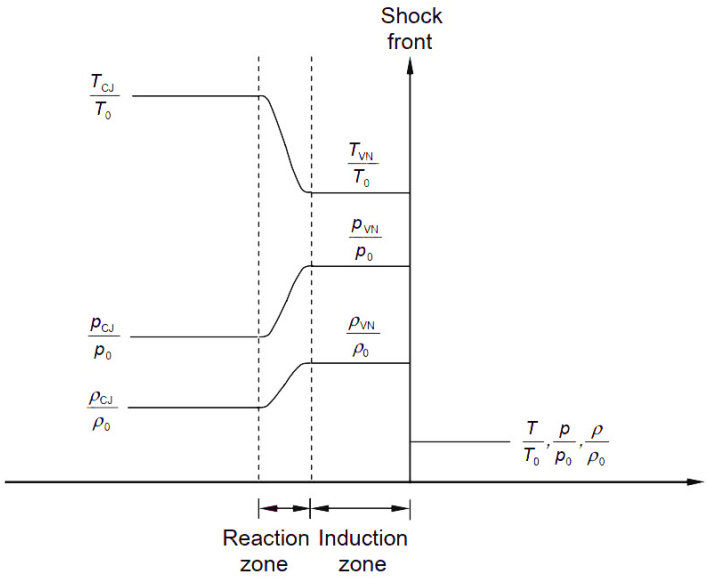

Figure 2.2 The ZND model for a detonation structure [6].

A detonation can be considered as a shock front followed by chemical reactions, where the region between the shock front and reaction wave is called the induction zone. In the induction zone, the reactants are preheated by the leading shock wave, where the active radical species are generated by thermal dissociation. When a sufficient number of free radicals is produced, the chain-branching reactions are triggered in the reaction zone. The rapid chemical energy release results in a rise in

temperature and a corresponding drop in pressure and density. The subsequent expanding burned products provide the forward thrust that supports the propagation of the leading shock [6].

In two or three dimensions, the detonation structure is more complex because of the transverse waves, which are intrinsic to detonation propagation. Several features can be observed at the detonation front. As shown in Figure 2.3 (a), an image of OH fluorescence from Ref. [49], the high concentration OH region corresponding to the reaction front is behind an incident shock, which is located between two curved Mach stems. High concentration OH can also be seen close to the Mach stems.

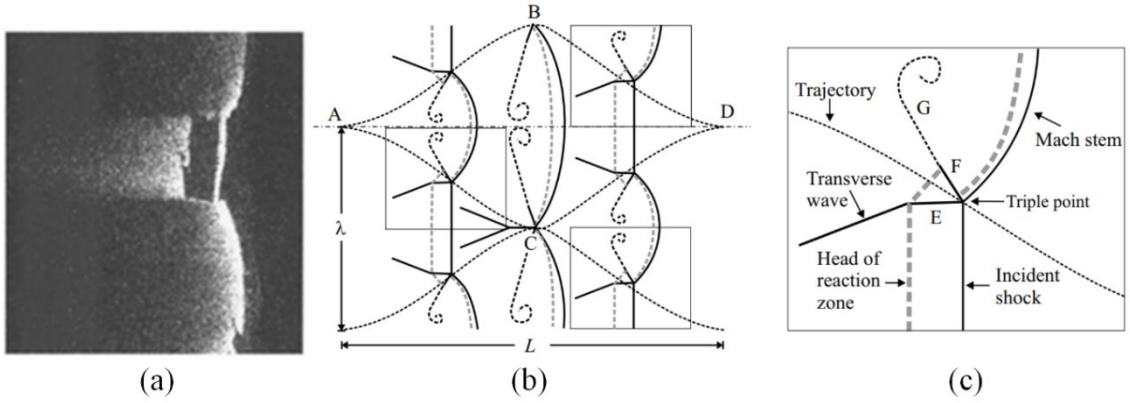

Figure 2.3 (a) Images of OH fluorescence behind detonation front [49], schematic of (b) regular detonation cells, (c) and enlargement of a triple point structure [30].

Figure 2.3 (b) and (c) show the schematic diagram of the detailed detonation front. The transverse wave, Mach stem and the incident shock merge in one point, which is named the triple point. A detonation cell is a closed “fish-scale” pattern cell formed between two trajectories of triple points (shown in Figure 2.3 (b) as the linked dash lines A-B-D-C-A). The length L and the width λ of the detonation cells are significant characteristic parameters for a detonation [30]. These parameters can be measured by the experimental smoke tracks method and are generally used to validate the chemical mechanisms in numerical simulations. The cell parameters of common detonative mixtures can be found in a published database [50]. The cellular structure is also observed in a three-dimensional detonation front. Similar triple point structures are generated, where there are more intricate transverse waves [30].

Figure 2.4 displays the schematic of the comparison between ideal 1D laminar flame and 1D detonation. The thermal diffusion of the products and mass transport leads to the reacting of the reactants in combustion, while the detonation is a self-compressed reacting process according to the ZND theory model. The leading shock wave compresses the reactants and results in the induction and ignition of the reactants. These coupling waves are considered as a detonation. The expansion of high-pressure products sustains the high-speed propagation of the detonation. The reaction zone is generally thinner than a subsonic flame under similar conditions front as the reactant is preheated and compressed by the shock wave.

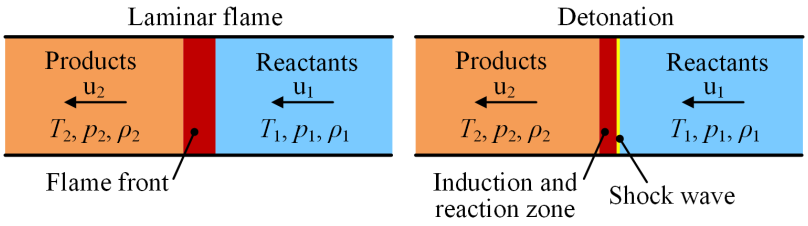

Figure 2.4 Schematic of 1D laminar flame and 1D detonation.

From these theories and descriptions above, the detonation is a kind of pressure-gain chemical reaction with a self-sustaining leading shock wave, which is essentially different from subsonic combustion or namely deflagration. Therefore, the application of detonations in propulsion and energy generation systems, where the subsonic combustion mode is presently dominant, also leads to considerable differences. Figure 2.5 shows a comparison of the thermodynamic cycles for different combustion processes. Related calculations indicate that the Fickett-Jacobs cycle, where a pressure-gain detonation works, can provide the highest efficiency compared with the Brayton cycle based on pressure-constant combustion [9].

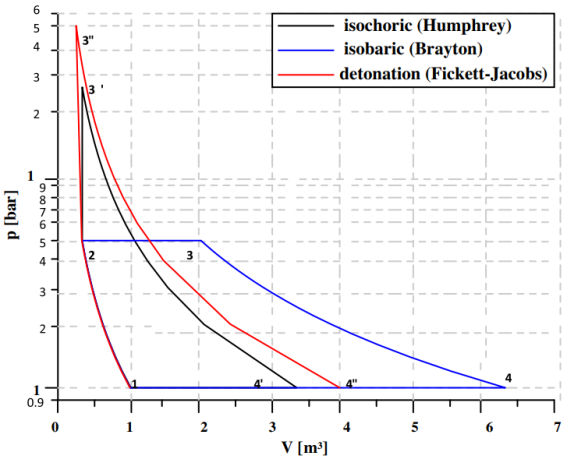

Figure 2.5 Thermodynamic Brayton-Joule, Humphrey, and Fickett-Jacobs cycles [9].

Due to the advantages of pressure-gain combustion for thermal efficiency, a broad range of potential detonation-based engines have been put forward, i.e., the pulse detonation engine (PDE) [51], the oblique detonation wave engine (ODWE) [52] and the rotating detonation engine (RDE) [20], etc. The general PDE is a tube-like device [53] as boxed with dashed lines in Figure 2.6 (a). The typical PDE operation cycle consists of serval stages [54], such as the filling of the fuel and the oxidizer, ignition, deflagration to detonation transition (DDT), the exhaust and a purge for the next cycle as demonstrated in Figure 2.6 (b). To decrease the tube length, different devices are required to shorten the DDT time and run-up distance, including solid obstacles such as Shchelkin spirals [55] or fluidic obstacles such as jets in cross flow [56]. As PDE needs the filling, ignition and DDT in every cycle, the operating frequency at $O\ (10^1) \sim O\ (10^2)$ Hz is limited by the valve's frequency and the DDT process.

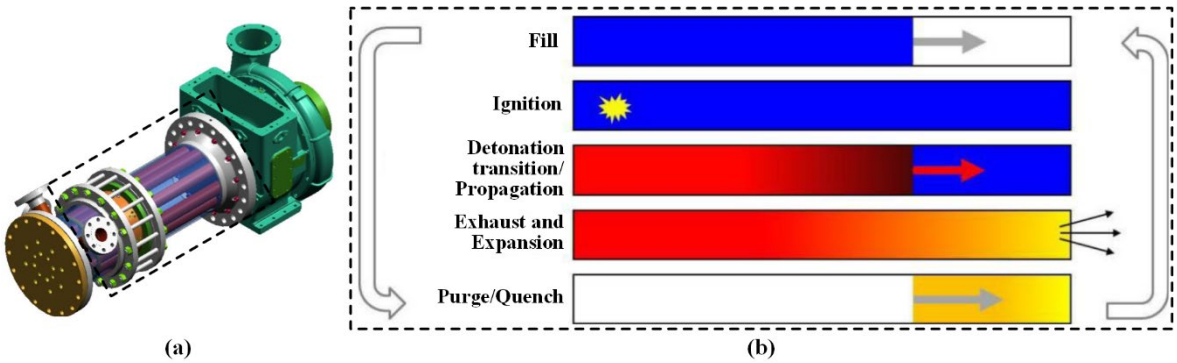

Figure 2.6 Pulse detonation-turbine hybrid engine [53] (a) and the schematic of PDE cycle [54] (b).

Another detonation-based engine is the ODWE which stabilizes the detonation through a wedge-shaped device or a ramp, as shown in Figure 2.7 (a). Its operation concept is similar to that in a conventional scramjet except for adopting an oblique detonation instead of supersonic combustion as a power source. The fuel and oxidizer are mixed upstream followed by a standing shock wave. The lower limit of ODWE operation is the C-J detonation velocity generally at Mach 5 to stabilize the oblique shock and induce its coupling with the reaction front. For this reason, ODWE is more likely to work in a high-speed flow and has potentials on applications to hypersonic flight. The requirement of a high-speed and high-enthalpy wind tunnel is also a great challenge for the ground experiments [58].

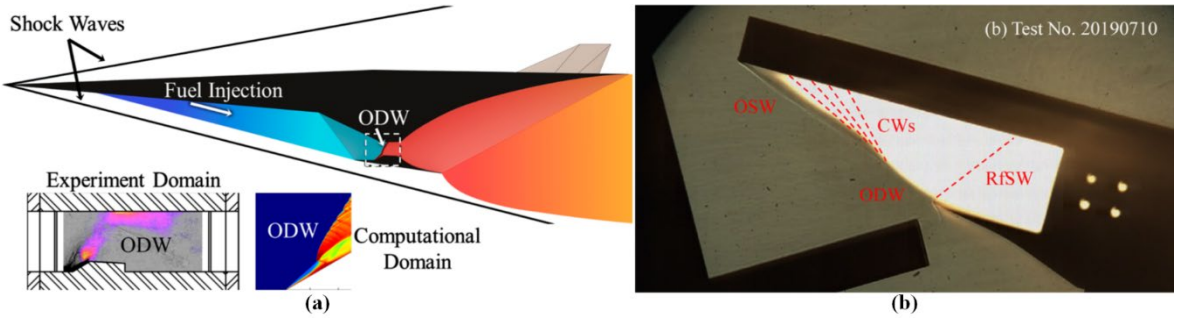

Figure 2.7 Schematic of ODWE concept [57] (a) and the schlieren photograph of ODWE experiments (b) [58].

During the last twenty years, the RDE has been extensively investigated theoretically, experimentally and numerically with varying geometries including the annular cylinder [59,60], the hollow cylinder [61,62] and the disk [63,64]. This thesis will only concentrate on the annular RDE, which is the most tested configuration. This kind of RDE uses one or more continuously propagating detonation waves in an annular chamber. Figure 2.8 shows a simplified physical model of an annular RDE and the photograph of the RDE operation in space. In an RDE, the fuel and air are both injected from the head of the chamber. A pre-detonator or a spark plug is implemented for igniting the detonation in the engine. A single detonation wave is depicted in Figure 2.8 (a), but there may be multiple detonation waves in different operating conditions. These waves rotate in the annulus and consume the reactants feeding continuously from the arrayed injectors.

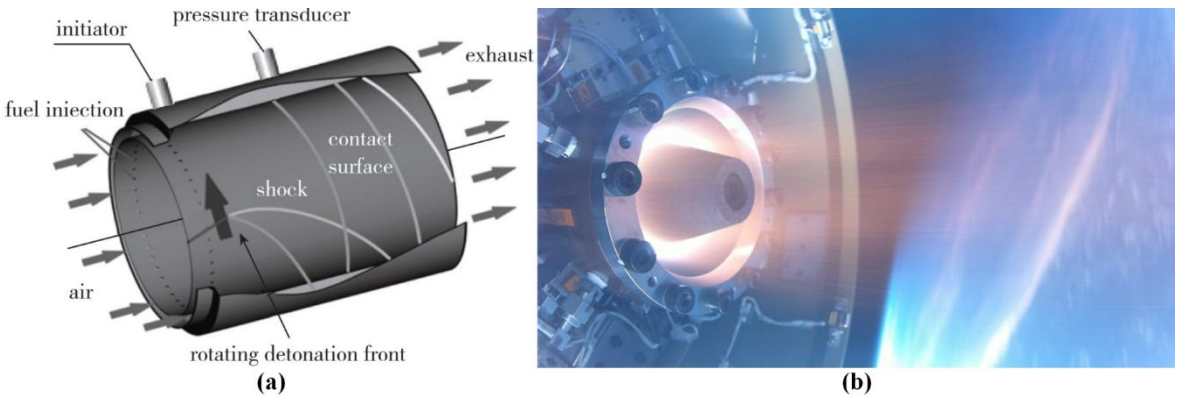

Figure 2.8 Schematic diagram of an annular RDE [9] (a) and RDE operation in space (b) [65].

As the detonation waves travel around the annulus at a high velocity (1.5 - 3 km/s), the fresh reactants injected into the combustor can only sustain a short period of time before being consumed. After that, the burnt high-pressure products are exhausted along the axial direction of the chamber, which provides the thrust for the whole RDE. Compared with PDEs, the continuous rotating detonation in RDEs enables a higher operating frequency at O (10^3) Hz without frequent initiation of detonation. In addition to the propulsion field, RDEs have more potential to be applied to a land-based power generation system due to their wider working range at relatively low-speed regions compared with ODWEs. In summary, different types of detonative engines have different benefits, limits and application scenarios [5]. This thesis only focuses on the RDE in the next chapters and the other detonative engines are not further discussed.

2.2 Rotating detonation engine (RDE)

In the 1960s, Voitsckhovskii [66] first studied the feasibility of a continuous rotating detonation engine with acetylene/oxygen premixed gas as propellants and verified the fundamental operating mode in the RDE at Lavrentyev Institute of Hydrodynamics (LIH) in Russia. Subsequently, Nicholls et al. [67] and Adamson et al. [68] applied this mode of detonation to rocket propulsion systems and carried out feasibility studies for the RDE at the University of Michigan. Although the tests were successful with a rotating detonation wave in the engine, it is observed that the detonation could hardly propagate at a self-sustaining mode. In the following 50 years, experimental studies on RDE were mainly conducted by Bykovskii et al. [69,70] at the LIH in Russia. The effects of combustion chamber configuration, outlet back pressure and other design parameters on RDE performance were investigated. Bykovskii's systemic work showed the potential and feasibility of RDE applied to propulsion devices, which influenced the development of RDE [10]. After entering the 21st century, the RDE, which satisfies the increasing demand for efficient, clean, and sustainable power and propulsion processes, has gradually attracted more attention of researchers.

Frolov et al. [71] tested the operating characteristics of hydrogen-air RDE with an outer diameter of 50 and 100 mm, respectively, as shown in Figure 2.9. They compared the specific impulse and thrust

of the RDE and a conventional rocket engine using pressure-constant combustion. The inflow pressure is controlled to achieve the same injection condition. The results show that the RDE can produce more thrust than the rocket engine even with less hydrogen injected. The specific impulse of the RDE is also increased by about 6% to 7% compared with the rocket engine under varying air-fuel ratios. Their experimental tests confirmed the advantages of the RDE applied to conventional propulsion systems. In their following work [72], the RDE was implemented within a rocket engine and fire tests were conducted. The experiments proved the possibility of using a liquid fuel film in the RDE combustor for both the stable operation and the active thermal protection.

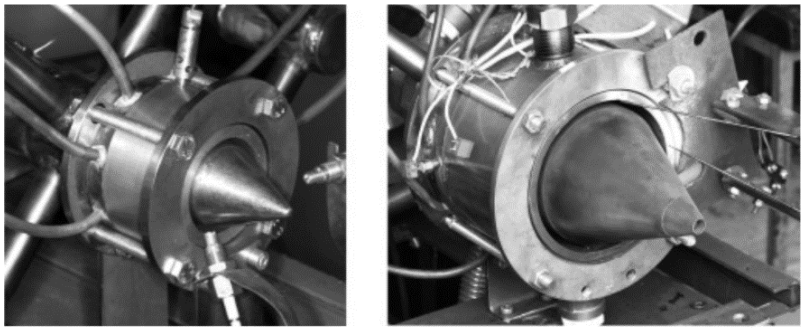

(a) (b)

Figure 2.9 Photographs of the RDE from Centre of Pulse Detonation Combustion in Moscow with an outer diameter (a) 50mm and (b)100mm [71].

Kindracki [73] used kerosene/air as a propellant in RDE experiments to study the initiation and propagation process of rotating detonation waves. They found that the kerosene/air mixture cannot achieve the self-sustained propagation of rotating detonation waves at room temperature, whereas the air with added hydrogen can initiate the detonation and maintain a self-sustained propagation mode in RDE. Furthermore, Wolanski [74] replaced the original combustion chamber in the GTD350 turbojet engine with a rotating detonation combustion chamber and conducted a large number of experimental tests. The experimental device is shown in Figure 2.10. In the experiment, a stable rotating detonation wave was successfully obtained by adding a small amount of hydrogen into kerosene. The experimental results also verified the feasibility of the engineering application of RDE on a turbine engine.

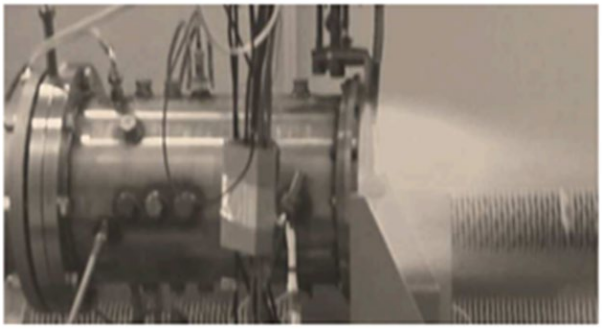

Figure 2.10 Photographs of the RDE in operation implemented within GTD350 turbojet engine from the Warsaw University of Technology [74].

Stephen et al. [75] carried out systematic experiments for RDE injection dynamics, small-scale RDE chamber design, inlet and outlet flow measurement, and exhaust emission measurement. In addition, a large-scale RDE test bench was designed independently using methane/air as propellent as shown in Figure 2.11. The operability of this RDE over a range of operating conditions is evaluated. The strong annular Mach disk and the shock train are observed in the supersonic exhaust. A recent work was reported in Purdue University using MHz-rate diagnostics in the RDE experiments [76]. The wave features were observed by the simultaneous orthogonal views of chemiluminescence and hydroxyl planar laser-induced fluorescence (OH-PLIF). The effects of reactant stratification were analysed in a bifurcated dual-wave detonation system.

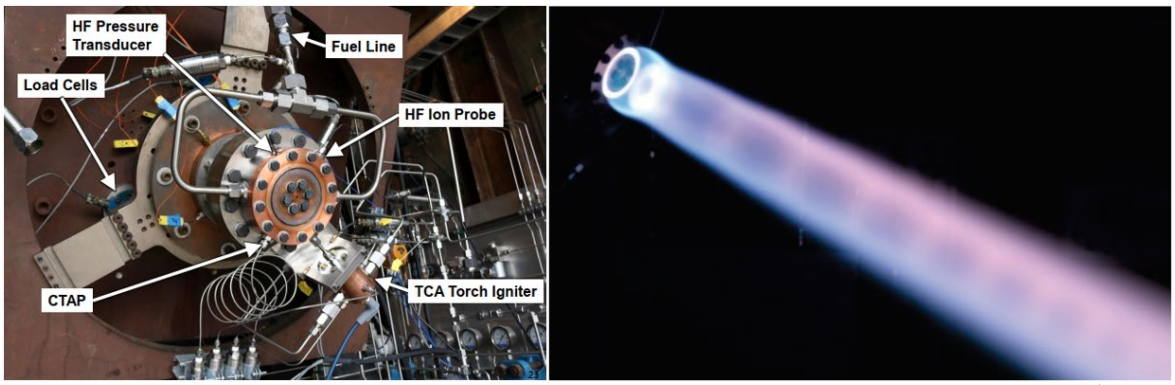

Figure 2.11 Photographs of the RDE from Purdue University (a) on test stand, (b) in operation [75].

Rankin et al. [77,78] replaced the outer wall of the RDE with transparent quartz glass. The experimental device is displayed in Figure 2.12. They used OH-based chemiluminescence methods to study the features in the flow field of the RDE, such as detonation wave height, detonation wave angle, oblique shock wave angle, shear layer angle and contact surface angle. Subsequently, this technology was adopted to conduct research on non-premixed RDE about the influences of air mass flow rate, equivalence ratio, air injection area, and fuel injection schemes.

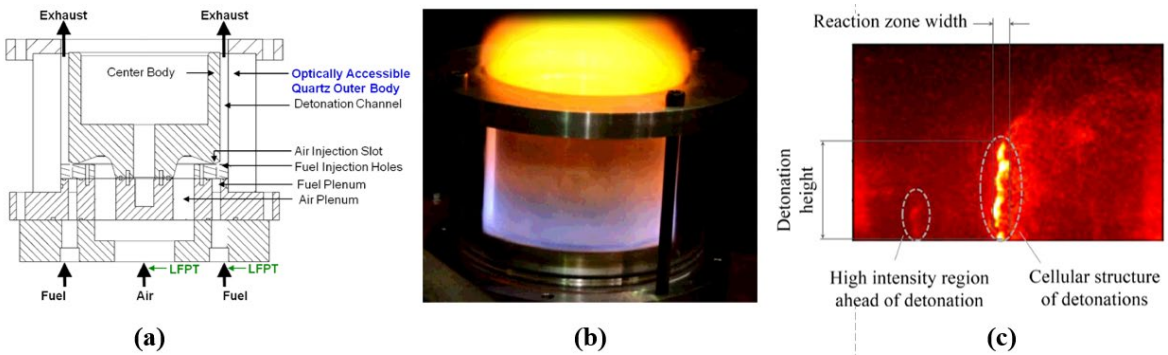

Figure 2.12 Images of the optically accessible RDE (a) schematic diagram, (b) photograph in operation, (c) instantaneous OH* chemiluminescence image [77].

The experimental results show that a single-wave to double-wave transition phenomenon occurs in the combustion chamber at a higher mass flow rate. It was found that the distribution of OH in the

chamber will become more scattered under lean conditions, while the OH under rich conditions is mainly concentrated in a narrow area near the detonation wave front. In the experiment, the high-pressure area in front of the detonation wave and the cell structure of the detonation wave were observed as shown in Figure 2.12 (c).

Anand et al. [79-81] conducted considerable experimental research work on RDE with different geometric injection configurations under different air and fuel mass flow rates (air mass flow 300 ~ 500 g/s and equivalence ratio 0.5 ~ 1.9). The experiment observed four kinds of instability phenomena: chaos instability, waxing and waning instability, mode switching instability and longitudinal pulsed detonation instability, as shown in Figure 2.13. They also carried out experimental studies on the injection schemes for the RDE, including three different fuel injection schemes and two air injection schemes. The experimental results show that the different injection schemes have similar working characteristics, and in the fuel injection scheme with the maximum length-to-diameter ratio, unstable detonation is observed in the RDE. The flow field characteristics of the fuel/air plenum of the RDE were also investigated. A strong pressure wave from the rotating detonation wave propagated back to the air injection port in the experiments.

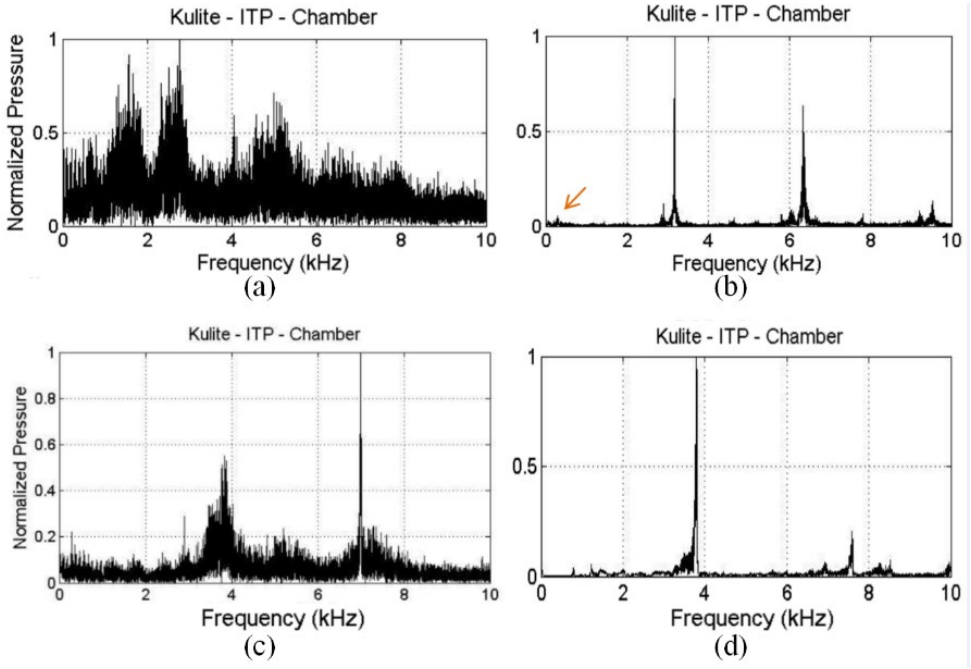

Figure 2.13 FFT plot of pressure in RDE under varying regime (a) chaos instability, (b) waxing and waning instability, (c) mode switching instability and (d) longitudinal pulsed detonation instability [79].

A hydrogen/air RDE manufactured by Pratt and Whitney was studied in the US Air Force Research Laboratory for further testing and development [82]. Conditions with different flow rates and equivalence ratios were tested to obtain the operating space matrix. In their test, the addition of extra oxygen not only increased the range of thrust output and operability, but also changed the operation mode from single-wave mode to two-wave mode. Figure 2.14 displays the photograph from the exit

of the RDE. The observed two detonation waves were co-rotating. This two-wave mode only occurred in a transient process. After two counter-rotating detonations collided with each other, two new co-rotating waves would be generated. In some cases, the two detonation waves would merge into a single wave or cease propagation.

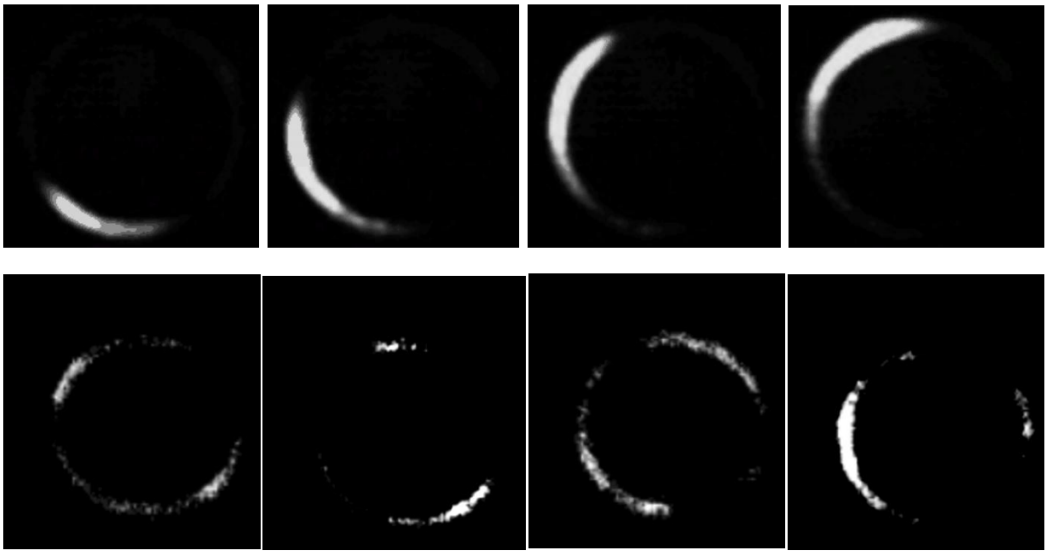

Figure 2.14 Photograph from the exit of the RDE in a single-wave mode (top row) and a two-wave mode (bottom row) [82].

The Laboratory of Combustion and Detonation (LCD) at the French National Centre for Scientific Research (CNRS) [83] conducted a study of the detonation process of a continuous rotary detonation engine using ethylene and oxygen as a propellant. High-speed photography and high-frequency pressure sensors were used to capture the detonation waves in the RDE. Figure 2.15 shows a multi-wave mode in the experiments with a structure consisting of seven waves. The results indicate that the occurrence of a state with multiple waves is related to the mass flow rate of the propellant. This is a dynamic and adaptative process when the mass flow rate is increased. The fresh gas mixture is injected with a higher height, as a result, the detonation wave tends to be unstable and produces additional wave heads.

Liu et al. [84] studied the effects of varying mass flow rates and equivalence ratios on hydrogen RDE at the National University of Defense Technology. Single-wave and hybrid two-wave modes were observed in the experiments. Different fuels were also tested in their following work, such as ethylene [85] and ammonia [86]. In addition, they experimentally verified the feasibility of air-breathing hydrogen RDE [87] in a direct-connect facility as shown in Figure 2.16. The detonation was successfully initiated and sustained more than three seconds in a supersonic flow, showing a relatively long-duration operation at that time. A similar air-breathing RDE was then tested using ethylene [88] as fuel and enhanced the understanding of the application of RDE in air-breathing mode compared with the common rocket-based mode.

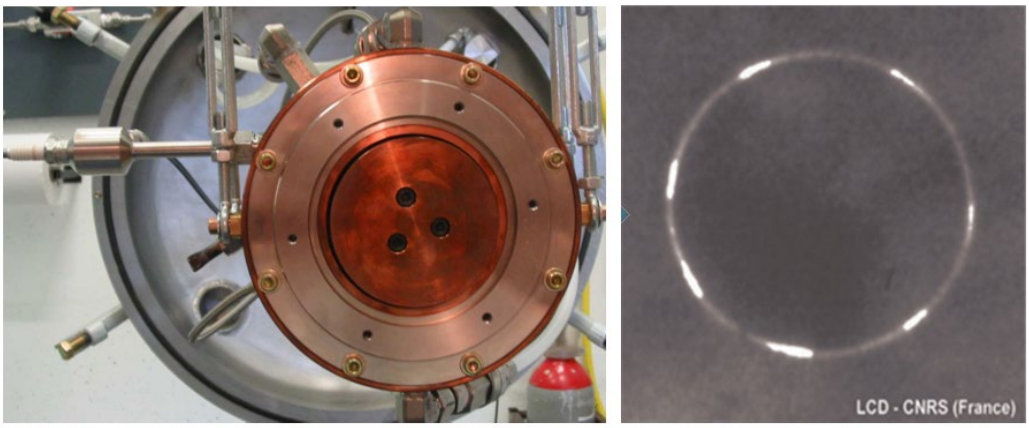

Figure 2.15 Photograph of the RDE (a) from French Laboratory of Combustion and Detonation and the high-speed photography of multi-wave mode in operation (b) [83].

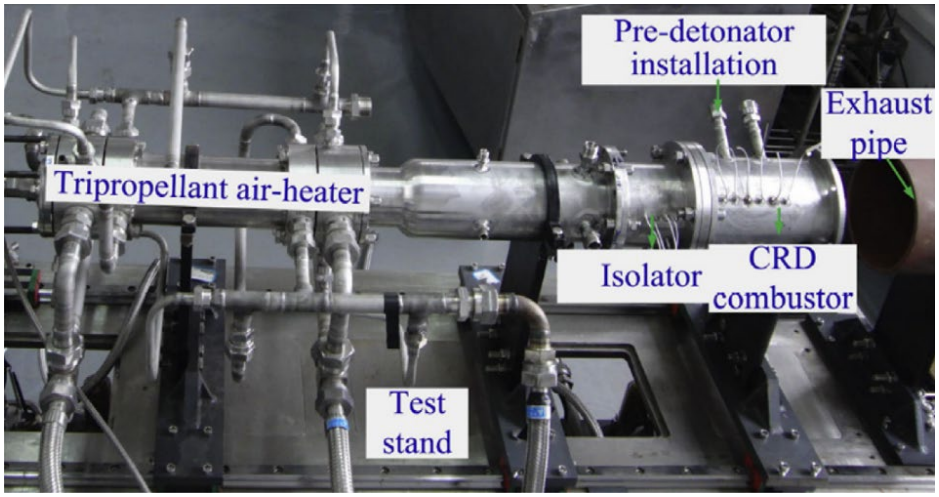

Figure 2.16 Photograph of the RDE in a direct-connect facility at the National University of Defense Technology [87].

Ma et al. [89,90] conducted experimental studies on the initiation of detonation in an RDE at Nanjing University of Science and Technology. An ordinary automotive spark plug, a high-energy spark plug and a thermal-jet tube were tested within a similar initial condition. The results showed that the ignition schemes had a limited influence on the operating frequency of RDE, whereas using a thermal jet shortened the formation time of detonation, as shown in Figure 2.17. Control of operation mode was achieved in the experiment by varying the mass flow rate and equivalence ratio [91]. Besides, they explored the effects of turbine guide vane on hydrogen RDE as an attempt to integrate the RDE combustor with conventional turbine engines [92,93].

Wang et al. [94,95] carried out experiments on active control of hydrogen-oxygen RDE. The multiple rotating detonation waves were induced through a tangential flow from the pre-detonator. This research group at Peking University conducted further hydrogen-air experiments on the study of the RDE operation mechanism, such as ignition, quenching, reinitiation and the stabilization of rotating detonation. Xie et al. [96-98] analysed the instabilities in a hydrogen RDE at Tsinghua University by

varying the mass flow rates and equivalence ratios. The experimental operating diagram indicated that the occurrence of fast deflagration is mainly determined by the fuel-injection conditions and the thermoacoustic instabilities. The high-frequency chaotic instability and low-frequency bulk mode instability were discussed. They also found that the increasing oxygen volume fraction in the air extended the rich/lean limit for a stable operation RDE.

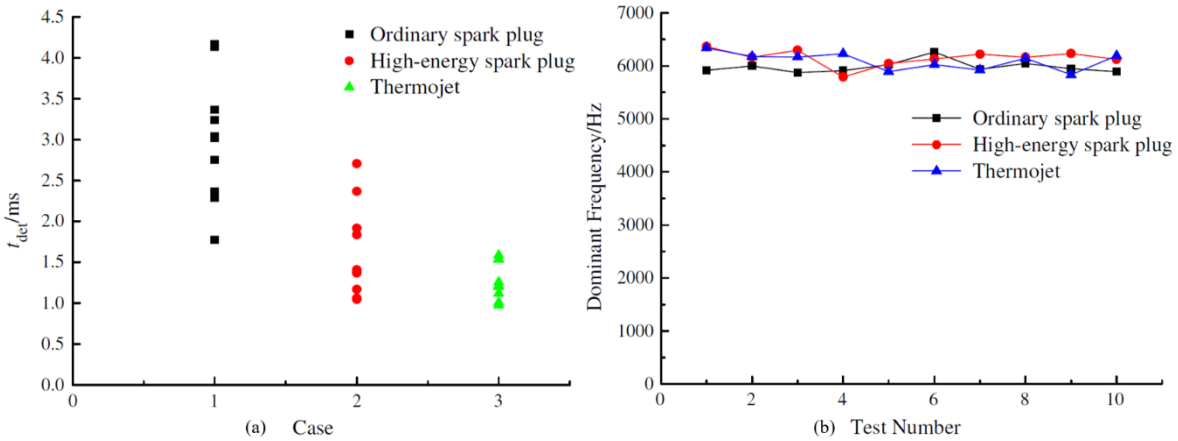

Figure 2.17 Statistics of detonation formation time (a) and the dominant frequency in an RDE [90].

A recent milestone in experiments was the first RDE flight operation record from the Institute of Space and Astronautical Science (ISAS) of the Japan Aerospace Exploration Agency (JAXA). A methane-oxygen RDE was stowed in a sounding rocket "S-520-31" and the space test project was conducted by Kasahara et al. [65]. The operating duration of RDE was up to six seconds in the space environment as shown in Figure 2.18. It reported a time-averaged thrust of 518 N and a specific impulse of 290 ± 18 s in the flight test.

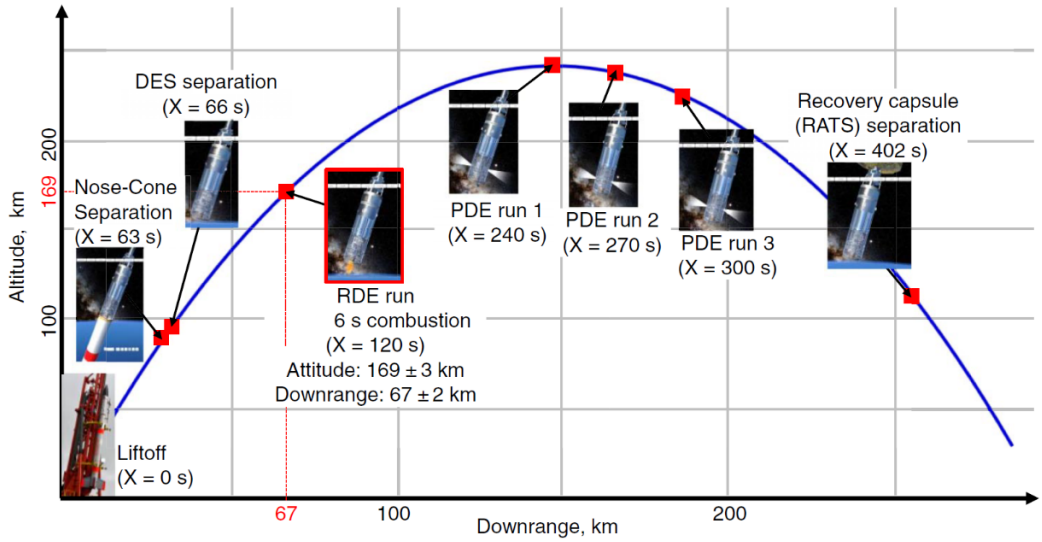

Figure 2.18 Flight sequence of detonation engine system from JAXA [65].

NASA reported its first full-scale RDE fire hot test at Marshall Space Flight Centre [99]. Gaseous hydrogen and liquid methane were adopted as propellants with liquid oxygen. In their experiments, copper-based alloys are combined with the additive manufacturing method to build up the RDE. De-

ionized water was used as active cooling and the liquid methane was adopted for regenerative cooling. The experiment reported a long duration of 133 seconds in a single test, indicating the used material and cooling system enabled the RDE to work in thermally extreme conditions.

In summary, researchers have carried out a large number of theoretical and experimental studies on different aspects of RDE, such as the geometry of the RDE chamber, the propellant injection conditions, the effect of initiation, the performance of blending fuels, the thrust of RDE implemented to turbojet engine, and the specific impulse of RDE compared with rocket engine, etc. Stable propagation of rotating detonation has been achieved and observed by experiments in different research groups around the world. Despite these achievements, there are still many challenges for further applications of RDE. One of the greatest challenges is to enhance the fuel-oxidizer mixing during a very short period due to the high velocity of detonation. Another increasing concern is thermal management of RDE for future long-duration operations.

2.2.1 Partially premixed RDE

As perfectly premixed injection may lead to flashbacks in RDE experiments, partially premixed schemes received increased attention in recent years. George et al. [100] attempted experiments in which hydrogen was blended into an ethylene-air RDE as shown in Figure 2.19. The basic concept is using the chemically active hydrogen as an assistant for the initiation and avoiding the flashback in a premixed hydrogen-air flow. However, the experiments went through flashback and instabilities when extending the operating duration and transition from a stable blended fuel state to a pure ethylene-air state.

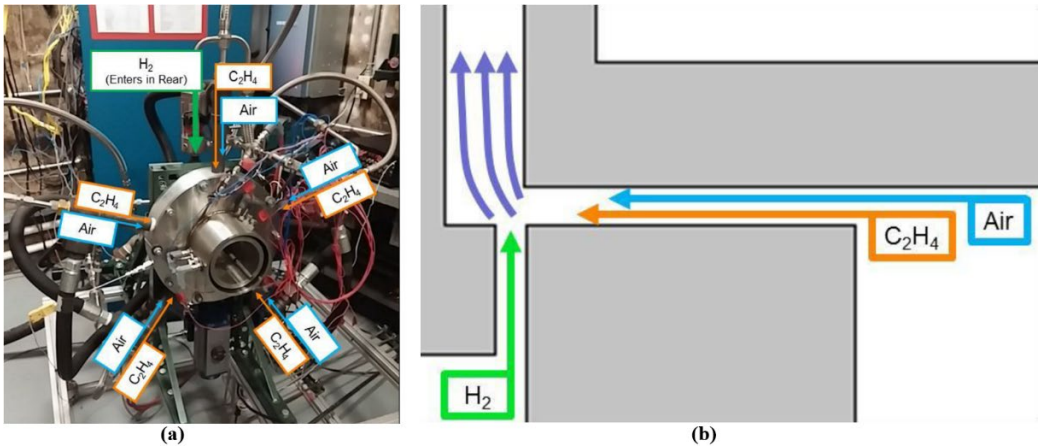

Figure 2.19 Photograph of hydrogen/ethylene fuel blending RDE (a) and schematic of the injection scheme (b) [100].

Li et al. [101] conducted RDE experiments based on liquid Jet A-1 and heated air. To improve the mixing, the liquid fuel was vaporised by a small amount of heated air before being injected into the fuel plenum. The concentration of the vapour-phase was set to 10%, higher than the upper explosive

limit. This resulted in a locally fuel-rich partially premixed condition and successfully prevented potential flashback into the fuel plenum.

Dunn et al. [18] carried out partially hydrogen-air RDE experiments with a premixed percentage from 5% to 20% in the air flow as shown in Figure 2.20. It was observed that the number of detonation waves increases from two to three only at a bypass rate of 5%. The detonation velocity increased slightly due to the presence of the premixture. Their following work [19] confirmed that the presence of premixing in the air flow increased detonation wave speeds. This increase was independent of the amount of the premixing fuel under different equivalence ratios.

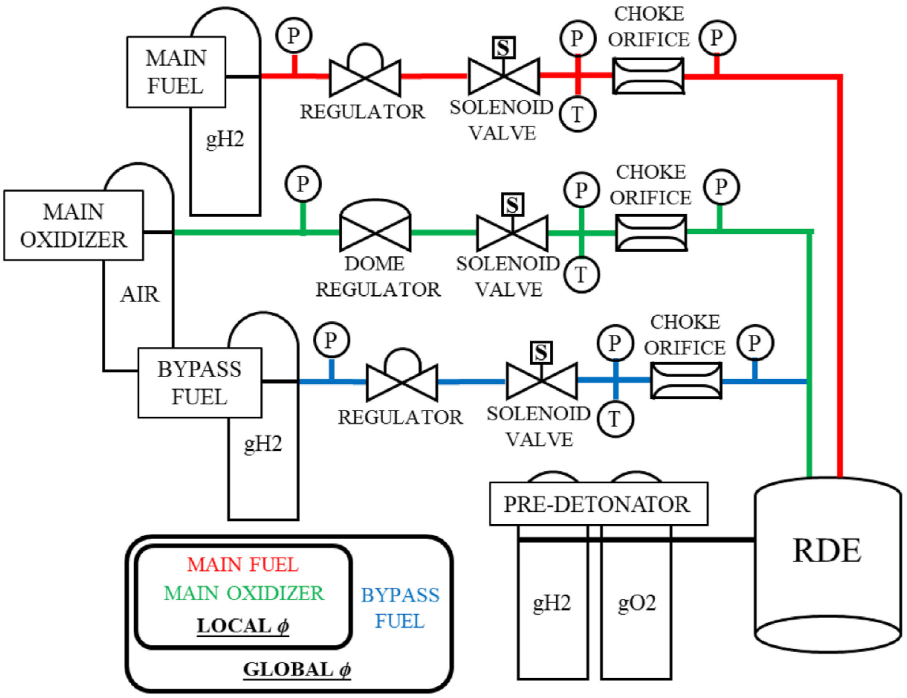

Figure 2.20 Schematic of the flow system piping and instrumentation diagram [19].

Ayers et al. [102] studied the effects of mixing in a variably premixed RDE with a narrow-channel configuration. In their experiments, a novel design for the injection enabled the operation with fully premixed, partially premixed, and non-premixed injection schemes. As depicted in Figure 2.21, a porous medium was adopted for the premixture injector to prevent flashback from the combustion chamber to the premixture plenum. Slight localized erosions in the material were observed after the operation. When reactants were more than 50% premixed, the experimental findings indicated that the detonation velocity increased from 57% to 65% of the C-J velocity.

Fiorino et al. [103] tested partially premixed schemes in a small-scale ethylene RDE. The premixed jet in crossflow enhances the local mixing and detonation stabilities. Xu et al. [104] conducted partially premixed kerosene/air RDE experiments. Their results showed that the combustion efficiency increased with increasing premixed equivalence ratio. The operation fuel-rich limit was extended when the partially premixed strategy was used. The flashback was observed when the

premixed equivalence ratio was excessively high. This led to a decrease on the combustion efficiency and even a detonation failure due to the pre-burning.

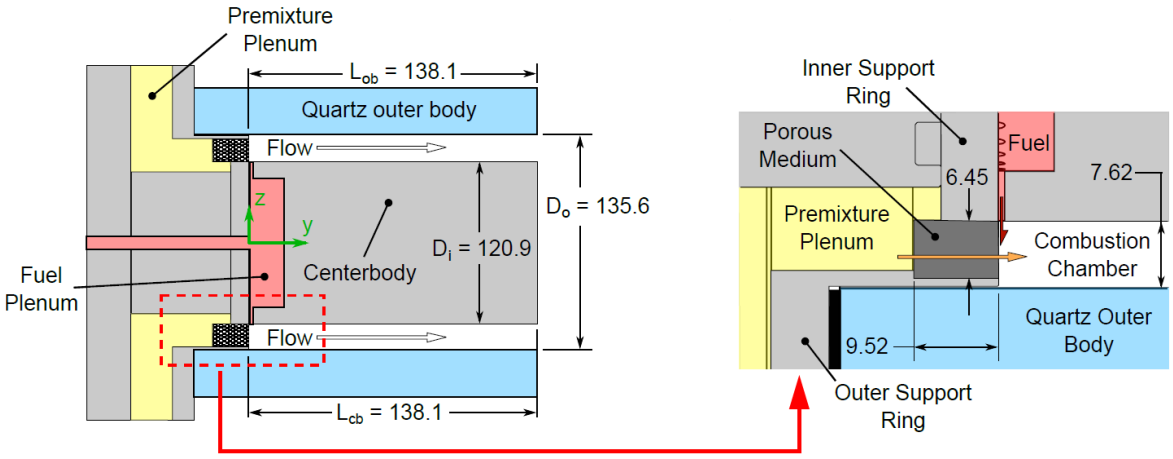

Figure 2.21 Cross-sections of the injection scheme for the configuration used for the variably premixed RDE [102].

There are only a limited number of studies focusing on the partially premixed RDE experimental configuration. Different premixing percentages were tested in the experiments based on varying fuels. Although additional measures have been taken in some of the experiments to suppress flashback, it is still risky to conduct premixed and partially premixed RDE experiments. There are obvious difficulties in accessing the internal flow field to improve the understanding of the effects of partial premixing on RDE performance.

2.2.2 Wall cooling of RDE

Bykovskii and Vedernikov [23] conducted pioneering experiments of measuring the heat flux to the walls of acetylene and hydrogen RDEs. The maximum temperature of the wall surface was estimated at around 513 K and the minimum temperature rise was recorded at around 393 K in the middle and the end of the combustor, respectively. The maximum heat flux was recorded in the heat-release region, indicating that the heat flux peaks generally occurred at the detonation heads. These heat flux peaks (~2.5 MW/m^2) are two to three times higher than the average heat flux (~1 MW/m^2) in the chamber. The fresh mixture was regarded as a regenerative cooling of the combustor walls, and they also suggested active cooling for a long-duration test.

Theuerkauf et al. [24,25] adopted water cooling in hydrogen RDE experiments as shown in Figure 2.22. The coolant was stagnant through the cooling passages in the walls of the RDE during each test. The measured transient temperature response data showed that the temperature increased during the startup stage of the RDE operation. This temperature rise ranged from 200 K to 240 K after the RDE worked in a stable mode. The transient peak heat flux was reported over 9 MW/m^2 and below 1 MW/m^2 at the base of the detonation channel.

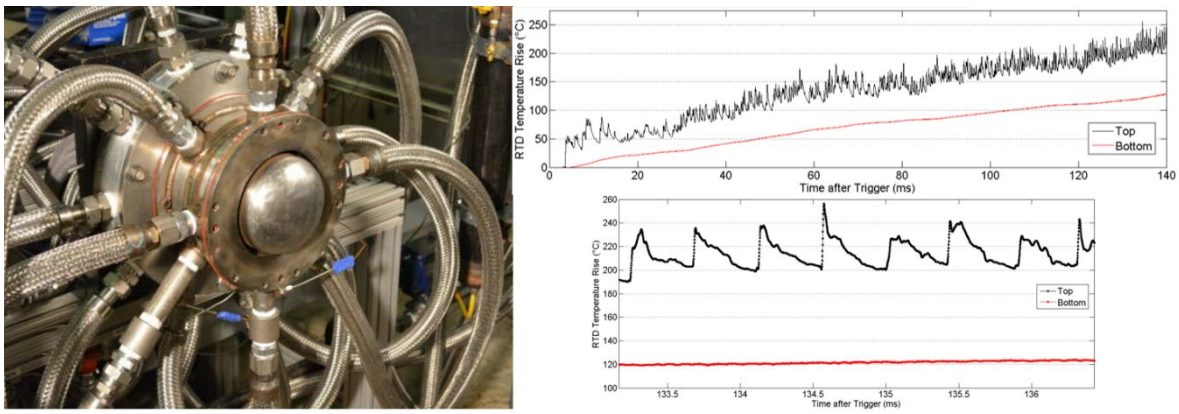

Figure 2.22 Photograph of the water-cooled RDE and its wall temperature rises recorded by resistance temperature detectors during operation [25].

The wall temperature rises in a long-duration test were more severe, as introduced in the work of Ishihara et al. The ethylene-oxygen RDE experiments ran without cooling, and nitrogen was injected after the operation as a gaseous cooling for the hardware. The heat flux in the experiments was reported on the order of 4 MW/m^2. The wall temperature of thickness 1.0 mm history showed a maximum temperature rise at around 900 K, as presented in [21].

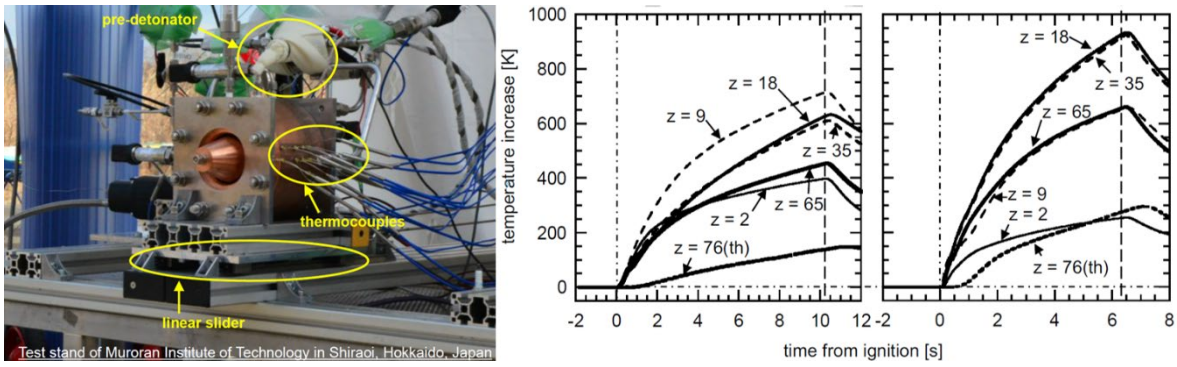

Figure 2.23 Photograph of the RDE ground test system with gaseous cooling after operation and its wall temperature rises [21].

Using the regenerative gaseous cooling was promising for a long-duration RDE operation. The air-cooling system simplified hardware manufacturing compared with the water-cooled system, and the regeneration ensured the energy transfer from the wall to the coolant remained in the engine during the operation [20]. The influences of wall cooling on multi-wave stable operation in an RDE were still unknown. The number of detonation heads in the RDE had a distinct influence on the local transient flow properties, which impacts the convection coefficient flow. This resulted in a complex relationship between RDE operation and the wall cooling system [105]. Besides, as water-filled walls brought difficulties in the non-invasive measurement for optical observation, the effects of cooling walls on the internal flow field remained unclear. It was necessary to find a way to explore the interactions between the cooled walls and the detonation waves, such as numerical simulations.

2.3 Numerical investigations of RDE

The propagation of rotating detonation waves is complicated and influenced by multiple factors. Investigating the features of the internal flow field of RDE is still difficult by experimental methods because it is challenging to capture the details of the highly unsteady and high-speed flow field in experiments. Numerical simulations provide the possibility to study these problems. Current analyses of the internal flow field structure and detonation wave propagation process of RDE are mostly based on numerical simulation results [6,7,9].

As shown in Figure 2.24, the 3D RDE can be unwrapped into a 2D plane. From the 2D view, a rotating detonation consists of a detonation front, an attached oblique shock, a transverse wave and a slip line. The detonation front propagates with the C-J velocity and consumes the propellant injected from the bottom of the chamber. The contact surface between fresh fuel and burnt products can also be observed. The unwrapped, or namely unrolled, 2D model is a practical simplification, which assumes that the parameters of the detonation wave are consistent along the radial direction. If the radius of the outer wall is large enough compared with the channel width, the 3D stretch and curvature effects can be neglected to some extent.

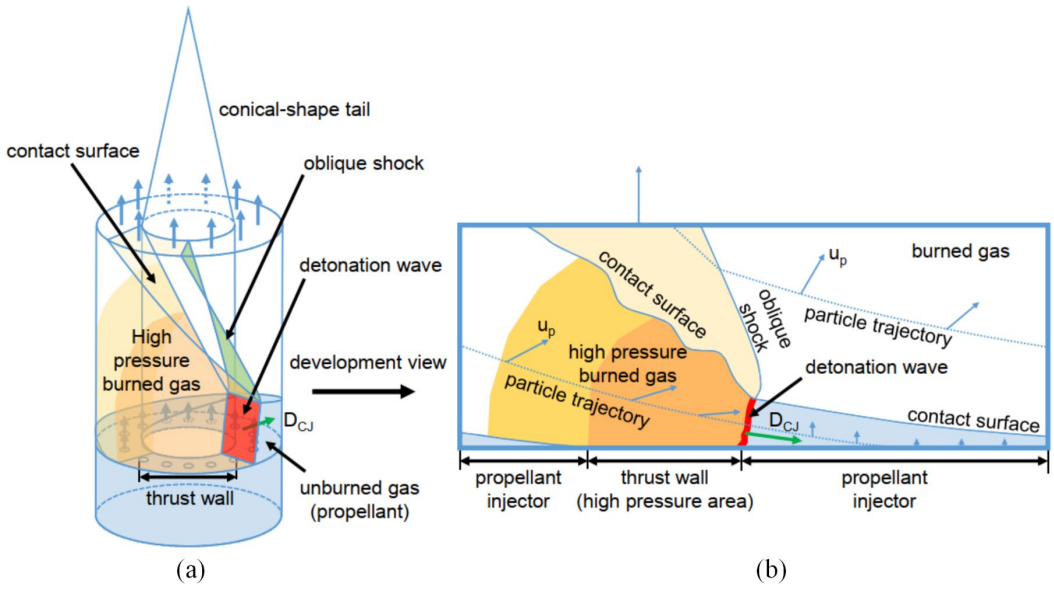

Figure 2.24 Schematic diagram of an annular RDE with an aerospike nozzle (a), and unwrapped plane of the combustor (b) [8].

At the early stage of RDE simulation studies, the 2D simulation played a significant role in investigating the inner flow field and the rotating detonation structure. Schwer et al. [106] simulated the unwrapped 2D plane based on Euler equations. In their simulation, a single-step Arrhenius reaction mode was used to study the hydrogen-air RDE. Figure 2.25 shows the flow structure of RDE from this work. The classical detonation wave structure was observed in the results, such as the rotating detonation wave, oblique shock wave, slip line, transverse wave and contact surface.

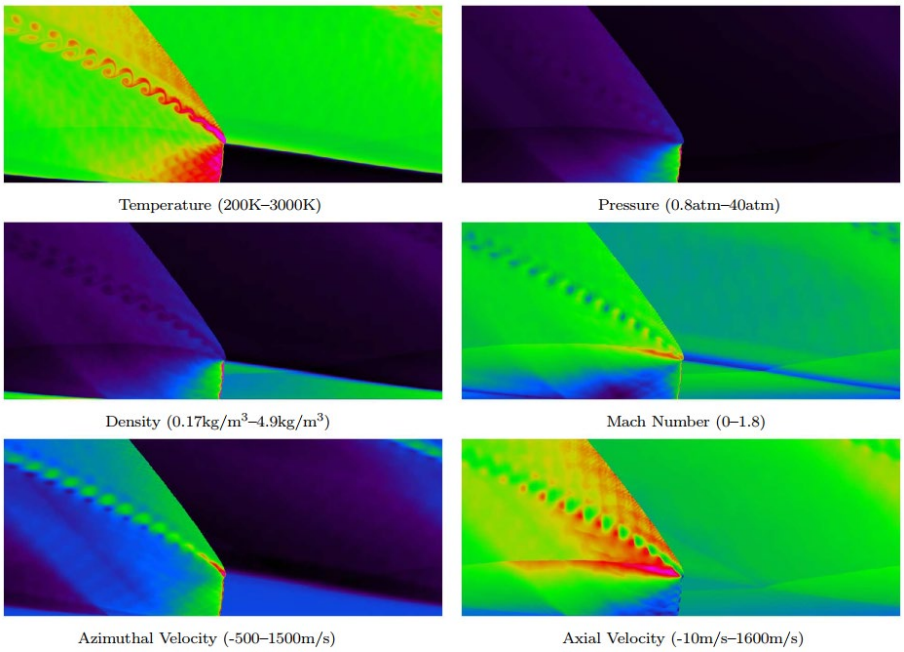

Figure 2.25 Unwrapped 2D simulation of hydrogen-air RDE [106].

In their subsequent work [107], the same numerical method was adopted to study the problem of high-pressure waves reflected back from the plenum. Methods for reducing the pressure back to the mixing chamber were investigated by adopting different injectors to get varying inflow patterns (shown in Figure 2.26). However, the numerical results indicate that it is difficult to suppress the high back pressure phenomenon by changing the geometry of injectors.

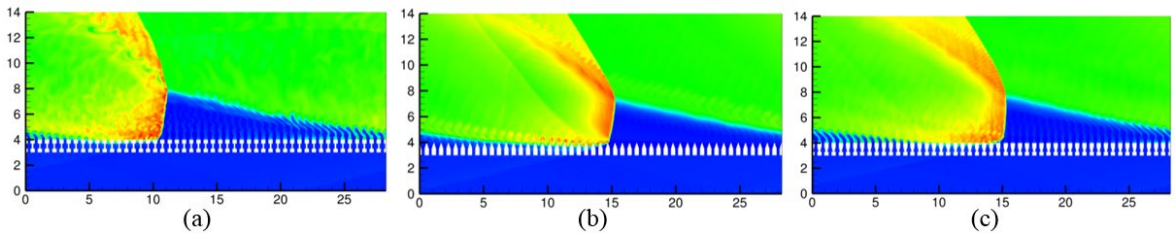

Figure 2.26 Unwrapped 2D simulation of hydrogen-air RDE with different injectors (a) cavity-slot, (b) nozzle-slot (c) diode-slot [107].

Schwer et al. [108] also used the single-step model for studying the performance of RDE with hydrogen and hydrocarbon fuels. The air and pure oxygen were supplied as oxidizers, respectively, by extending the single-step model. The results show that the simulations are sensitive to the temperature-dependent thermodynamic properties, especially for the hydrocarbon fuel and oxygen mixture as shown in Figure 2.27.

Nordeen et al. [109] explored the mixing effects in a 2D Euler simulation with a mixedness fraction to represent the sub-scale mixedness of the continuously injected reactants. This simulation used a simplified chemical induction parameter model for hydrogen-air reactions. The result showed that the varying mixedness changed the time-averaged flow field but its influences on RDE performance is limited to an order of 1–2 %.

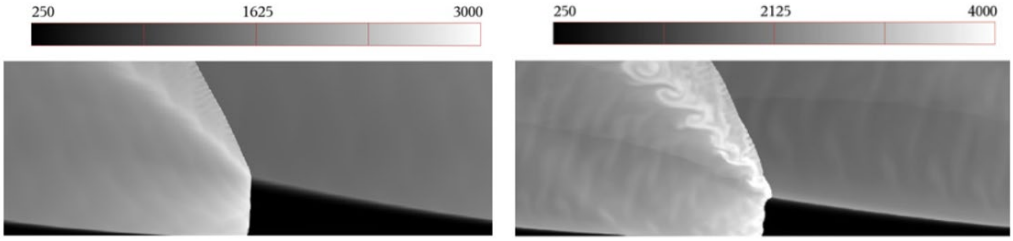

(a) (b)

Figure 2.27 Unwrapped 2D simulation of (a) ethylene-air RDE and (b) ethylene-oxygen RDE [108].

In other published work, 2D simulations based on Euler equations with single-step or two-step model were used to study the effect of different inlet stagnation pressure and back pressure on detonation characteristics and engine performance [110], the injection performance on reproducing experimental results [111], the influence of detonation wave and the contact surface on the paths of flow particles [112]. However, the single-step model is not flexible to simulate the mixing process and the chemical mechanisms have an essential influence on the detonation simulations.

Subramanian et al. [113] developed a new approach to simulating the non-premixed RDE. A 3D nonreacting simulation is conducted to extract the probability density function of the hydrogen mass fraction. This spatially and temporally varying function is used in the inlet boundary condition of 2D RDE. This enabled the reacting non-premixed simulation using detailed chemistry in 2D. The effects of inhomogeneous fuel-air mixing were analysed in the single-wave mode. A lower mean detonation velocity was observed in the non-premixed case. The pressure peaks were related to the local equivalence ratio. The result also showed that the fuel–product stratification had a significant impact on the detonation velocity deficit.

Fujii et al. [114] used a reduced chemical model with 10 species and 10 reduced elementary reactions for ethylene-oxygen RDE 2D simulations. In this work, different nozzle numbers were studied for the operation of RDE as shown in Figure 2.28. When the nozzles were placed separately with a large width of burned gas between ethylene and oxygen, the detonation velocity was observed having a significant deficit compared with the C-J velocity. The burned gas in RDE made a great difference in the detonation propagation under the non-premixed condition.

Liu et al. [115] used a detailed chemistry model with 9 species and 23 reactions based on Euler equations to study the instabilities in hydrogen-air RDE. Multi-wave mode was observed in this work. The instability with low frequency or high frequency was observed in the RDE chamber both in single-wave and two-wave modes.

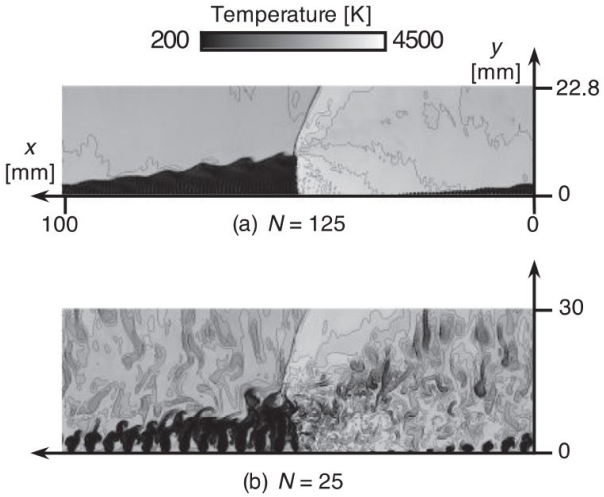

Figure 2.28 Temperature distributions of non-premixed ethylene-oxygen RDE (a) 125 nozzles and (b) 25 nozzles [114].

Pan et al. [116] investigated the wave behaviour in a hydrogen RDE using a detailed chemical model with 8 species and 48 elementary reactions based on 3D Euler equations. The unwrapped 3D simplification is a kind of model between the simplified 2D unwrapped model and the practical 3D annulus model as displayed in Figure 2.29. This kind of simplification can also be seen in Schwer's work [117]. In addition to the 3D unwrapped model, Pan et al. conducted some simulations on a 3D annulus tube. The results showed that a small size of detonation cells was observed in the tube along the concave wall. This indicated that the detonation wave near the concave wall was convergent and stronger than that near the divergent convex wall. The effect of curvature could not be neglected in the rotating detonation wave.

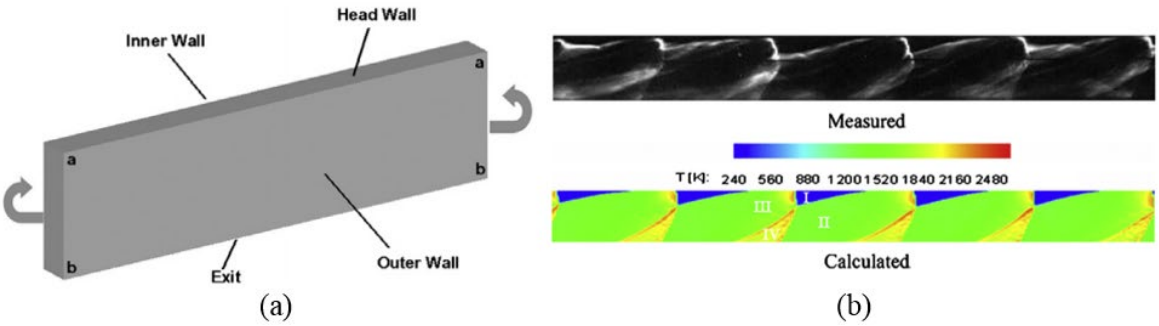

Figure 2.29 Schematic diagram of the unwrapped 3D RDE (a) computational domain (b) comparison of experiments and numerical temperature distribution [116].

Considering the effect of stretch and curvature on the annular RDE, a 3D annulus model in simulations is necessary and feasible with nowadays increased computing power. Tsuboi et al. [118] evaluated the thrust performance of a hydrogen-oxygen 3D RDE by solving Euler equations with a detailed chemistry model and AUSMDV flux scheme. The results showed that the specific impulse in 2D simulations was larger than that in 3D simulations. In the 3D annular RDE shown in Figure 2.30, the curvature of the flow field along the circumferential direction was changing. The varying curvature influences the propagation of the rotating detonation, which was essentially ignored in 2D

simulations. Uemura et al. [119] adopted the same numerical methods for the study of the transverse wave generation mechanism. They found that when the oblique shock wave was strong enough, a reactant pocket would appear between the oblique shock wave and rotating detonation wave. A further local detonation was triggered by the compression and combustion of the unreacted gas pocket.

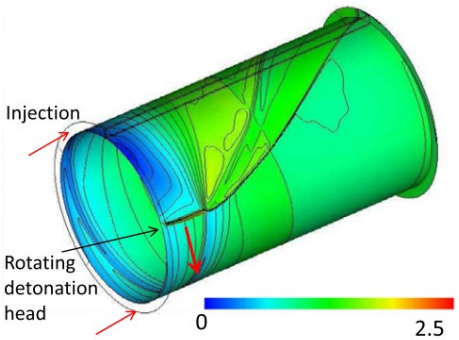

Figure 2.30 Instantaneous Mach number contours in 3D RDE [118].

In terms of mixing process in a non-premixed RDE, not only the detonation waves should be captured accurately, but also the influences of turbulence should be considered. Sun et al. carried out a series of work [120-122] on 3D RDE simulations based on the RANS method with ANSYS Fluent. In their work, a detailed Arrhenius reaction model containing 7 species and 8 reactions was adopted for the hydrogen-air mixture. Some premixed and non-premixed injection patterns were systematically studied. In premixed conditions, the rotating detonation occurred along the whole radial direction, whereas the detonation only appeared near the outer wall in non-premixed conditions and the inner wall is filled with burnt gas [120]. Figure 2.31 displays the region of non-premixed injected gas which has a nearly triangular shape as the same as that in a premixed condition. The penetration height of the pure hydrogen is higher than that of the premixed hydrogen-air mixture under the same ambient pressure.

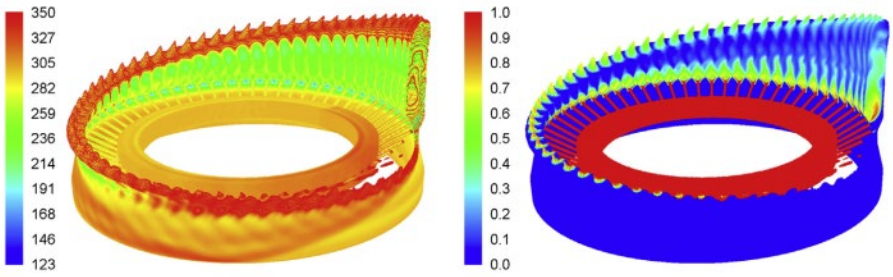

Figure 2.31 Contour of the mixing process ahead of RDE [122].

Katta et al. [123] solved the Navier-Stokes equations for their 3D hydrogen-air simulations. Figure 2.32 displays one of the numerical cases. A clear difference between the results calculated by N-S equations and the Euler equations is the contact interface. Using an inviscid simulation cannot correctly reproduce the Kelvin–Helmholtz instabilities within the vortical structures along the contact

interface, which is resolved by the N-S solver and shown in the figure. In this work, a two-step chemical model was applied to reduce the calculation cost. The mesh resolution is able to capture the detonation wave, but still insufficient to correctly get the detailed structure of RDE if a detailed chemistry model is used.

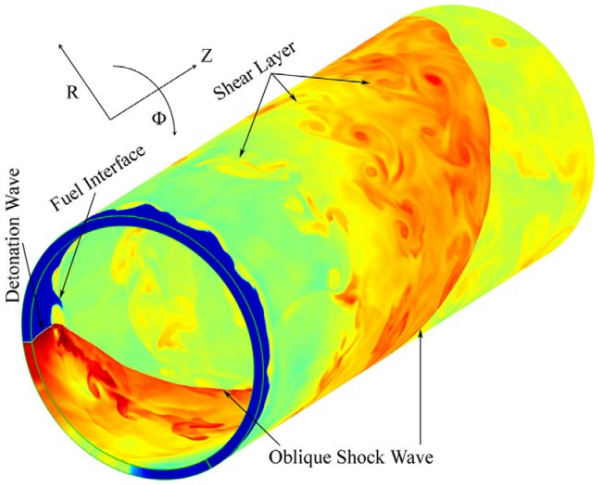

Figure 2.32 Temperature distribution of the 3D hydrogen-air RDE [123].

In the field of shock and detonation simulation, the shock-capturing method is required to accurately and efficiently approximate the strong discontinuity. Various methods, such as flux-corrected transport (FCT) [106-107], flux difference splitting (FDS) [120,124], and AUSM-type [118,125] schemes, were employed in rotating detonation simulations, each with its own set of advantages and limitations. Determining the most suitable method for a particular detonation simulation is challenging, as the choice of flux scheme is also according to the spatial and temporal integration method in use. Some studies [113,124] employ a MUSCL-type method for the reconstruction of convection terms. The high-order method is still expensive for RDE simulations based on multi-specie and multi-step chemistry.

Summarising the published numerical work on RDE in the last decade, there is a tendency that the numerical method is changing from solving inviscid Euler equations with simplified single-step or two-steps chemical models on a coarse mesh [7,106-112] to solving viscous Navier-Stokes equations with detailed chemical models on a high-resolution mesh [114,120-122,126-128]. This tendency is related to the changing of research objectives in RDE. In the early stage of RDE simulation, the primary aim was studying and displaying the structure of rotating detonation waves in the chamber. Most computational studies used continuous premixed reactants, and the diffusion term makes no difference on a relatively coarse mesh. The single-step model with particular induction parameters is also beneficial to the computing efficiency.

Due to these pioneering numerical studies, there is a more consistent understanding of the basic wave structures of the flow field in RDE and the propagation process of detonation waves. However, the premixed propellant may cause a dangerous backfire phenomenon in practical experiments. The

demand to study non-premixed injection is gradually growing. The numerical simulations need also to assist the novel experimental design and analysis, such as the partially premixed RDEs in Section 2.2.1 and the cooling system of RDEs in Section 2.2.2.

Mixedness fraction [109,113] was introduced in the simulations as a measure to quantify the transition from premixed injection to non-premixed injection. These attempts at varying mixedness in the 2D effective unwrapped model can be regarded as a kind of partially premixed injection. No known 3D RDE simulations have yet focused on partially premixed simulations. As the mixing is essentially a 3D process, the 3D simulations of partially premixed RDE are also important to help the understanding of the effects of partial premixture on the RDE internal flow structure.

For the cooling wall effects on RDEs, there are only a limited number of published numerical studies. Cock et al. [129] used a hybrid RANS-LES method in the 3D simulation of a premixed hydrogen-air RDE adopting the induction parameter combustion model. A case with isothermal walls of 800 K showed less deflagration compared with the case with adiabatic walls. The cellular structure disappeared in the simulation with isothermal walls. In their following work [130], a reduced hydrogen mechanism was adopted including 7 species and 7 reactions to simulate the non-premixed RDE. An over-prediction was found on the detonation velocity compared with the experimental results. The adiabatic and isothermal boundary conditions for the annulus walls made a difference in detonation wave frequencies. These frequencies were also found to be related to the burned products ahead of the detonation front.

Unsteady RANS simulations were carried out by Strakey et al. [131] to study the effect of different wall conditions on RDE performance losses. Premixed and non-premixed hydrogen-air mixtures were simulated by a single-step chemistry mechanism. The results showed that the heat loss to the isothermal walls of 300 K was the main source of the performance loss compared with the viscous wall effects. The single-step chemistry model was likely overpredicting the deflagration in the contact surface of the fill zone.

Wang et al. [125] conducted simulations based on a 2D annular model and used a single-step chemistry mechanism to simulate the premixed hydrogen-air mixture. The simulation tested adiabatic walls and different wall temperatures ranging from 400 K to 1500 K. The wall temperature was found to be related to some particular detonation front structures, such as the boundary oblique detonation. A higher wall temperature heated the mixture in front of detonation waves, resulting in an increase in the reaction rate when detonation occurred.

In their subsequent work [132], a 3D premixed RDE simulation was carried out based on an in-house code solving the Navier-Stokes equations. The low-temperature walls (300 K) led to a detonation quenching after ignition as shown in Figure 2.33. In the case with walls at 900 K, the detonation went through a quenching and re-initiation process. The case with a 600 K wall presented a similar stable mode but estimated a lower detonation velocity as compared with the adiabatic case.

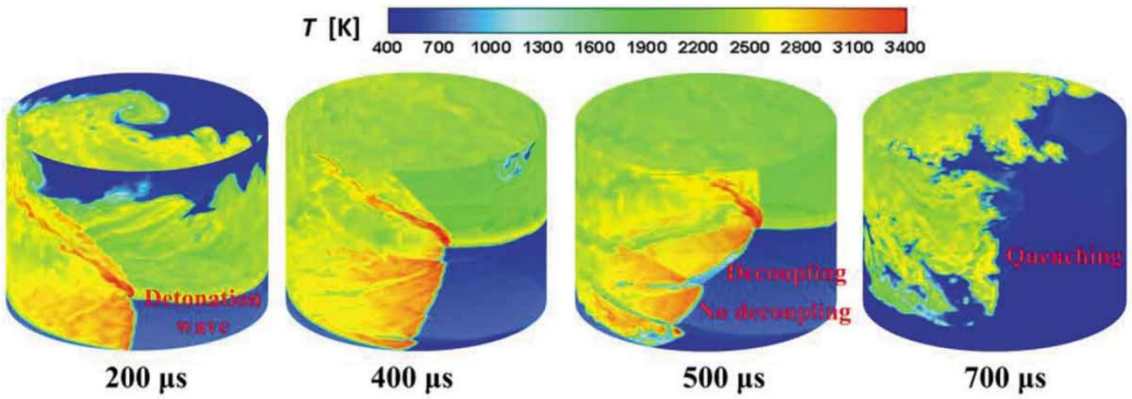

Figure 2.33 Temperature distribution in the RDE with isothermal walls of 300 K during the quenching process [132].

Liu et al. [133] studied the effects of isothermal walls using their in-house code based on an IDDES method. A reduced hydrogen chemistry model was used in the simulation containing 7 species and 8 reactions. The premixed hydrogen-air was continuously injected and different wall temperatures were tested. The result showed that the adiabatic wall caused the formation of a reactant deficit, as presented in Figure 2.34. The deflagration in the vicinity of the walls was a source of the RDE performance losses. The low-temperature isothermal walls improve the thrust and specific impulse of RDE, while the detonation velocity discrepancy was not notable.

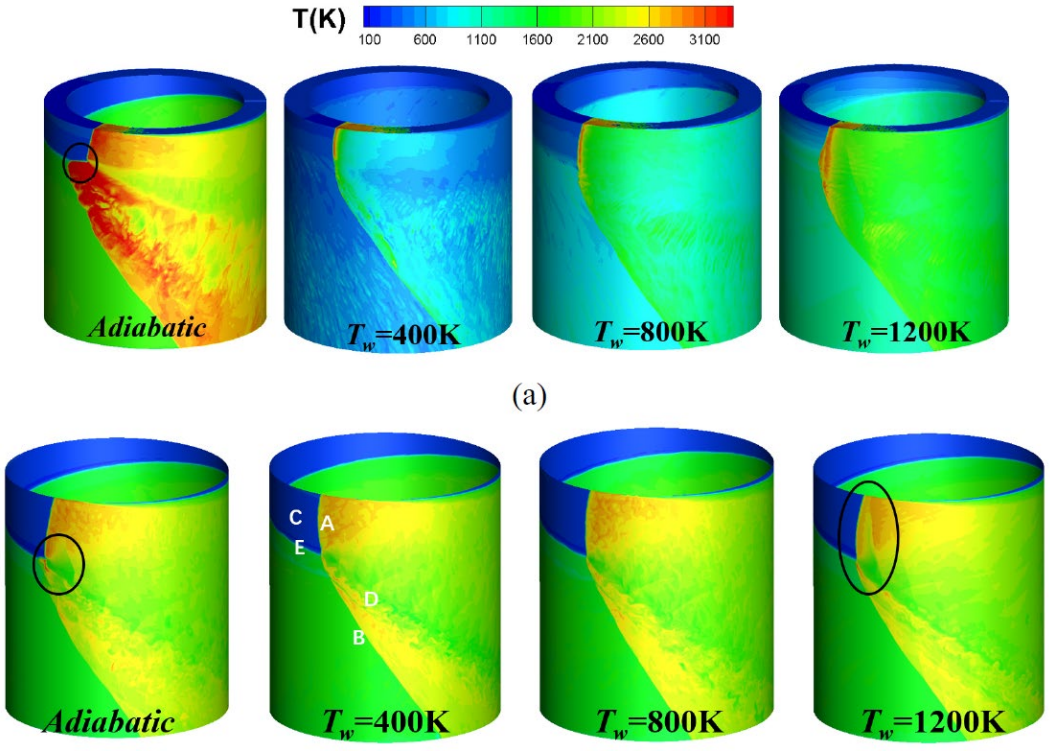

Figure 2.34 Temperature distribution in the RDE with different wall conditions [133].

In the RDE simulation progress, the chemistry model is an important aspect when solving both the high-speed detonation and the subsonic deflagration. A simplified one- or two-step chemical model is normally created to suit a particular mixture or condition, which lacks the flexibility and accuracy

to simulate different propellants, partial premixing, or a non-premixed process in RDE. The induction parameters used in these simplified models are sensitive for detonation prediction but a too simplified approach to capturing the heat release of the deflagration in the contact surface. It is necessary to use a detailed chemical model for the RDE simulations, especially in further fundamental studies.

Another obvious aspect is the increased use of a viscous solver in RDE simulations which are generally regarded as convection-dominated problems. In order to deeply understand the detonation propagation process and the internal flow structure of RDE, a high-resolution simulation should be conducted to resolve both the detonation and subsonic deflagration in RDE. The Euler solvers predict a smooth interface between the fuel and products, whereas simulations using a Navier-Stokes solver can accurately capture the contact surface and deflagration in the flow field. The diffusion term also plays an important role in the mixing process in a non-premixed RDE.

As a result, the Navier-Stokes equations with a detailed chemistry model have been gradually used in the RDE simulations. A new challenge is that directly solving the Navier-Stokes equations with a detailed chemical model is quite expensive especially in 3D simulations. It is necessary to find a method that can improve the computational efficiency and also maintain the simulation accuracy.

2.4 Applications of AMR to RDE simulations

An effective approach for capturing supersonic combustion and discontinuous flow structures is adaptive mesh refinement (AMR), which includes both unstructured AMR and structured AMR strategies. Unstructured AMR provides the geometrical flexibility of unstructured meshes, but it requires additional memory storage for connectivity information. The strong irregular memory access patterns are not friendly to the super-scalar computers and bring challenges on load balancing with distributed memory. Examples of unstructured AMR frameworks include GrAL [134], PYRAMID [135] and ParFUM [136].

In contrast, structured AMR can mitigate some of these computational challenges at the cost of reduced geometrical flexibility. The structured AMR can be classified into tree-type AMR and block-structured AMR (SAMR) based on the specific data structure. The tree-type AMR employs binary-tree, quad-tree or oct-tree structures in one, two and three dimensions, respectively. Coarse cells are replaced or overlayed by refined cells, creating a new level based on the tree structure. Examples of the tree-type AMR include PARAMESH [137] and Athena++ [138]. The SAMR uses a patch-wise refinement approach, which clusters flagged cells into different rectangular blocks. A multi-level hierarchy of embedded grid patches is created by successively refining cells from respectively coarser parents. Some examples of SAMR frameworks include AMROC [30], Chombo [139] and AMReX [140] (previously BoxLib).

Despite that these AMR approaches have various advantages and disadvantages from a computational perspective, the AMR method is suitable and used for solving detonation problems where a strong discontinuity is present. For example, some researchers have already applied the AMR technique to RDE simulations. Yi et al. [141] carried out 2D simulations by solving Euler equations and a one-step Arrhenius model based on Paramesh [137], then extended the work to simulate a 3D annular RDE [142]. Swiderski et al. [143,144] implemented the AMR technique into the in-house code REFLOPS USG (REactive FLOw solver for Propulsion Systems on UnStructured Grids) based on the Favre averaged Navier-Stokes equations with a single-step reversible global reaction. Sato et al. [145] solved the 3D Euler equations with a detailed chemical model based on UMdetFOAM. Pal et al. [146-149] adopted the commercial CFD code, CONVERGE, to conduct the URANS [146,148] and LES [147,149] simulations with a detailed chemistry model, AMR technique and a modified cut-cell Cartesian method.

Some simulations of RDEs are conducted using solvers based on the structured adaptive mesh refinement (SAMR) method. Eude et al. [150] used the WENO-based Euler solver with detailed chemistry in the AMROC framework on a Cartesian mesh and a cylindrical mesh to study the 3D effects compared with the 2D simulations. Recently, Luan et al. [151] simulated the 2D unwrapped RDE model based on the generic framework of AMROC. Nadakkal et al. [152] reported the use of AMReX-PeleC [153] to simulate a 2D RDE with an embedded boundary method. In summary, there are only a few viscous solvers with full chemistry and AMR technique for a non-Cartesian geometry up to date. No open-source code based on block-structured adaptive mesh refinement was available when this thesis began. It is promising to develop such a solver used for high-speed reacting flows and specifically for rotating detonation simulations.

The AMROC framework serves as a natural platform to achieve this goal. As introduced in Section 1.1, AMROC employs the block-structured AMR strategy and was initially developed on a Cartesian mesh. Since its initial release two decades ago [30], it has undergone continuous updates and expansions [33,35-36]. AMROC has been widely used to deal with detonation problems [31-32]. In recent years, AMROC has been extended into different branches for various purposes. For example, the lattice Boltzmann method (LBM) has been incorporated for low-speed incompressible and weakly compressible flow [154], and the two-temperature model has been implemented for hypersonic flow on two-dimensional overset meshes [42]. In this study, AMROC is extended to curvilinear adaptive meshes in both two and three dimensions. This extension allows for the computation of high-speed reacting flows in a non-Cartesian geometry using body-fitted meshes. Specifically, the block-structured AMR on curvilinear meshes focuses on application to the rotating detonation simulations.

2.5 Chapter Summary

In summary, the rotating detonation engine has been regarded as a promising power device that can be used both in power-generation systems and in the propulsion area. With the development of RDE experiments, there are still many scientific and practical problems that need to be solved by using numerical methods as assistants. Firstly, the injection and mixing of propellants are important to sustain the stable propagation of rotating detonation waves. The partially premixed RDE has attracted increasing attention in recent years, whereas the effect of the premixing in 3D RDE internal flow structure is still unclear. Secondly, as the operation time has been improved from hundreds of milliseconds to hundreds of seconds, the study of the cooling walls on RDE has shown its needs for a long-duration test. The current numerical studies are mainly focused on the cooling wall effects on a single-wave mode of premixed RDE and use one-step or reduced chemistry. The simulations of a multi-wave mode of non-premixed RDE are necessary to improve the understanding of wall effects.

To achieve these goals, effective AMR solvers can be used to reduce the computational cost especially for a 3D viscous simulation. There are only a few viscous solvers with full chemistry and AMR technique for a non-Cartesian geometry. The dynamic mesh adaption technique has not been applied comprehensively enough for the simulation of RDEs. The number of published studies on AMR application to RDE simulation is relatively limited, especially compared to the number of overall RDE simulation studies. It is promising and necessary to develop such a solver for the high-resolution simulations in RDE.

Chapter 3 Numerical methods

3.1 Governing equations

3.1.1 Euler equations

The calculations in this thesis are based on the AMROC-Clawpack framework [30]. Firstly, the multi-species Euler equations with a detailed chemical model in three-dimensional form are solved as governing equations for inviscid flows and are written as

$$\frac{\partial Q}{\partial t}+\frac{\partial F}{\partial x}+\frac{\partial G}{\partial y}+\frac{\partial H}{\partial z}=S\,, \tag{3.1}$$

$$Q=\begin{bmatrix}\rho_1\\ \vdots\\ \rho_{Nsp}\\ \rho u\\ \rho v\\ \rho w\\ \rho E\end{bmatrix},\ F=\begin{bmatrix}\rho_1 u\\ \vdots\\ \rho_{Nsp}u\\ \rho u^2+p\\ \rho uv\\ \rho uw\\ (\rho E+p)u\end{bmatrix},\ G=\begin{bmatrix}\rho_1 v\\ \vdots\\ \rho_{Nsp}v\\ \rho uv\\ \rho v^2+p\\ \rho wv\\ (\rho E+p)v\end{bmatrix},\ H=\begin{bmatrix}\rho_1 w\\ \vdots\\ \rho_{Nsp}w\\ \rho uw\\ \rho vw\\ \rho w^2+p\\ (\rho E+p)w\end{bmatrix},\ S=\begin{bmatrix}\dot{\omega}_1\\ \vdots\\ \dot{\omega}_{Nsp}\\ 0\\ 0\\ 0\\ 0\end{bmatrix}, \tag{3.2}$$

where Q are the conservative variables, F, G and H are the convective fluxes in the x-, y- and z-direction, respectively. S are chemical source terms, where i = 1, 2, …, N_{sp}. N_{sp} is the total number of species and ρ_i is the density of component i. The multi-species ideal gas state equation,

$$p=\sum_{i=1}^{N_{sp}}\rho_i\frac{\mathrm{R_u}}{W_i}T\,, \tag{3.3}$$

is used to close Equation (3.1). Besides, E in Equation (3.2) indicates the total unit energy and is given as

$$E=\sum_{i=1}^{N_{sp}}Y_i h_i-\frac{p}{\rho}+\frac{1}{2}\left(u^2+v^2\right), \tag{3.4}$$

where h_i is the specific enthalpy of species i computed by

$$h_i=h_{\mathrm{ref},i}^0+\int_{T_{\mathrm{ref}}}^{T}C_{\mathrm{P}_i}dT\,. \tag{3.5}$$

The specific heat at constant pressure C_{P_i} of species i is dependent on temperature and calculated by the polynomial functions in the CHEMKIN II library [155]. $\dot{\omega}_i$ in Equation (3.2) is the mass generation rate of component i, which can be calculated by a chemical reaction mechanism of J steps as

$$\dot{\omega}_i = \sum_{j=1}^{J}\left(\nu_{ji}^{\mathrm{r}} - \nu_{ji}^{\mathrm{f}}\right)\left[k_j^{\mathrm{f}}\prod_{n=1}^{N_{\mathrm{sp}}}\left(\frac{\rho_n}{W_n}\right)^{\nu_{jn}^{\mathrm{f}}} - k_j^{\mathrm{r}}\prod_{n=1}^{N_{\mathrm{sp}}}\left(\frac{\rho_n}{W_n}\right)^{\nu_{jn}^{\mathrm{r}}}\right],\ i = 1,\ldots N_{\mathrm{sp}}. \tag{3.6}$$

The rate constants of forward and reverse chemical reactions are given by the Arrhenius formula:

$$k_j^{\mathrm{f/r}}(T) = A_j^{\mathrm{f/r}} T^{\beta_j^{\mathrm{f/r}}} \exp\left(-\frac{E_j^{\mathrm{f/r}}}{RT}\right). \tag{3.7}$$

The CHEMKIN II library [155] is incorporated into AMROC to solve the detailed chemical reactions and thermodynamic properties. The chemical kinetics are integrated by a semi-implicit generalised Runge–Kutta method of fourth order (GRK4A) [30]. A second-order accurate Strang splitting method is adopted for the stiff source term treatment.

3.1.2 Navier-Stokes equations

The multi-species Navier-Stokes equations with a detailed chemical model in three-dimensional form are also solved as governing equations:

$$\frac{\partial Q}{\partial t} + \frac{\partial\left(F - F_{\mathrm{V}}\right)}{\partial x} + \frac{\partial\left(G - G_{\mathrm{V}}\right)}{\partial y} + \frac{\partial\left(H - H_{\mathrm{V}}\right)}{\partial z} = S, \tag{3.8}$$

where F_{V}, G_{V} and H_{V} denote the viscous fluxes in the x-, y- and z-direction, respectively. The definition of inviscid fluxes can be found in Equation (3.2). The viscous fluxes are given as

$$F_{\mathrm{V}} = \begin{bmatrix} J_{x,i} \\ \tau_{xx} \\ \tau_{xy} \\ \tau_{xz} \\ k\dfrac{\partial T}{\partial x} + \displaystyle\sum_{j=1}^{N_{sp}} h_j J_x + u\tau_{xx} + v\tau_{xy} + w\tau_{xz} \end{bmatrix}, \tag{3.9}$$

$$G_{\mathrm{V}} = \begin{bmatrix} J_{y,i} \\ \tau_{yx} \\ \tau_{yy} \\ \tau_{yz} \\ k\dfrac{\partial T}{\partial y} + \displaystyle\sum_{j=1}^{N_{sp}} h_j J_y + u\tau_{xy} + v\tau_{yy} + w\tau_{yz} \end{bmatrix}, \tag{3.10}$$

$$H_{\mathrm{V}} = \begin{bmatrix} J_{z,i} \\ \tau_{zx} \\ \tau_{zy} \\ \tau_{zz} \\ k\dfrac{\partial T}{\partial z} + \displaystyle\sum_{j=1}^{N_{sp}} h_j J_z + u\tau_{zx} + v\tau_{zy} + w\tau_{zz} \end{bmatrix}. \tag{3.11}$$

The diffusion fluxes $J_{x,i}$, $J_{y,i}$ and $J_{z,i}$ are related to the species gradients by Fick's law:

$$J_i = \rho Y_i \left[\left(-\frac{1}{X_i} \right) D_i \left(\nabla X_i + (X_i - Y_i) \frac{\nabla P}{P} \right) - \frac{D_i^T}{\rho Y_i} \frac{\nabla T}{T} \right], \tag{3.12}$$

where Y_i is the mass fraction and X_i is the molar fraction. D_i is the mixture-averaged diffusion coefficient of species i and D_i^T is the mixture-averaged thermal diffusion coefficient, which are calculated through the CHEMKIN II TRANSPORT library [155]. In the momentum and energy fluxes, τ denotes the viscosity stress. The stresses in all directions are given as

$$\tau_{xx} = -\frac{2}{3}\mu(\nabla \cdot \mathbf{v}) + 2\mu \frac{\partial u}{\partial x},\ \tau_{yy} = -\frac{2}{3}\mu(\nabla \cdot \mathbf{v}) + 2\mu \frac{\partial v}{\partial y},\ \tau_{zz} = -\frac{2}{3}\mu(\nabla \cdot \mathbf{v}) + 2\mu \frac{\partial w}{\partial z}, \tag{3.13}$$

$$\tau_{xy} = \tau_{yx} = \mu \left(\frac{\partial u}{\partial y} + \frac{\partial v}{\partial x} \right),\ \tau_{xz} = \tau_{zx} = \mu \left(\frac{\partial u}{\partial z} + \frac{\partial w}{\partial x} \right),\ \tau_{yz} = \tau_{zy} = \mu \left(\frac{\partial v}{\partial z} + \frac{\partial w}{\partial y} \right), \tag{3.14}$$

$$\nabla \cdot \mathbf{v} = \left(\frac{\partial u}{\partial x} + \frac{\partial v}{\partial y} + \frac{\partial w}{\partial z} \right), \tag{3.15}$$

where μ is the averaged values for the mixture viscosity. In the energy fluxes, $k\partial T / \partial x$, $k\partial T / \partial y$ and $k\partial T / \partial z$ are thermal flux terms and the k is the thermal conductivity. Similarly, both the mixture viscosity and thermal conductivity are computed through the CHEMKIN II TRANSPORT library [155]. The unit energy and specific enthalpy are given by Equation (3.4) and (3.5).

3.2 Mapping method

In AMROC, the ghost fluid method (GFM) is presently used to handle the non-Cartesian physical boundaries [35]. The staircase approximation of the boundary introduces accuracy losses, which can be avoided by using curvilinear body-fitted meshes. A mapping method for 2D geometry transformations [34] has recently been implemented into AMROC [42]. This method enables the numerical methods based on a Cartesian mesh to be applied to a body-fitted mesh, which is beneficial to modelling the near-wall region of non-Cartesian geometries.

Generally, there are two different approaches for the coordinate transformation. The first one is working in the computational space and uses transformed governing equations for the physical variables [157]. The numerical method based on Cartesian mesh can be used without change. The second one is working in the physical space and derives the finite volume method on the nonuniform mesh with a capacity function [34]. The latter is adopted in AMROC for the finite volume method on mapped structured meshes, cf. [158].

The coordinates of a uniform Cartesian mesh (ξ, η, ζ) in computational space are firstly mapped into the coordinates of a non-uniform structured mesh (x, y, z) in physical space by a mapping function,

$$\begin{cases} x = f_1(\xi,\eta,\zeta) \\ y = f_2(\xi,\eta,\zeta) \\ z = f_3(\xi,\eta,\zeta) \end{cases}. \tag{3.16}$$

A cell-centred finite volume method [34] is used to discretise equations in physical space. An example for the 2D multi-component Euler equations is given as

$$\begin{aligned} Q_{ij}^{n+1} = Q_{ij}^{n} - \frac{\Delta t}{|A_{ij}|}\Big[&\left(\tilde{F}_{i+1/2,\,j}^{n}\cdot\tilde{L}_{i+1/2,\,j} - \tilde{F}_{i-1/2,\,j}^{n}\cdot\tilde{L}_{i-1/2,\,j}\right) \\ &+\left(\tilde{G}_{i,\,j+1/2}^{n}\cdot\tilde{L}_{i,\,j+1/2} - \tilde{G}_{i,\,j-1/2}^{n}\cdot\tilde{L}_{i,\,j-1/2}\right)\Big] + \Delta t\cdot S\ . \end{aligned} \tag{3.17}$$

$|A_{ij}|$ in Equation (3.17) is the area of the physical cell indexed (i, j). The fluxes with tilde are the flux per unit length normal to physical interfaces between these cells. The L with tilde is the physical length of the interfaces. The unit physical flux can be calculated by the unit computational flux. For example, the unit physical flux $\tilde{F}_{i+1/2,\,j}^{n}$ normal to the edge between cells (i, j) and (i+1, j) has a relationship with the unit computational flux $F_{i+1/2,\,j}^{n}$,

$$\tilde{F}_{i+1/2,\,j}^{n}\cdot\tilde{L}_{i+1/2,\,j} = F_{i+1/2,\,j}^{n}\cdot L_{i+1/2,\,j}\,. \tag{3.18}$$

$\tilde{L}_{i+1/2,\,j}$ is the physical edge length and $L_{i+1/2,\,j}$ is the edge length in the computation cell. For the unit computational flux we write,

$$F_{i+1/2,j}^{n} = F(Q_{i+1/2,\,j}^{n,\,l},\ Q_{i+1/2,\,j}^{n,\,r})\,, \tag{3.19}$$

for whose approximation a numerical flux scheme is needed. The final discretised form of the 2D Euler equations in the code is given as,

$$\begin{aligned} Q_{ij}^{n+1} = Q_{ij}^{n} &- \frac{\Delta t}{|C_{ij}|\Delta\xi}\left(\tilde{F}_{i+1/2,\,j}^{n}\cdot\frac{\tilde{L}_{i+1/2,\,j}}{\Delta\eta} - \tilde{F}_{i-1/2,\,j}^{n}\cdot\frac{\tilde{L}_{i-1/2,\,j}}{\Delta\eta}\right) \\ &- \frac{\Delta t}{|C_{ij}|\Delta\eta}\left(\tilde{G}_{i,\,j+1/2}^{n}\cdot\frac{\tilde{L}_{i,\,j+1/2}}{\Delta\xi} - \tilde{G}_{i,\,j-1/2}^{n}\cdot\frac{\tilde{L}_{i,\,j-1/2}}{\Delta\xi}\right) + \Delta t\cdot S\ , \end{aligned} \tag{3.20}$$

where the capacity function $|C_{ij}|$ is the area ratio of the physical cell to the computational cell indexed (i, j). For 3D Navier-Stokes equations, the Equation (3.17) can be written as

$$\begin{aligned} Q_{ijk}^{n+1} = Q_{ijk}^{n} &- \frac{\Delta t}{|C_{ijk}|\Delta\xi}\left[\left(\tilde{F}-\tilde{F}_{\mathrm{V}}\right)_{i+1/2,\,j,k}^{n}\cdot\frac{\tilde{A}_{i+1/2,\,j,k}}{\Delta\eta\Delta\zeta} - \left(\tilde{F}-\tilde{F}_{\mathrm{V}}\right)_{i-1/2,\,j,k}^{n}\cdot\frac{\tilde{A}_{i-1/2,\,j,k}}{\Delta\eta\Delta\zeta}\right] \\ &- \frac{\Delta t}{|C_{ijk}|\Delta\eta}\left[\left(\tilde{G}-\tilde{G}_{\mathrm{V}}\right)_{i,j+1/2,k}^{n}\cdot\frac{\tilde{A}_{i,\,j+1/2,k}}{\Delta\xi\Delta\zeta} - \left(\tilde{G}-\tilde{G}_{\mathrm{V}}\right)_{i,j-1/2,k}^{n}\cdot\frac{\tilde{A}_{i,j-1/2,k}}{\Delta\xi\Delta\zeta}\right] \\ &- \frac{\Delta t}{|C_{ijk}|\Delta\zeta}\left[\left(\tilde{H}-\tilde{H}_{\mathrm{V}}\right)_{i,j,k+1/2}^{n}\cdot\frac{\tilde{A}_{i,j,k+1/2}}{\Delta\xi\Delta\eta} - \left(\tilde{H}-\tilde{H}_{\mathrm{V}}\right)_{i,j,k-1/2}^{n}\cdot\frac{\tilde{A}_{i,j,k-1/2}}{\Delta\xi\Delta\eta}\right] + \Delta\mathrm{t}\cdot S. \end{aligned} \tag{3.21}$$

$\left|C_{ijk}\right|$ in Equation (3.21) represents the volume ratio of the physical cell to the computational cell indexed (i, j, k). The inviscid fluxes $\left[\tilde{F},\, \tilde{G},\, \tilde{H}\right]^{\mathrm{T}}$ and the viscous fluxes $\left[\tilde{F}_{\mathrm{V}},\, \tilde{G}_{\mathrm{V}},\, \tilde{H}_{\mathrm{V}}\right]^{\mathrm{T}}$ are calculated separately and the details are introduced in the following subchapters. The terms behind the numerical fluxes are the ratio of the area of the respective facet.

For the mapped meshes, a transformation is required before computing the fluxes. The velocities in the Cartesian coordinate system in physical space are rotated to the normal or tangential direction of the physical cell face [34]. Here a transformation matrix T_{s} [158] is used to rotate the velocities and calculate the flux normal to the face. The unit physical flux can be computed as

$$F^{n}_{i+1/2,\,j} = T_{\mathrm{s}}^{-1} F\left(TQ^{n,\,l}_{i+1/2,\,j},\; TQ^{n,\,r}_{i+1/2,\,j}\right), \tag{3.22}$$

with

$$T_{\mathrm{s}} = \begin{bmatrix} 1 & 0 & 0 & 0 & 0 & 0 \\ 0 & \ddots & 0 & 0 & 0 & 0 \\ 0 & 0 & 1 & 0 & 0 & 0 \\ 0 & 0 & 0 & n_x & n_y & 0 \\ 0 & 0 & 0 & -n_y & n_x & 0 \\ 0 & 0 & 0 & 0 & 0 & 1 \end{bmatrix}. \tag{3.23}$$

n_x and n_y are the unit normal vectors of the physical edges. After the computing, the inverse matrix T_{s}^{-1} is used to rotate the flux back to the Cartesian coordinate system in physical space. For 3D equations, the transformation matrix T_{s} can be written as

$$T_{\mathrm{s}} = \begin{bmatrix} 1 & 0 & 0 & 0 & 0 & 0 & 0 \\ 0 & \ddots & 0 & 0 & 0 & 0 & 0 \\ 0 & 0 & 1 & 0 & 0 & 0 & 0 \\ 0 & 0 & 0 & a_x & a_y & a_z & 0 \\ 0 & 0 & 0 & b_x & b_y & b_z & 0 \\ 0 & 0 & 0 & c_x & c_y & c_z & 0 \\ 0 & 0 & 0 & 0 & 0 & 0 & 1 \end{bmatrix}. \tag{3.24}$$

a_x, a_y and a_z are the components of the unit normal vector of the physical interface. b and c are the unit tangential vectors, which can be computed by an orthogonalization method. The detailed computation of these vectors will be introduced in Section 3.9. Similarly, after being solved in Riemann solvers, the fluxes are rotated back to the direction in physical space by the inverse matrix T_{s}^{-1}.

3.3 Inviscid fluxes

3.3.1 Advective Upstream Splitting Method (AUSM)

For the finite volume method, the Riemann problem should be solved to get the flux through the interface between two control volumes. The Advective Upstream Splitting Method (AUSM) flux scheme developed by Liou [159] is implemented in the mapped solver for the Riemann problem. This method combines the computational efficiency of the flux vector splitting methods and the robustness of the flux difference splitting methods. The multi-component AUSM flux scheme is given below. The mass flux reads

$$F=\frac{1}{2}\left(M_{1/2}+\left|M_{1/2}\right|\right)a_{\mathrm{L}}\begin{bmatrix}\rho_1\\ \vdots\\ \rho_i\\ \rho u\\ \rho v\\ \rho w\\ \rho E+P\end{bmatrix}_{\mathrm{L}}+\frac{1}{2}\left(M_{1/2}-\left|M_{1/2}\right|\right)a_{\mathrm{R}}\begin{bmatrix}\rho_1\\ \vdots\\ \rho_i\\ \rho u\\ \rho v\\ \rho w\\ \rho E+P\end{bmatrix}_{\mathrm{R}}+P_{1/2}\begin{bmatrix}0\\ \vdots\\ 0\\ 1\\ 0\\ 0\\ 0\end{bmatrix}_{\mathrm{R}}. \tag{3.25}$$

The Mach number at the interface is given by

$$M_{1/2}=M_{\mathrm{L}}^{+}+M_{\mathrm{R}}^{-}, \tag{3.26}$$

and the Mach number is split as

$$M^{\pm}=\begin{cases}\pm\frac{1}{4}\left(M\pm1\right)^2, & \text{if } \left|M\right|\le 1\\ \frac{1}{2}\left(M\pm\left|M\right|\right), & \text{otherwise}\end{cases}. \tag{3.27}$$

The pressure at the interface is given by

$$P_{1/2}=P_{\mathrm{L}}^{+}+P_{\mathrm{R}}^{-}, \tag{3.28}$$

and the pressure is split as

$$P^{\pm}=\begin{cases}\frac{P}{4}\left(M\pm1\right)^2\left(2\mp M\right), & \text{if } \left|M\right|\le 1\\ \frac{P}{2}\left(M\pm\left|M\right|\right)/M, & \text{otherwise}\end{cases}. \tag{3.29}$$

Similarly, the transformation matrix T_s in Equation (3.23) is used to rotate the velocities and calculate the flux normal to the edges. After the splitting, the inverse matrix T_s^{-1} is used to rotate the flux back to the direction in physical space. The CFL condition of ASUM for 1D Euler equations is given by

$$CFL_x^{\mathrm{C}} = \max\left[\left(|u| + a\right)\frac{\Delta t}{\Delta x}\right] < 1, \tag{3.30}$$

where u is the rotated velocity, from which the speed of sound a is derived. The physical cell length Δx is utilized in this CFL condition. The global CFL number is defined by the maximum value in all spatial dimensions.

3.3.2 Hybrid Roe/HLL scheme

A hybrid Roe/HLL scheme [30] is also used in this thesis to calculate the inviscid flux. This scheme incorporates the Roe method with entropy correction and the HLL (Harten-Lax-Van Leer) method. It is a robust and reliable scheme when simulating detonation problems. The multi-component Roe/HLL scheme on the mapped structured mesh is given below.

Firstly, the state vectors are rotated to the orthogonal direction of the interface. The flux on the interface can be computed by

$$F = \frac{1}{2}\left[F_{\mathrm{L}} + F_{\mathrm{R}} - \left|\hat{A}\right|\left(Q_{\mathrm{R}} - Q_{\mathrm{L}}\right)\right]. \tag{3.31}$$

$\hat{A}$ is a constant matrix for the Riemann problem that approximates the original Jacobian. The data difference $\left(Q_{\mathrm{R}} - Q_{\mathrm{L}}\right)$ can be defined as a set of waves W_m propagating at some wave speed s_w, and is given as

$$Q_{\mathrm{R}} - Q_{\mathrm{L}} = \sum_{m=1}^{M} W_m \,. \tag{3.32}$$

By projecting the data difference onto the right eigenvectors of the diagonalizable matrix, the data difference is given as

$$Q_{\mathrm{R}} - Q_{\mathrm{L}} = \sum_{m=1}^{M} \alpha_m r_m \,. \tag{3.33}$$

α_m is the wave strength and r_m is the eigenvectors of the matrix $\hat{A}$. Equation (3.31) can be rewritten as

$$F = \frac{1}{2}\left(F_{\mathrm{L}} + F_{\mathrm{R}} - \sum_{m=1}^{N_{\mathrm{eq}}} \alpha_m \left|\hat{\lambda}_m\right| r_m\right). \tag{3.34}$$

In order to compute the flux, one requires the solutions of the wave strength α_m, the eigenvalues $\hat{\lambda}_m$ and the right eigenvectors r_m. N_{eq} is the total number of equations, which is equal to N_{sp}+4 for the 3D multi-component equations. N_{sp} is the total number of species.

The wave strength α_m for the multi-component equations is computed by

$$\begin{cases} \alpha_m = \dfrac{\Delta p \mp \hat{\rho}\hat{a}\Delta u}{2\hat{a}^2}, & m = 1 \ \ or \ \ m = N_{sp} + 4 \\ \alpha_m = \Delta\rho_i - \hat{Y}_i \dfrac{\Delta p}{\hat{a}^2}, & m = 2, ..., N_{sp} + 1 \\ \alpha_m = \hat{\rho}\Delta v, & m = N_{sp} + 2 \\ \alpha_m = \hat{\rho}\Delta w, & m = N_{sp} + 3 \end{cases} . \tag{3.35}$$

The symbol Δ denotes the difference operator of the quantities and the superscript ^ denotes the Roe average of the quantities. The standard Roe averages are given as

$$\begin{cases} \hat{\rho} = \sqrt{\rho_{\mathrm{L}} + \rho_{\mathrm{R}}} \\ \hat{q} = \dfrac{\sqrt{\rho_{\mathrm{L}}}\, q_L + \sqrt{\rho_{\mathrm{R}}}\, q_R}{\sqrt{\rho_{\mathrm{L}}} + \sqrt{\rho_{\mathrm{R}}}}, & q = u, v, w, H, Y_i, T, \dfrac{1}{\bar{W}} \end{cases} . \tag{3.36}$$

Use the average temperature to compute the specific heats for each species, then the averaged mixture specific heats at constant pressure and the averaged specific heat ratio are written as

$$\hat{C}_p = \sum_{i=1}^{N_{sp}} Y_i \hat{C}_{p,i}, \quad \hat{\gamma} = \frac{\mathrm{R_u}}{\hat{\bar{W}}\hat{C}_p - \mathrm{R_u}} . \tag{3.37}$$

The average speed of sound is computed by

$$\hat{a} = \sum_{i=1}^{Nsp} \hat{Y}_i \hat{\phi}_i - (\hat{\gamma} - 1)\hat{U}^2 + (\hat{\gamma} - 1)\hat{H} , \tag{3.38}$$

where $\hat{\phi}_i$ is the average partial derivative of p with respect to Y_i, and $\hat{U}^2$ is the sum of the square of the average velocities,

$$\hat{\phi}_i = (\hat{\gamma} - 1)\left(\frac{\hat{U}^2}{2} - \hat{H}\right) + \hat{\gamma}\mathrm{R}_i\hat{T}, \quad \hat{U}^2 = \left(\hat{u}^2 + \hat{v}^2 + \hat{w}^2\right). \tag{3.39}$$

The matrix of right eigenvectors is given as

$$\begin{bmatrix} \hat{Y}_1 & 1 & 0 & \cdots & 0 & 0 & 0 & \hat{Y}_1 \\ \vdots & 0 & \ddots & 0 & \vdots & \vdots & \vdots & \vdots \\ \vdots & \vdots & 0 & \ddots & 0 & \vdots & \vdots & \vdots \\ \hat{Y}_{N_{sp}} & 0 & \cdots & 0 & 1 & 0 & 0 & \hat{Y}_{N_{sp}} \\ \hat{u} - \hat{a} & \hat{u} & \cdots & \cdots & \hat{u} & 0 & 0 & \hat{u} + \hat{a} \\ \hat{v} & \hat{v} & \cdots & \cdots & \hat{v} & 1 & 0 & \hat{v} \\ \hat{w} & \hat{w} & \cdots & \cdots & \hat{w} & 0 & 1 & \hat{w} \\ \hat{H} - \hat{u}\hat{a} & \hat{U}^2 - \dfrac{\phi_1}{\hat{\gamma}} & \cdots & \cdots & \hat{U}^2 - \dfrac{\phi_{N_{sp}}}{\hat{\gamma}} & \hat{v} & \hat{w} & \hat{H} + \hat{u}\hat{a} \end{bmatrix} . \tag{3.40}$$

The eigenvalues for the matrix $\hat{A}$ are given as

$$\begin{aligned}
&\hat{\lambda}_1 = \hat{u} - \hat{a}, \\
&\hat{\lambda}_m = \hat{u}, \quad m = 2, ..., N_{sp} + 3, \\
&\hat{\lambda}_m = \hat{u} + \hat{a}, \quad m = N_{sp} + 4.
\end{aligned} \tag{3.41}$$

Now, the quantities required for calculating the flux on the interface are all available. In addition, the density and pressure in the intermediate states of the linearized Riemann problem are evaluated to check their plausibility.

$$\begin{cases} q_{\mathrm{L}}^{*} = q_{\mathrm{L}} + \alpha_1 r_1 \\ q_{\mathrm{R}}^{*} = q_{\mathrm{R}} - \alpha_{N_{sp}+4} r_{N_{sp}+4} \end{cases}, \ q = \rho, u, e, a \ . \tag{3.42}$$

If density and pressure are positive, the HLL method will not be used. A multi-dimensional entropy correction [160] is employed to avoid the violation of the entropy condition. A mass fraction positivity correction [161] is also used to avoid unphysical solutions. The details of the corrections method can be found in Ref. [30]. The 1D CFL condition of the Roe method is given as

$$CFL_x^{\mathrm{C}} = \max\left[\left(|\hat{u}| + \hat{a} \right) \frac{\Delta t}{\Delta x} \right] < 1 . \tag{3.43}$$

If one of the quantities in terms of density and pressure is negative, the HLL method will be used to recompute the flux. The HLL method approximates the solution of the Riemann problem simply by two discontinuous waves. The flux on the interface is computed by

$$F = \begin{cases} F_{\mathrm{L}}, & s_{\mathrm{L}} > 0 \\ \dfrac{s_{\mathrm{R}} F_{\mathrm{L}} - s_{\mathrm{L}} F_{\mathrm{R}} + s_{\mathrm{R}} s_{\mathrm{L}} \left(Q_{\mathrm{R}} - Q_{\mathrm{L}} \right)}{s_{\mathrm{R}} - s_{\mathrm{L}}}, & s_{\mathrm{L}} \le 0 \le s_{\mathrm{R}} \\ F_{\mathrm{R}}, & s_{\mathrm{R}} < 0 \end{cases} . \tag{3.44}$$

s_{L} and s_{R} denote approximations to the smallest and largest signal speed involved in the Riemann problem. The speeds are estimated by,

$$\begin{aligned}
s_{\mathrm{L}} &= \min\left(u_{\mathrm{L}} - a_{\mathrm{L}}, u_{\mathrm{R}} - a_{\mathrm{R}} \right) \\
s_{\mathrm{R}} &= \max\left(u_{\mathrm{L}} + a_{\mathrm{L}}, u_{\mathrm{R}} + a_{\mathrm{R}} \right)
\end{aligned} \tag{3.45}$$

The CFL condition of the HLL method for 1D Euler equations is given in the same form as in Equation (3.30).

3.3.3 HLLC scheme

The standard HLLC (Harten-Lax-Van Leer Contact) method [162] has also been implemented with pressure–based wave speed estimates to solve the inviscid flux on the interface. The pressure in the star region is estimated by the primitive variable Riemann solver (PVRS). Compared to the described HLL scheme, the HLLC scheme uses a three-wave model and resolves the contact discontinuity. Firstly, the pressure at the interface is evaluated as

$$p^* = \max(0, p_{\text{pvrs}}),\ \ p_{\text{pvrs}} = \frac{1}{2}(p_{\text{L}} + p_{\text{R}}) - \frac{1}{2}(u_{\text{R}} - u_{\text{L}})\overline{\rho}\overline{a}, \tag{3.46}$$

and

$$\overline{\rho} = \frac{1}{2}(\rho_{\text{L}} + \rho_{\text{R}}),\ \ \overline{a} = \frac{1}{2}(a_{\text{L}} + a_{\text{R}}). \tag{3.47}$$

For the three-wave model, the left, right and intermediate wave speeds are estimated as

$$s_{\text{L}} = u_{\text{L}} - a_{\text{L}} q_{\text{L}},\ \ s_{\text{R}} = u_{\text{R}} + a_{\text{R}} q_{\text{R}}, \tag{3.48}$$

with

$$q_K = \begin{cases} 1 & \text{if } p^* \le p_K, \\ \left[1 + \dfrac{\gamma+1}{2\gamma}\left(\dfrac{p^*}{p_K} - 1\right)\right]^{1/2} & \text{if } p^* > p_K, \end{cases} \tag{3.49}$$

where the subscript K denotes the left or the right state, and

$$s^* = \frac{p_{\text{R}} - p_{\text{L}} + \rho_{\text{L}} u_{\text{L}}(s_{\text{L}} - u_{\text{L}}) - \rho_{\text{R}} u_{\text{R}}(s_{\text{R}} - u_{\text{R}})}{\rho_{\text{L}}(s_{\text{L}} - u_{\text{L}}) - \rho_{\text{R}}(s_{\text{R}} - u_{\text{R}})}. \tag{3.50}$$

The flux at the interface is then evaluated as

$$F = \begin{cases} F_{\text{L}}, & s_{\text{L}} > 0, \\ F_{\text{L}} + s_{\text{L}}\left(Q_{\text{L}}^* - Q_{\text{L}}\right), & s_{\text{L}} \le 0 < s^*, \\ F_{\text{R}} + s_{\text{R}}\left(Q_{\text{R}}^* - Q_{\text{R}}\right), & s^* \le 0 < s_{\text{R}}, \\ F_{\text{R}}, & s_{\text{R}} > 0, \end{cases} \tag{3.51}$$

with the intermediate state vectors

$$Q_K^* = \left(\frac{s_K - u_K}{s_K - s^*}\right) \begin{bmatrix} \rho_K Y_{K,1} \\ \vdots \\ \rho_K Y_{K,N_{sp}} \\ \rho_K s^* \\ \rho_K v_K \\ \rho_K w_K \\ \rho_K E_K + \left(s^* - u_K\right)\left[\rho_K s^* + \dfrac{\rho_K}{s_K - u_K}\right] \end{bmatrix}. \tag{3.52}$$

The CFL condition of the HLLC method for 1D Euler equations is given in the same form as in Equation (3.30).

3.4 MUSCL-Hancock method

For the mapped solver in AMROC, a second-order accurate MUSCL-Hancock method [163] is used for the inviscid flux reconstruction. The MUSCL part reconstructs primary variables or conservative variables in space and the Hancock part is used to update the reconstructed variables by half a time step. The method is developed for a Cartesian mesh and needs to be modified to work on the mapped mesh. In AMROC, the reconstruction is carried out using gradients calculated on computational meshes. Considering the MUSCL reconstruction for the Cartesian mesh,

$$\begin{aligned} Q_{i,j}^{l,n} &= Q_{i,j}^{n} - \frac{1}{2}\varepsilon_i(1+\omega)\delta_{i-1,j}\frac{\Delta x_c}{2} - \frac{1}{2}\varepsilon_i(1-\omega)\delta_{i,j}\frac{\Delta x_c}{2}, \\ Q_{i,j}^{r,n} &= Q_{i,j}^{n} + \frac{1}{2}\varepsilon_i(1-\omega)\delta_{i-1,j}\frac{\Delta x_c}{2} + \frac{1}{2}\varepsilon_i(1+\omega)\delta_{i,j}\frac{\Delta x_c}{2}. \end{aligned} \tag{3.53}$$

ε_i denotes the limiter and the Minmod limiter is used for all the cases in the present work. The value of the coefficient ω is set to 0 as a linear reconstruction. δ is the discrete gradient and an example is given by

$$\delta_{i,j} = \frac{Q_{i+1,j} - Q_{i,j}}{\Delta x_c}. \tag{3.54}$$

Δx_c is the interval between the centroid of cell (i, j) and cell (i+1, j). In the computational space, namely on a Cartesian mesh, Δx_c is uniform and equal to the cell size. However, for the mapped mesh, the physical interval should be taken into account. The modified slope for the mapped mesh is therefore,

$$\delta_{i,j} = \frac{Q_{i+1,j} - Q_{i,j}}{L_{i+1,j}^{-} + L_{i,j}^{+}}. \tag{3.55}$$

In 2D problems, $L_{i,j}^{+}$ is the interval between the centroid of cell (i, j) and the centroid of the interface (i+1/2, j) in physical space. $L_{i,j}^{-}$ is the distance between the centroid of cell (i, j) and the interface (i-1/2, j). Similarly, $L_{i+1,j}^{-}$ is the distance between the centroid of cell (i+1, j) and interface (i+1/2, j). The MUSCL reconstruction for the mapped mesh is given as

$$\begin{aligned} Q_{i,j}^{l,n} &= Q_{i,j}^{n} - \frac{1}{2}\varepsilon_i(1+\omega)\frac{(Q_{i,j} - Q_{i-1,j})L_{i,j}^{-}}{L_{i-1,j}^{+} + L_{i,j}^{-}} - \frac{1}{2}\varepsilon_i(1-\omega)\frac{(Q_{i+1,j} - Q_{i,j})L_{i,j}^{+}}{L_{i+1,j}^{-} + L_{i,j}^{+}}, \\ Q_{i,j}^{r,n} &= Q_{i,j}^{n} + \frac{1}{2}\varepsilon_i(1-\omega)\frac{(Q_{i,j} - Q_{i-1,j})L_{i,j}^{-}}{L_{i-1,j}^{+} + L_{i,j}^{-}} + \frac{1}{2}\varepsilon_i(1+\omega)\frac{(Q_{i+1,j} - Q_{i,j})L_{i,j}^{+}}{L_{i+1,j}^{-} + L_{i,j}^{+}}. \end{aligned} \tag{3.56}$$

A similar correction on the mapped mesh for the high-resolution method can be found in Ref. [34]. In 3D problems, the L is replaced by the interval between the centroid of adjacent hexahedra and the centroid of the interface. Another implementation is employing the MUSCL-Hancock method in the computational space. The variables Q in the physical space are transformed to computational space

$\boldsymbol{Q} = \boldsymbol{J}Q$ by using the Jacobian determinant of the grid $\boldsymbol{J} = \det | \partial (x, y, z)/\partial (\xi, \eta, \zeta) |$. The standard MUSCL reconstruction is conducted in the computational space. After the reconstruction, the variables are transformed back to the physical space and are integrated by half a time step before being used for the flux estimation in a Riemann solver.

3.5 Numerical instabilities

Some numerical instabilities were found in physical problems that involve a large gradient in terms of specific heat ratio [164]. The conservative scheme may cause the instabilities on the contact surface. This issue has gained more attention in the multi-phase simulation field than in single-phase multi-component flow simulations. However, the latter scenario also presents a large gradient in specific heat ratio.

A non-reacting jet test is conducted as shown in Figure 3.1. A pure ethylene jet is injected into the chamber filled with oxygen at 300 K. The results show that the unphysical low-temperature region is the source of the computational crash when using the Roe/HLL scheme to simulate the multi-species flow field with a large specific heat ratio difference. As compared, the HLLC scheme shows reasonable results even though the oscillation still exists when the fully conservative scheme is maintained.

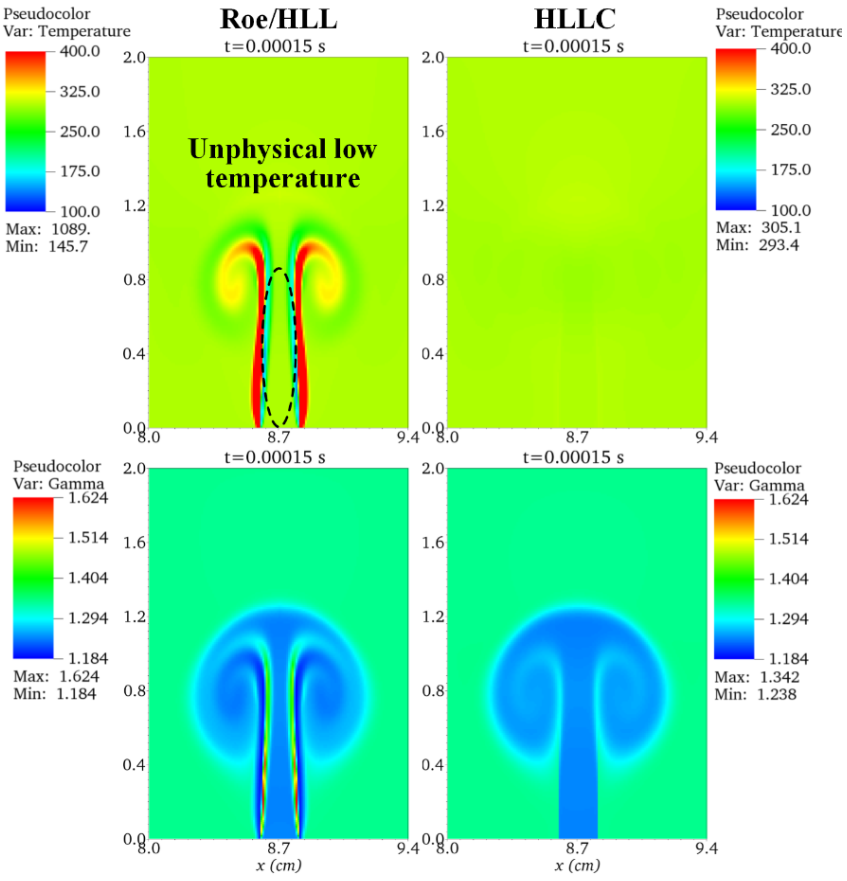

Figure 3.1 Pseudo-colour images of temperature (top) and specific heat ratio (bottom) distribution.

Breaking the conservation is a possible way to avoid the numerical oscillations [164,165]. The so called "double-flux scheme" [165] is a kind of method that computes the fluxes on the interface twice with the assumption that the specific heat ratio is maintained across the interface. The numerical pressure and velocity oscillations can be supressed with a compromise of conservation losses. One approach to decreasing the conservation error is combining the double-flux scheme with a high order numerical method, i.e., WENO [166] and high order DG [167].

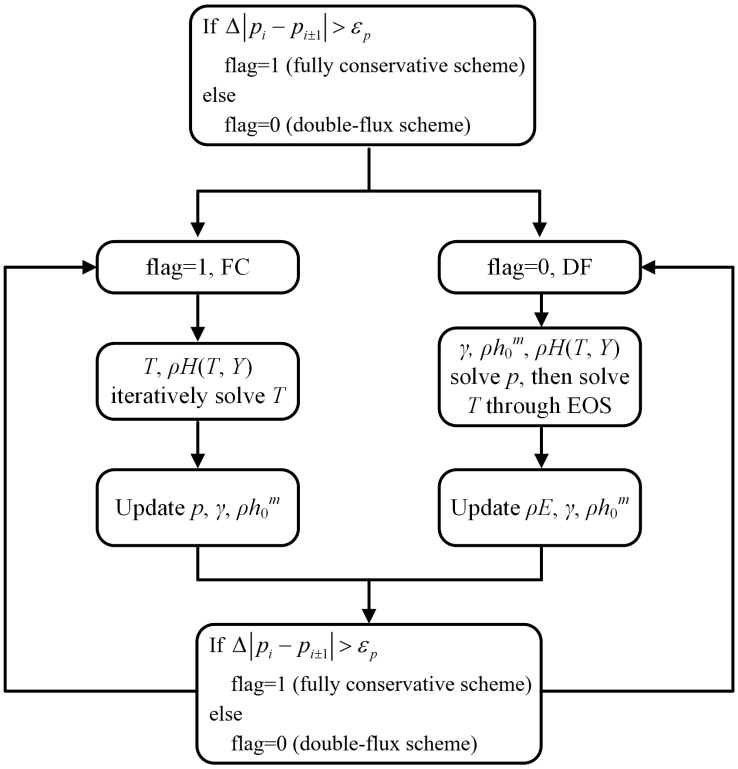

Figure 3.2 Flowchart of the implemented first-order hybrid-flux scheme in AMROC.

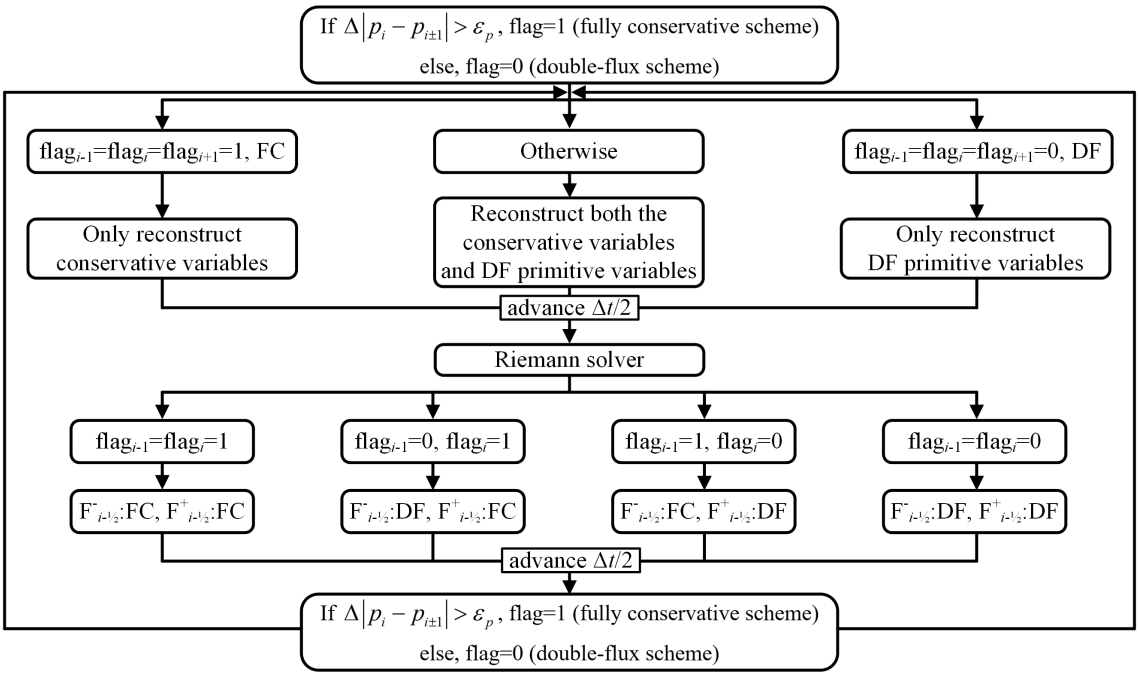

Figure 3.3 Flowchart of the implemented second-order hybrid-flux scheme in AMROC.

Another method, namely the hybrid-flux scheme [168,169], is a combination of the non-conservative double-flux scheme and the fully conservative scheme. As shown in Figure 3.2, the scaled pressure gradient $\Delta|p_i - p_{i\pm1}|$ is used to flag the region where the fully conservative (FC) scheme is used (flag = 1), otherwise the double-flux (DF) scheme (flag = 0) is employed. This method is used to flag the shock wave in the flow field. This hybrid scheme can be extended to second-order accuracy combined with the MUSCL-Hancock method. As depicted in Figure 3.3, the reconstruction is based on the flagging results and then the first half time step advancement is conducted. Then, the respective schemes on both sides of the interface are employed in the Riemann solver according to the flag value. Finally, the second half time step advancement is conducted. However, the non-conservative method brings errors when approximating the strong discontinuity. Hence, the fully conservative scheme is employed especially near the shock wave, which is flagged by the scaled pressure gradient and the given threshold ε_p.

Figure 3.4 shows the comparison of the jet test with different schemes. The results show that the numerical oscillations are suppressed even when using the fully conservative HLLC scheme, resulting in a reasonable temperature field compared to that using fully the conservative Roe/HLL scheme. The conservation errors in shock tube problems are compared in Figure 3.5 using fully conservative (FC), double-flux (DF), and hybrid-flux (HF) schemes. The use of a hybrid-flux scheme (ε_p = 1 kPa) can reduce the conservation errors in terms of mass and energy compared with the double-flux scheme. This reduction is observed in cases employing both the first-order and second-order methods. However, it still introduces some mass losses, which leads to a numerical crash in reacting flow simulations, i.e., RDE simulations. As discussed above, for all the non-premixed RDE simulations, the fully conservative HLLC scheme is used in this thesis.

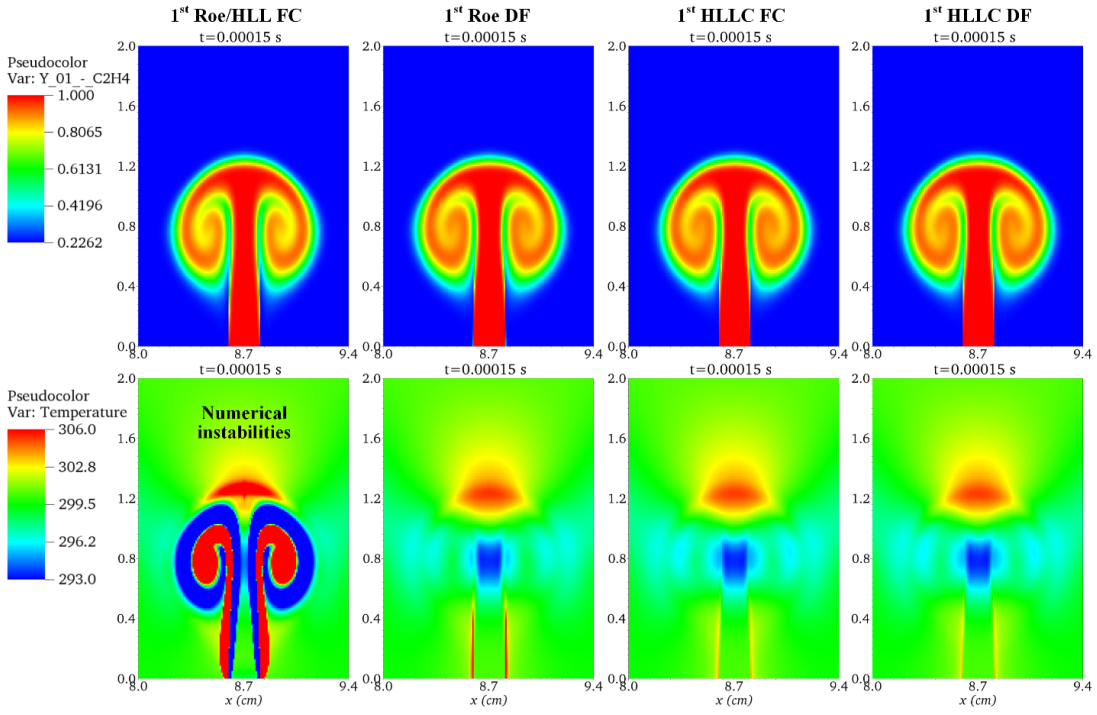

Figure 3.4 Pseudo-colour images of species of C_2H_4 (top) and temperature (bottom) distribution.

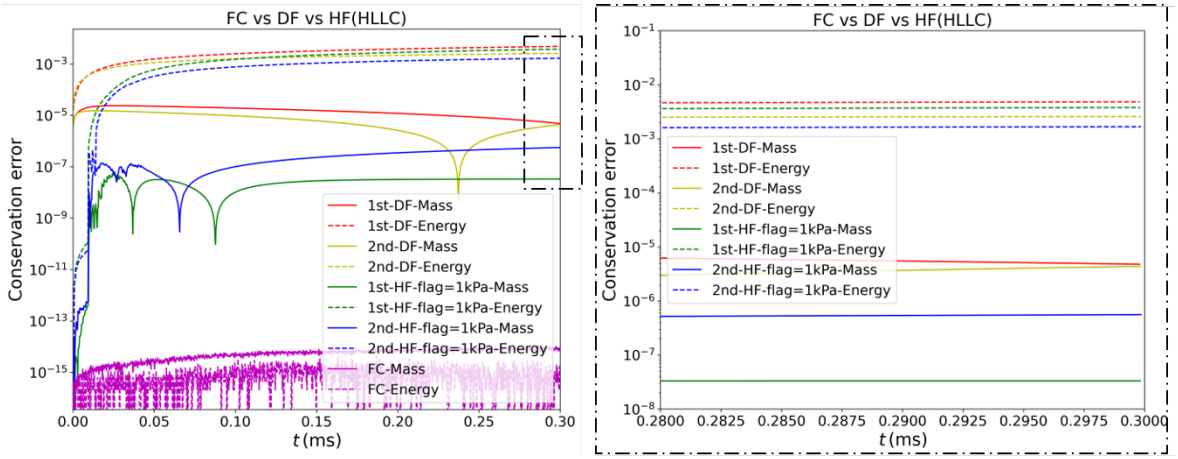

Figure 3.5 Conservation errors of mass and energy with different schemes.

3.6 Viscous fluxes

The viscous fluxes F_V and G_V in Equation (3.8) on mapped structured meshes must be calculated at each face in physical space. Considering the rotating method used for the inviscid fluxes, the velocities could be aligned with the physical interface in each cell. However, the derivatives of the velocities with respect to the x- and y-directions are calculated by the velocities at each face, which are not always in the same direction in the physical space. To calculate the derivatives of a variable, φ, in physical space, a coordinate transformation [157] is used as

$$\begin{aligned}
\frac{\partial \varphi}{\partial x} &= \left(\frac{\partial \varphi}{\partial \xi}\right)\left(\frac{\partial \xi}{\partial x}\right) + \left(\frac{\partial \varphi}{\partial \eta}\right)\left(\frac{\partial \eta}{\partial x}\right) + \left(\frac{\partial \varphi}{\partial \zeta}\right)\left(\frac{\partial \zeta}{\partial x}\right), \\
\frac{\partial \varphi}{\partial y} &= \left(\frac{\partial \varphi}{\partial \xi}\right)\left(\frac{\partial \xi}{\partial y}\right) + \left(\frac{\partial \varphi}{\partial \eta}\right)\left(\frac{\partial \eta}{\partial y}\right) + \left(\frac{\partial \varphi}{\partial \zeta}\right)\left(\frac{\partial \zeta}{\partial y}\right), \\
\frac{\partial \varphi}{\partial z} &= \left(\frac{\partial \varphi}{\partial \xi}\right)\left(\frac{\partial \xi}{\partial z}\right) + \left(\frac{\partial \varphi}{\partial \eta}\right)\left(\frac{\partial \eta}{\partial z}\right) + \left(\frac{\partial \varphi}{\partial \zeta}\right)\left(\frac{\partial \zeta}{\partial z}\right).
\end{aligned} \tag{3.57}$$

The derivatives of the computational coordinates with respect to the physical coordinates ($\partial\xi/\partial x$, $\partial\eta/\partial x$, $\partial\zeta/\partial x$, etc.) are obtained either from the analytic mapping functions or using second-order accurate numerical derivatives. The derivatives of the flow variables ($\partial\varphi/\partial\xi$, $\partial\varphi/\partial\eta$, $\partial\varphi/\partial\zeta$, etc.) are calculated on the computational meshes, and the derivatives at the interface (i-1/2, j, k) are given by

$$\left(\frac{\partial \varphi}{\partial \xi}\right)_{i-1/2,j,k} = \frac{\varphi_{i,j,k} - \varphi_{i-1,j,k}}{\Delta\xi}, \tag{3.58}$$

$$\left(\frac{\partial \varphi}{\partial \eta}\right)_{i-1/2,j,k} = \frac{1}{2}\left(\frac{\varphi_{i,j+1,k} - \varphi_{i,j-1,k}}{2\Delta\eta} - \frac{\varphi_{i-1,j+1,k} - \varphi_{i-1,j-1,k}}{2\Delta\eta}\right), \tag{3.59}$$

$$\left(\frac{\partial \varphi}{\partial \zeta}\right)_{i-1/2,j,k} = \frac{1}{2}\left(\frac{\varphi_{i,j,k+1} - \varphi_{i,j,k-1}}{2\Delta\zeta} - \frac{\varphi_{i-1,j,k+1} - \varphi_{i-1,j,k-1}}{2\Delta\zeta}\right). \tag{3.60}$$

The derivatives of φ in computational space at the interface (i, j-1/2, k) and (i, j, k-1/2) can be derived in a similar way. In addition, the effects of viscous fluxes should be considered when calculating the CFL condition [170],

$$CFL_x^{\mathrm{D}} = CFL_x^{\mathrm{C}} + \frac{\Delta t}{\Delta x^2}\max\left(\frac{8}{3}\frac{\mu}{\rho}, \frac{2k}{C_{\mathrm{v}}\rho}, D_1, \cdots, D_i, \cdots, D_{Nsp}\right), \tag{3.61}$$

where CFL_x^{C} is the CFL number calculated in the schemes of inviscid fluxes presented in Section 3.3. The diffusion coefficient D_i of species i, the mixture viscosity μ, and the thermal conductivity k are calculated by the methods introduced in Section 3.1.2. The global CFL number is defined by the maximum value in all directions. The next global time step is calculated from the CFL number of the previous time step and a user-specified target CFL number. Since the method is strictly explicit, a target CFL number less than one is used in all the cases. Decreasing the CFL number can improve the stability of a computation, but it is more expensive.

3.7 Adaptive mesh refinement

AMROC currently adopts the block-structured adaptive mesh refinement technology (SAMR), which was first proposed by Berger and Oliger and was used to solve hyperbolic partial differential equations [28]. This method employs a patch-wise refinement approach. The meshes are dynamically flagged by using specified refinement criteria [30,36]. These flagged cells are then grouped into a region of various-sized rectangular blocks. By successively creating refined meshes from respectively coarser parents, a multi-level hierarchy of embedded grid patches is created, as shown in Figure 3.6.

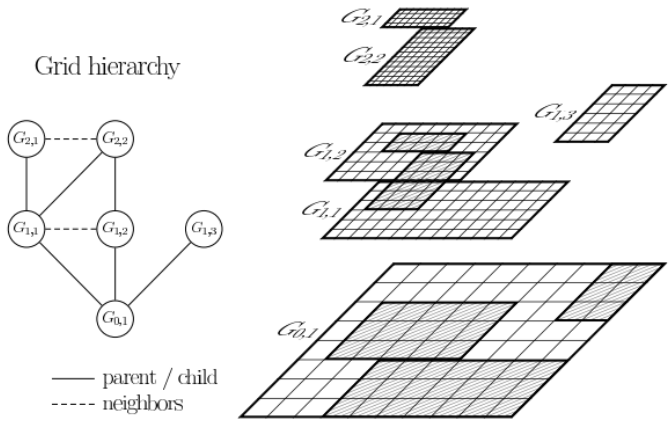

Figure 3.6 The block-structured refinement grids of the AMR method [30].

Using the Berger-Colella AMR method, the main finite volume integrator is effectively separated from the adaptive strategy. The numerical schemes are employed simultaneously on grids at different levels. The curvilinear structured mesh [171] can be applied to the entire AMR technique since the AMROC structured data layout is preserved in the present solver. For instance, to generate the

coordinates of grids at a higher level (l+1) or a lower level (l−1), the coordinates of the flagged uniform Cartesian grids in computational space at level l are refined or coarsened, respectively. By using the specific mapping strategy on each level, the new coordinates in computational space ($\xi_{l\pm1}$, $\eta_{l\pm1}$, $\zeta_{l\pm1}$) are used to generate curvilinear structured grids in physical space ($x_{l\pm1}$, $y_{l\pm1}$, $z_{l\pm1}$) at the new level.

For parallelisation, the hierarchical mesh is distributed to processors based on a space-filling curve [30] in computational space. The domain decomposition aims to improve the efficiency and scalability of the simulation by distributing the computation in parallel across multiple processors or computational nodes. In this process, the computational domain is divided based on the amount of computational work required in each region. Continuous redistribution, while the mesh is changing, ensures a balanced workload at run time. The redistribute process is given at a specified frequency on the base level to ensure that the region of interest is dynamically captured by the highest-level mesh.

3.7.1 Refinement criteria

In AMROC, two different types of criteria are used to flag the grids [30]. The first one is evaluating the differences between the adjacent cells. It can be considered as gradients multiplied by the step size (named scaled gradients) in all directions. Cell (i, j) is flagged if one of the inequalities

$$\begin{aligned}
&\left|w\left(Q_{i+1,j}\right)-w\left(Q_{i-1,j}\right)\right|>\varepsilon_w,\\
&\left|w\left(Q_{i,j+1}\right)-w\left(Q_{i,j-1}\right)\right|>\varepsilon_w,\\
&\left|w\left(Q_{i+1,j+1}\right)-w\left(Q_{i-1,j-1}\right)\right|>\varepsilon_w,\\
&\left|w\left(Q_{i+1,j-1}\right)-w\left(Q_{i-1,j+1}\right)\right|>\varepsilon_w
\end{aligned} \tag{3.62}$$

is satisfied for an arbitrary scalar quantity w, which is derived from the vector of state Q. The constant ε_w denotes a prescribed threshold value. Similarly, the scaled gradients between the adjacent 3D cells involve seven inequalities. A cell is flagged for further refinement when one of its scaled gradients is beyond the given threshold in any direction.

The local truncation error is estimated by Richardson extrapolation [35,36] as another adaptation criterion. For simplicity, let $H^{\Delta t}$ be a one-step explicit difference operator with time step Δt. The local truncation error of order o satisfies

$$Q\left(x,t+\Delta t\right)-\mathrm{H}^{\Delta t}\left(Q\left(x,t\right)\right)=\mathbb{C}\Delta t^{o+1}+O\left(\Delta t^{o+2}\right). \tag{3.63}$$

$\mathbb{C}$ is a constant in the leading-order term of the right-hand side (RHS). The second term of RHS $O\left(\Delta t^{o+2}\right)$ represents an error of the o+2 th order of magnitude. If Q is sufficiently smooth, the local error at t+Δt after two time steps with Δt is

$$Q(x,t+\Delta t)-\mathrm{H}_2^{\Delta t}\left(Q(x,t-\Delta t)\right)=2\mathbb{C}\Delta t^{o+1}+O\left(\Delta t^{o+2}\right), \tag{3.64}$$

and the local error at $t+\Delta t$ after one time step with $2\Delta t$ is

$$Q(x,t+\Delta t)-\mathrm{H}^{2\Delta t}\left(Q(x,t-\Delta t)\right)=2^{o+1}\mathbb{C}\Delta t^{o+1}+O\left(\Delta t^{o+2}\right). \tag{3.65}$$

Subtracting (3.64) from (3.65) we obtain the relation

$$\mathrm{H}_2^{\Delta t}\left(Q(x,t-\Delta t)\right)-\mathrm{H}^{2\Delta t}\left(Q(x,t-\Delta t)\right)=\left(2^{o+1}-2\right)\mathbb{C}\Delta t^{o+1}+O\left(\Delta t^{o+2}\right). \tag{3.66}$$

Equation (3.66) is applied to estimate the leading-order term $\mathbb{C}\Delta t^{o+1}$ of the local error at $t+\Delta t$. The criterion based on this form requires a discrete solution $\mathcal{Q}(x,t-\Delta t)$ on a cell two times coarser than the current cell at level l. The restriction of $Q(x,t-\Delta t)$ is used to approximate the initial data on the coarser cell. Then $Q(x,t)$ and $\mathcal{Q}(x,t-\Delta t)$ are updated as usual. Finally, a second coarsened solution $\bar{\mathcal{Q}}(x,t+\Delta t)$ is derived by prolongation of $Q(x,t+\Delta t)$. More details of the restriction and prolongation operators are given in Section 3.7.2 and Section 3.7.3. The leading-order term of the local error of quantity w is approximated by neglecting the high order terms in Equation (3.66),

$$\tau_{i,j}^{w}\approx\frac{\left|w\left(\bar{\mathcal{Q}}_{i,j}(x,t+\Delta t)\right)-w\left(\mathcal{Q}_{i,j}(x,t+\Delta t)\right)\right|}{2^{o+1}-2}. \tag{3.67}$$

The practical usage of τ^{w} is a combination with relative and absolute error,

$$\frac{\tau_{i,j}^{w}}{\max\left(w\left(\mathcal{Q}_{i,j}(x,t+\Delta t)\right),S_w\right)}>\eta_w. \tag{3.68}$$

S_w is the scaling factor for relative error of quantity w, which is an empirical parameter. In this paper, the relation (3.68) is used as a refinement criterion in terms of the mass fractions Y_i for the reactive problems. The scaling limit S_{Yi} is set as the 1% of the maximal value of the mass fractions Y_i in the C-J equilibrium state. If the relation (3.68) is satisfied, all four cells below the coarsened cell (i, j) are flagged for refinement.

Although the relative error criteria of multiple species are used for some of the reactive problems in this paper, it is recommended for users of AMROC to choose the mass fraction of the most relevant chemical species. The number of species criteria can be reduced if a strict temperature scaled gradient criterion is used. Based on the specific problems, there are different possible choices for the threshold. The user-specified threshold can be determined by running some test computations on a coarse mesh. More universal, sophisticated and efficient refinement criteria will be a potential improvement of the current strategy.

3.7.2 Restriction

Transferring values from fine to coarse cells is called restriction in AMR algorithms. The restriction strategy in AMROC for the Cartesian mesh is that the value of the coarse cell is the average of its refined cells, as displayed in Figure 3.7 (a).

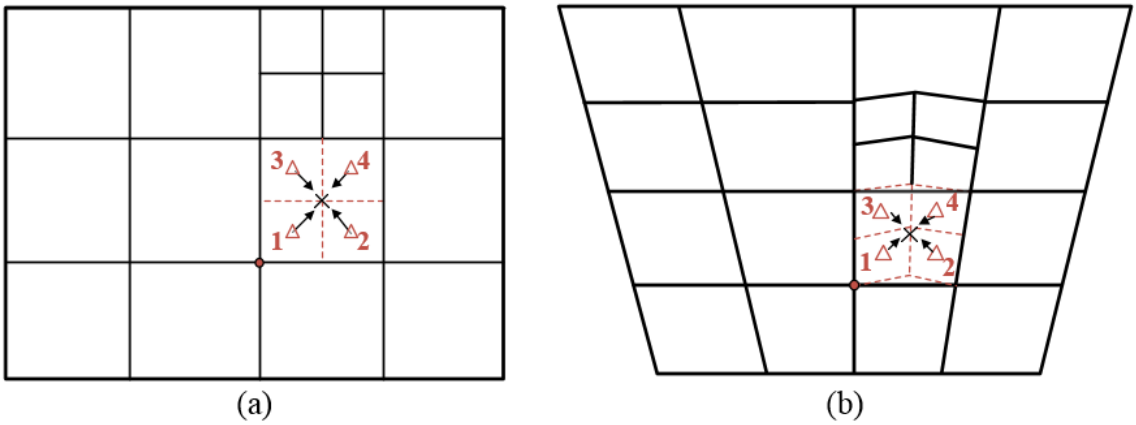

Figure 3.7 The restriction operation on a 2D (a) Cartesian mesh, (b) Mapped structured mesh.

The average can be a conservative arithmetic mean as the four fine cells have equal area,

$$Q_c = \frac{1}{n^2}\sum_{k=1}^{n^2} Q_{f,k}\ , \tag{3.69}$$

where subscript c denotes the coarse cell and the subscript f denotes the fine cell. The n is the refinement factor between these two levels. For the mapped mesh as shown in Figure 3.7 (b), the area weights of each fine cell should be counted to satisfy the conservation,

$$Q_c = \frac{\sum_{k=1}^{n^2} A_{f,k} Q_{f,k}}{A_c}\ . \tag{3.70}$$

where A is the area of each quadrilateral cell. An equivalent method is used in Ref. [172], in which the weights of a capacity function are used in the restriction. It is noted that this restriction is conservative even though the overlapped refined cells are not exactly aligned with their coarse grid cells, but it may cause accuracy losses when the total area of refined cells is not equal to the area of their coarse grid cells.

For 3D restriction, the weight of the area is replaced by the weight of the volume. Figure 3.8 shows an example of the restriction operation on 3D meshes with a refinement factor of 2. The restriction strategy is such that the value of the coarse element (displayed by the blue dot) is determined by its n^3 fine sub-elements (displayed by the red dots) through

$$Q_c = \frac{\sum_{k=1}^{n^3} V_{f,k} Q_{f,k}}{V_c}\ . \tag{3.71}$$

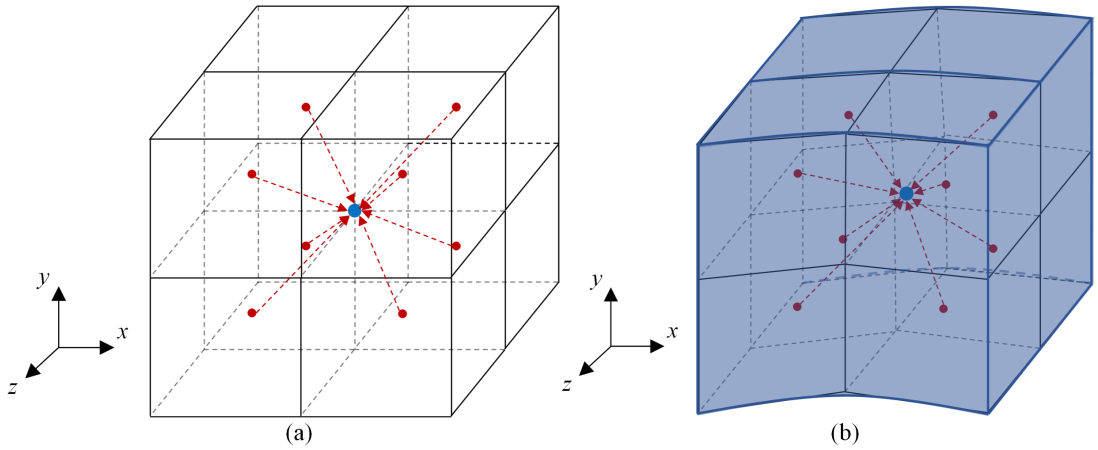

Figure 3.8 The restriction operation on a 3D (a) Cartesian mesh, (b) Mapped structured mesh.

3.7.3 Prolongation

Another important change for an AMR scheme on a mapped mesh is the prolongation operation from coarse to fine cells. For the Cartesian mesh, a bilinear space-interpolation is used in AMROC to pass the information from coarse to fine cells. The value of a newly refined cell is determined by the nearest four coarse cells, as shown in the same colour in Figure 3.9 (a).

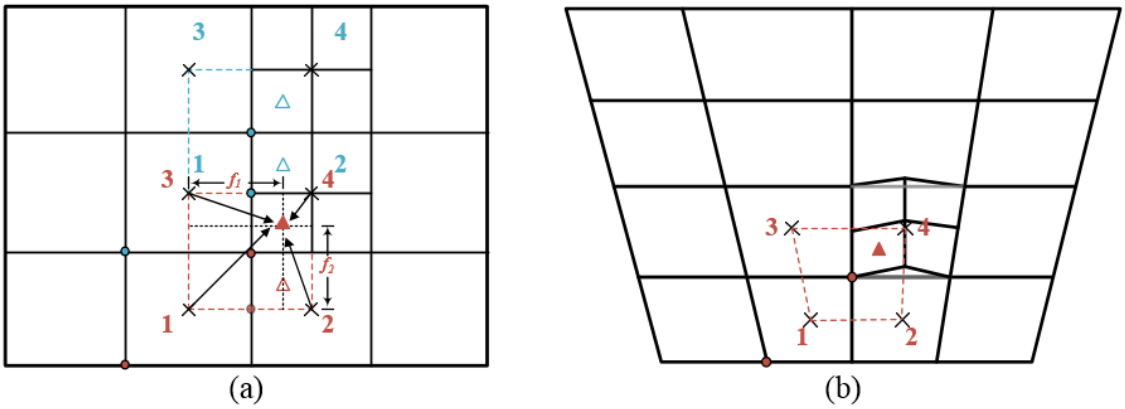

Figure 3.9 The prolongation operation on a 2D (a) Cartesian mesh, (b) Mapped structured mesh.

For example, the value of the fine cell with the red solid triangle in its centre can be solved as

$$Q_f = (1-f_1)(1-f_2)Q_{c,1} + f_1(1-f_2)Q_{c,2} + f_2(1-f_1)Q_{c,3} + f_1 f_2 Q_{c,4}\,. \tag{3.72}$$

The refinement factor in this figure is 2, so both the factors of f_1 and f_2 in the figure are 0.75. For the mapped mesh displayed in Figure 3.9 (b), the factors cannot be determined directly from the geometry. The physical coordinates of each cell centre are adopted to calculate factors f_1 and f_2 by solving the nonlinear equations numerically,

$$\begin{cases} x_f = (1-f_1)(1-f_2)x_{c,1} + f_1(1-f_2)x_{c,2} + f_2(1-f_1)x_{c,3} + f_1 f_2 x_{c,4} \\ y_f = (1-f_1)(1-f_2)y_{c,1} + f_1(1-f_2)y_{c,2} + f_2(1-f_1)y_{c,3} + f_1 f_2 y_{c,4} \end{cases}. \tag{3.73}$$

Then, Equation (3.72) is used to complete the prolongation. Similarly, the value of a 3D refined cell can be computed by the nearest n^3 coarse cells, as shown in Figure 3.10 (a). A trilinear interpolation is used for the value transfer. Figure 3.10 gives an example of the prolongation operation with a refinement factor of 2. The value of a newly refined cell (displayed by the red colour) is determined by the nearest eight coarse cells (displayed by the blue colour). To illustrate the prolongation operation, the locations of the centroid of each cell are extracted in Figure 3.11.

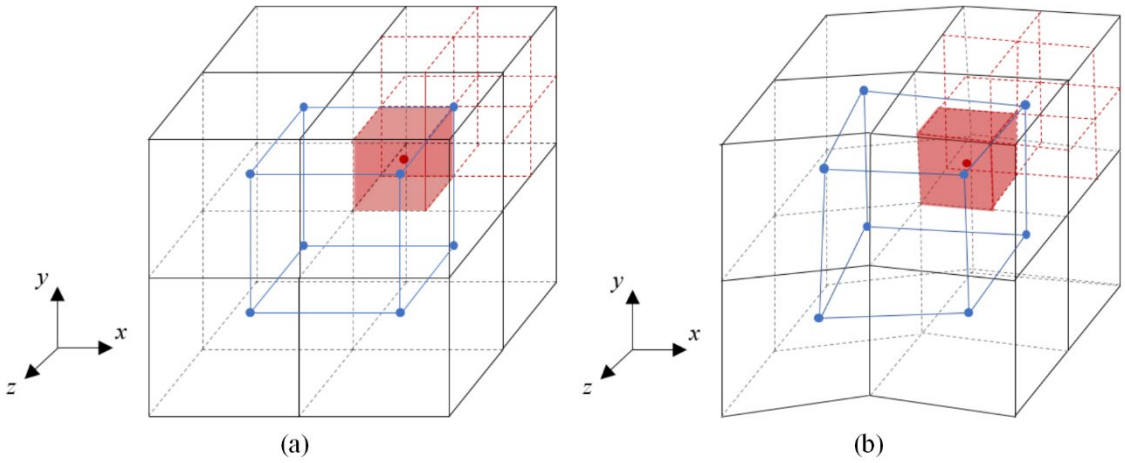

Figure 3.10 The prolongation operation on a 3D (a) Cartesian mesh, (b) Mapped structured mesh.

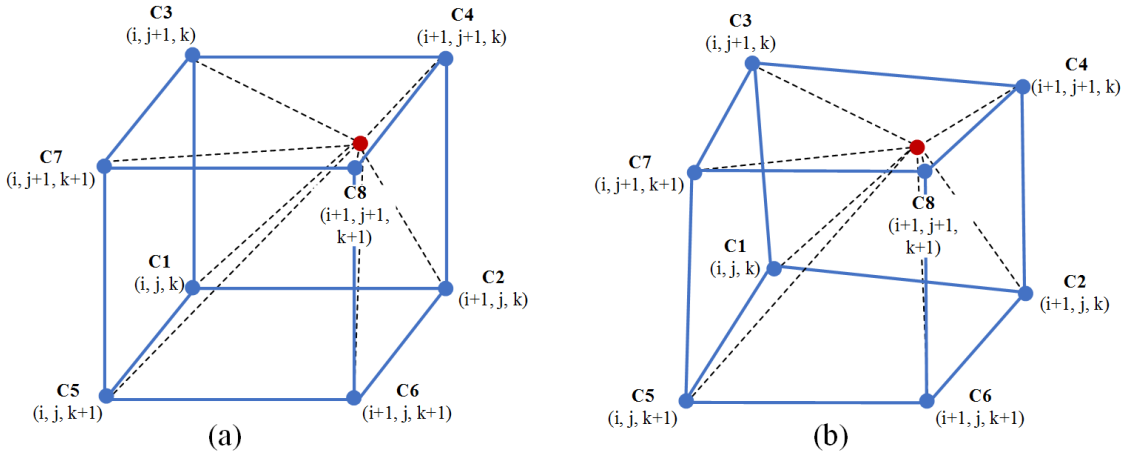

Figure 3.11 Schematic diagram of the centroid locations on (a) Cartesian mesh, (b) Mapped structured mesh.

A new element is generated by connecting the centroids of each coarse cell. The value in the refined cell can be computed by

$$\begin{aligned} Q_f = (1-f_3)\left\{(1-f_2)\left[(1-f_1)Q_{c,1} + f_1 Q_{c,2}\right] + f_2\left[(1-f_1)Q_{c,3} + f_1 Q_{c,4}\right]\right\} \\ + f_3\left\{(1-f_2)\left[(1-f_1)Q_{c,5} + f_1 Q_{c,6}\right] + f_2\left[(1-f_1)Q_{c,7} + f_1 Q_{c,8}\right]\right\} \end{aligned}. \tag{3.74}$$

For the Cartesian meshes, coefficients f_1, f_2, and f_3 can be easily computed from the indices because the element is a cube. For the mapped meshes, the element is an irregular hexahedron. The coefficients can be obtained by numerically solving the nonlinear equations with the relations of the physical coordinates,

$$\begin{cases} x_{\mathrm{f}} = (1-f_3)\left[(1-f_1)(1-f_2)x_{\mathrm{c},1} + f_1(1-f_2)x_{\mathrm{c},2} + f_2(1-f_1)x_{\mathrm{c},3} + f_1 f_2 x_{\mathrm{c},4}\right] \\ \quad + f_3\left[(1-f_1)(1-f_2)x_{\mathrm{c},5} + f_1(1-f_2)x_{\mathrm{c},6} + f_2(1-f_1)x_{\mathrm{c},7} + f_1 f_2 x_{\mathrm{c},8}\right] \\ y_{\mathrm{f}} = (1-f_3)\left[(1-f_1)(1-f_2)y_{\mathrm{c},1} + f_1(1-f_2)y_{\mathrm{c},2} + f_2(1-f_1)y_{\mathrm{c},3} + f_1 f_2 y_{\mathrm{c},4}\right] \\ \quad + f_3\left[(1-f_1)(1-f_2)y_{\mathrm{c},5} + f_1(1-f_2)y_{\mathrm{c},6} + f_2(1-f_1)y_{\mathrm{c},7} + f_1 f_2 y_{\mathrm{c},8}\right] \\ z_{\mathrm{f}} = (1-f_3)\left[(1-f_1)(1-f_2)z_{\mathrm{c},1} + f_1(1-f_2)z_{\mathrm{c},2} + f_2(1-f_1)z_{\mathrm{c},3} + f_1 f_2 z_{\mathrm{c},4}\right] \\ \quad + f_3\left[(1-f_1)(1-f_2)z_{\mathrm{c},5} + f_1(1-f_2)z_{\mathrm{c},6} + f_2(1-f_1)z_{\mathrm{c},7} + f_1 f_2 z_{\mathrm{c},8}\right] \end{cases}. \tag{3.75}$$

The Newton-Raphson method [173] is used to solve the nonlinear equations. If this method is not convergent within given iteration steps, the gradient descent algorithm would be used.

3.7.4 Refinement parameters

A number of general parameters are prescribed in the AMR algorithm. Unless otherwise mentioned, the following adaptive refinement settings are used in all of the computations in this work. The refinement flags are always set, and the grid hierarchy is recomposed at each coarser level time step. The buffer width is set to 2 in order to mark two more cells around the flagged cells. The clustering algorithm's threshold is set to 0.7, which indicates that the programme generates successively smaller grids until the ratio between flagged and all cells in each new grid exceeds this given threshold.

3.7.5 Fluxes correction

It is well known that the flux across coarse-fine interfaces in the Berger-Colella algorithm is not automatically strictly conservative. Hence, a flux correction or namely a flux fix-up is used before updating the states. In the updated formula of all cells, the coarse flux is approximated with all modified neighbouring cells by the sum of all overlying fine-level fluxes. For simplicity, only the 2D fix-up process is described here, as depicted in Figure 3.12, and the 3D method can be deduced naturally by canonical extension.

As an example on Cartesian meshes [30], the correct update for Q in cell (j, k) on level i is given as

$$\begin{aligned} &\delta F^{d,i+1}_{j-\frac{1}{2},k} = -F^{d,i}_{j-\frac{1}{2},k}, \\ &\delta F^{d,i+1}_{j-\frac{1}{2},k} = \delta F^{d,i+1}_{j-\frac{1}{2},k} + \frac{1}{r^{i+1^2}} \sum_{l=0}^{r^{i+1}-1} \sum_{n=0}^{r^{i+1}-1} F^{d,i+1}_{v+\frac{1}{2},w+l}\left(t + n\Delta t^{i+1}\right), \\ &\breve{Q}^{i}_{jk}\left(t+\Delta t^{i}\right) = Q^{i}_{jk}\left(t+\Delta t^{i}\right) + \frac{\Delta t^{i}}{\Delta x^{i}} \delta F^{d,i+1}_{j-\frac{1}{2},k}. \end{aligned} \tag{3.76}$$

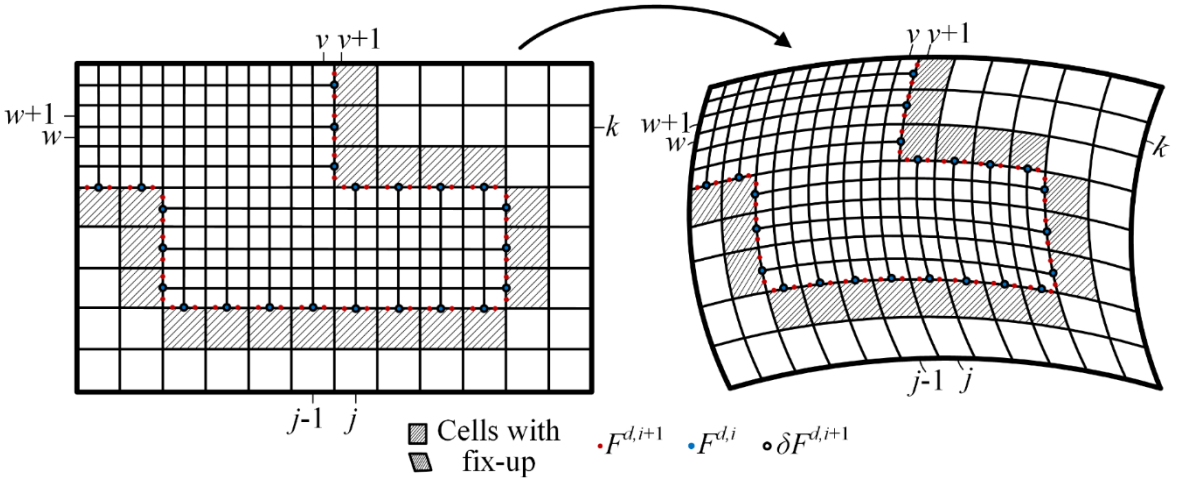

Figure 3.12 Schematic of the flux correction on a Cartesian mesh (left) and on a mapped mesh (right).

As shown in Figure 3.12, the shaded cells at the coarse level are fixed up with the correction term δF on the interface. An analogous correction method is used to update the Q on a mapped mesh. The flux difference on a mapped mesh is computed as

$$\begin{aligned}\delta F^{d,i+1}_{j-\frac{1}{2},k} &= -F^{d,i}_{j-\frac{1}{2},k}\frac{\Delta y^{i}}{\Delta \eta^{i}},\\ \delta F^{d,i+1}_{j-\frac{1}{2},k} &= \delta F^{d,i+1}_{j-\frac{1}{2},k} + \frac{1}{r^{i+1^2}}\sum_{l=0}^{r^{i+1}-1}\sum_{n=0}^{r^{i+1}-1} F^{d,i+1}_{v+\frac{1}{2},w+l}\left(t+n\Delta t^{i+1}\right)\frac{\Delta y^{i+1}}{\Delta \eta^{i+1}}.\end{aligned} \tag{3.77}$$

If the refinement factor r^{i+1} is set to 2 between level i and level $i+1$, this term $\delta F^{d,i+1}_{j-\frac{1}{2},k}$ can be expanded as

$$\begin{aligned}\delta F^{d,i+1}_{j-\frac{1}{2},k} = -F^{d,i}_{j-\frac{1}{2},k}\frac{\Delta y^{i}}{\Delta \eta^{i}} + \frac{1}{4}\Bigg[& F^{d,i+1}_{v+\frac{1}{2},w}(t)\frac{\Delta y^{i+1}_{w}}{\Delta \eta^{i+1}} + F^{d,i+1}_{v+\frac{1}{2},w+1}(t)\frac{\Delta y^{i+1}_{w+1}}{\Delta \eta^{i+1}}\\ & + F^{d,i+1}_{v+\frac{1}{2},w}\left(t+\Delta t^{i+1}\right)\frac{\Delta y^{i+1}_{w}}{\Delta \eta^{i+1}} + F^{d,i+1}_{v+\frac{1}{2},w+1}\left(t+\Delta t^{i+1}\right)\frac{\Delta y^{i+1}_{w+1}}{\Delta \eta^{i+1}}\Bigg].\end{aligned} \tag{3.78}$$

The difference on the coarse-fine interface is finally integrated into the state vectors by using the capacity function in the respective coarse grid cell by applying

$$\breve{Q}^{i}_{jk}\left(t+\Delta t^{i}\right) = Q^{i}_{jk}\left(t+\Delta t^{i}\right) + \frac{\Delta t^{i}}{\left|C_{jk}\right|^{i}\Delta \xi^{i}}\delta F^{d,i+1}_{j-\frac{1}{2},k}. \tag{3.79}$$

The conservation of the entire scheme is hence maintained.

3.8 Boundary conditions

In AMROC, the boundary conditions are specified by using ghost cells around a Cartesian mesh (see Ref. [30]). In the present solver, the state vectors are initialised in the physical space, where the velocities are orthonormal to the Cartesian coordinate system. As a result, the inflow and outflow

boundary conditions are the same as those based on the Cartesian mesh. However, the symmetry and reflected wall boundary conditions need to be modified. For a symmetry or reflecting wall boundary condition, the normal velocity on the physical boundary should be zero and there is no flow across the boundary. The transformation matrix is used to rotate the velocity of inner domain cells to align with the physical boundary. Then, the normal and tangential velocities on the boundary are eliminated by setting the value of the velocity in the ghost cell to be equal and opposite to the velocity in the domain cell. After that, the velocity in ghost cells is transformed back to the orthonormal direction of the Cartesian coordinate, respectively.

3.9 Geometric information

For the mapped structured mesh, some subroutines are constructed in AMROC to compute the geometric information of quadrilateral and hexahedron meshes, such as the area of faces, the volume of elements, the centroids of faces, the centroids of elements and the rotation matrices. In the 2D solvers, the area, the centroid of the quadrilateral and 2D rotation matrix T_s are calculated by the method in Ref. [162]. The details will not be described here.

In the 3D solvers, the volume of the hexahedron is calculated by decomposing it into three polygonal pyramids as illustrated in Figure 3.13.

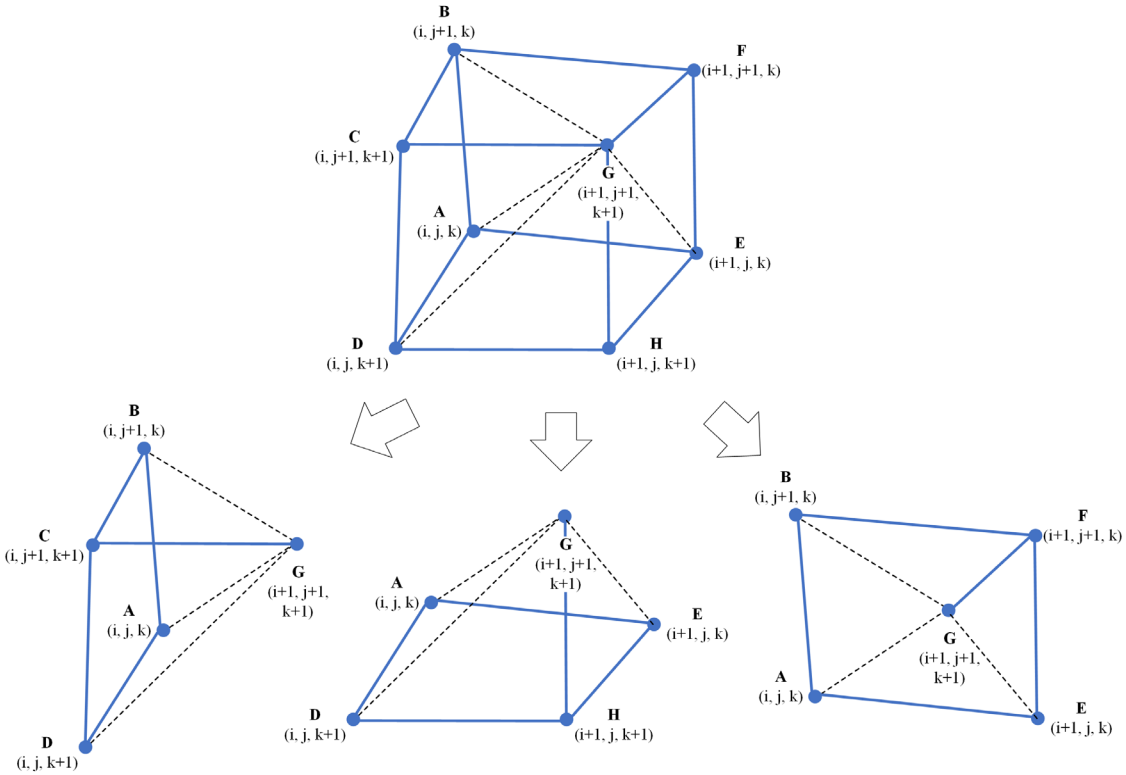

Figure 3.13 Schematic diagram of decomposing the 3D cell into polygonal pyramids.

The method used for calculating the volume is similar to the method in Ref. [174] but with some variations. Here are some descriptions about the computation process. As every face is shared by two

adjacent elements, only one side along each direction is computed for one element. The subroutine starts by computing the inwards unit normal vectors of the left side, bottom side and back side sequentially for each element.

The normal vectors can be calculated by the cross product of any two vectors in the face with the right-hand rule. For example, the inwards normal vector of the left side (A-B-C-D-A) can be computed by the cross product of the vector A-B and the vector A-D. The half modulus of the normal vector is the area of the triangle (A-B-D-A). The unit normal vector $\vec{n}$ is also obtained after normalization. The area of the triangle (C-D-B-C) can be computed in the same way. The centroid of the quadrilateral (A-B-C-D-A) is calculated by

$$X_{\text{quadrilateral}} = \frac{X_{\text{triangle1}} A_{\text{triangle1}} + X_{\text{triangle2}} A_{\text{triangle2}}}{A_{\text{quadrilateral}}}, \tag{3.80}$$

where X is the x, y, and z coordinates of the centroid and A is the area. The centroid of a triangle is overlapped with its geometric centre.

The volume of each pyramid is given as

$$V_{\text{pyramid}} = \frac{1}{3} \times A_{\text{quadrilateral}} \times \left(\overrightarrow{\text{AG}} \cdot \vec{n} \right). \tag{3.81}$$

The volume of the hexahedron is the sum of the three pyramids. The centroid of each pyramid is given as

$$X_{\text{pyramid}} = 0.75 X_{\text{quadrilateral}} + 0.25 X_{\text{G}}, \tag{3.82}$$

where X_{G} is the x, y, and z coordinates of the vertex G. The centroid of the hexahedron is computed by

$$X_{\text{hexahedron}} = \frac{\sum_{n=1}^{3} V_{\text{pyramid-}n} X_{\text{pyramid-}n}}{V_{\text{hexahedron}}}, \tag{3.83}$$

The 3D rotation matrix T_{s} on each interface can be derived from the unit normal vector [175]. a_x, a_y and a_z correspond to each of these components of the unit normal vector $\vec{n}$, as shown in Figure 3.14. If the absolute value of a_y is greater than the absolute value of a_z, other unknown components of the matrix can be calculated by Equation (3.84). Otherwise, the unknown components of the matrix are computed by Equation (3.85). All the mesh information is stored in auxiliary arrays with an interface provided by the original Clawpack codes. The information is updated at the beginning of each time step because the meshes are dynamically changing. These arrays are used for the mapping and other calculations as mentioned in previous sections. Especially for the AMR operations, this process is slightly expensive under current configurations. Some classes will be developed in the future to keep the mesh information in memory to make the AMR more efficient at the next stage.

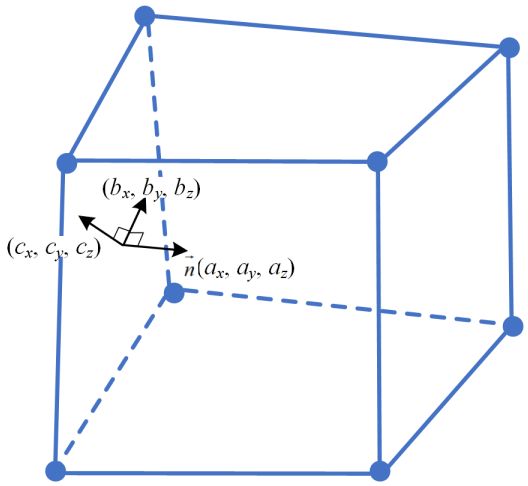

Figure 3.14 Schematic diagram of the normal and tangential vectors on the left side.

$$\begin{cases} b_x = \dfrac{a_y}{\sqrt{2a_y^2 + a_x^2 + a_z^2 - 2a_z a_x}}, c_x = a_y b_z - a_z b_y \\ b_y = \dfrac{a_z - a_x}{\sqrt{2a_y^2 + a_x^2 + a_z^2 - 2a_z a_x}}, c_y = a_z b_x - a_x b_z \\ b_z = \dfrac{-a_y}{\sqrt{2a_y^2 + a_x^2 + a_z^2 - 2a_z a_x}}, c_z = a_x b_y - a_y b_x \end{cases} . \tag{3.84}$$

$$\begin{cases} c_x = \dfrac{a_z}{\sqrt{2a_z^2 + a_x^2 + a_y^2 - 2a_y a_x}}, b_x = c_y a_z - c_z a_y \\ c_y = \dfrac{-a_z}{\sqrt{2a_z^2 + a_x^2 + a_y^2 - 2a_y a_x}}, b_y = c_z a_x - c_x a_z \\ c_z = \dfrac{a_y - a_x}{\sqrt{2a_z^2 + a_x^2 + a_y^2 - 2a_y a_x}}, b_z = c_x a_y - c_y a_x \end{cases} . \tag{3.85}$$

3.10 Chapter summary

In this chapter, the numerical methods implemented into AMROC have been presented. As the data structure remains unchanged when applying these methods on structured mesh, this chapter only covers the amendments based on the Cartesian AMROC framework. A second-order accurate finite volume method has been used with grid-aligned Riemann solvers for thermally perfect gas mixtures. Detailed, multi-step chemical kinetic mechanisms were employed and numerically incorporated with a splitting approach. The adaptive mesh refinement technique used modified prolongation and restriction operators. The flux along the coarse-fine interface was considered in a correction procedure to ensure the conservation of the whole solver. These methods provided guides for users who have a similar block-structured AMR solver and can extend their own code in a similar way.

Chapter 4 Verification and validation

4.1 Verification

4.1.1 Method of manufactured solutions

In this subsection, the method of manufactured solutions (MMS) is employed to verify the solver on different mapped meshes. The MMS has been used in many published studies to verify CFD codes and test the accuracy of the scheme [176,177]. In the present solver, the chemical source terms are replaced by some analytical source terms to construct the Euler equations and Navier-Stokes equations with manufactured solutions. In this section, the specific heat ratio is assumed to be a constant to simplify the derivation in terms of enthalpy in the analytical source terms.

An error analysis is conducted to make a comparison between the analytical solutions and the numerical results. The global L_2 norm of the error function is given by

$$\mathrm{L}_2 = \sum_{l=1}^{\max level} \sqrt{\frac{\left(q_{\mathrm{numerical}} - q_{\mathrm{exact}}\right)^2 A}{A_{\mathrm{total}}}}. \tag{4.1}$$

In order to test the accuracy of the adaptive mapped method, three types of meshes are used in this section. The first one is a stretched mesh mapped by a clustering function [178] that reads

$$\begin{cases} x = \xi * L_{\mathrm{x}} \\ y = r_d * L_{\mathrm{y}} \left[1 + \dfrac{\sinh\left[\beta\left(\eta - A\right)\right]}{\sinh(\beta A)} \right], \quad A = \dfrac{1}{2\beta} \ln\left(\dfrac{1 + \left(e^{\beta} - 1\right) r_d}{1 + \left(e^{-\beta} - 1\right) r_d} \right), \end{cases} \tag{4.2}$$

where the clustering factor β is 5 and the factor r_d is 0.5 for the mesh stretched in the centre. L_x and L_y are the total length of the domain in the x- and y-direction, respectively. The following function is used to generate a skewed mesh, where the angle of inclination is 15 degrees in each direction:

$$\begin{cases} x = \xi + \eta \tan\left(\dfrac{\pi}{12}\right) - 0.5 \\ y = 2 \times \left(\eta + \xi \tan\left(\dfrac{\pi}{12}\right) \right) \end{cases}. \tag{4.3}$$

In addition, a distorted mesh [179] is generated by applying

$$\begin{cases} x = \xi + L_{\mathrm{x}} S_{\mathrm{x}} \sin\left(\dfrac{2\pi\xi}{L_{\mathrm{x}}}\right) \sin\left(\dfrac{2\pi\eta}{L_{\mathrm{y}}}\right) \\ y = \eta + L_{\mathrm{y}} S_{\mathrm{y}} \sin\left(\dfrac{2\pi\xi}{L_{\mathrm{x}}}\right) \sin\left(\dfrac{2\pi\eta}{L_{\mathrm{y}}}\right) \end{cases}, \tag{4.4}$$

where the subscripts x and y denote the direction. L is the total length of the domain and S is the scaling factor in the respective direction. The scaling factor S is set as 0.075 for each direction. Both

of these factors satisfy the constraint $0 \le 2\pi S \le 1$ to ensure that the mesh does not tangle. These three types of meshes are shown in Figure 4.1.

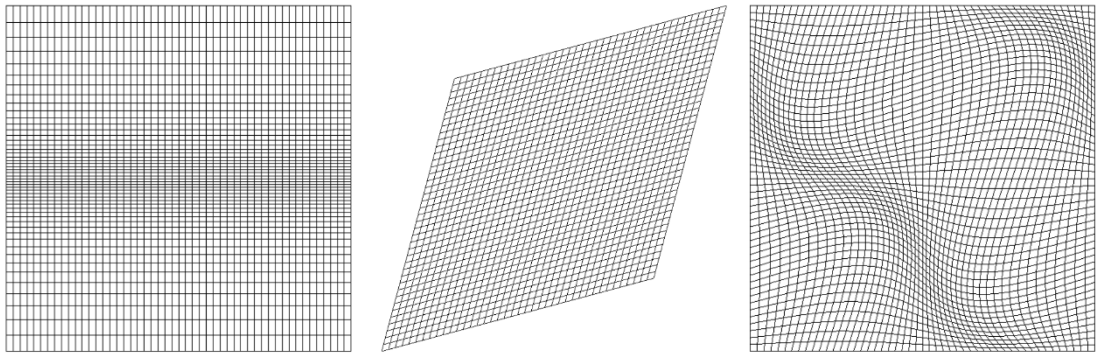

Figure 4.1 Schematic diagram of (a) a stretched mesh, (b) a skewed mesh and (c) a distorted mesh.

4.1.2 2D inviscid MMS

The general form of the solutions is given as

$$\phi(x,y)=\phi_0+\phi_x f_{s,x}(a_{\phi_x}\pi x)+\phi_y f_{s,y}(a_{\phi_y}\pi y)\,. \tag{4.5}$$

ϕ denotes the variables and it could be density, velocity and temperature, etc. ϕ_0, ϕ_x, ϕ_y, a_x and a_y are constants. $f_{s,x}$ and $f_{s,y}$, are trigonometric functions of sines and cosines. The detailed functions and coefficients are given in Table 4.1.

Table 4.1 Constants for 2D Euler supersonic manufactured solutions.

ϕ	ϕ_0	ϕ_x	$f_{s,x}$	a_{ϕ_x}	ϕ_y	$f_{s,y}$	a_{ϕ_y}
ρY-O_2 (kg/m^3)	0.75	0.1	sin	1.0	0.2	cos	0.75
ρY-N_2 (kg/m^3)	1.0	-0.15	cos	0.5	0.1	cos	1.0
u (m/s)	800	60	sin	1.5	30	sin	0.75
v (m/s)	850	40	cos	1.0	50	sin	1.25
T (K)	1000	100	cos	1.0	75	cos	0.5

The solutions are smoothly varying in the physical space. One feature of the MMS is that the analytical solutions exist on arbitrary domains, so all the meshes introduced previously can be tested in this case.

The domain is set as [-150 cm, -30 cm] × [30 cm, 150 cm] in the computational space. Three refinement levels are utilized with refinement factor 2 for each level. The AUSM scheme is used in this part. The CFL number in this case is set to 0.1. The whole domain is initialized with a mixture

of oxygen and nitrogen. A Dirichlet boundary condition is used for the inflow boundary and extrapolation is used for the supersonic outflow boundary.

Figure 4.2 gives examples where the mapped mesh is a-priori refined at a specific region. The dynamic refinement is deactivated in this case to enable the comparison between analytical value and numerical solutions in the same cells. The fixed refinement also tests the operations for information transfer between the fine mesh and coarse mesh.

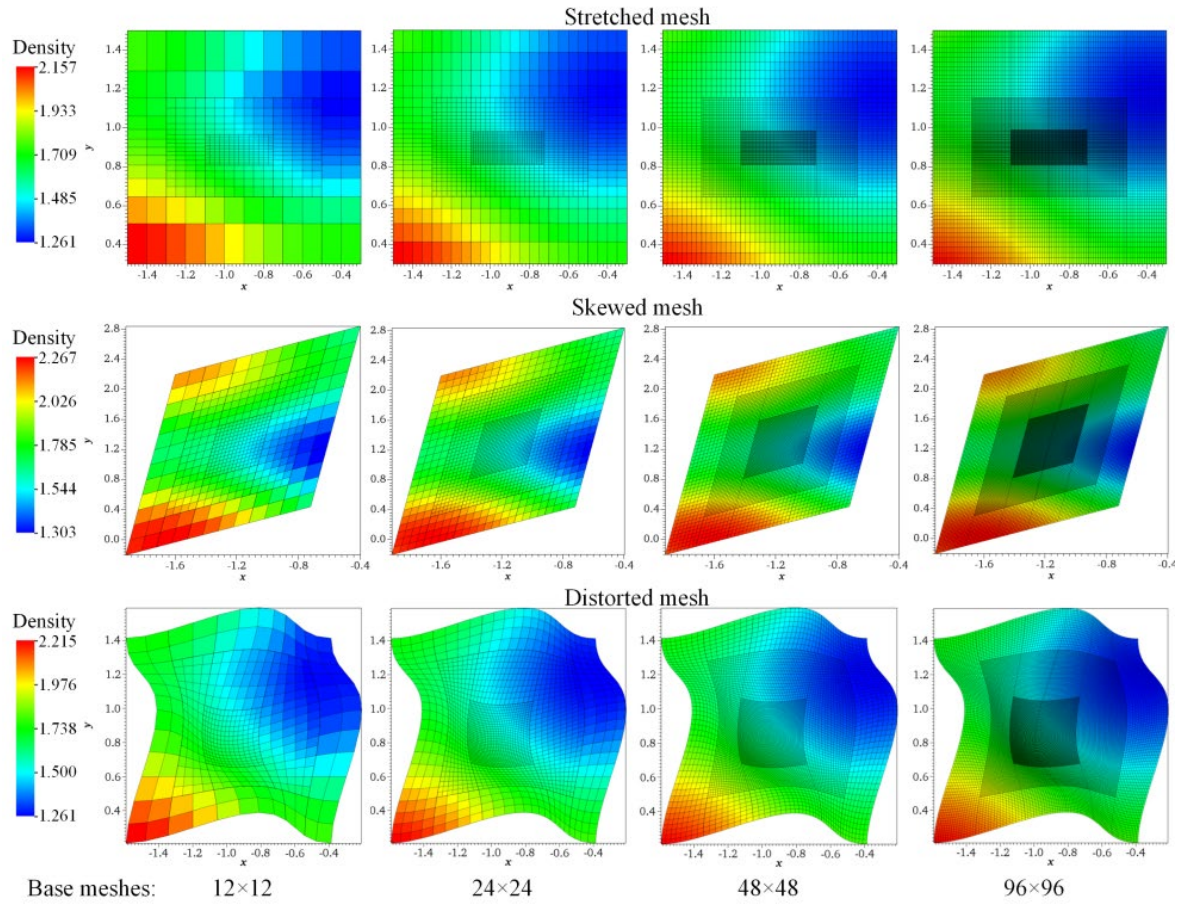

Figure 4.2 Statically refined meshes and corresponding density distribution at t = 0.02 s.

The numerical solutions including density, mass fraction of oxygen, momentum and energy density are compared with analytical manufactured solutions. The errors in terms of the L_2 norm are shown in Figure 4.3. It can be observed that the numerical error decreases with the increasing number of base cells for each of the variables. This confirms that the present solver can achieve second order of accuracy when simulating the smoothly varying flow field on a hierarchically refined mapped mesh.

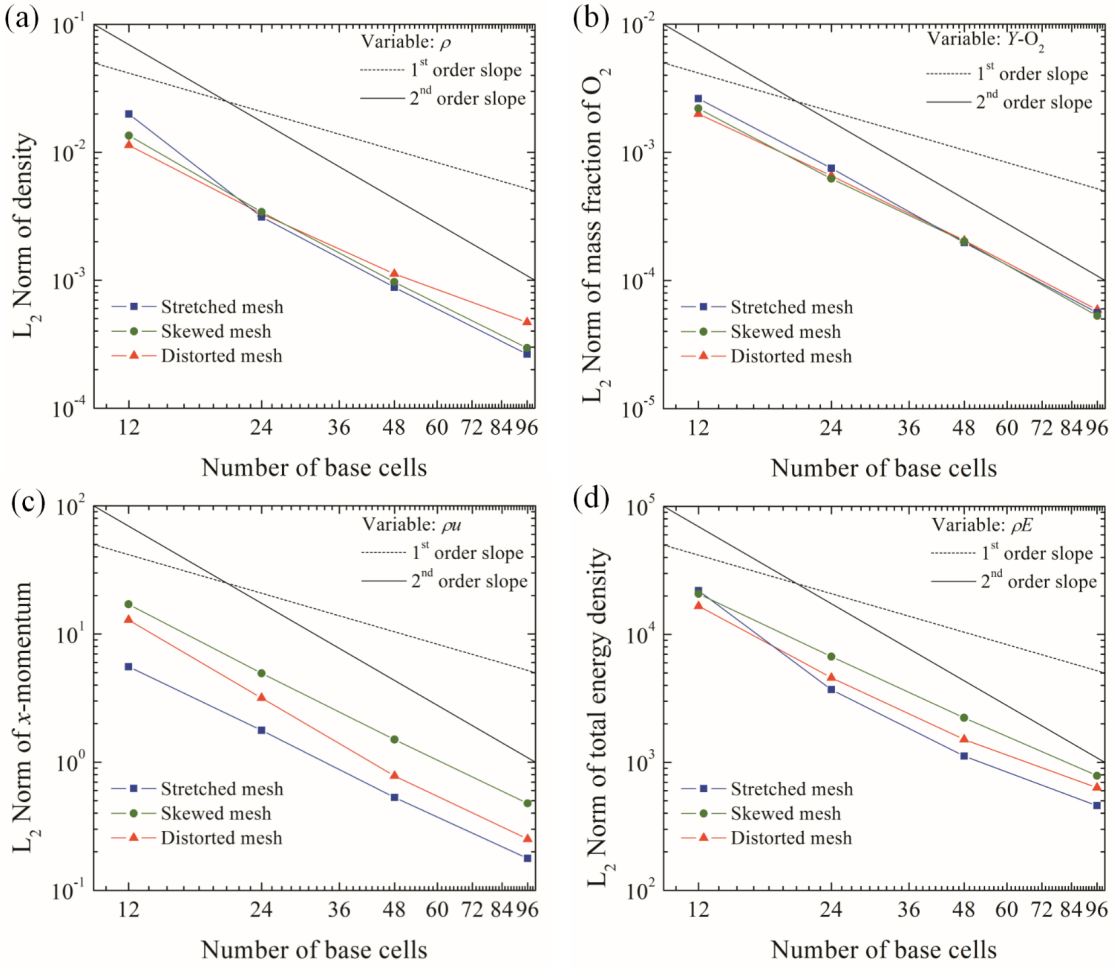

Figure 4.3 L_2 norm of (a) density, (b) mass fraction of oxygen, (c) *x*-momentum, (d) total energy density when using the MMS on different mapped meshes for 2D Euler equations.

4.1.3 2D viscous MMS

For the 2D viscous solver, the viscosity of the mixture, the thermal conductivity of the mixture and the diffusion coefficients for each species are added to the solutions shown in Table 4.1. The additional functions and coefficients are given in Table 4.2. It is noted that the order of magnitude of the viscous terms is artificially raised to increase the influence of diffusions. It is not physically correct, but it is useful to verify the solver in a supersonic case, where the convection is dominant [177]. The Roe-HLL hybrid scheme is employed in this part, and other numerical methods are the same as those used in the inviscid cases.

The three types of meshes shown in Figure 4.2 are also used for the viscous solver. The numerical solutions including density, mass fraction of oxygen, momentum and energy density are compared with analytical manufactured solutions. The errors in terms of the L_2 norm are shown in Figure 4.4. It is observed that the present solver can achieve second order of accuracy when simulating a viscous problem.

Table 4.2 Constants for 2D Navier-Stokes supersonic manufactured solutions.

ϕ	ϕ_0	ϕ_x	$f_{s,x}$	a_{ϕ_x}	ϕ_y	$f_{s,y}$	a_{ϕ_y}
μ (kg/(m·s))	1.0	0.5	sin	0.5	0.3	cos	1.0
k (W/(m·K))	1.0	0.5	cos	1.5	0.3	sin	0.75
D-O_2 (m^2/s)	1.0	0.5	sin	0.5	0.3	cos	1.0
D-N_2 (m^2/s)	1.0	0.5	cos	1.5	0.3	sin	0.75

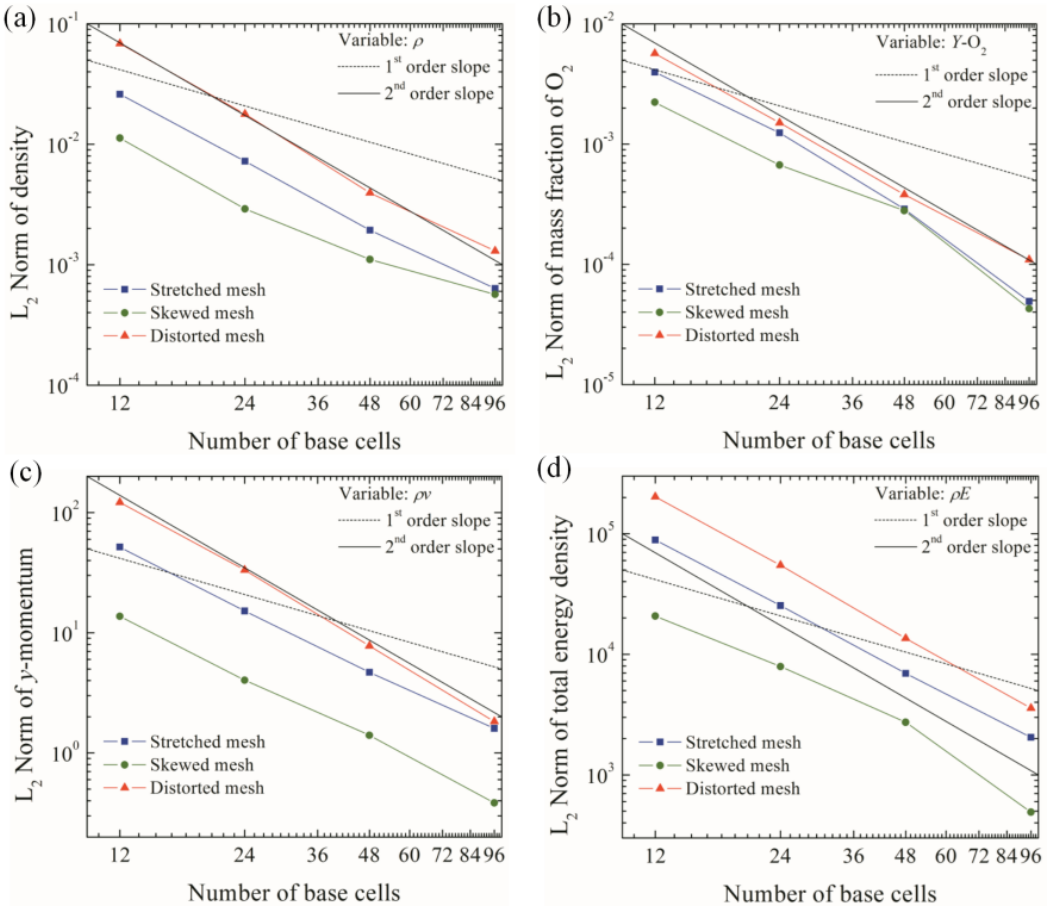

Figure 4.4 L_2 norm of (a) density, (b) mass fraction of oxygen, (c) y-momentum, (d) total energy density when using the MMS on different mapped meshes for 2D Navier-Stokes equations.

4.1.4 3D inviscid MMS

To verify the 3D inviscid solver, the Equation (4.5) turns into a 3D form that reads

$$\phi(x,y,z)=\phi_0+\phi_x f_{s,x}(a_{\phi_x}\pi x)+\phi_y f_{s,y}(a_{\phi_y}\pi y)+\phi_z f_{s,z}(a_{\phi_z}\pi z)\,. \tag{4.6}$$

The parameters for 3D manufactured solution are given in Table 4.3.

Table 4.3 Constants for 3D Euler supersonic manufactured solutions.

ϕ	ϕ_0	ϕ_x	$f_{s,x}$	a_{ϕ_x}	ϕ_y	$f_{s,y}$	a_{ϕ_y}	ϕ_z	$f_{s,z}$	a_{ϕ_z}
ρY-O_2 (kg/m^3)	0.75	0.1	sin	1.0	0.2	cos	0.75	0.1	sin	0.5
ρY-N_2 (kg/m^3)	1.0	-0.15	cos	0.5	0.1	cos	1.0	0.2	cos	0.75
u (m/s)	800	60	sin	1.5	30	sin	0.75	40	sin	0.5
v (m/s)	850	40	cos	1.0	50	sin	1.25	60	sin	0.5
w (m/s)	800	50	cos	1.25	60	sin	0.75	40	sin	1.0
T (K)	1000	100	cos	1.0	75	cos	0.5	50	cos	0.75

The whole domain is initialized with a mixture of oxygen and nitrogen. A Dirichlet boundary condition is used for the inflow boundary and extrapolation is used for the supersonic outflow boundary. The CFL number in this case is set to 0.2. The domain is set as [-150 cm, -30 cm] × [30 cm, 150 cm] × [50 cm, 170 cm] in the computational space. Similarly, the three different types of meshes are used. The meshes used in the following chapters are presented in 0, as shown in Figure 4.5.

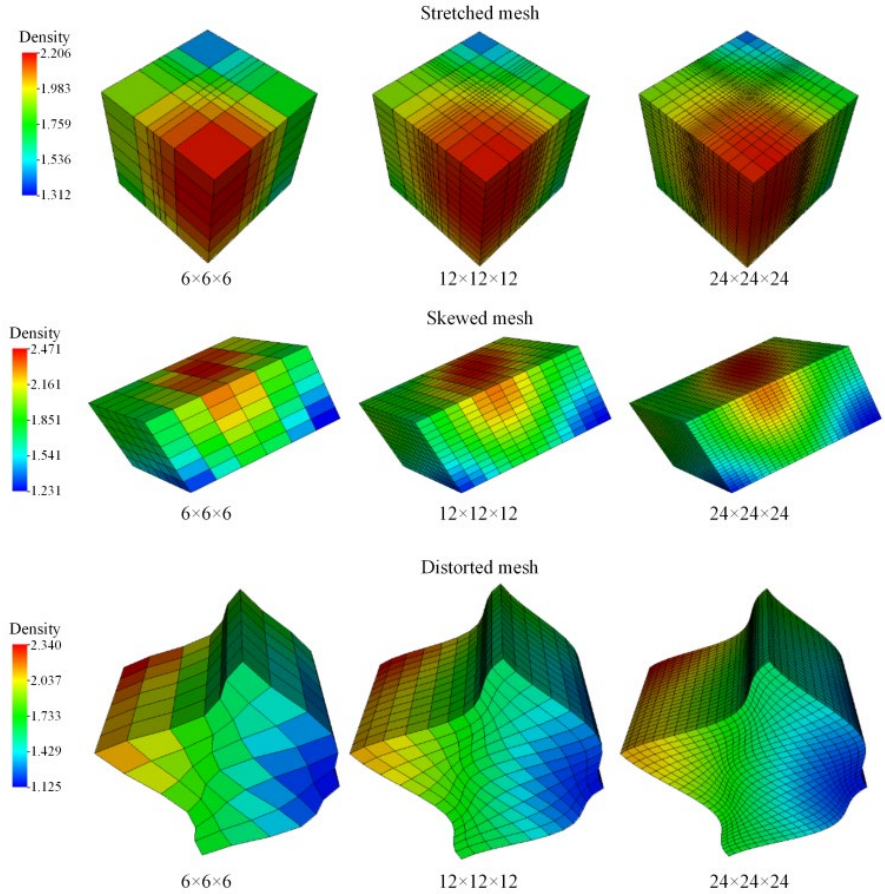

Figure 4.5 The meshes used for 3D inviscid MMS and corresponding density distribution at t = 0.02 s.

The extension of the stretched mesh is given in Equation (A.1) in the three-dimensional form. The skewed mesh is extended to the form in Equation (A.2). Equation (A.3) is adopted to generate the 3D distorted mesh. The density distribution on these three types of meshes at t = 0.02 s is shown in Figure 4.5. The global L_2 norms in terms of density, density of oxygen, momentum, and energy density on different mapped meshes are drawn in Figure 4.6. The order of accuracy is also shown graphically in this figure, confirming that the inviscid 3D solver approaches second-order accuracy when the mesh is refined.

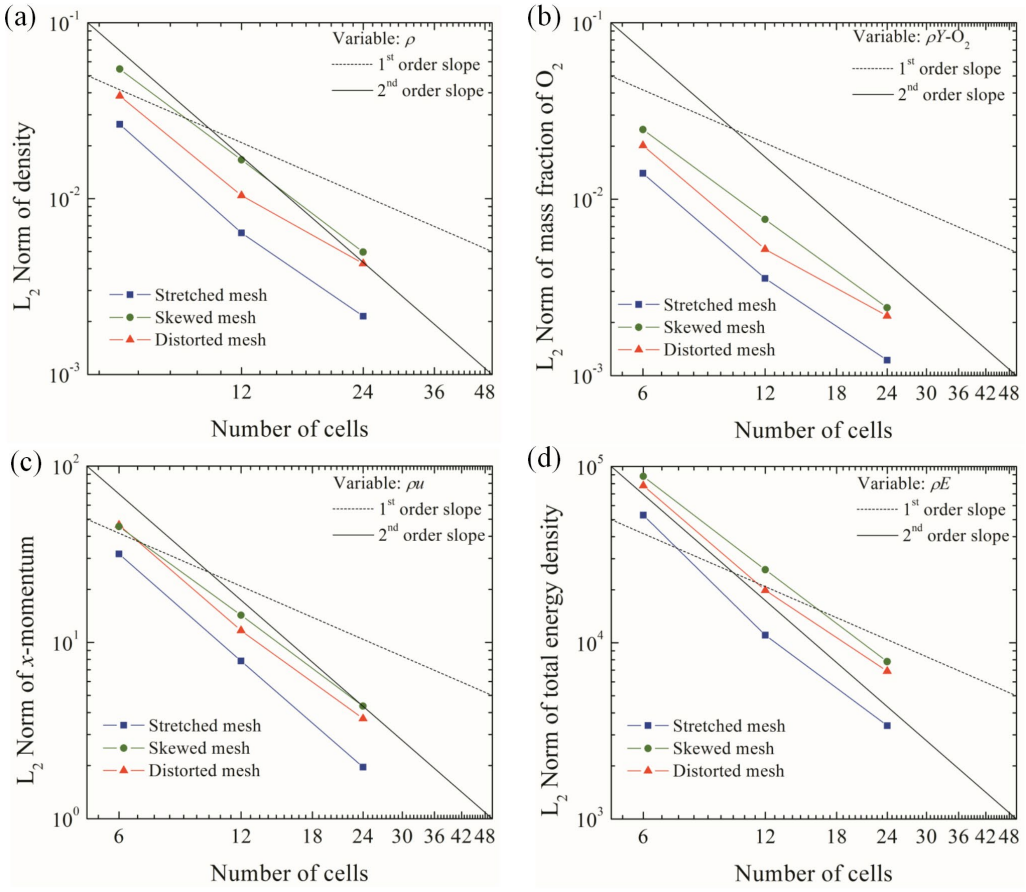

Figure 4.6 L_2 norm of (a) density, (b) density of oxygen, (c) x-momentum, (d) total energy density when using the MMS on different mapped meshes for 3D Euler equations.

4.1.5 3D viscous MMS

The 3D viscous flow is also tested by using the MMS. The HLLC scheme is used, and the CFL number in this case is set to 0.2. The whole domain is initialised with a mixture of oxygen and nitrogen. A Dirichlet boundary condition is used for the inflow boundary, and extrapolation is used for the supersonic outflow boundary. The domain is set as [-150 cm, -30 cm] × [30 cm, 150 cm] × [50 cm, 170 cm] in the computational space. The mapping functions for the stretched mesh, the skewed mesh and the distorted mesh are given in Equation (A.1), Equation (A.4) and Equation (A.3), respectively. A three-level refinement is used with a refinement factor of two for each level as shown in Figure 4.7.

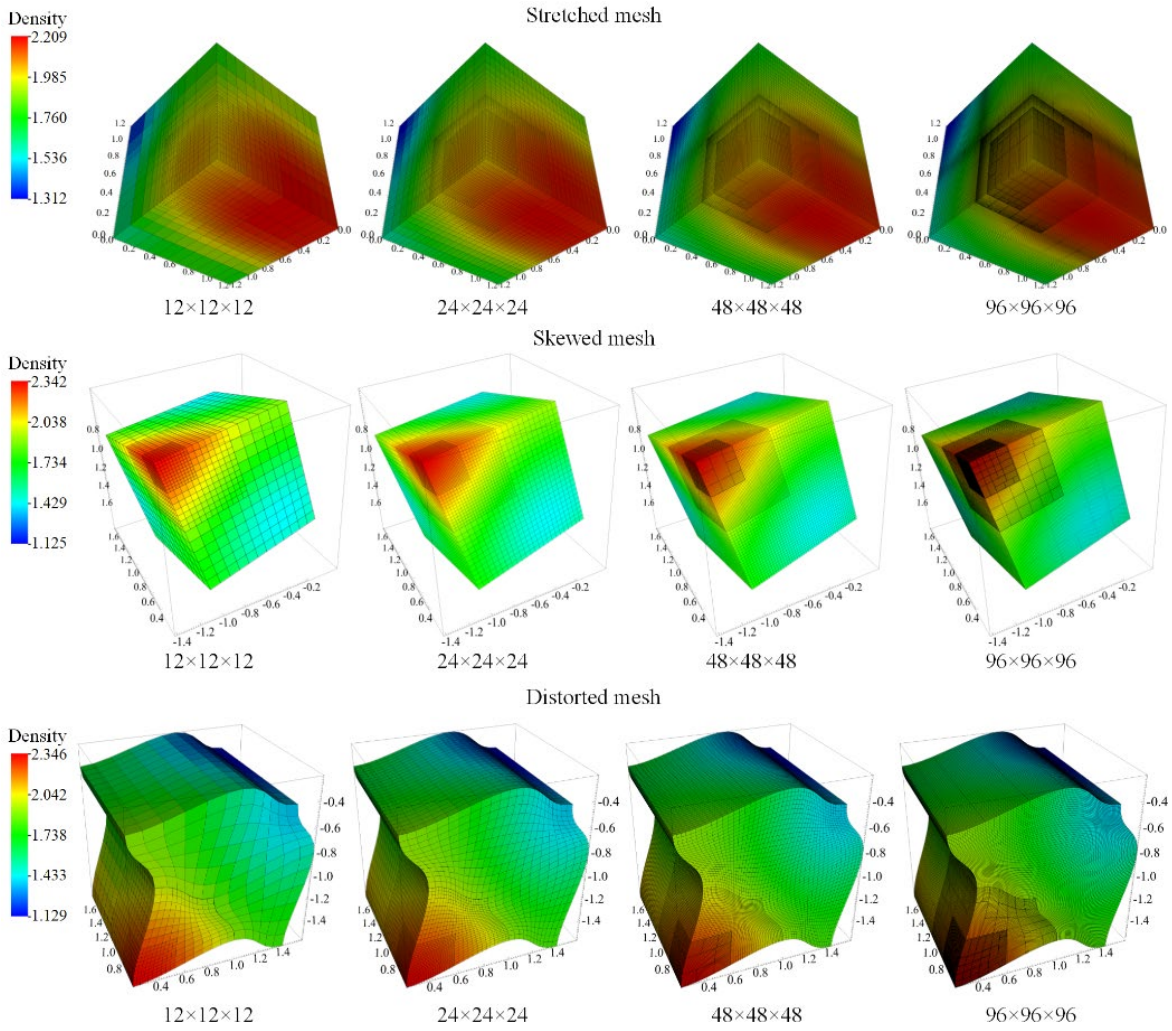

Figure 4.7 The meshes used for 3D viscous MMS and corresponding density distribution at $t = 0.01$ s.

The initial parameters are used the same as in Table 4.3. In addition, the transport data are given in Table 4.4. The diffusive parameters are increased artificially to produce viscous fluxes of comparable magnitude to the inviscid fluxes.

Table 4.4 Constants for 3D Navier-Stokes supersonic manufactured solutions.

ϕ	ϕ_0	ϕ_x	$f_{s,x}$	a_{ϕ_x}	ϕ_y	$f_{s,y}$	a_{ϕ_y}	ϕ_z	$f_{s,z}$	a_{ϕ_z}
μ (kg/(m·s))	1.0	0.5	sin	0.5	0.3	cos	1.0	0.2	sin	0.75
k (W/(m·K))	1.0	0.3	cos	1.0	0.5	sin	1.0	0.4	cos	0.45
D-O_2 (m^2/s)	1.0	0.25	sin	0.5	0.4	cos	0.75	0.3	cos	1.0
D-N_2 (m^2/s)	1.0	-0.25	cos	0.75	0.5	sin	0.5	0.2	sin	0.75

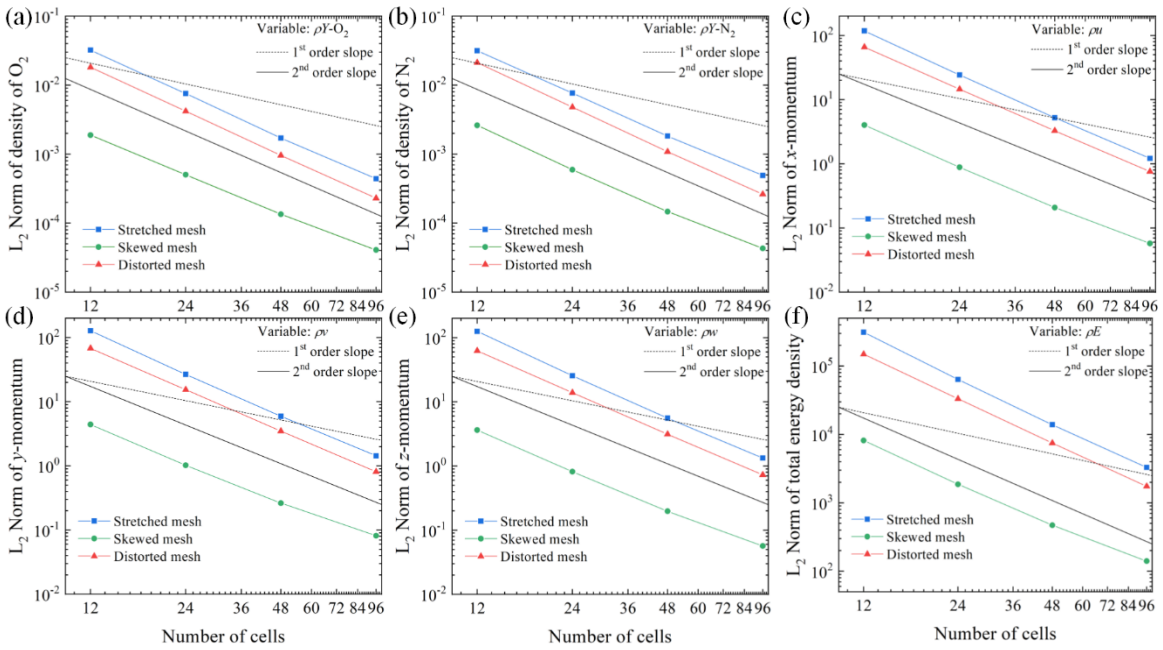

Figure 4.8 L_2 norm of (a) density of oxygen, (b) density of nitrogen, (c) *x*-momentum, (d) *y*-momentum, (e) *z*-momentum, (f) total energy density when using the MMS on different mapped meshes.

Figure 4.8 shows the global L_2 norms in terms of density, momentum, and energy density on various mapped meshes. This figure also depicts the order of accuracy, confirming that the current solver can achieve second-order accuracy when simulating a 3D smoothly varying viscous flow field on a hierarchically refined mapped mesh.

4.1.6 Conservation test

A conservation test is carried out to verify the flux fix-up procedures. A uniform inviscid flow goes through a cube domain with an edge length of 0.2 m. The velocity is 200 m/s in each direction. A distorted mesh is generated through the function given in Equation (A.3). The base mesh of 100 × 100 × 100 cells is centrally distorted with three levels of refinement. Periodic boundary conditions are used for all the boundaries. The target CFL number is 0.8 in this case, and it is run up to 0.1 ms, corresponding to 10 cycles. The total conservative error at time *t* is computed as

$$\mathrm{Err}(t)=\left|\frac{\sum_{i=1}^{N_{\max}}\left[Q_i(0)-Q_i(t)\right]V_i}{\sum_{i=1}^{N_{\max}}Q_i(0)V_i}\right|. \tag{4.7}$$

The volume V_i of the cell i is taken into account when computing the difference between the state $Q_i(t)$ at t and the initial state $Q_i(0)$. $N_{\max}$ is the total number of cells. As shown in Figure 4.9, in the case without a fix-up on fluxes, the errors in terms of conservative variables start at 10^{-8} and reach 10^{-3} at the end of the calculation. An accumulated conservation error is observed when the fix-up is not used. In the case with a fix-up on fluxes, the conservation errors are negligible and are close

to the machine error. This case tests the conservation of the inter-level operations, the flux fix-up method and confirms that the present solver is globally conservative on a multi-level mapped mesh.

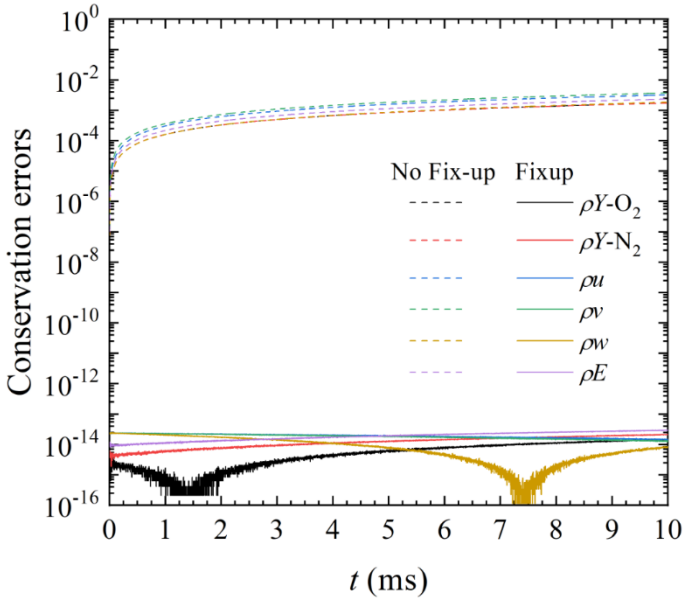

Figure 4.9 Conservation errors in terms of conservative variables versus time.

4.2 Validation

4.2.1 Multispecies shock tube

This benchmark is a modified version of Sod's shock tube considering a multi-species mixture. It has been used to verify the robustness of numerical schemes in previous work [180,181]. In this case, a mixture of hydrogen-oxygen-argon at molar ratios 2:1:7 is initialized in the shock tube. A computational domain of 100 mm in length and of 50 mm in height is simulated with slip wall boundary conditions in all directions. The Cartesian mesh, the stretched mesh in Equation (4.2) and the distorted mesh in Equation (4.4) are used for the 2D simulations. The Cartesian mesh is used as a comparison to exclude the influence of the mapping. For the adaptive cases, the base mesh contains 100 cells in the x-direction. The maximal refinement level is set as three with a uniform refinement factor of 2 on each level. The respective minimum mesh size is 0.25 mm in each direction. Correspondingly, in the cases without adaptive refinement, the same mesh resolution is used. The Roe/HLL scheme is used in this case and the CFL number is set to 0.5.

The initial conditions give a discontinuity of density and pressure in the middle of the tube (x = 50 mm). The initial temperature and pressure are given by

$$\begin{cases} T_{\mathrm{L}}=400\ \mathrm{K}, P_{\mathrm{L}}=8\ \mathrm{kPa}, & \text{if } x \le 50\mathrm{mm} \\ T_{\mathrm{R}}=1200\ \mathrm{K}, P_{\mathrm{R}}=80\ \mathrm{kPa}, & \text{otherwise} \end{cases}. \tag{4.8}$$

Figure 4.10 shows the density, horizontal velocity, temperature, and the ratio of specific heats profiles along the centre line in the tube at 40 μs. The numerical results on different meshes are in good agreement with the results in Ref. [180,181].

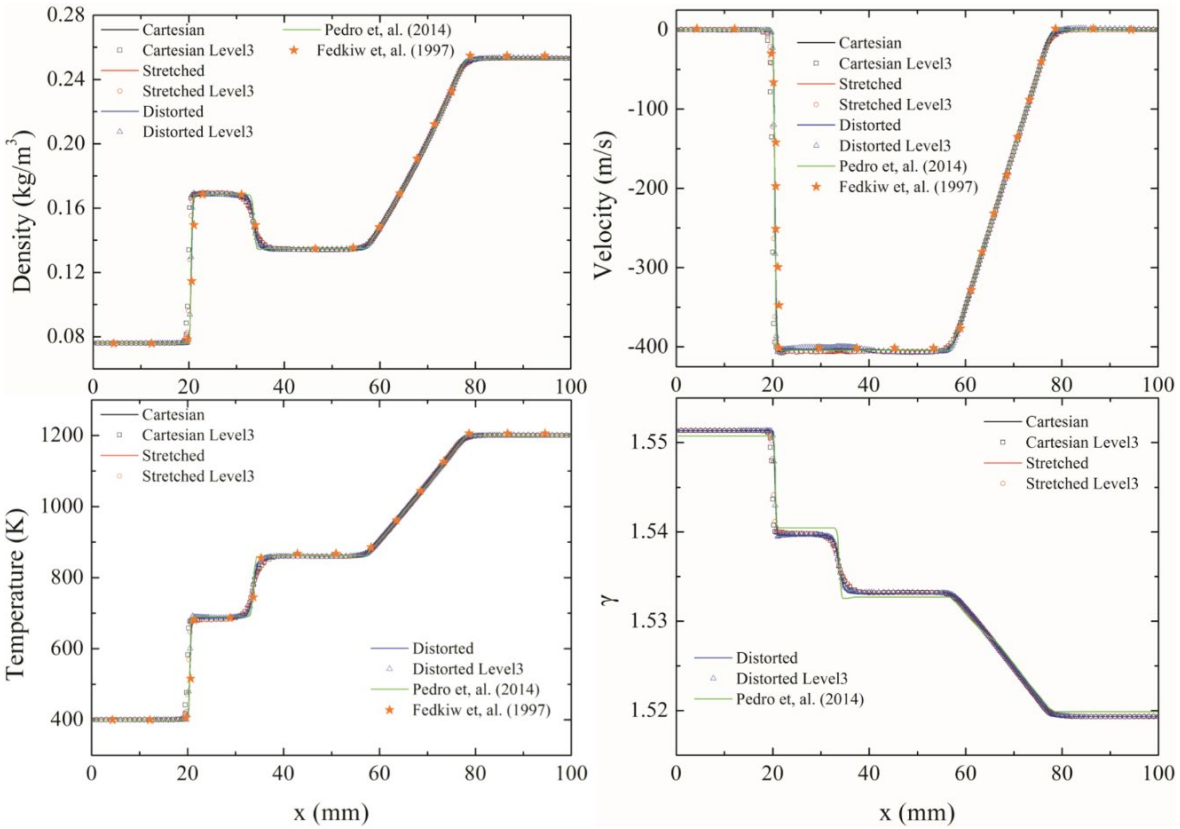

Figure 4.10 Numerical solutions of multispecies shock tube problem.

In addition to the 2D case, a 3D shock tube simulation is also conducted. To decrease the computational costs, the length and time scale in the 3D case are set to a quarter of those in the 2D case. The size of the computation domain is 25 mm × 12.5 mm × 12.5 mm. The base mesh size is set as the same as that in the 2D case. A distorted mesh in Equation (A.3) is used with three refinement levels and the refinement factor is 2 for each level. The refinement indicator threshold values for density and pressure are ε_ρ=0.002 kg/m^3 and ε_p=4 kPa. The adaptive computation uses approximately 2.6 M to 5.8 M cells in total instead of 16 M cells in the uniform case. Figure 4.11 displays that the shock wave, the contact discontinuity and the rarefaction wave are all captured by the refined meshes. The data on the line plotted with red dots in this figure is extracted.

Figure 4.12 shows the comparison of the density, horizontal velocity, temperature, and the ratio of specific heats profiles on the extracted line. The numerical results on the 3D distorted mesh are in good agreement with the results in 2D simulation and Ref. [180,181]. In addition to the Roe/HLL scheme, the HLLC scheme is also tested as shown in Figure 4.13. The result shows that the difference is not noticeable between these two schemes. More cells are flagged to be refined on level 2 in the rarefaction wave when the HLLC scheme is adopted. The locations of the shock wave, the contact

discontinuity and the rarefaction wave are correctly captured by the present 3D solver using the finest meshes.

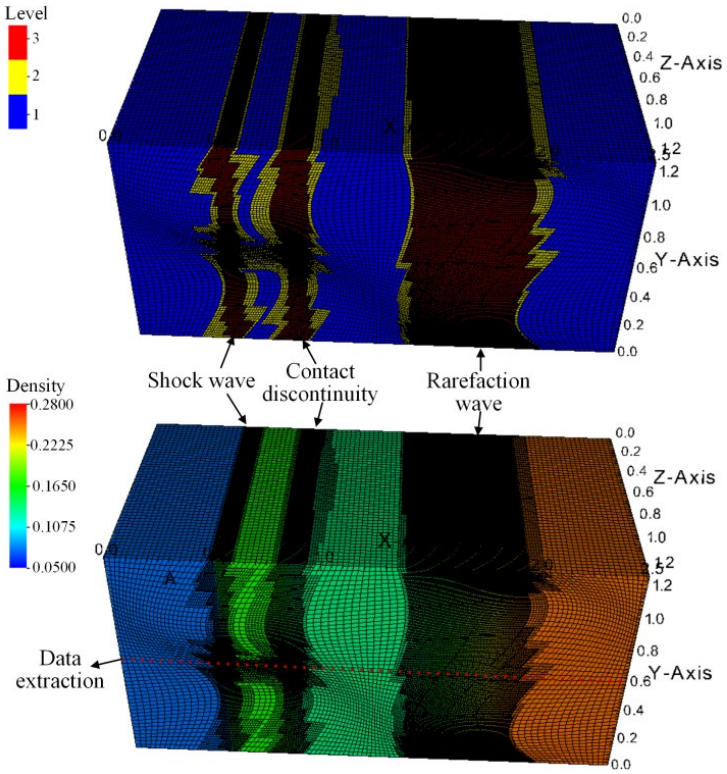

Figure 4.11 Pseudo-colour image of the refinement levels and the density distribution.

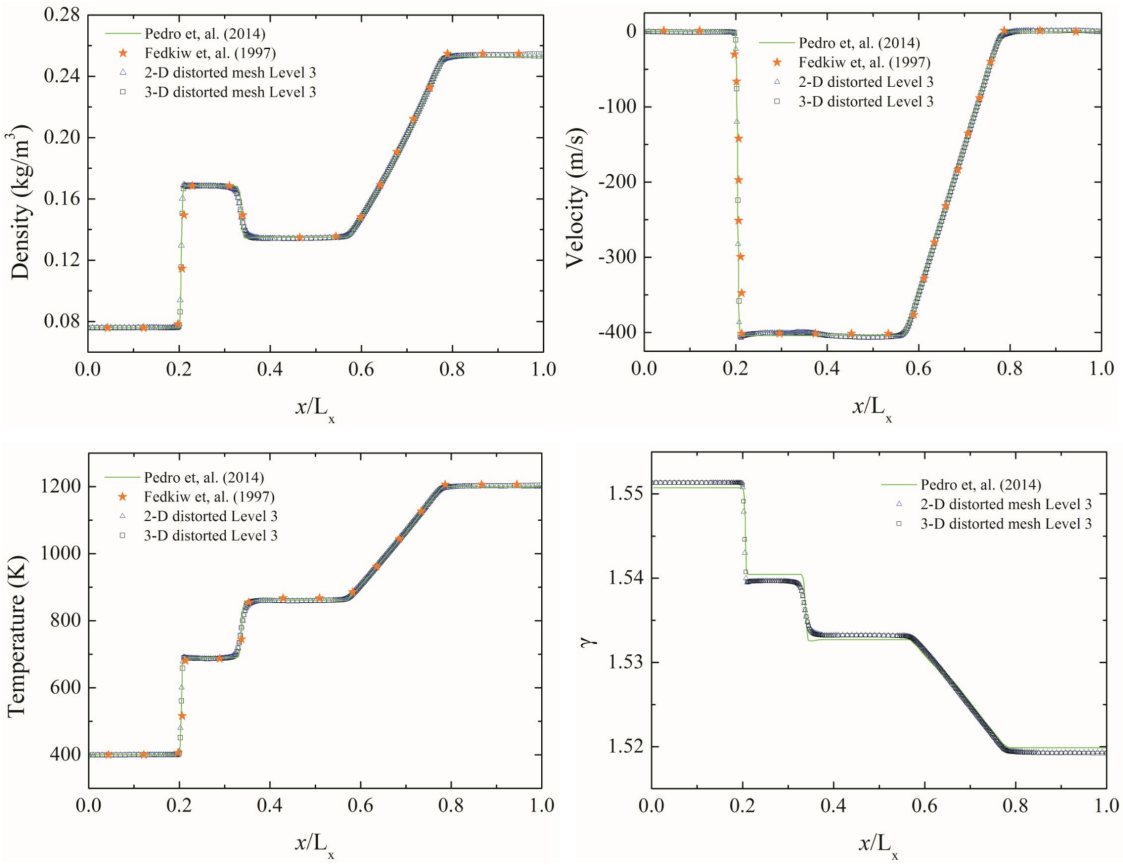

Figure 4.12 Comparison of numerical solutions of multispecies shock tube problem.

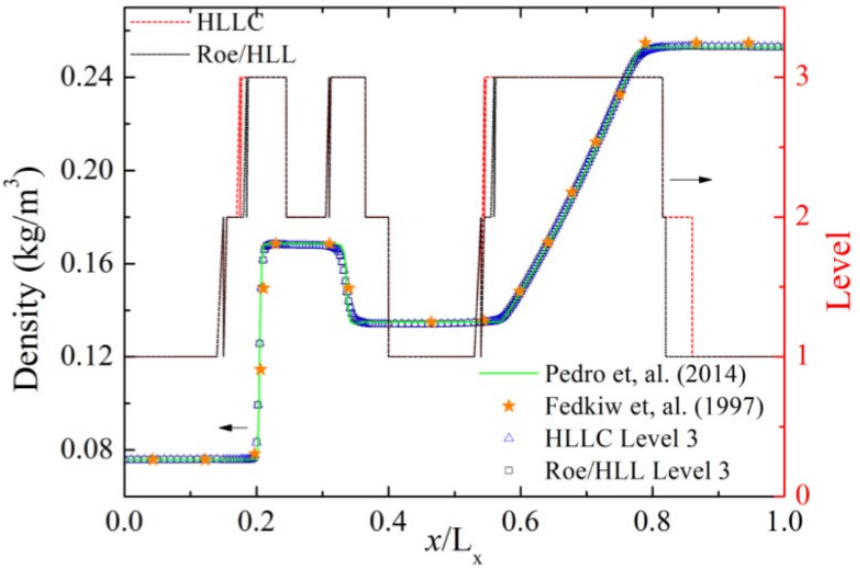

Figure 4.13 Density and refinement level profiles on the extracted line.

4.2.2 Multispecies shock box

This benchmark is a modified two-dimensional Riemann problem in a shock box, which involves the interaction of multispecies shocks with slip walls [182]. The size of the shock box is 1000 mm × 1000 mm. The distorted mesh in Equation (4.4) is tested in this case. The number of cells in the base mesh is 128 in each direction and three refinement levels are used with a uniform refinement factor of 2. The refinement indicator threshold ε_ρ is 0.05 kg/m^3 and ε_p is 16 kPa. The CFL number in this case is set to 0.8. The whole domain is initialized with a mixture of oxygen and nitrogen at molar ratios of 1:3.76. The initial condition is

$$\begin{cases} \rho_L = 1.225 \text{ kg/m}^3, P_L = 101.325 \text{ kPa}, & \text{if } x \le 250\text{mm and } y \le 250mm \\ \rho_R = 4.9 \text{ kg/m}^3, P_R = 405.300 \text{ kPa}, & \text{otherwise} \end{cases}. \tag{4.9}$$

This condition gives two shock waves in each direction at the beginning, and then the shock waves propagate towards the slip walls. Figure 4.14 displays the results at 2 ms in computational space and physical space, respectively. This figure is overlapped by the base meshes with every 8th cell point for a better display and comparison.

The convergent shocks are reflected by the lower-left corner. The pressure and Mach number distributions are in good agreement with the results in Ref. [182]. The reflected shock wave is captured by the finest mesh as shown in Figure 4.15. The locally enlarged image shows how the distorted mesh is refined in this case.

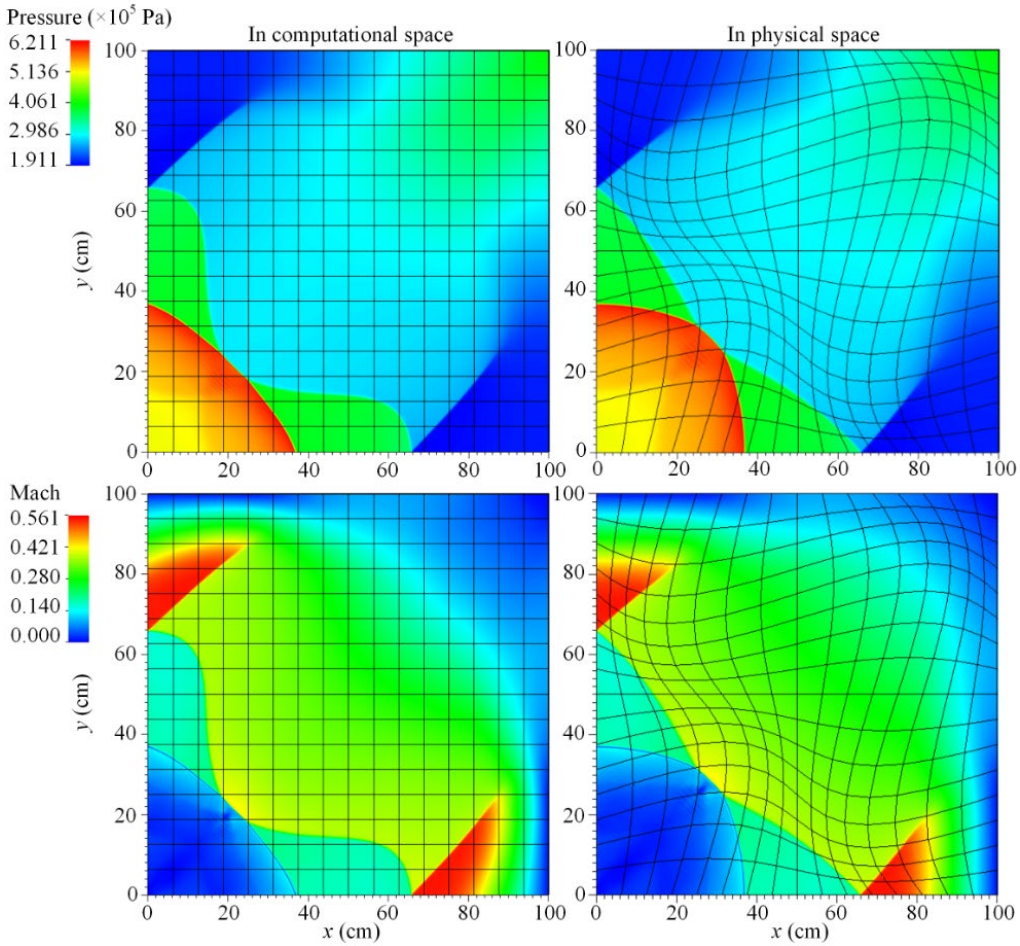

Figure 4.14 Numerical solutions of multispecies shock box problem.

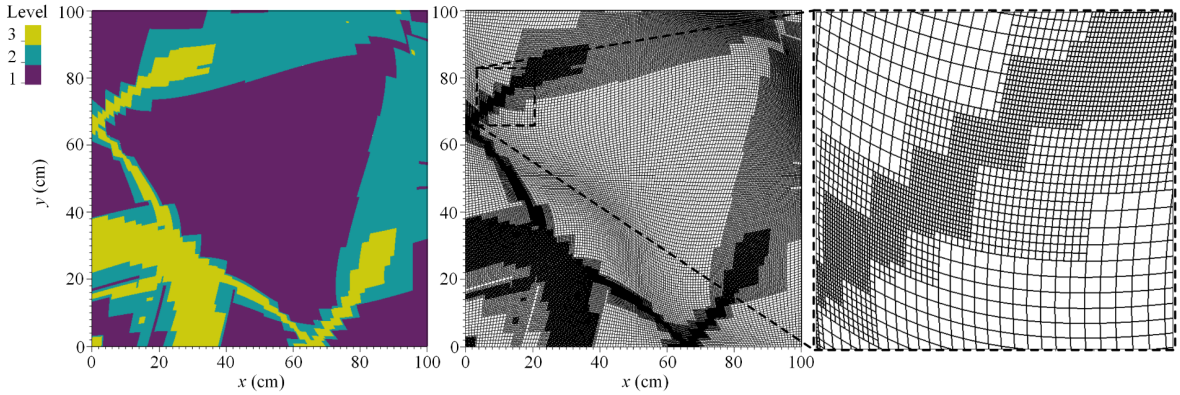

Figure 4.15 Pseudo-colour image of the refinement levels and the image of the distorted refined mesh.

Figure 4.16 shows the results computed through different Riemann solvers. The implemented AUSM, Roe/HLL and HLLC schemes can simulate the correct location of the reflected shock waves and expansion waves in the shock box problem. A numerical oscillation is observed behind the leading curved shock when the AUSM scheme is used, whereas this oscillation is eliminated by using the Roe/HLL or HLLC scheme.

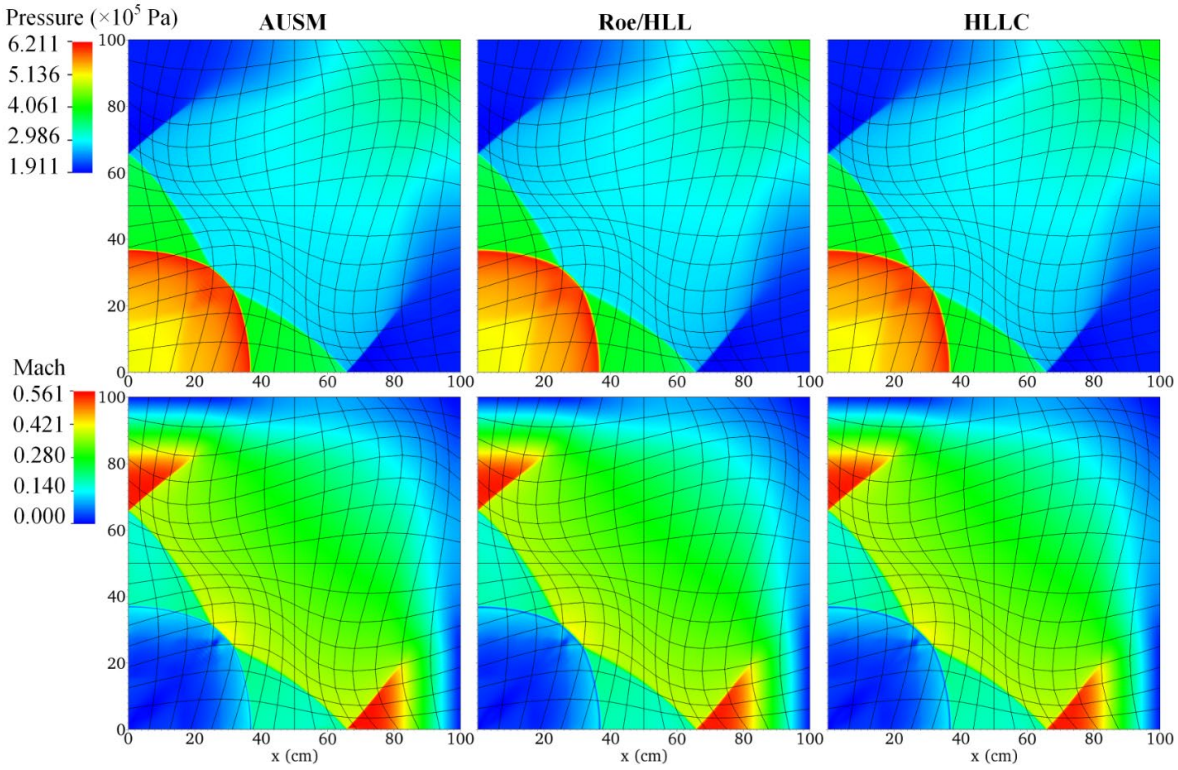

Figure 4.16 Numerical solutions of multispecies shock box problem with different schemes.

4.2.3 Lid-driven cavity

The simulation of flow in a lid-driven cavity is a classical benchmark for viscous solvers [183]. The complex structure in the lid-driven cavity consists of multiple rotating recirculating regions on the corners of the cavity. Although it is an essentially incompressible problem, it has been also used to validate the compressible viscous solver. To eliminate the influences of the compressibility, the Mach number of the driven flow is set as 0.08 for all the cases in this section.

The height of the square box is 1000 mm. The domain is filled with air at 100 kPa and 348 K. The Reynolds number based on lid velocity is set to 1000 in this case. A stretched mesh is utilised as presented in Equation (A.5), and the number of base cells is 256 in each direction. This case is simulated both on a uniformly stretched mesh and on a stretched mesh with three refinement levels (refinement factor of 2) fixed on the corners. The top wall moves with a velocity calculated from the Mach number. All the other walls are no-slip walls. The target CFL number in this case is set to 0.9. The viscosity is computed by the given Reynolds number and the box length. The specific heat ratio is set as a constant of 1.4 and the Prandtl number is 0.75.

Figure 4.17 displays the streamlines of the flow field in the cavity. It shows that the viscous solver can reproduce correct flow features in the whole domain. The primary vortex and the vortexes on the corner are all captured. Besides, the horizontal velocity and the vertical velocity along the centre lines are compared with the results by Ghia et al. [183]. The results are in good agreement with their results as shown in Figure 4.18.

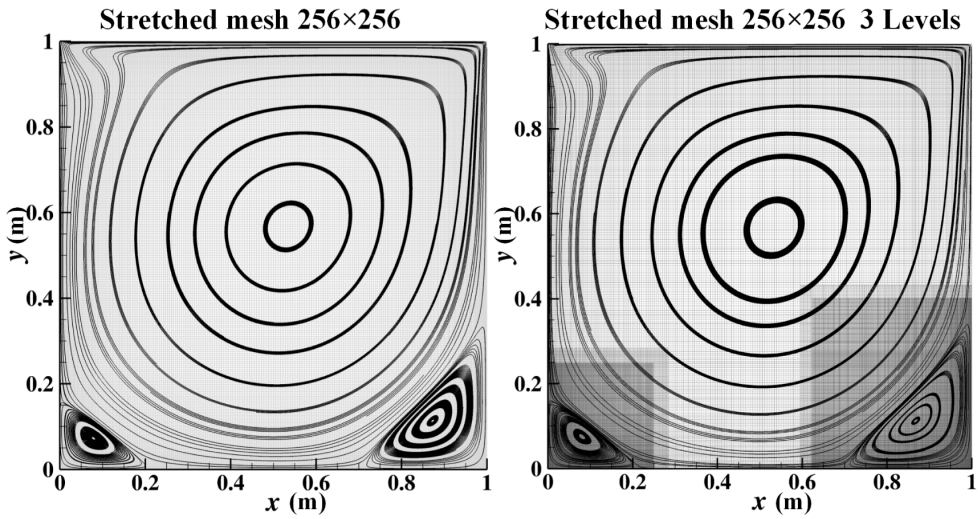

Figure 4.17 Flow field shown by streamlines on a stretched mesh (left) and on an adaptive refined stretched mesh (right).

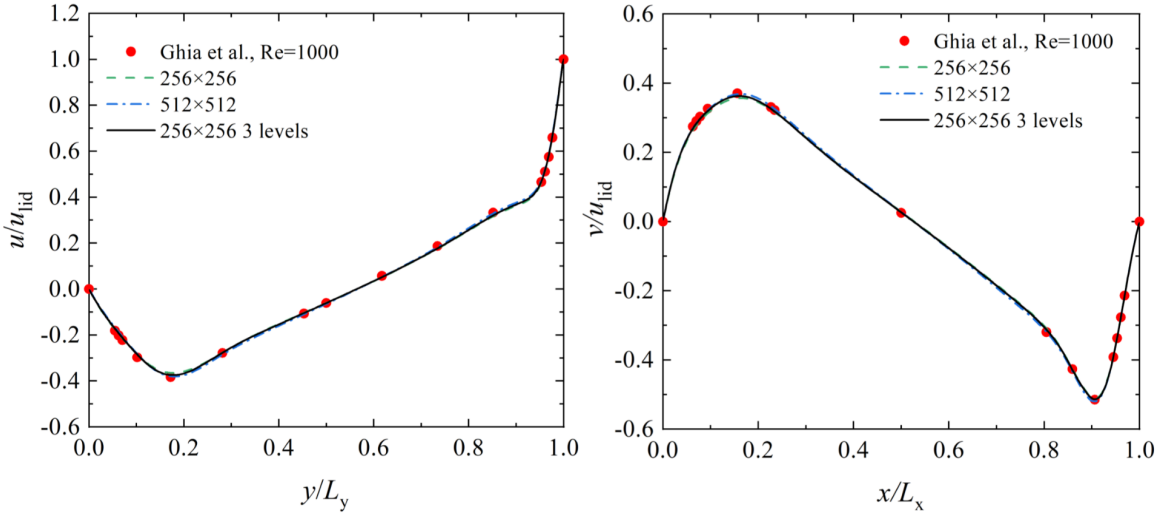

Figure 4.18 Velocity profiles: Normalised u-velocity along the vertical centreline (left) and normalised v-velocity along the horizontal centreline (right).

4.2.4 Laminar boundary layer flow over a flat plate

The accuracy of the current viscous solver is tested using a simulation of the laminar flow across a flat plate at zero incidence. The domain has a geometry of 20 cm ×3 cm ×2 cm, with a 50 ×40 ×5 cell base mesh. The boundary layer is effectively resolved using a stretched mesh with a three-level refinement as shown in Figure 4.19. The mapping for the stretched mesh is given in Equation (A.6). In this case, the freestream Mach number is set as 0.2 and the Reynolds number is 10000 based on the plate length. As depicted in Figure 4.19, a 5 cm slip wall is included prior to the start of the non-slip wall boundary condition on the bottom. The subsonic inlet boundary condition is used for the left boundary. The subsonic outlet boundary condition is used for the top and right boundary. A slip wall boundary condition is applied to the sides. The Roe/HLL scheme is used and the CFL number is set to 0.5.

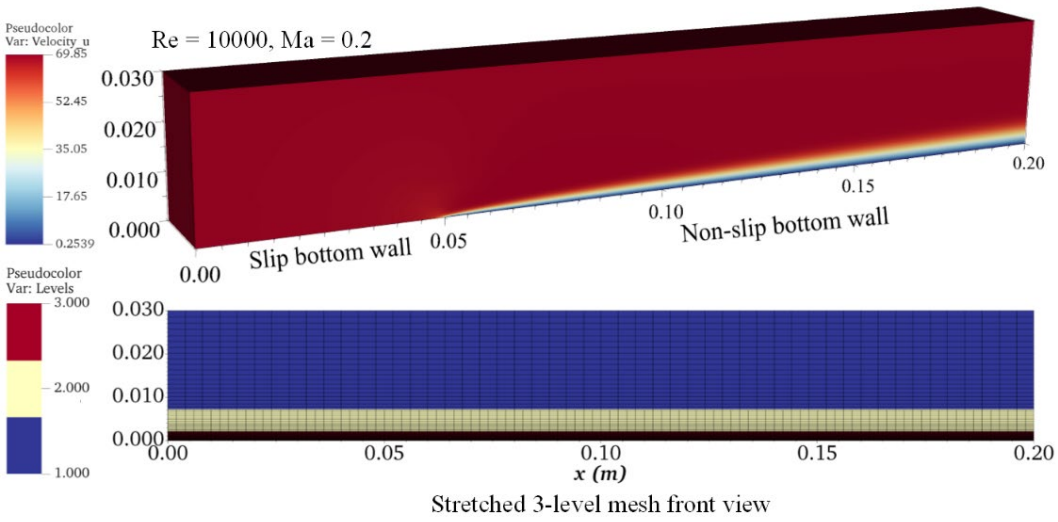

Figure 4.19 Mesh and velocity fields of the laminar flat plate boundary layer case.

The first 10 cells off the bottom boundary are refined to level 3, and the 11th to 20th cells in the 40 cells are refined to level 2. The height of the first cell off the bottom wall is 3.43641×10^{-5} m. The non-dimensional horizontal velocity and the skin friction coefficient are compared with the Blasius solution. Figure 4.20 shows that the 3D numerical results are in good agreement with the Blasius solution.

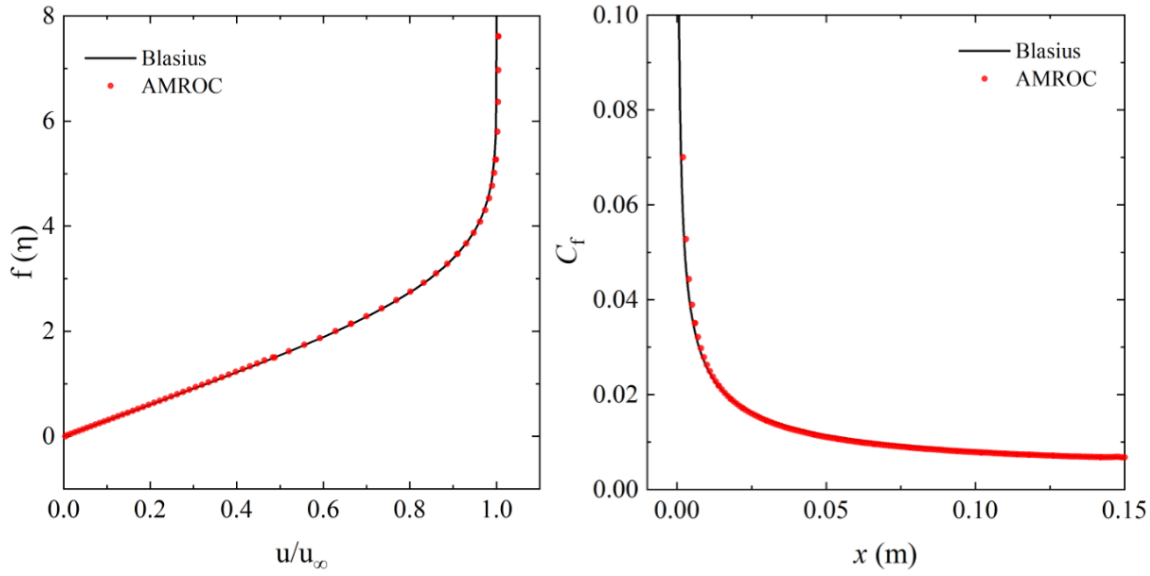

Figure 4.20 Laminar flat plate boundary layer: non-dimensional velocity components at Re = 8000 (left) and estimation of the skin friction coefficient (right).

4.2.5 Non-premixed planar co-flow flame

The 2D non-premixed co-flow flame is tested to validate the accuracy of the diffusion in reacting flows. Although the solver is developed for compressible high-speed reacting flows, it is expected to perform well enough in the low-speed flame regime. The computational configurations are referred

to Ref. [184] as shown in Figure 4.21. The computational domain is extended in the horizontal direction to exclude the potential influences from the boundaries. The whole bottom boundary is set to inlet and equally distributed with fuel and co-flow on each side. The fuel consists of 50% CH_4 and 50% H_2 at 305 K (volume percentage), and the co-flow consists of 3% O_2, 85% N_2, 6.5% CO_2, and 5.5% H_2O at 1300 K (mass percentage). The initial static pressure for the inlet is set to 100 kPa and the inlet velocity is 1 m/s. The subsonic outlet boundary condition is set for the top and sides. The ambient pressure is given as 100 kPa.

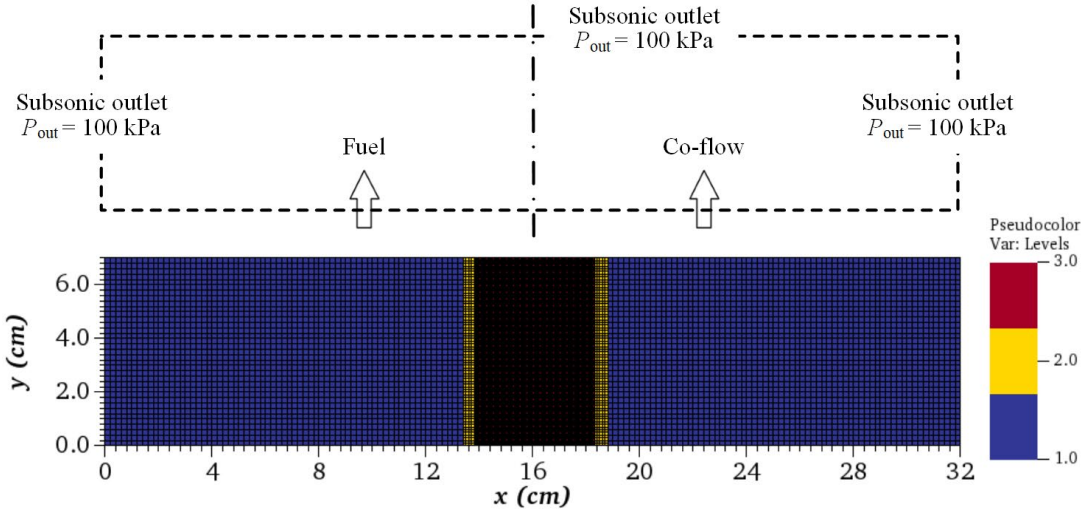

Figure 4.21 Computational domain and mesh for the co-flow flame simulation.

The domain length is 320 mm with a total height of 70 mm. The base Cartesian mesh is set to 160 × 35 cells with three refinement levels fixed in the centre, and the refinement factor is 2 for each level. The Cartesian mesh is employed to exclude the influence of the mapping. As shown in Figure 4.21, the region between 140 mm and 180 mm is always flagged to be refined to the highest level. The target CFL number in this case is set to 0.9. The detailed GRI 3.0 mechanism is used [185] for combustion, which consists of 53 species and 325 reactions.

As the explicit method is used in the present solver, the computation of the low-speed flame requires millions of time steps to achieve a steady state. To reduce the computational cost, the chemical reaction is first deactivated to get a steady cold flow field as shown in Figure 4.22. The non-premixed gases flowing through the entire domain take 0.07 s. After t = 0.28 s, the flow structure remains unchanged and the flow field is regarded as having reached a steady state at this time as shown in Figure 4.23. The diffusion on the interface yields a smooth variation of the temperature and species. The data are extracted from the horizontal line at y=30 mm downstream of the inlet. The fuel and co-flow result in a non-uniform equivalence ratio across the domain. The flow field changes from a fuel-rich to a fuel-lean state in the centre.

Another simulation is conducted based on the cold flow field at t = 0.28 s, in which the chemical reactions are activated. As shown in Figure 4.24, the time-averaged OH distribution is qualitatively compared with the numerical results in [184]. The non-premixed flame is observed but with a

difference in the shape of the flame. In the present simulation, the flame is closer to the hot co-flow side and a curved surface is observed near the inlet plane. A possible explanation is that the fluctuating velocity field has an influence on the properties transport.

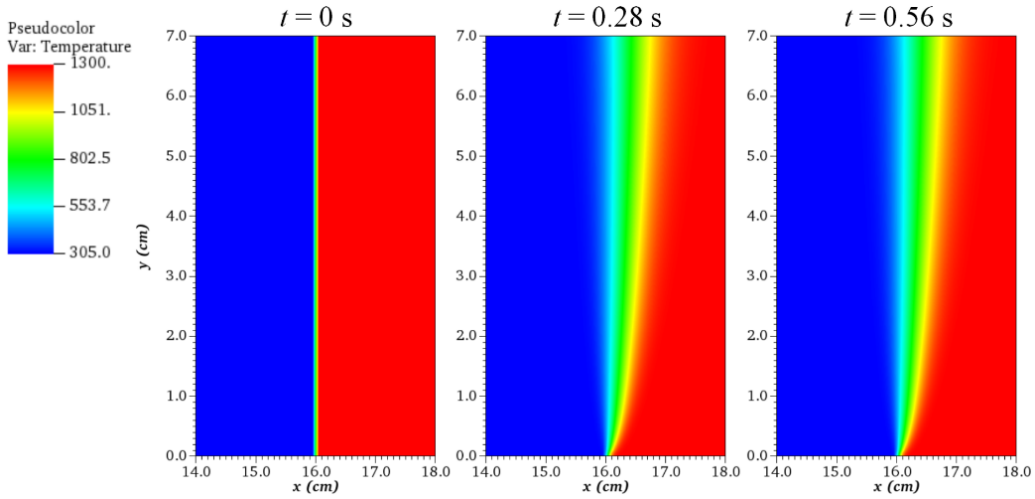

Figure 4.22 Pseudo-colour image of the temperature at different times.

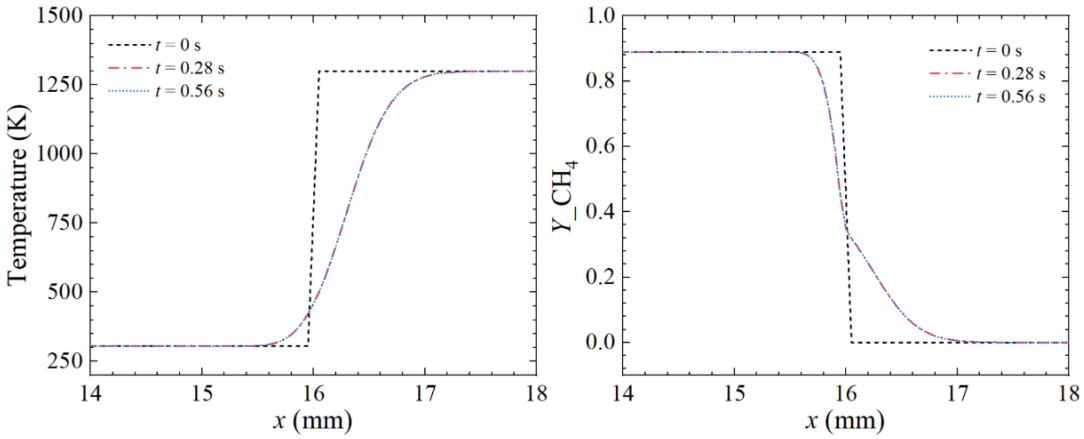

Figure 4.23 Profiles of temperature and CH_4 mass fraction at y=30 mm.

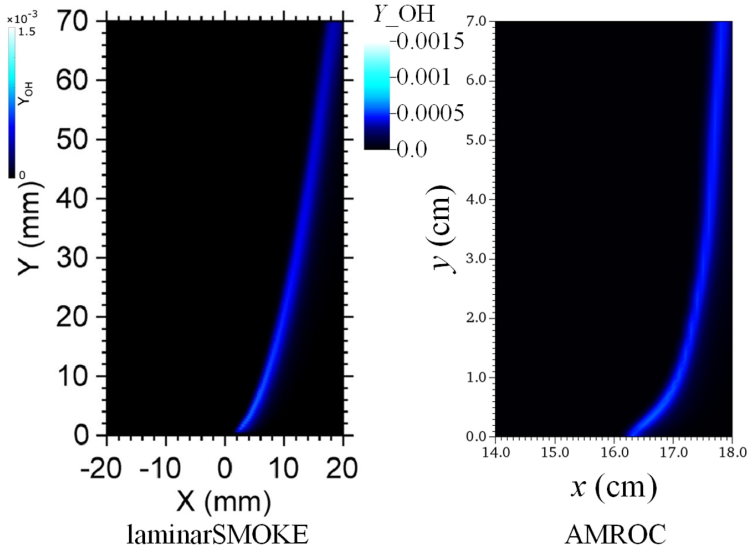

Figure 4.24 Distributions of OH mass fraction in the 2D methane co-flow flame, results from [184] (left) and present results (right).

As introduced in Section 3.5, using the conservative scheme to solve contact discontinuities may lead to pressure and velocity oscillation when the local gradient of specific heat ratio is large. In this case, the small oscillation plays an obvious role on the low-speed flow field. Figure 4.25 shows the pressure and velocity profiles at 30 mm downstream of the inlet. Despite that the fluctuation of pressure remains below 0.01%, the small fluctuating horizontal velocity leads to the difference in the species distribution. As a result, the shape of the present flame differs from the numerical results in [184].

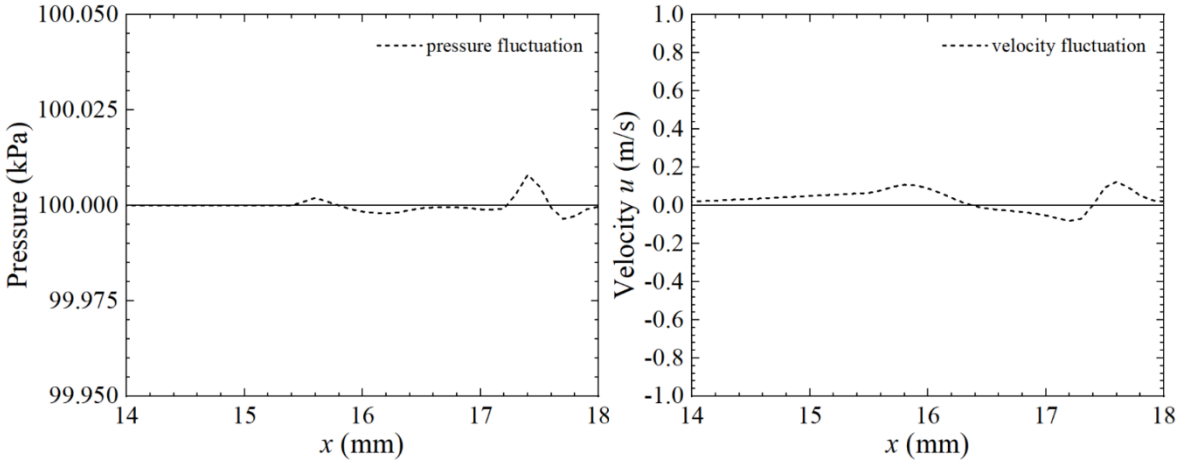

Figure 4.25 Profiles of pressure and velocity at y=30 mm.

It is noted that employing the explicit method to address low-speed flame problems is notably inefficient compared to the implicit method. As the explicit time integration in AMROC is developed for high-speed compressible flows, the time step is limited by the CFL number and the speed of sound in the Riemann problem. The explicit method takes millions of small time steps before reaching the steady state. In contrast, the stable CFL number can often be far greater than one in the implicit approach and the computations can rapidly converge to a steady state. However, this case shows a comparative result using the present solver in non-premixed reacting flows simulations. It also validates the solver's capabilities in solving detailed chemical mechanisms.

4.2.6 Shock bubble combustion

The shock-driven combustion problem [186] of a 2D hydrogen bubble is tested to validate the viscous solver with chemical source terms. This validation case demonstrates the evolution of a hydrogen bubble and its interaction with a shock wave at Mach 2. The numerical configuration is shown in Figure 4.26. A hydrogen sphere is initialised in the region on the left-hand side of the domain consisting of air. The temperature, pressure and velocity in different regions are also shown in the figure.

The distorted mesh in Equation (4.4) is used in this case. The base mesh is set to 1024 × 512 cells with three refinement levels, and the refinement factor is 2 for each level. The refinement indicator

thresholds are given in terms of the temperature, density and pressure as $\varepsilon_T = 500$ K, $\varepsilon_\rho = 0.05$ kg/m^3 and $\varepsilon_p = 16$ kPa. The Jachimowski hydrogen/air mechanism [187] is used, which consists of 9 species and 19 reactions. The target CFL number in this case is set to 0.9.

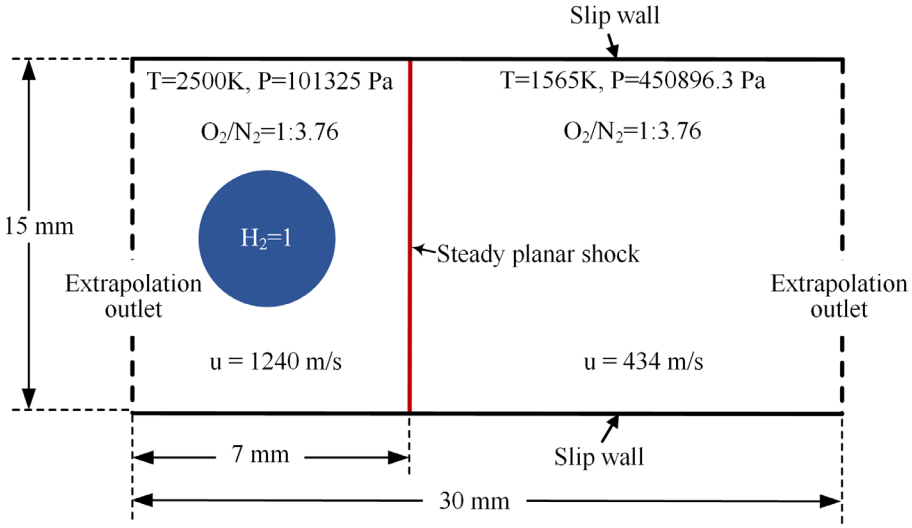

Figure 4.26 Computational domain and numerical configurations of the shock bubble combustion problem.

Figure 4.27 is the pseudo-colour image of the hydrogen mass fractions distribution (grey scale) superimposed on the pressure contours with black lines. At t = 1.5 μs, the hydrogen bubble collides with the stationary shock wave. The refracted, transmitted, reflected and incident pressure waves are all captured by the finest cells as shown in the figure. At t = 3.5μs, two reflected waves form on both sides of the bubble, and a secondary transmitted wave can be observed upstream of the bubble. Besides, a vortex is generated inside the hydrogen bubble. These features are in good agreement with the results in previous studies [186,188,189].

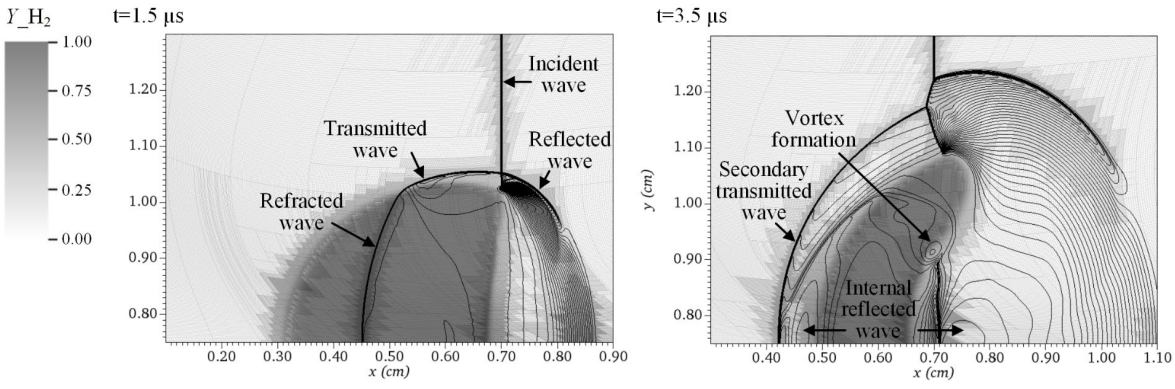

Figure 4.27 Pseudo-colour image of the hydrogen mass fraction (grayscale) superposed on line contours of pressure (1–7.4 bar) at 1.5 μs and 3.5 μs.

Figure 4.28 shows a comparison of the pressure profile on the vertical central line between the present result and published numerical results. The present solver's numerical result, plotted with a purple dot line and an orange solid line respectively, agrees well with Ref [189] when using a similar

distorted mesh at the same mesh resolution. There are some differences between the results obtained by AMROC and literature solutions predicted by Billet et al. [186] and Attal et al. [188] in terms of the strength and locations of the waves. In the solution predicted by Attal et al., the position of the secondary transmitted wave differs from the results in the other three cases. In the work conducted by Billet et al., a higher pressure is predicted from x=0.55 cm to x=0.66 cm. In the present simulation, the strength of the right reflected wave is observed to decrease with a coarser mesh and is close to their predictions. However, the location of the location of the secondary transmitted wave and left reflected wave still differs from their results.

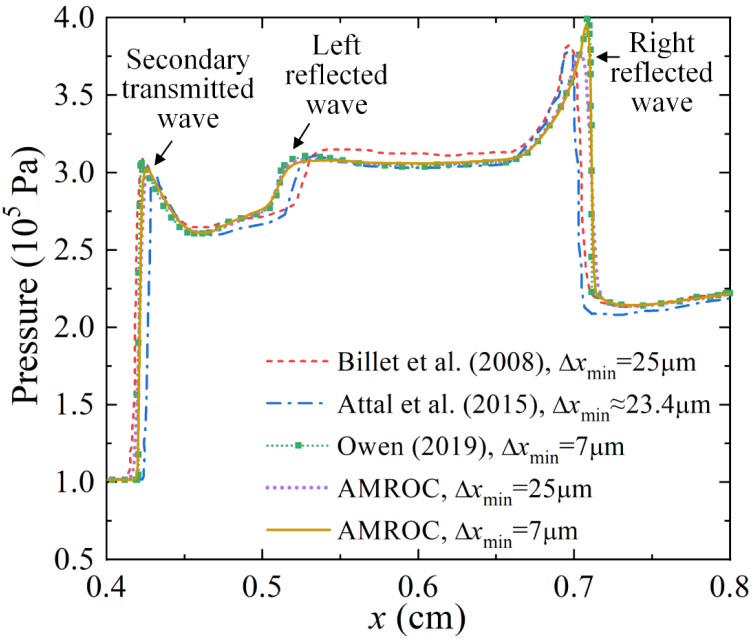

Figure 4.28 Pressure on the vertical central line.

Table 4.5 shows the difference between the numerical methods used in the literature and the present solver. The different approach to computing diffusion coefficients has an influence on the hydrogen bubble size and the distance between the two reflected waves. The use of a quasi-conservative method can also lead to a different shock location. These discrepancies in numerical methods may result in the differences of the solutions.

Table 4.5 Comparison of the numerical methods used for shock bubble combustion.

	Billet et al. (2008) [186]	Attal et al. (2015) [188]	Owen (2019) [189]	AMROC
AMR used	No	Yes	Yes	Yes
Discretisation	FDM	FVM	FVM	FVM
Inviscid fluxes	MUSCL, AUSM+	PPM	PPM	MUSCL-Hancock Roe/HLL

	Billet et al. (2008) [186]	Attal et al. (2015) [188]	Owen (2019) [189]	AMROC
Viscous fluxes (transport parameters: the dynamic viscosity μ, the thermal conductivity k and diffusion coefficients D)	μ, k and D are computed using 'eglib' library additionally considering the Soret effect and volume viscosity	μ and k are computed by mixture averaging formulas and D is the binary diffusion coefficients	μ and k are estimated by using mixture averaging formulas and D is computed by a given Lewis number	μ and D are computed by mixture averaging formulas and k is computed by a species-dependent thermal diffusion ratio.
Minimum mesh size	25 μm	~23.4 μm	7 μm	7 and 25 μm
Domain size	Half domain	Full domain	Full domain	Full domain
Outflow boundary conditions	Subsonic characteristic outflow	Extrapolated outflow	Extrapolated outflow	Extrapolated outflow
Conservation of hyperbolic terms	Quasi-conservative double-flux	Conservative	Conservative	Conservative

4.3 Chapter summary

In this chapter, the developed solver was comprehensively verified and validated with different benchmark tests. These tests confirmed that the current solver could achieve second-order accuracy and was globally conservative on a hierarchically refined structured mesh. The solver was then validated by solving multi-dimensional Riemann problems accurately. Although the solver was originally developed for high-speed reacting flows, i.e., supersonic combustion and detonation, namely convection-dominated problems, the diffusion terms were also validated by low-speed benchmarks. The solver was also tested to reproduce the flow features in a high-speed reacting viscous flow, in which the shock interacted with a flame. In the next chapter, the extended solver is used to simulate more complex high-speed reacting flows.

Chapter 5 Simulations of high-speed reacting flows

After being verified and validated with some benchmark tests, the present solvers are further tested to simulate more complex high-speed reacting flows, such as unsteady shock-induced combustion, 2D cellular detonation structure, 3D detonation in a pipe and detonation wave/boundary layer interaction. The purpose of this chapter is to demonstrate the accuracy and robustness of the developed solver in solving high-speed reacting flows.

5.1 Unsteady shock-induced combustion

Unsteady Shock-induced combustion (SIC) is usually used to validate the code for supersonic combustion [190,191]. In this section, Lehr's SIC experiments [192] at Mach 4.18 and Mach 4.48 are simulated. The 2D axisymmetric Euler equations with detailed chemical kinetics are solved as

$$\begin{aligned} &\frac{\partial yQ}{\partial t}+\frac{\partial yF}{\partial x}+\frac{\partial yG}{\partial y}=yH+S, \\ &H=\begin{bmatrix}0 & \cdots & 0 & 0 & p/y & 0\end{bmatrix}^{\mathrm{T}}, \\ &S=\begin{bmatrix}\dot{\omega}_1 & \cdots & \dot{\omega}_{N\mathrm{sp}} & 0 & 0 & 0\end{bmatrix}^{\mathrm{T}}, \end{aligned} \tag{5.1}$$

where an additional axisymmetric source term H is added to simulate the 2D axisymmetric flow [193]. The second-order accurate MUSCL-Hancock scheme with Minmod limiter is used for the reconstruction. The inviscid flux on mapped meshes is evaluated by a grid-aligned AUSM method. The Strang splitting is adopted for the reactive source term and the modified Jachimowski hydrogen/air reaction mechanism [187] is employed. This mechanism contains 9 species and 19 elementary reactions and has been used in the hydrogen-air shock bubble combustion case.

The region behind the blunt body in Lehr's experiments is modelled as displayed in Figure 5.1, where the diameter of the hemispherical head is 15 mm. For the axisymmetric problem, one half of this region is simulated by setting the bottom as a symmetry boundary, as shown in Figure 5.1. The base mesh is generated through the functions described in Equation (A.7). The supersonic flow consisting of a stoichiometric hydrogen-air mixture travels from left to right, which is equivalent to the blunt body moving with a supersonic speed. The initial temperature of the mixture is 293 K and the pressure is set as 42.66304 kPa.

For the calculations, there are 250 base cells in the radial direction and 200 base cells in the circumferential direction, with 3 levels (refinement factors are 2, 2) adaptively refined on the fly. The minimum radial mesh is about 3.5 μm and the minimum circumferential mesh is around 4.375 μm. For comparison, meshes with 2 levels and 4 levels of refinement are tested to study the effect of mesh size on this problem. The case without refinement is also tested.

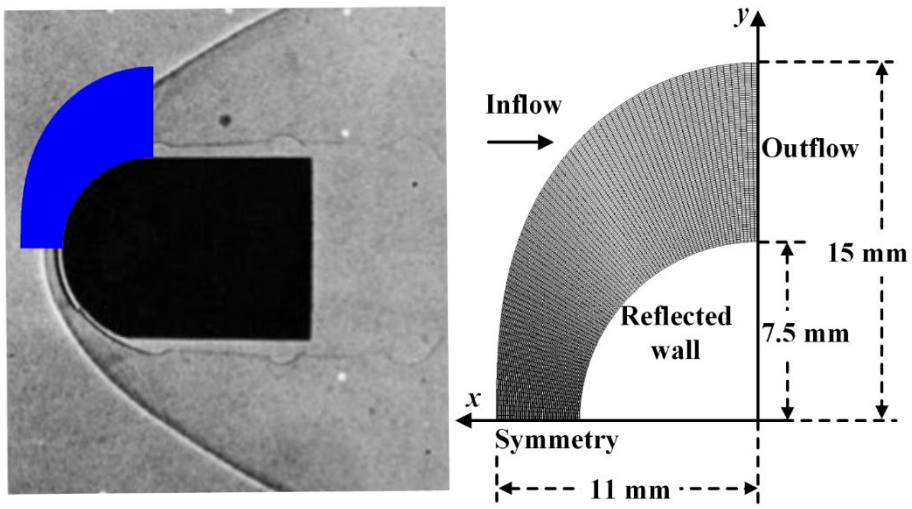

Figure 5.1 The physical model (left) and computational domain (right) of SIC.

The calculations in this section are performed on the high-performance computing cluster Iridis 5 at the University of Southampton, where 40 cores (Intel Xeon E5-2670 2.0GHz) were used for cases with 1 to 3 refinement levels and 80 cores were used for cases with 4 refinement levels. The refinement criteria are given in Table 5.1. The scaled gradients are given as, ε_T=500 K , ε_ρ=0.02 kg/m^3 , ε_p=16 kPa .

Table 5.1 Refinement indicators used for simulating shock-induced combustion.

Refinement indicators	Species					
	H	H_2	O	O_2	OH	H_2O
S_Y ($\times 10^{-4}$)	0.03	0.3	0.2	1.5	1.6	21.8
η_Y ($\times 10^{-4}$)	10	4	10	4	10	3

The regular oscillation of the bow shock wave and reaction front is one of the crucial parameters in unsteady shock-induced combustion. To illustrate the oscillation in the unsteady process, the temperatures and densities on the stagnation streamline are extracted at different times as shown in Figure 5.2. When the base mesh is used without AMR, the minimum cell is 14 μm. Under this mesh resolution, the reaction front oscillates at a lower frequency and the oscillation of the bow shock cannot be captured. When the mesh is refined, the locations of bow shock and reaction front oscillate regularly at a higher frequency, and the wave's stand-off distance is closer.

In addition to the temperature distribution, the x-t diagram of the refinement level is also displayed in Figure 5.3. With the aid of Figure 5.2, it can be observed that all the oscillating bow shocks and reaction waves are dynamically captured by the highest-level mesh.

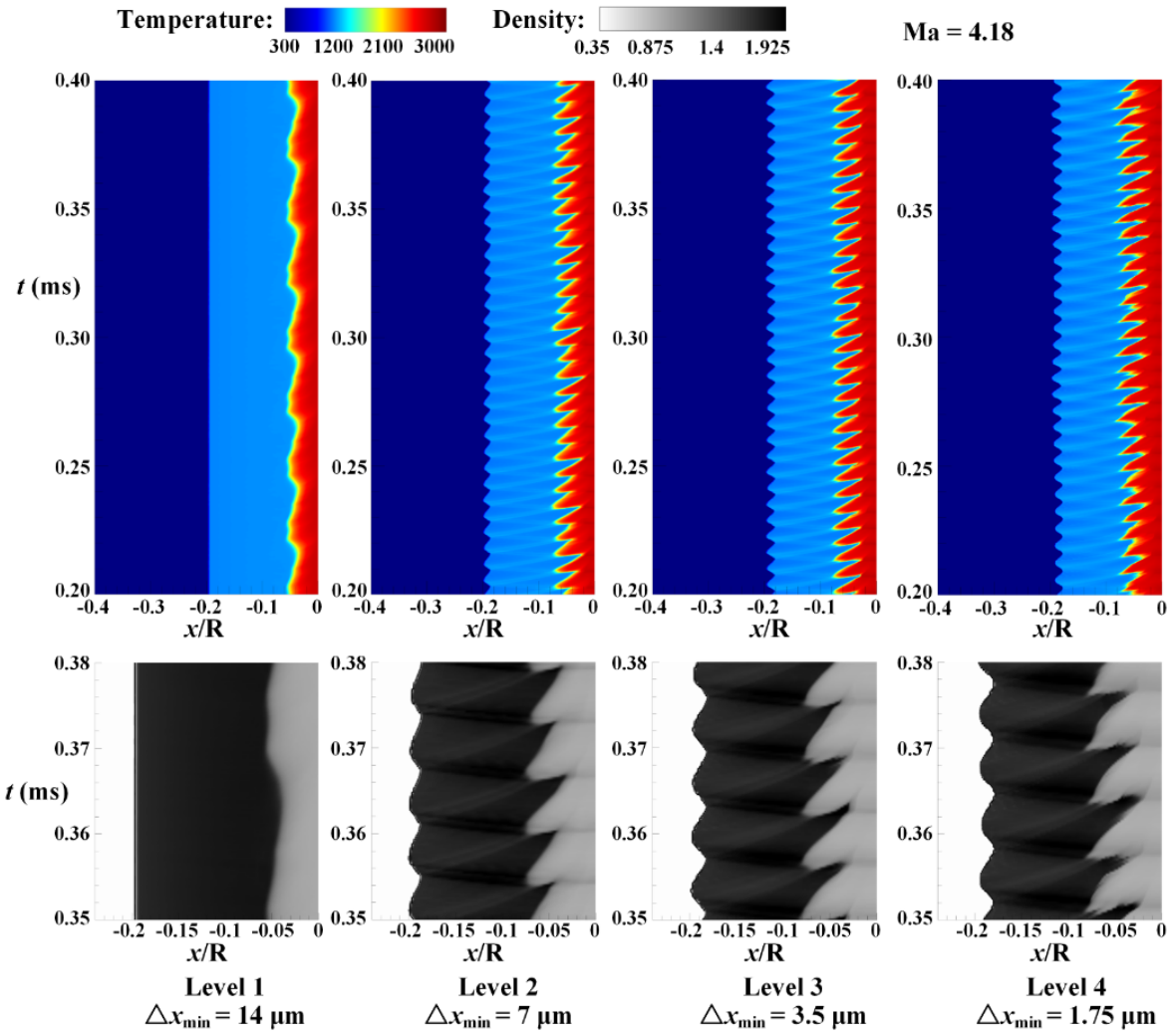

Figure 5.2 *x-t* diagram of temperature on the stagnation streamline under different mesh resolution.

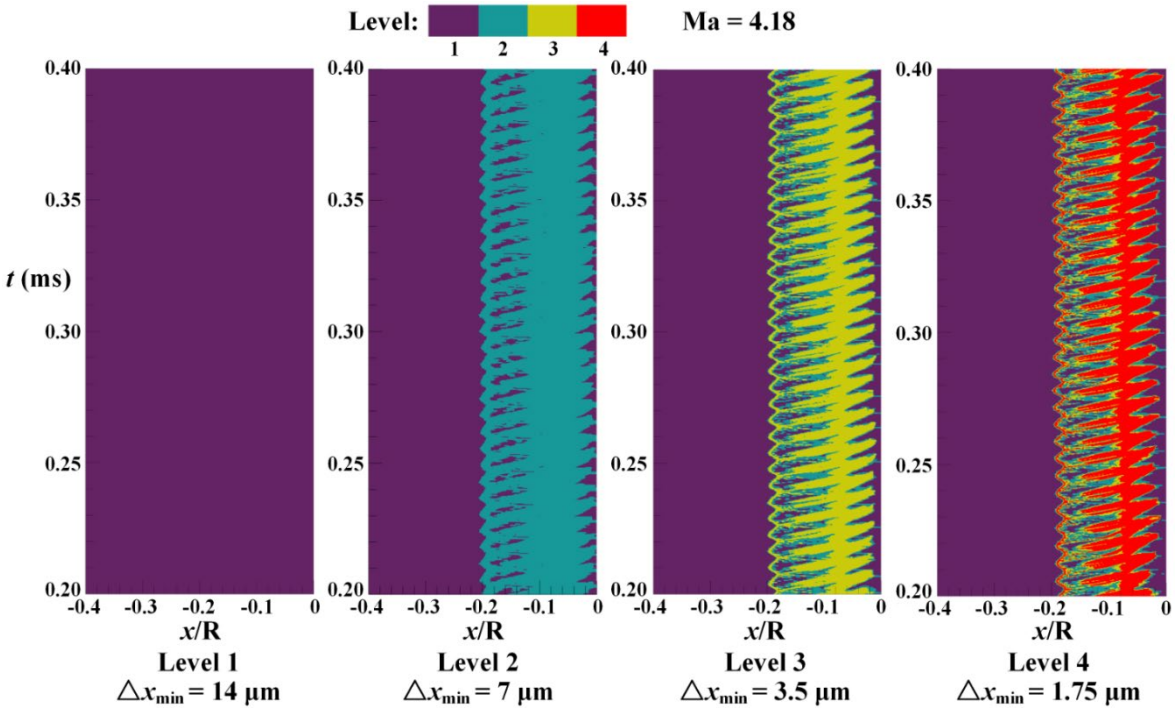

Figure 5.3 *x-t* diagram of the domain of refinement levels (indicated by colour) on the stagnation streamline under different mesh resolution.

In order to analyse the oscillation characteristics, the Fast Fourier Transform (FFT) is utilized. Due to the adaptive time step in the AMR solver, the time intervals for data processing are non-uniform. A linear interpolation is used to determine the mass fraction profiles from 0.2 ms to 0.4 ms with uniform time intervals. As a result, the frequency resolution is 5 kHz for all the cases. Figure 5.4 displays the frequencies of the water mass fraction oscillation at the stagnation point under different refinement levels. Similar to the results shown in Figure 5.3, only the coarsest mesh provides an incorrectly low frequency of 40 kHz. The frequency is convergent on a finer mesh. The frequency in the numerical solution is 160 kHz on a two-level or three-level refined mesh, which is close to the frequency, 148 kHz, obtained in Lehr's experiment. Although a closer frequency 155 kHz can be obtained by increasing the mesh refinement level up to 4, the three-level refinement is considered a good trade-off between the computational efficiency and cost. Therefore, all the meshes are refined with three levels in the following SIC calculations.

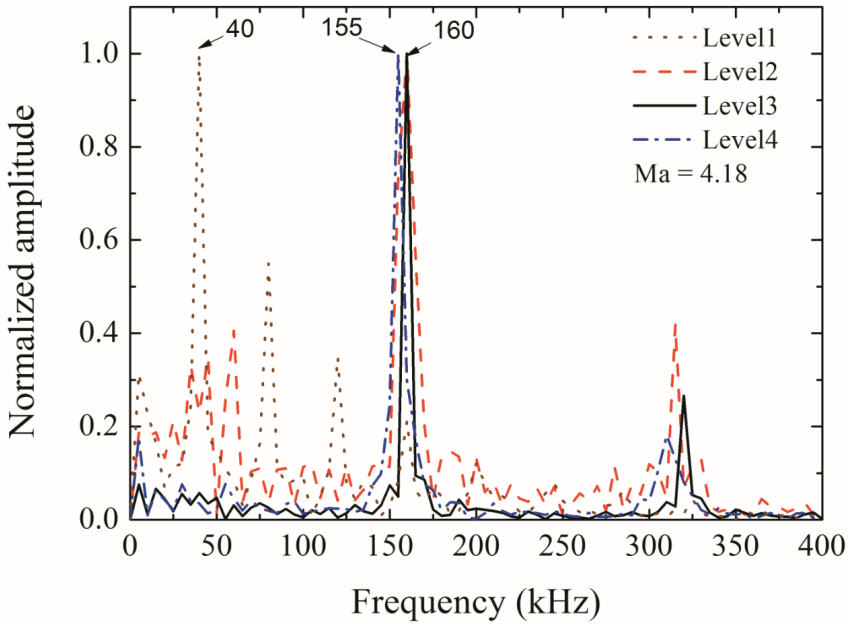

Figure 5.4 Frequencies of mass fraction of H_2O oscillation at the stagnation point under different mesh resolution.

Table 5.2 Comparison of uniformly refined and dynamically adaptive simulations for the shock-induced combustion problem at Mach 4.18 from t = 0 ms to t = 0.2 ms.

Ma = 4.18	Uniform		Adaptive	
Δx_{min} (μm)	Cells	Run time (cpu·h)	Level	Run time (cpu·h)
14	50,000	36.7		
7	200,000	240.0	2	308.6
3.5	800,000	1286.7	3	1193.5
1.75	3,200,000	9590.6	4	5521.6

Table 5.2 gives timing data from present dynamically adaptive simulations versus uniform computations under the same mesh size. The benefit in computational costs from dynamic mesh adaptation is apparent when the mesh resolution is high. It should be pointed out that for such a classical problem, the chosen computational domain is already reduced to include all the potential physical features. The advantage of adaptive simulations is not remarkable when the number of cells is small.

A detailed two-dimensional structure can be seen in Figure 5.5. The combustion is induced by the bow shock wave in front of the blunt body. Several typical characteristics can be inferred from the results. Firstly, the reaction wave is separated from the bow shock wave, while the reaction front is corrugated and unstable. Another feature is the existence of waves, i.e., the compression wave, reflected wave and contact discontinuity, between the bow shock wave and the reaction front. The interaction of waves and the stagnation surface of the blunt body has been considered as the source of the pressure and combustion oscillations.

The adaptively refined mapped mesh is also shown in Figure 5.5. All wave structures mentioned above are captured and refined by the finest mesh (Level 3 mesh). The enlarged region shows how the body-fitted mesh is refined near the bow shock and the reaction front. The region without shock waves and reactions uses the coarsest mesh, which effectively reduces the computational cost in the high-resolution simulations.

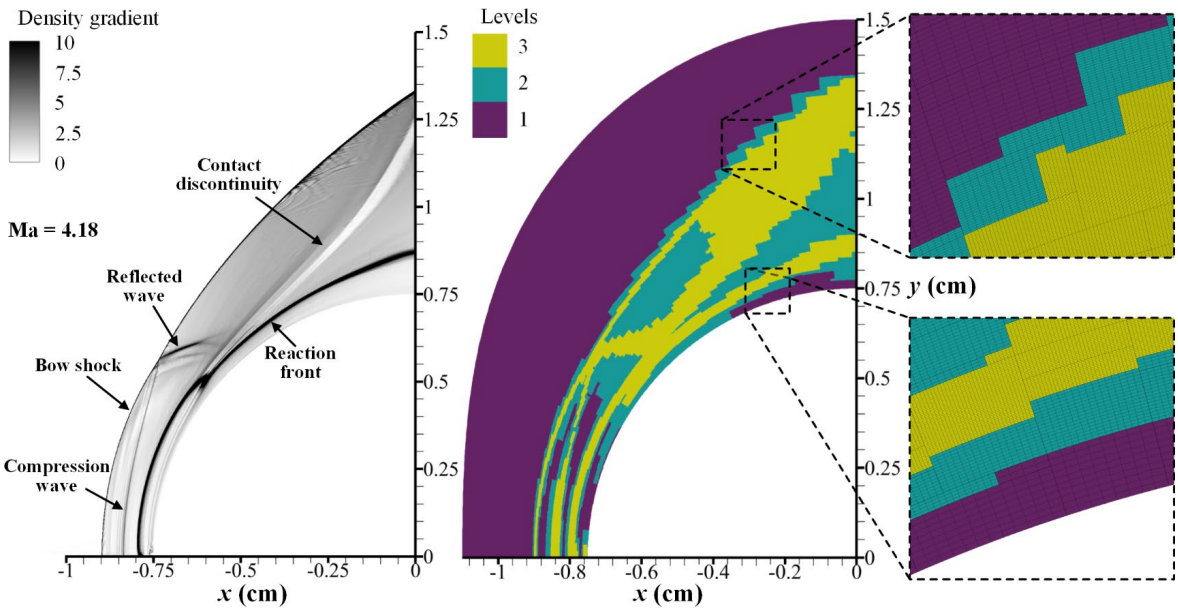

Figure 5.5 The density gradients and corresponding refinement levels distribution.

In order to study the effects of refinement criteria on the simulations, the Mach 4.18 case is simulated on a three-level mesh with Roe/HLL scheme. In addition to the refinement criterion used in Table 5.1 (Criterion-2), a looser (Criterion-1) and a stricter criterion (Criterion-3) are tested with different refinement indicators given in Table 5.3. The scaling factors S_Y for all the three criteria are identically

given as the same as in Table 5.1, which is set as the 1% of the maximal value of the mass fractions Y_i in the C-J equilibrium state.

Table 5.3 Refinement indicator values used for simulating shock-induced steady combustion.

Criterion	Computational cost (cpu·h)	Scaled gradient ε			Local truncation error η_Y ($\times 10^{-4}$)					
		T (K)	ρ (kg/m^3)	p (kPa)	H	H_2	O	O_2	OH	H_2O
1	974.2	1000	0.04	32	20	8	20	8	20	6
2	1622.8	500	0.02	16	10	4	10	4	10	3
3	2424.0	250	0.01	8	5	2	5	2	5	1.5

The iso-contours of these indicators on level 2 and corresponding density gradient distribution are depicted in Figure 5.6. The Criterion-1 case uses a relatively loose criterion, where the bow shock wave and reaction front are captured by the finest mesh. The indicators of scaled gradient of density and pressure are used to achieve adaptation to the shocks. The indicators of the scaled gradient of temperature and the errors of mass fractions are employed to flag the reaction front and the compression waves near the stagnation line. In a stricter case (Criterion-2), the contact discontinuities are flagged to refine to the finest meshes. The Criterion-3 case uses the strictest refinement indicators, and a large part of the region behind the bow shock is unnecessarily refined to the highest level.

The scaled gradient of density has a vital influence on flagging the region without shock and flame but with contact discontinuities. A suitable criterion should ensure that all the main physical features are captured by the finest mesh, meanwhile, the flagged cells should be as few as possible. Table 5.3 also shows that the computational cost increases obviously when more cells are refined. Considering the balance of accuracy and computational cost, the set of refinement indicators in Table 5.1 (Criterion-2) is appropriate, and all the following SIC cases adopt this criterion.

Figure 5.7 shows a comparison between the numerical results calculated by the solver based on the AMR mapped mesh and Lehr's experiments. The numerical solutions are in good agreement with the experimental results. The shock-induced combustion is observed in front of the blunt body and the bow shock stand-off distance is nearly the same as that in the experiments. The flame surface is also corrugated, due to the interaction of the waves in the flow field. It is noted that the experimental schlieren image at Mach 4.48 is taken at a 12° angle from the perpendicular direction, which provides a possible explanation why the reaction front location is slightly different to the experimental result.

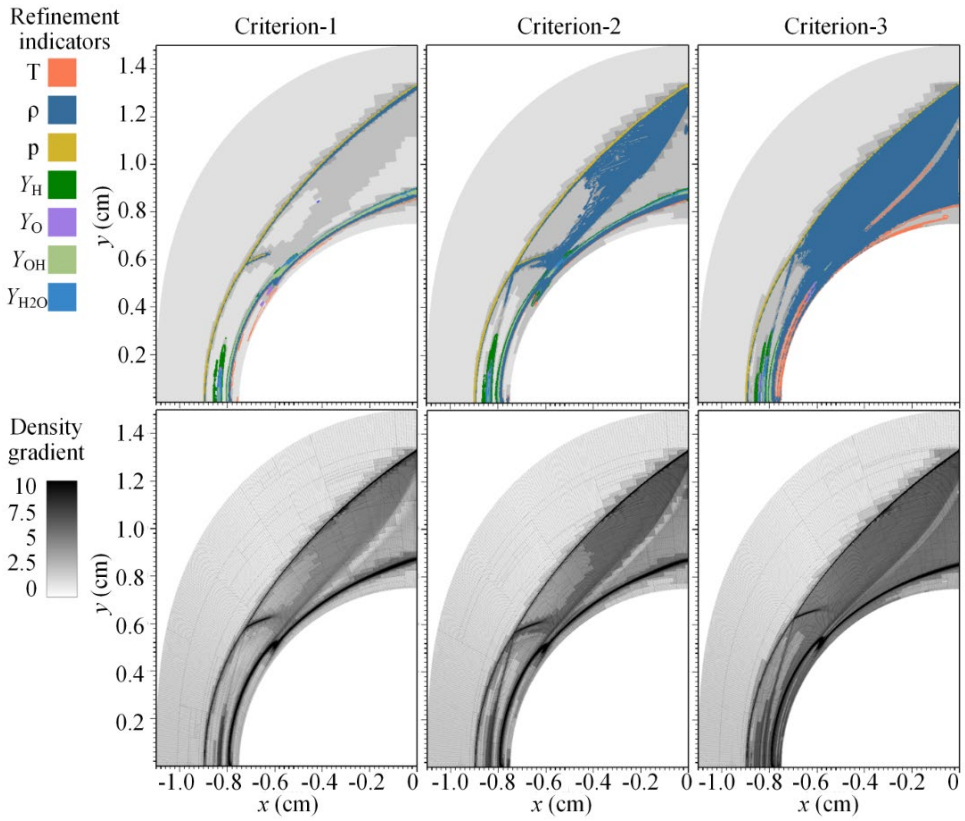

Figure 5.6 Active refinement indicators on level 2 and the density gradients distribution under different refinement criteria for a 3-level computation.

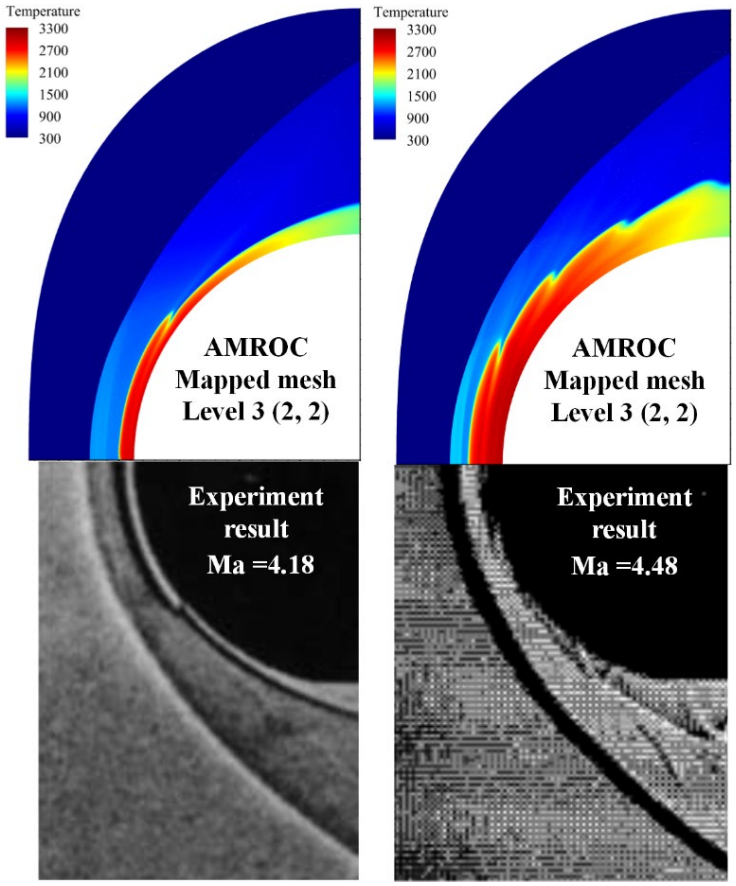

Figure 5.7 A comparison between the numerical temperature distribution from the AMR mapped mesh solver and the experimental schlieren images [192].

In addition to using the Jachimowski mechanism, the UCSD hydrogen/air mechanism [194] is also used in the tests on a mapped mesh with 3 levels of refinement. As seen in Figure 5.8, both reaction models predict a regular oscillation at Mach 4.18. An instability mode is observed in the case with the UCSD model when the inflow Mach is 4.48. The high-frequency oscillation is coupled with a relatively low frequency in this mode, whereas the Jachimowski model still gives a stable high-frequency oscillation. Some previous work [195][196] has reported this unstable phenomenon with different chemical mechanisms.

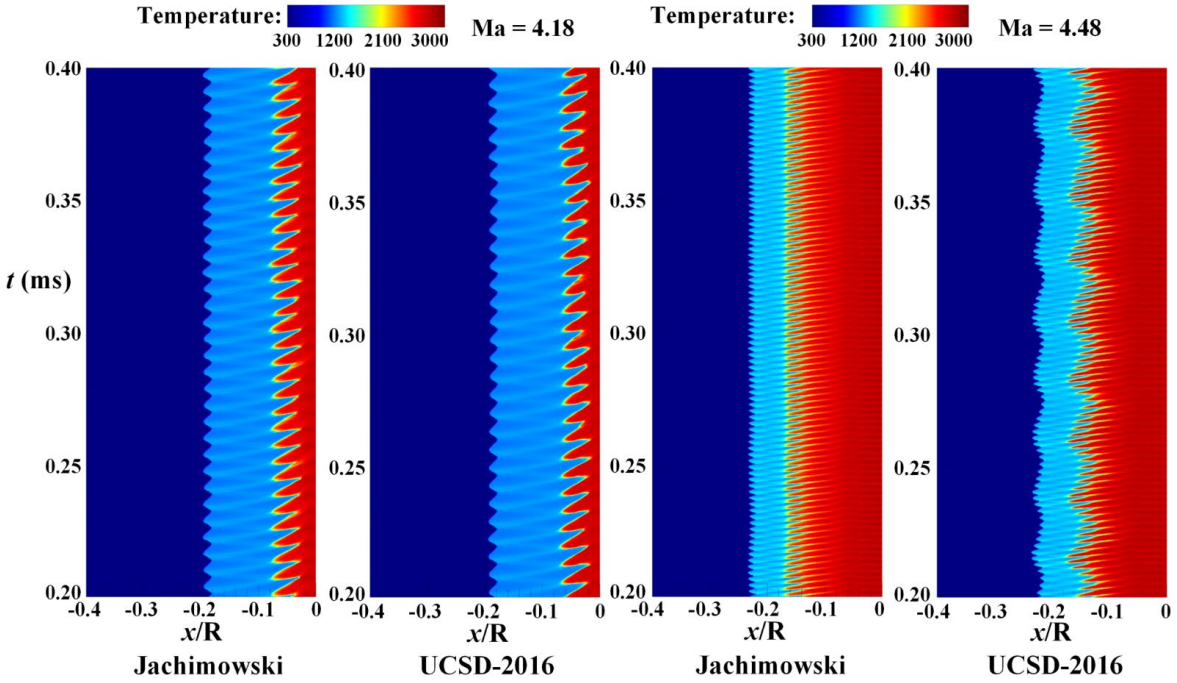

Figure 5.8 *x-t* diagram of temperature along the stagnation streamline at Mach 4.18 and Mach 4.48 on a three-level refined mapped mesh.

As shown in Table 5.4, the Jachimowski model predicts that the frequency of oscillation is 160 kHz, determined by the FFT method as mentioned previously. The UCSD model gives a frequency of 145 kHz, but slightly less than the experimental frequency of 148 kHz. For the Mach 4.48 case, a relatively low frequency is observed when using the UCSD model, whereas the Jachimowski model gives a stable high-frequency oscillation at 425 kHz. In contrast to the Mach 4.18 case, the Jachimowski model gives a better agreement with the experimental frequency at Mach 4.48.

Table 5.4 Comparison of the oscillation frequency.

Frequency (kHz)	Ma = 4.18	Ma = 4.48
Experiment [192]	148	425
Jachimowski	160	425
UCSD-2016	145	395

The test cases have shown that the mapped mesh solver developed in this work can predict the oscillation of unsteady shock-induced combustion. The numerical results are in good agreement with the experiments when a suitable reaction model is used. As described, the chemical mechanism plays a vital role in predicting the correct oscillation.

5.2 2D cellular detonation structure

Simulations of cellular detonation structure are conducted to test the accuracy of the reactive solver on a mapped mesh when chemically reactive source terms are present. The computational domain is a rectangular channel with a length of 1000 mm and a height of 32 mm. A mixture of hydrogen-oxygen-argon at molar ratios 2:1:7 is initialized in the channel. The initial temperature is 298 K and the pressure is 10 kPa. The one-dimensional detonation ZND solution for these parameters is used as planar initial conditions to establish a detonation wave in the left of the tube at location x=46 mm. An unreacted pocket is set behind the detonation front to generate an initial perturbation.

The detailed Westbrook hydrogen mechanism [197] is used in this case, which contains 9 species and 34 elementary reactions. Both a Cartesian mesh and a stretched mesh are used in this case. The stretched mesh is generated by Equation (4.2). The base mesh in this case is 2000×128 cells with five refinement levels. The refinement factor is 2 for each level. The induction length of the detonation is about 0.878 mm under the initial condition. Thus, the maximum resolution can be up to 56.2 Pts/L_{in} (points per induction length) with the adaptive mesh. The refinement criteria are given in Table 5.5 and the scaled gradient thresholds are given as, ε_{T} = 500 K, ε_{ρ} = 0.03 kg /m^3, ε_{p} = 40 kPa.

Table 5.5 Refinement indicators used for simulating 2D cellular detonation structure.

Refinement indicators	Species					
	H	H_2	O	O_2	OH	H_2O
S_Y ($\times 10^{-4}$)	0.2	1.2	1	10	1.3	8.5
η_Y ($\times 10^{-4}$)	5	2	5	2	5	1

Figure 5.9 displays the detonation propagation on a Cartesian mesh and a stretched mesh. The detonation propagation velocity can be calculated through tracking the location of the maximum pressure gradient in the flow field. The numerical results show that the detonation velocity is around 1645.24 m/s on the Cartesian mesh and 1641.82 m/s on the stretched mesh, which is close to the C-J velocity of 1629.34 m/s obtained by Cantera [198] and with the detonation toolbox [199]. The triple points are clearly resolved at the detonation front, where the transverse wave, Mach stem and the incident shock merge. A similar cellular structure is captured by the stretched mesh.

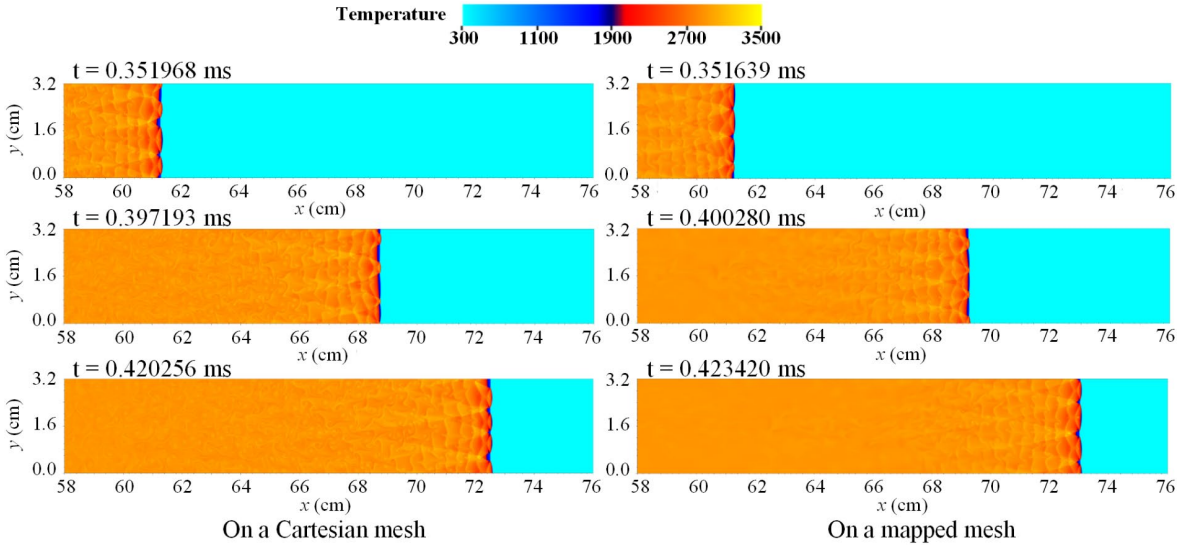

Figure 5.9 Numerical solutions of 2D detonation propagation on a Cartesian mesh (left) and a stretched mapped mesh (right).

More detailed images of the stretched mesh are shown in Figure 5.10. The mesh is clustered at the centre of the tube. The whole detonation front and the slip lines behind are captured by the highest-level meshes. A locally enlarged image shows the triple point structure at the detonation front overlapped by non-uniform refined meshes. The opacity of the mesh is set as 50% to the visualization when the mesh is extremely dense.

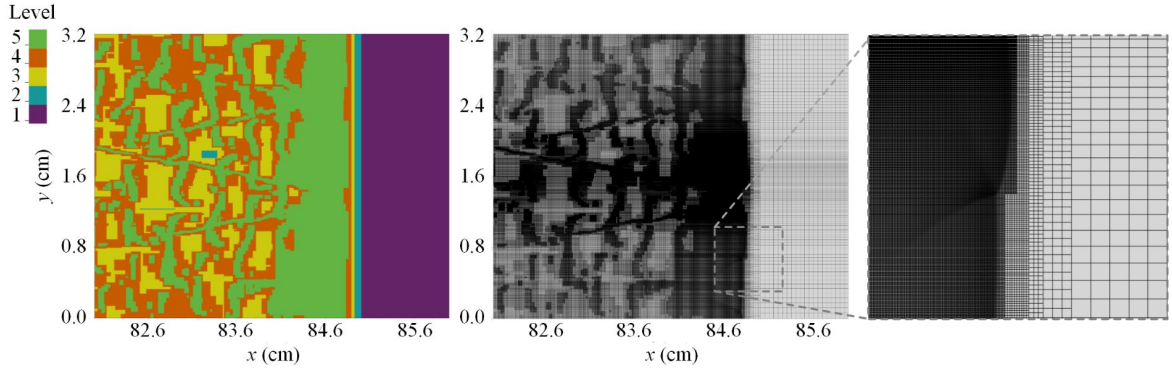

Figure 5.10 Pseudo-colour image of the refinement levels and the image of the stretched refined mesh.

The numerical detonation cells are illustrated by the trajectories of triple points in the flow field, which is captured by tracking the maximum of the vorticity in the whole domain on the base mesh. A detonation cell is a closed “fish-scale” pattern formed between two trajectories of triple points (seen in Figure 5.11). The numerical detonation cell size ranges from 8 to 10 mm, which is close to the value of 11.4 mm predicted by Cantera with a correlation function [200]. However, the numerical cell size is much smaller than the experimental extrapolation value of around 40 mm [201] under the same initial condition. A similar lower prediction of detonation cell size in previously published simulations [202,203] is explained by the considerable heat loss at the channel walls in standard experiments [204].

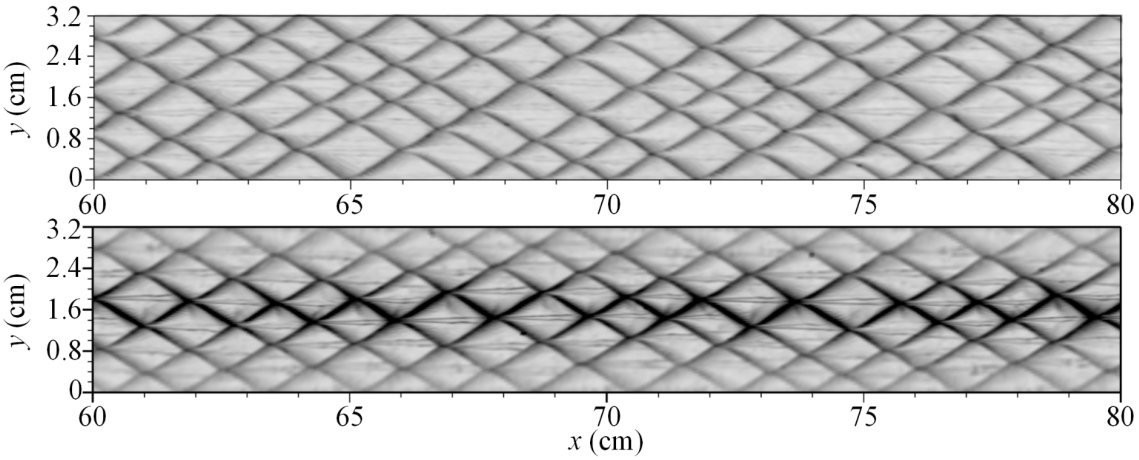

Figure 5.11 Trajectory of triple points on Cartesian mesh (top) and mapped mesh (bottom).

5.3 3D detonation in a smooth pipe bend

Simulations of detonation propagation in a smooth pipe bend are conducted to test the accuracy of the reactive solver on a mapped mesh. For small radii and large bending angles, i.e., pipe bends of a 90-degree angle, the detonation wave structure is not maintained and triple point quenching can be observed at the outer side, while the detonation fails with the originally regular cellular structure. The computational domain and initial conditions are set according to an experimental configuration [205]. In the present configuration, the channel width (4 cm) is at the length of 2.5 cells size and the channel height (1.6 cm) is at the length of 1 cell size. The computational domain and the numerical configuration are illustrated in Figure 5.12.

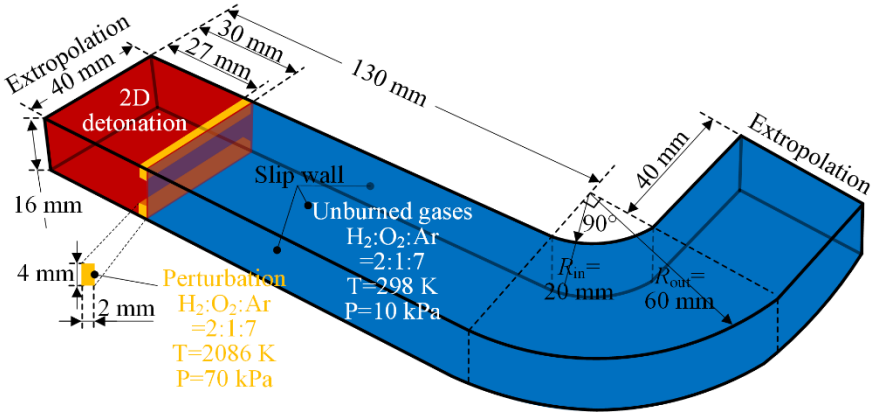

Figure 5.12 Computational domain and numerical configuration of the detonation in a smooth pipe bend.

The pipe is filled with a perfectly stirred stoichiometric hydrogen and oxygen mixture with 70% argon as dilution. The initial temperature is 298 K and the static pressure is 10 kPa. In order to speed up the calculation, the 2D numerical results of detonation cells under the same conditions are initialised at the start of the pipe. Two unreacted sheets at 2086 K and 70 kPa are placed behind the

detonation front as initial perturbations. The induction length L_{in} of the detonation is computed as 0.875 mm given the initial condition.

The base mesh is generated through Equation (A.8). A four-level mesh is used in this case and the refinement factor for each level is 2. The base mesh size is 0.25 mm (3.5 pts/L_{in}) in the η- and ζ-direction using 160 ×960 ×64 cells. In the ξ-direction, the base mesh size is around 0.242 mm along the central line, 0.363 mm on the outer wall, and 0.121 mm on the inner wall of the pipe bend. The mesh size at the finest level is 0.03025 mm (29 pts/L_{in}) on the central plane and changes from 0.015 mm (58 pts/L_{in}) to 0.045 mm (19.4 pts/L_{in}) in the bend. The refinement criteria for temperature, density and pressure are given as ε_T = 500 K, ε_ρ = 0.05 kg/m^3 and ε_p = 40 kPa, respectively. The adaptive computation uses approximately 86.1 M to 118.5 M instead of 5033.16 M cells in a uniform case. The calculations are performed on 480 cores (Intel Xeon E5-2670 2.0GHz). Typical run times for a simulated time of 120 μs were approximately 6.5 days wall clock time.

Figure 5.13 shows the accumulative results of the maximum pressure in the flow field on the base mesh. The triple point is formed in the third direction after a short time and the 3D cellular structure can be observed. When the detonation travels through the 90-degree bend, the cellular structure disappears near the inner wall, indicating that the detonation fails to be self-sustained. On the outer wall, the detonation is highly overdriven and transverse waves are generated after being reflected by the wall.

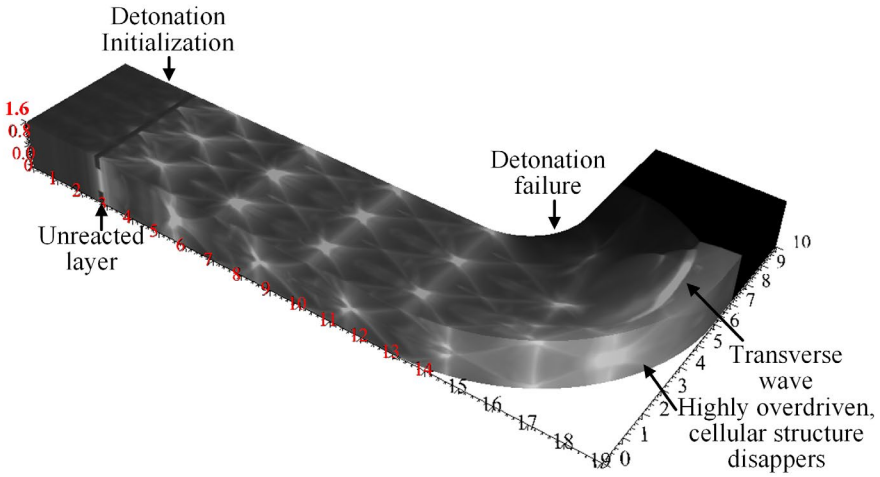

Figure 5.13 Image of the detonation cellular structure on the base.

The detonation cellular front is visualised by the iso-volume of the OH mass fraction and the iso-surfaces of the pressure as shown in Figure 5.14. The temporal development of the triple point line (TPL) structure is given in the schematic diagram. The front of the cellular structure can be divided into three different types of regions [206]. The M-M region is constructed by both sets of Mach stems. The I-I region is constructed by both sets of incident shock waves and the M-I region is mixed, showing both types of waves. The cellular structure of the front was not recorded in the experiment [206], but the straight part of the pipe can be considered a rectangular channel. In Figure 5.14, the

TPLs on the detonation front in both dimensions do not collide with each other simultaneously, presenting a rectangular type out of phase [207-209].

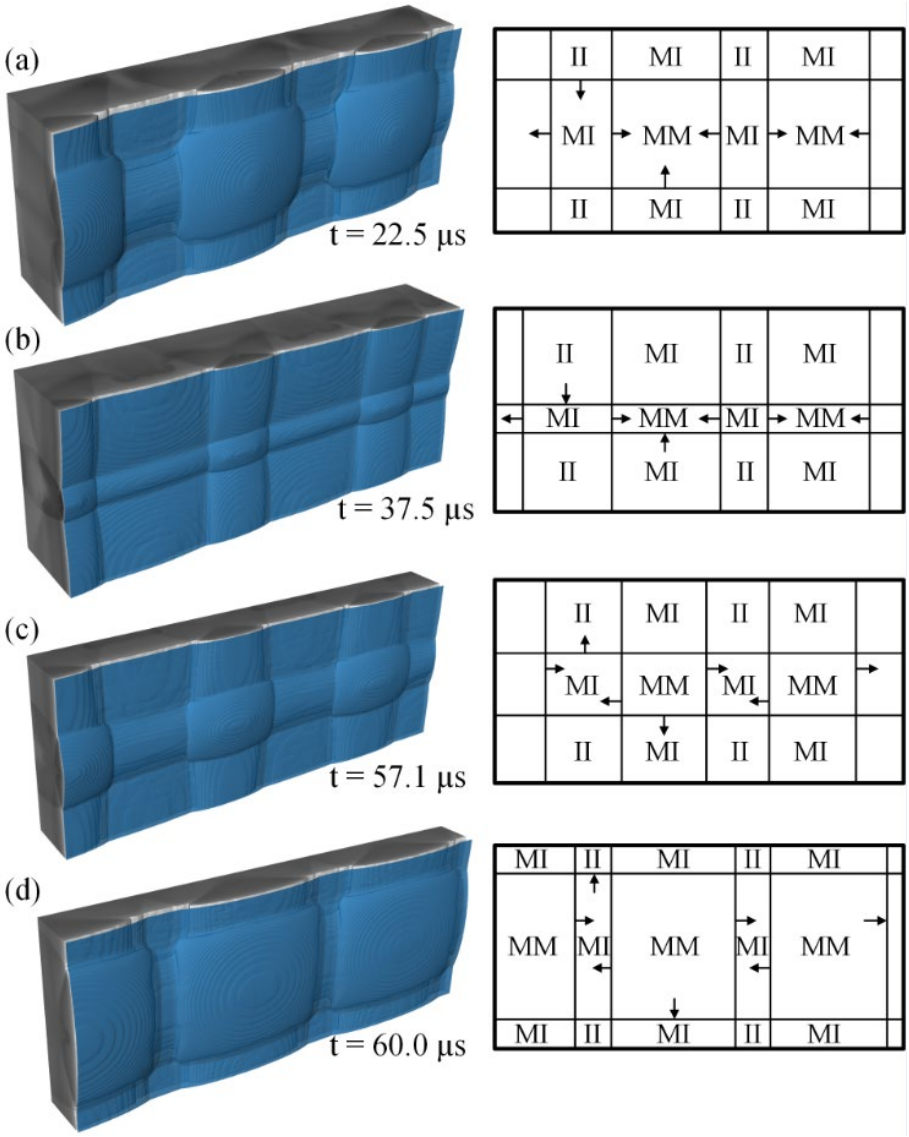

Figure 5.14 Snapshots of the iso-volume of the OH mass fraction, overlapped by the pressure iso-surfaces at 20 kPa in 80% opacity blue (left) in the pipe and schematic front view of the periodic triple point line structure (right); Mach stem-Mach stem (MM), Mach stem–incident shock (MI), and incident shock–incident shock (II).

Figure 5.15 presents the decoupled phenomena of the leading shock wave and the reaction front in the bend. The TPLs are not parallel to the wall because of the different local velocities at different radii, and the reaction front detaches from the shock near the inner wall. At 90 μs, the cellular structure finally disappears. Two formed transverse waves move along the radial direction. A large unburned and preheated region is observed at 105 μs. The detonation is only sustained near the outer wall in an over-driven state.

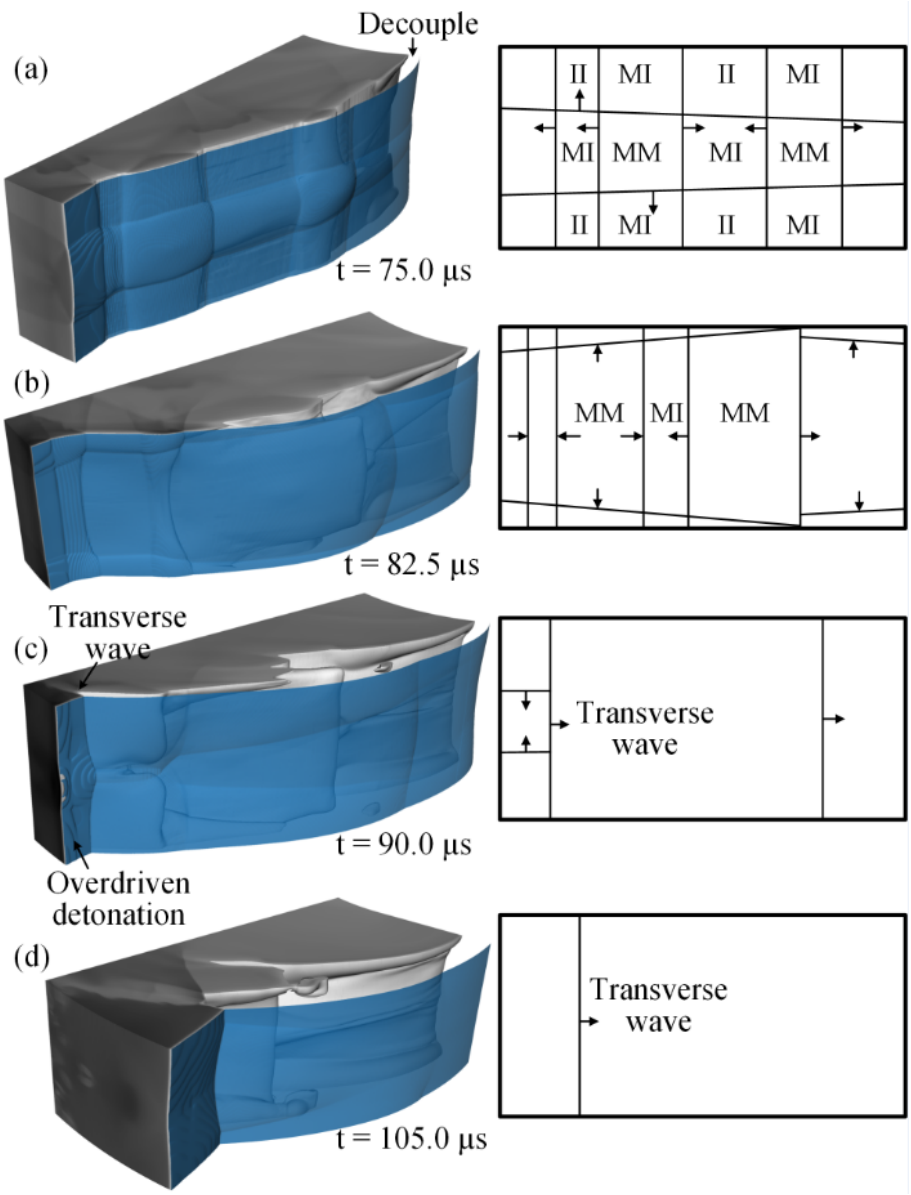

Figure 5.15 Snapshots of the iso-volume of the OH mass fraction, overlapped by the pressure iso-surfaces at 20 kPa in 80% opacity blue (left) in the pipe bend and schematic front view of the periodic triple point line structure (right); Mach stem-Mach stem (MM), Mach stem–incident shock (MI), and incident shock– incident shock (II).

The slices on the bottom wall are extracted to make a comparison with the experimental results. As depicted in Figure 5.16, the locations of the decoupled leading shock wave and the reaction front are in good agreement with the experimental schlieren images. The figures also show that the main features, including the leading shock waves and the flame front, are dynamically captured by the finest meshes.

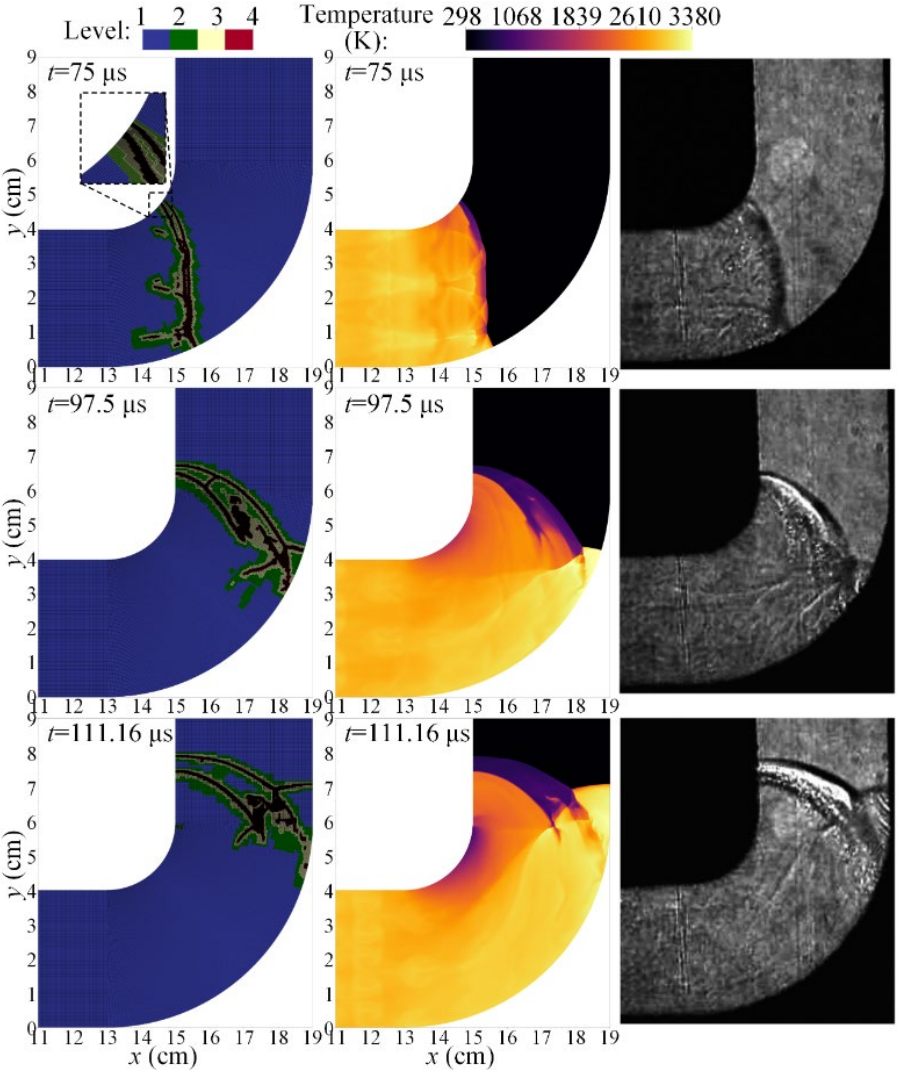

Figure 5.16 Pseudo-colour image of refinement levels, temperature and experimental schlieren in Ref. [205].

5.4 3D detonation in round tubes

In addition to the rectangular channel, the 3D detonation structure is also simulated in a round tube to test the capability of the present solver. Experimental studies [210] and numerical simulations [211] both show that the cross-section shape and geometry confinement have effects on the detonation propagation mode and characteristics. Besides, the experimental observed spinning detonation [212] is a unique phenomenon in the round tube and it still has attracted researchers' attention in recent years [213,214].

However, there have been only a limited number of 3D numerical studies on these problems over the past decades [211,215-218], because the combination of detailed chemistry models and high-resolution simulation is computationally quite expensive. The use of the adaptive mesh refinement technique can be particularly beneficial for this problem. In this section, the detonation is numerically

studied in round tubes with two different diameters. These 3D simulations are aimed at estimating the performance of the AMR technique for simulations of detonations in round tube problems.

To establish a cylindrical body-fitted mesh without singularity in the centre, a convex combination mapping strategy [219] based on a single block hierarchy is used in the present work as shown in Equation (A.9). The premixed stoichiometric hydrogen and oxygen mixture with 70% argon are filled in a round tube. The diameter of the tube D is 16 mm, corresponding to one detonation cell size λ. In order to decrease the computational cost, a nearly stationary reaction front under Galilean transformation is studied by setting the inflow velocity of the unburned gas as C-J velocity. The length of the tube is 30 mm and a 1D ZND structure is initialised from 0 to 20 mm. An unreacted rectangular pocket is initially placed behind the reaction front at 2086 K and 70 kPa. The slip and adiabatic boundary conditions are set for the wall. An extrapolation boundary condition is employed for both the inlet and outlet.

A three-level mesh is used in this case and the refinement factor for each level is 2. The base mesh size is 0.125 mm (7 pts/L_{in}) and the finest mesh size is 0.03125 mm (28 pts/L_{in}). The refinement criteria for temperature, density and pressure are given as, $\varepsilon_T = 500$ K, $\varepsilon_\rho = 0.03$ kg/m and $\varepsilon_P = 4$ kPa, respectively. The adaptive computation uses approximately 11.0 M to 38.2 M instead of 256.1 M cells in a uniform case. The calculations are performed on 480 cores (Intel Xeon E5-2670 2.0GHz). Typical run times for a simulated time of 100 μs were approximately 6 days wall clock time.

Figure 5.17 shows the slices of the temperature gradients in a detonation cell evolution period. At 123 μs, the triple points on the y- and z-planes are observed where the Mach stems, incident shock wave and transverse wave interact. The slip lines curl into vortices and embedded jets behind the incident shock [202]. The triple points on both planes all move towards the centre of the tube. At 127 μs, the triple points collide and new triple points are generated, which then move towards the wall. The jet behind the detonation front is detached from the leading shock. A new jet is formed after the collision in the centre. New triple points are reflected by the wall and finally travel to the centre again at 137 μs, resulting in a similar structure compared with that at 123 μs. A whole period of the cellular structure evolution is completed and the duration is around 14 μs.

Figure 5.18 displays the iso-surface in terms of the density at different times. The iso-surface is coloured by the temperature contours. Although the small structures in the wake of the shock are still not sharply resolved, the 3D figure provides a good impression that the detonation propagates in the rectangular mode with a single cellular structure. The TPLs move to the tube centre and interact with the forward vortex ring. The vortex rings are detached and propagate downstream. A pair of new forward vortexes are formed after the collisions of TPLs, which causes the front to bulge. New TPLs are also generated and move to the wall, starting a new period of the cellular structure evolution.

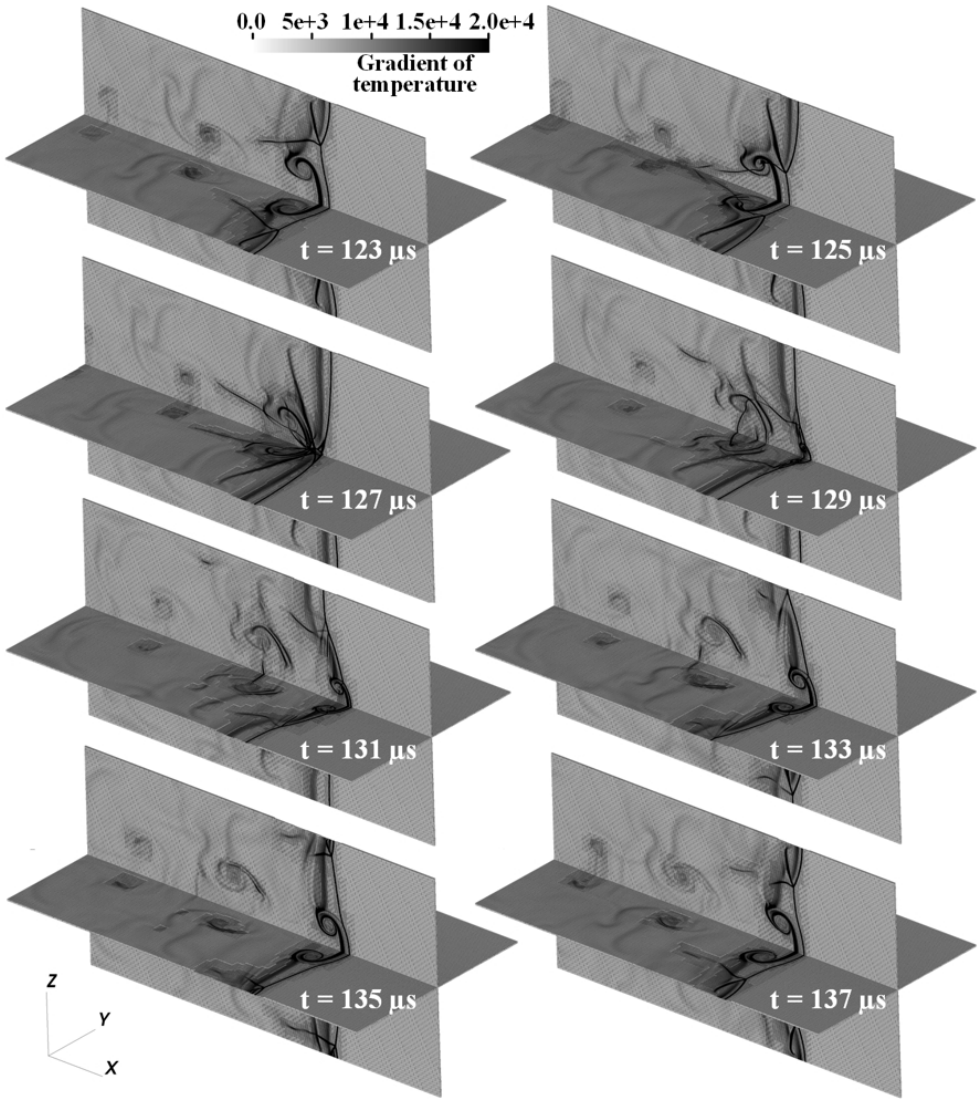

Figure 5.17 Snapshots of the slices of the gradient of temperature, overlapped by the meshes at 80% opacity.

Figure 5.19 shows that the mesh around the detonation head and at the corners is adaptively refined to improve the accuracy of simulations. More processors are used in the refined regions with higher workloads. The hierarchical mesh is distributed to processors based on a space-filling curve [30] in computational space. Continuous redistribution, while the mesh is changing, is ensuring a balanced workload at run time.

In addition to the round tube with a diameter of one detonation cell, a half detonation cell size tube is also simulated with the same initial configurations. As displayed in Figure 5.20, the detonation propagates in a rectangular mode at the early stage. Similar evolution of triple points and jets behind the incident shock is observed. At t = 120 μs, a single head detonation wave is generated at the front and the cellular pattern disappears. The detonation spins in a counterclockwise direction from the right-hand side view. A typical spinning detonation is observed and propagates spirally to the outlet even in the Galilean frame. Compared with the case with $D = 0.5\,\lambda$, the transverse wave is constrained

when the duct diameter is smaller than the detonation cell size. Only a single transverse wave remains and results in the spinning mode [6].

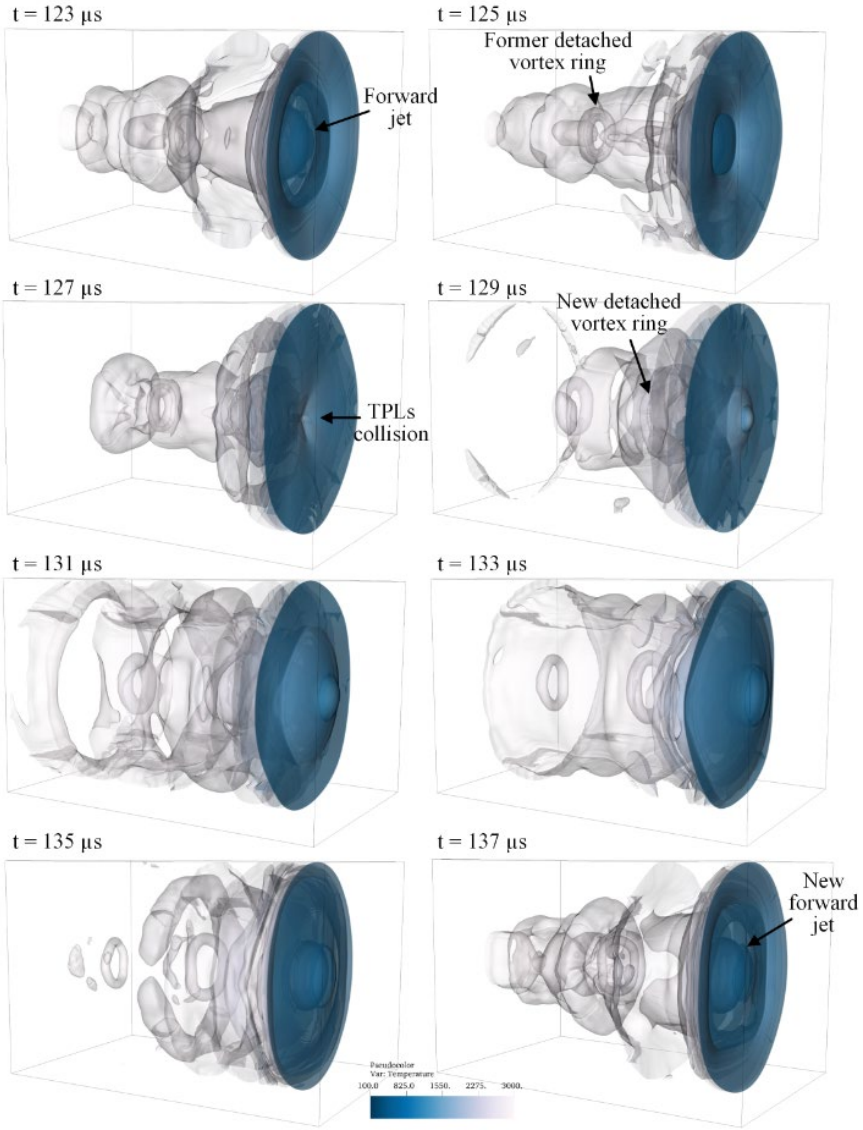

Figure 5.18 Pseudo-colour image of the temperature based on the iso-surfaces of the density in 40% opacity, $D=\lambda$.

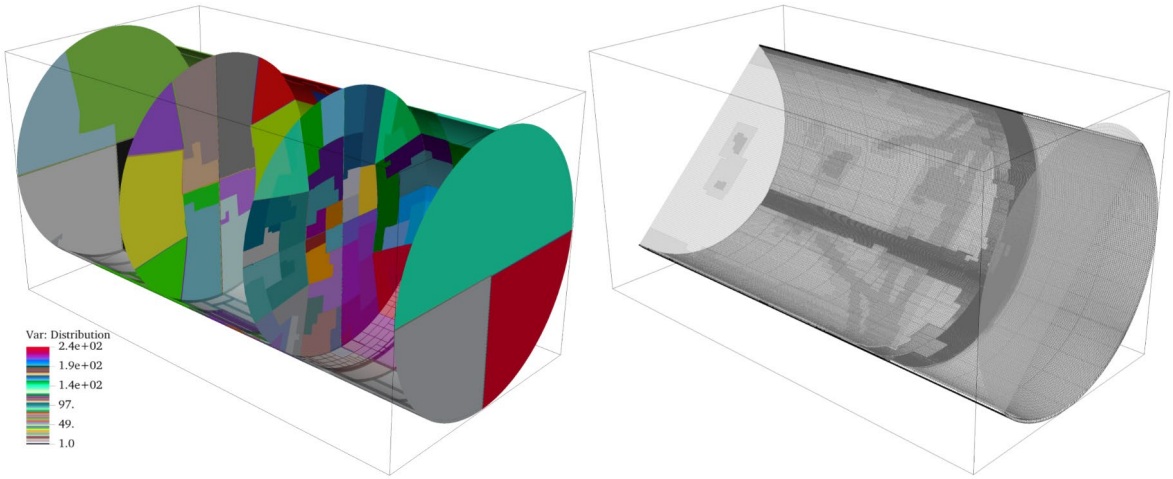

Figure 5.19 Slice of processors distribution and slice of girds with 40% opacity.

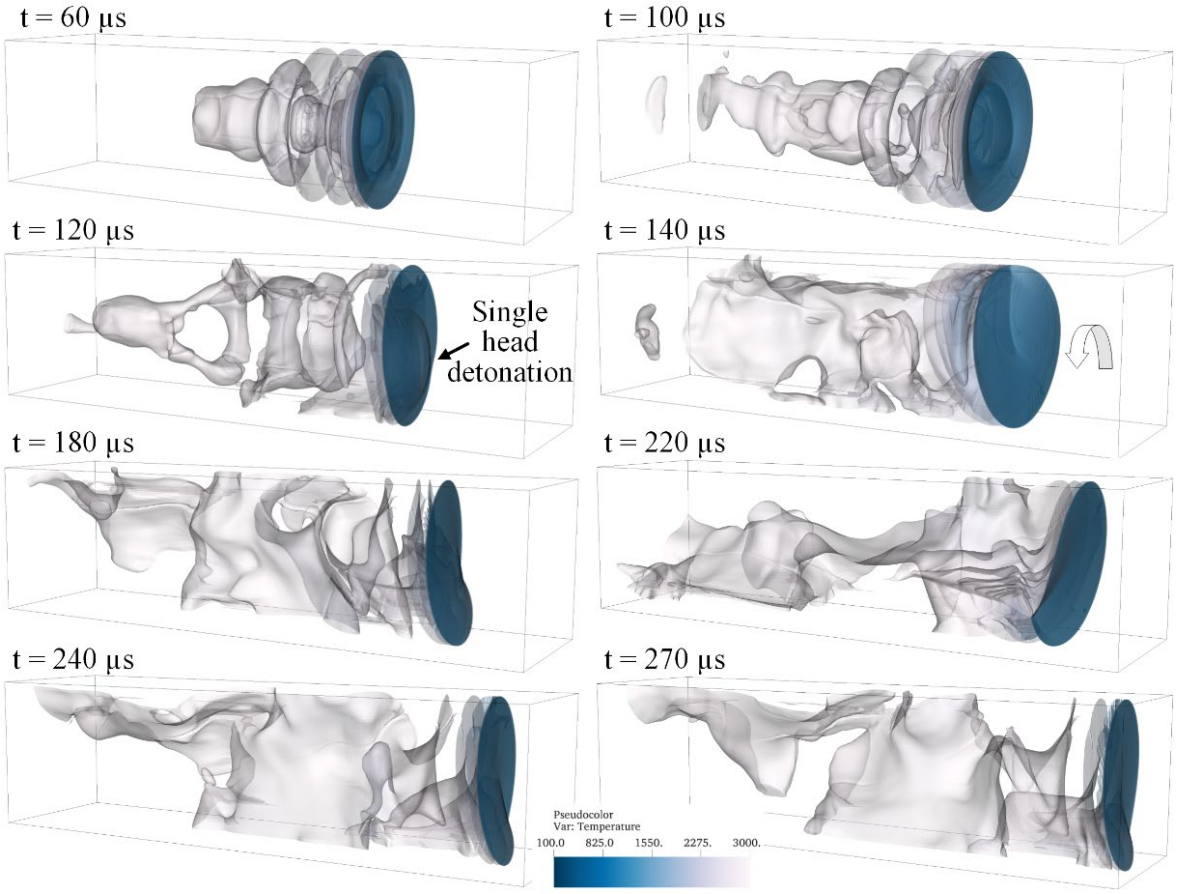

Figure 5.20 Pseudo-colour image of the temperature based on the iso-surfaces of the density in 40% opacity, D=0.5λ.

5.5 Detonation wave/boundary layer interaction

In the previously studied configurations, the unburned gases are considered stationary with respect to the reaction front, and slip boundary conditions are employed for the walls. However, with a high-speed inflow, the effects of bifurcated shock structures on shock-flame interactions become obvious [220]. In addition, the interaction of the boundary layer can impact the timing, location, and manner in which detonation occurs [221]. These factors are not negligible and are referred to as detonation wave/boundary layer interactions (DWBLI).

In order to test the capability of the present solver for simulating reactive boundary flow, a DWBLI case [31] is simulated using the solver on an adaptive stretched mesh. The computational domain is set as a cuboid with a length of 85 mm, a height of 42 mm and a width of 16 mm. A high-speed hydrogen-oxygen-nitrogen mixture flows through a channel from the right-hand to the left-hand side. The interaction between the detonation and boundary layer is studied.

The initial temperature of the unburned $H_2/O_2/N_2$ mixture is 581 K and the pressure is set as 36.1 kPa with the molar ratio 0.56:1.0:2.9. The induction length L_{in} of the detonation is computed as 2.15 mm under this condition. The domain is initialised with a 1D ZND solution from x = 0 mm to x = 50 mm.

The right-hand boundary is given a Dirichlet boundary condition. The inflow velocity is set as 1532 m/s. The left-hand boundary is set as an extrapolated outflow boundary. The top and bottom boundaries are non-slip adiabatic walls from x = 0 mm to x = 80 mm, otherwise the boundaries are slip. The front and back boundaries are slip adiabatic walls.

A stretched mesh is used as the base mesh in this case, and the mesh stretching ratio is set as 1.05 in the boundary layer as presented in Equation (A.6). The initial base mesh resolution is 340 ×400 ×64 cells. The height of the first layer mesh is 5.61 $\times 10^{-6}$ m and the viscous shear layer thickness is estimated as 5.59 $\times 10^{-5}$ m [31]. Hence, around 7 cells are distributed in the viscous length of the boundary layer. The respective first 60 layers of cells from the top and bottom boundary are not adaptively refined in the computing process. The coarsest base cell in the channel centre is 0.28 mm. With a three-level refinement (2, 2), the coarsest cell in the domain is 0.07 mm (30.7 pts/L_{in}). The refinement criteria for temperature, density and pressure are given as ε_T = 500 K, ε_ρ = 0.03 kg/m^3 and ε_p = 40 kPa, respectively. A finer resolution is used in the 2D simulation based on a five-level Cartesian mesh in Ref. [31], in which 5 cells are ensured in the viscous scale but a higher resolution is used for the detonation structure (137.8 pts/L_{in}).

It is noted that the viscous boundary layer and the viscous structure are still not fully resolved even under the present resolution. However, the mesh resolution is chosen based on our available computing resources for the validation of the prototype solver. Using the stretched mesh provides an approach to simulate the detonation problem involving viscous boundary layers efficiently compared to using a uniform mesh. In this case, the adaptive computation uses approximately 10.8 M to 88.0 M instead of 557.1 M cells in a uniform case. The calculations are conducted on 240 cores (Intel Xeon E5-2670 2.0GHz). Typical run times for a simulated time of 145 μs were approximately 12 days wall clock time.

Figure 5.21 (a) shows the slices of the pseudo-colour image of the temperature gradient on the z = 0 mm plane. The leading oblique shock, boundary layer flame and detonation front are observed in the numerical result. The vortex structures in the shear layer induced by the Kelvin–Helmholtz (KH) instability are also captured. Figure 5.21 (b) is the mass fraction of OH superposed on pressure contours. The detonation front in the central flow is composed of a stand-off Mach stem and the subsequent reaction front. It is described as a Mach stem-induced detonation (MSID). The unburned pockets are also observed and further confirm the accuracy of the present solver when simulating this problem.

As shown in Figure 5.21 (c) and (d), the base mesh used in this case is stretched near the non-slip boundaries. The boundary flow is solved by the stretched mesh itself, while the AMR is used in the domain interior except for the near-boundary region to improve the accuracy for solving the shock wave and detonation wave. These figures also show that the main features in the central flow are captured by the highest-level mesh.

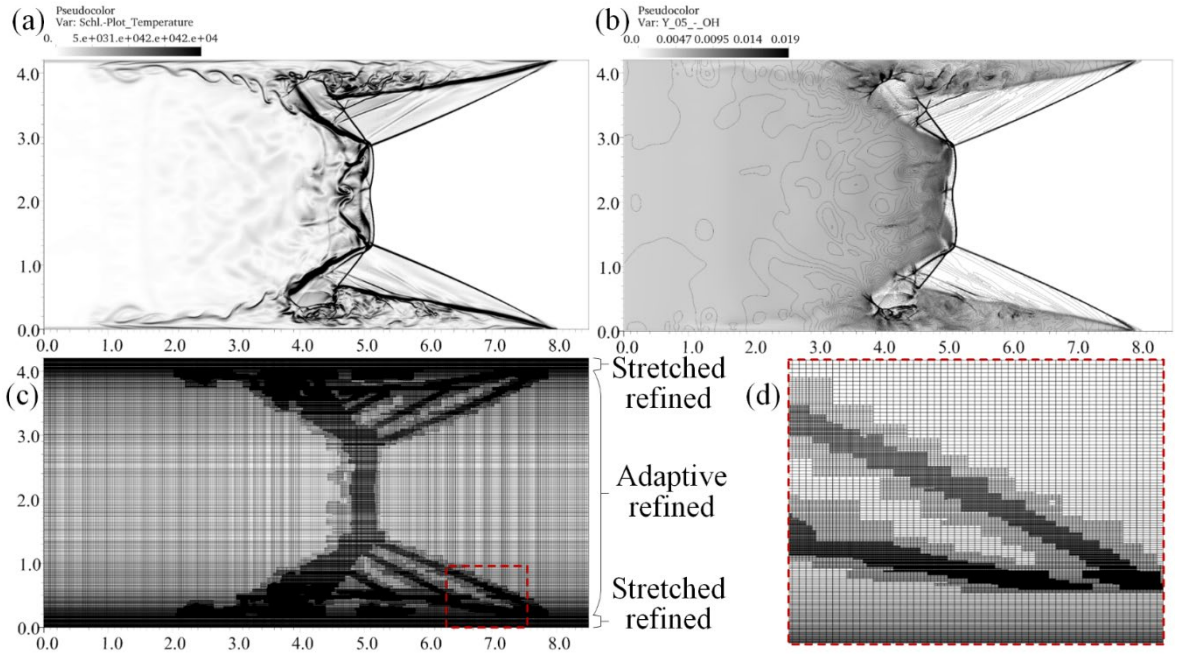

Figure 5.21 Slices of grey scale image of the temperature gradient, mass fraction of OH superposed on line contours of pressure and image of meshes at t = 60 μs.

Figure 5.22 illustrates the slices of the pseudo-colour image of temperature at various times. At t = 0 μs, the 1D ZND solution is initialised on a Galilean frame. At t = 50 μs, temperature recovery is observed near the non-slip part of the top and bottom wall. The oblique shock-induced combustion (OSIC) and boundary auto ignition result in a flame in the boundary layer. The Mach stem-induced detonation (MSID) front stands in the middle main stream. The slip lines behind the triple points develop into unstable shear layers downstream because of the KH instability. A pair of large-scale unburned pockets is formed between the MSID and the OSIC. Small unburned pockets are also observed in the boundary layer flame and are consumed in the following time sequences. Unstable combustion in the boundary layer has been considered as the main source for the oblique shock fluctuation.

The fluctuating oblique shock waves lead to an unsymmetrical structure and also force the triple points to move towards the channel centre. As a result, the height of the Mach stem eventually decreases and the Mach stem finally vanishes after the two oblique shock waves collide. Figure 5.22 shows that the reaction front behind the Mach stem is detached from the intersection point and propagates downstream at t = 50 μs. The OSIC/MSID pattern turns into a pure OSIC pattern and only the OSIC is maintained in the channel.

Figure 5.23 displays the typical OSIC/MSID pattern in a 3D density iso-surface image coloured by the temperature. The small vortexes are resolved in the boundary layer. The present 3D results reproduce some typical features, which are also observed in previous experiments and the 2D simulations of Ref. [31]. The main difference between our present numerical result and the 2D

numerical result is that our 3D simulation predicts a faster formation of the OSIC/MSID pattern. An OSIC/MSID mode is observed at t = 70 μs in the 3D simulation, whereas a similar structure is formed only at t = 235 μs in the 2D simulation. Besides, a mode change is observed in the 3D results instead of dynamically maintaining it as in the 2D results. A possible reason is that the 3D simulation has more fluctuations in the z-direction. As shown in Figure 5.22 and Figure 5.23, the non-uniform temperature distribution on the bottom wall also indicates the 3D influences.

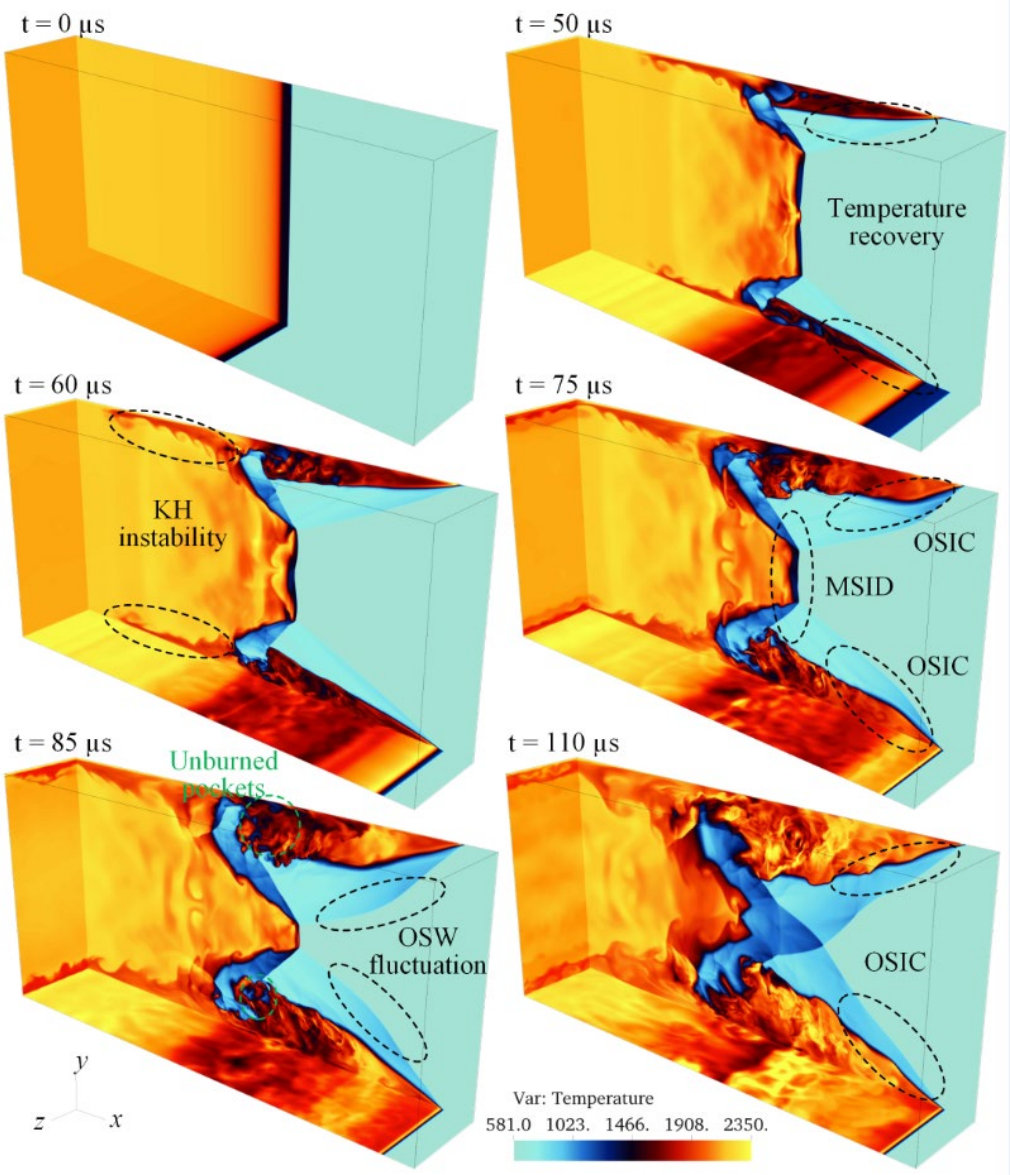

Figure 5.22 Slices of pseudo-colour image of the temperature at different times.

Figure 5.24 compares the experimental schlieren images with our simulations. In the OSIC/MSID mode, the Mach stem (MS) couples with following the reaction front (RF) in the middle of the channel. The slip lines behind the triple points develop into unstable shear layers (SS) downstream due to the KH instability. The turbulent boundary layers (TBL) interact with the MSID and result in the recirculation zone. In the OSIC mode, the Mach stem disappears and the reaction zones (RZ) are expanded. The main difference between the experiments and the present simulation is that the mode transition is observed from an OSIC/MSID mode to an OSIC mode in simulation, while in the

experiments, the mode transition occurs when the equivalence ratio varies slightly. However, the real 3D effects on this problem need to be studied by adopting the non-slip wall boundary conditions on both the front and back sides [220]. In addition, the temperature of the wall also plays an influential role in the OSIC. These factors are beyond the scope of this work and require further study.

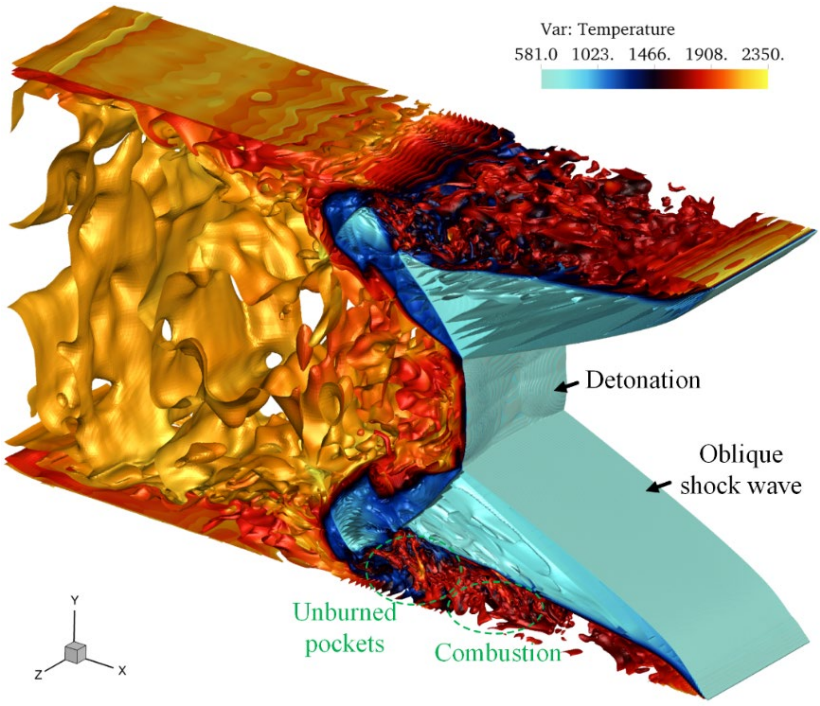

Figure 5.23 Pseudo-colour image of the temperature based on the iso-surfaces of the density at t = 70 μs for the OSIC/MSID structure.

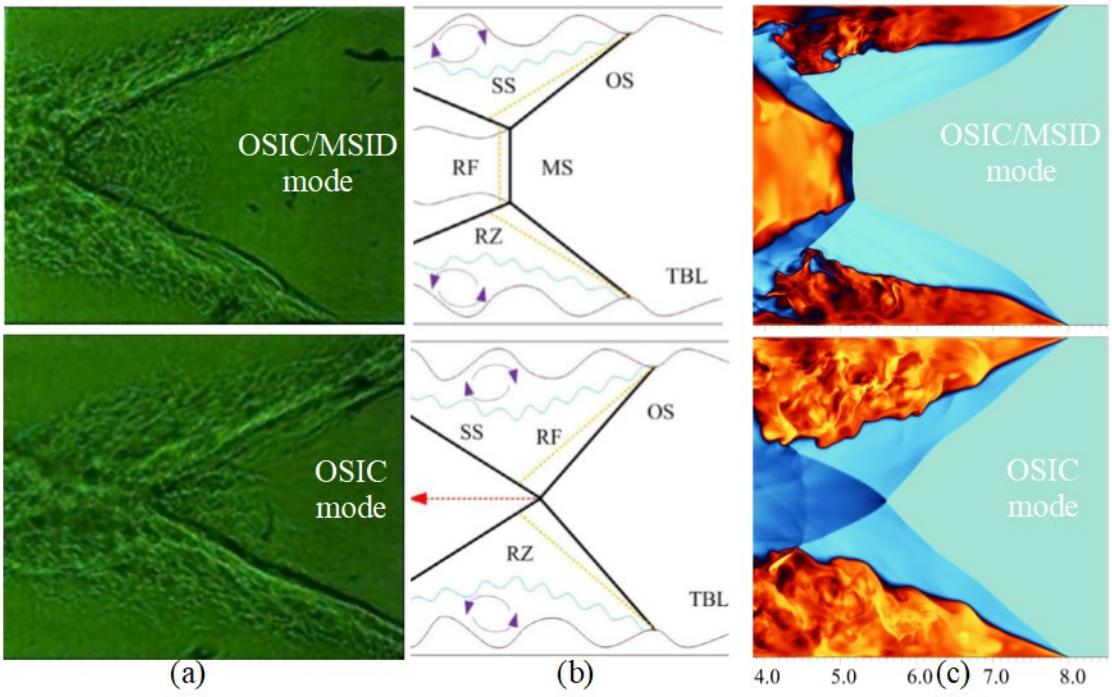

Figure 5.24 Comparison of front structure, (a) experimental schlieren [31], (b) schematic of structure [31], and (c) present numerical temperature fields.

5.6 Chapter summary

In this chapter, the solver was first used to simulate unsteady shock-induced combustion. The physically oscillating reaction fronts were dynamically captured by the adaptive curvilinear meshes. The numerical frequencies of oscillations were in good agreement with those in experiments. The 2D cellular detonation structure was then simulated and reported a similar detonation cell size to the predicted value. The 3D detonation structure was studied in a pipe bend and a round pipe, respectively. The decoupling of detonation in the bend was compared to experimental results. The 3D cellular structure was also analysed. Besides, the solver was adopted to study the 3D detonation wave/boundary layer interaction problem. The simulation qualitatively reproduced the different wave patterns observed in experiments. The simulations in this chapter were conducted to demonstrate the robustness and capability of the present solver in handling high-speed reacting flows, especially large-scale 3D detonation. In the following chapters, the solver is applied to specific rotating detonation simulations.

Chapter 6 Numerical configurations of RDE

The two types of RDE experimental configurations are introduced in this chapter. The numerical set-ups and the simplified numerical model are also provided. The impact of the mesh resolution on RDE simulations is then tested via a mesh dependence analysis. To evaluate the accuracy of the simplified model, the numerical solutions are compared with the experiment results. The workload balance and scalabilities of the present solver are tested at the end of this chapter.

6.1 Ethylene/oxygen RDE

The ethylene RDE at the University of Southampton (UoS) [222] is simulated as a first realistic configuration. As shown in Figure 6.1, the outside diameter of the chamber is fixed at d = 75 mm. A modular design with multiple inserts allows for inner chamber heights ranging from 35 to 50 mm and chamber widths ranging from 0.7 to 1.2 mm. In accordance with the modular strategy, injector plates with 30, 45, or 60 orifice injectors have been produced, each with a 0.5 mm orifice diameter.

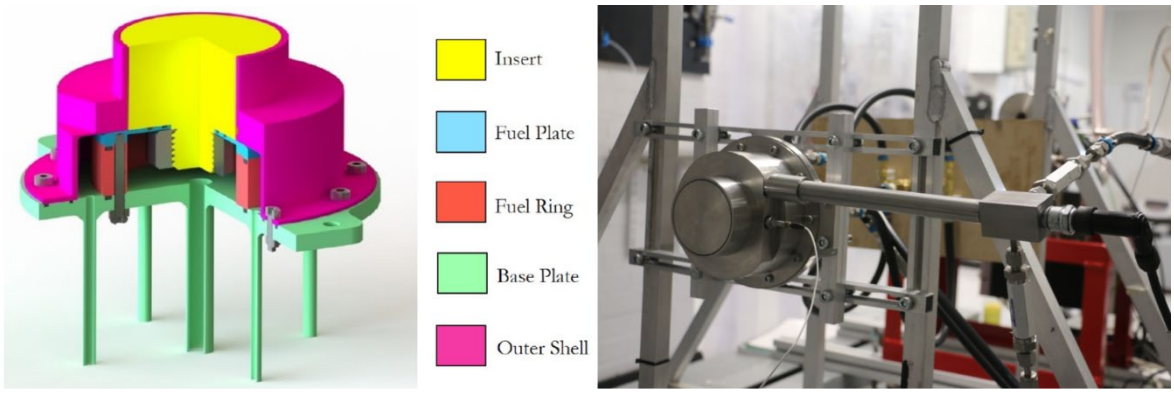

Figure 6.1 Schematic and photograph of the UoS RDE [222].

The ethylene plenum is filled by a single central pipe, and the oxygen plenum is filled by four pipes that are evenly spaced around the baseplate. The volumetric flow rates for oxygen and ethylene can be determined for each injector-oxygen slit chamber arrangement with a specified equivalence ratio, and the required mass flow rates can subsequently be estimated from the appropriate injector area. The mass flow in the experiment is controlled through the injection pressure, and checked by the application of digital mass flow meters. The UoS RDE has a small geometry, which results in a lower computational cost and enables batch calculations within a reasonable amount of time. Hence, this geometry is initially employed for both 2D and 3D premixed calculations.

6.1.1 2D unwrapped plane

A typical 2D unwrapped model for the UoS RDE is introduced first with some simplifications (see Figure 6.2). The length of the unwrapped domain is 236 mm, which corresponds to an annulus

chamber with a diameter of 75 mm. The left and right sides are periodic boundaries to simulate the detonation propagation in an annular chamber. The top side is set as a supersonic outflow boundary condition, where the physical variables are extrapolated from the inner domain. The premixed ethylene/oxygen mixtures are injected from 2 mm wide slots on the bottom that are spaced 2 mm apart. The axial velocity, static pressure and temperature of the inflow are prescribed in the ghost cells. The total number of the injectors is 59, which is also close to the experimental value of 60. The multi-component 2D Euler equations are solved as governing equations. The Roe/HLL scheme is employed in this case. A reduced ethylene/oxygen reaction mechanism [223] is used for the ethylene RDE, which contains 10 species and 10 reactions. Nitrogen is considered an inert gas and nitrogen chemistry is neglected.

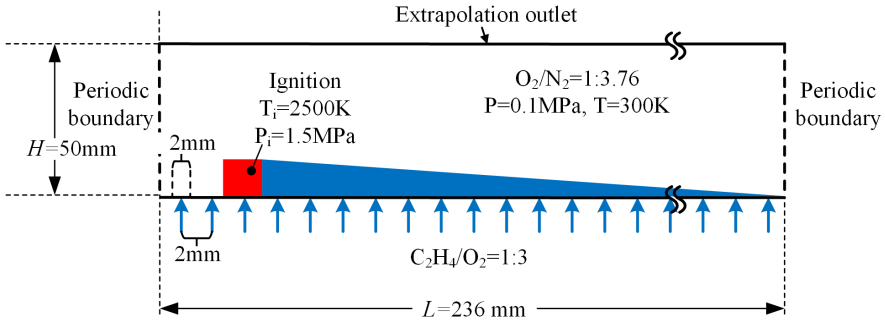

Figure 6.2 Configurations of 2D ethylene RDE simulations (E-2D-75).

The initial pressure in the whole domain is set as 0.1 MPa and the temperature is 300 K. A small region of [10 mm, 20 mm] × [0, 10 mm] is initialized by setting the pressure to 1.5 MPa and temperature to 2500 K in order to ignite the detonation directly. A triangular region, filled with a stoichiometric ethylene-oxygen mixture, is used to sustain the propagation of the detonation in the first cycle. Otherwise, the chamber is filled with pure air to prevent the high-temperature burned gas from inducing detonation in the reverse direction. This baseline configuration is named E-2D-75, where the E indicates the fuel is ethylene, 2D denotes the simulating dimensions, and 75 is the estimated outer diameter of the RDE at a unit of millimetres. A similar naming rule is used in the introduction of following cases.

Some studies report that the initiation of detonation in RDE does not change the number of waves, namely the steady state is independent of the initial set-up, whereas some recent studies [224,225] show the dependence on initiation. The study on the mechanism of the detonation multiplicity and rotating direction is still ongoing. Hence, only one single detonation wave is initiated along one direction in all cases in this thesis to exclude the effects of the initial conditions. The detonation velocity is a vital parameter in the RDE simulations, which is calculated by the flow velocity and the injection velocity, as illustrated in Figure 6.3. The average flow velocity is computed by the frequency of pressure profiles using the FFT method.

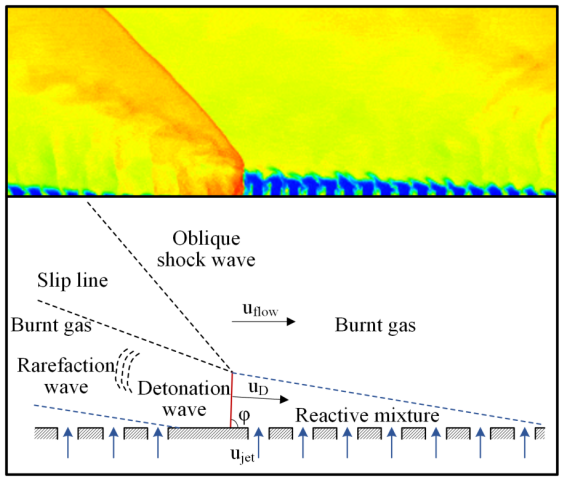

Figure 6.3 Schematic diagram of a rotating detonation wave structure.

6.1.2 3D annulus

In addition to the 2D unwrapped model, a 3D annular model is constructed as shown in Figure 6.4. A cylindrical mapping is used to generate the domain of the annular chamber as shown in Equation (A.10). For the 3D case, a stoichiometric ethylene-oxygen mixture with 20% nitrogen dilution is injected from equally distributed 2mm wide slots on the head plane. Nitrogen is considered an inert gas. A layer of stoichiometric ethylene-oxygen-nitrogen mixture is initialised with a height of 10 mm. Patches of pure nitrogen and 1D ZND solutions of the mixture are used to artificially generate a single stable detonation wave in the first cycle. A velocity inlet is used for the injection and the top side is set as an extrapolation outflow boundary condition. Other boundaries are considered adiabatic slip walls. The refinement indicator threshold value for density is 0.2 kg/m^3. The CFL number in this case is set to 0.8. Similarly, this case is named as E-3D-75.

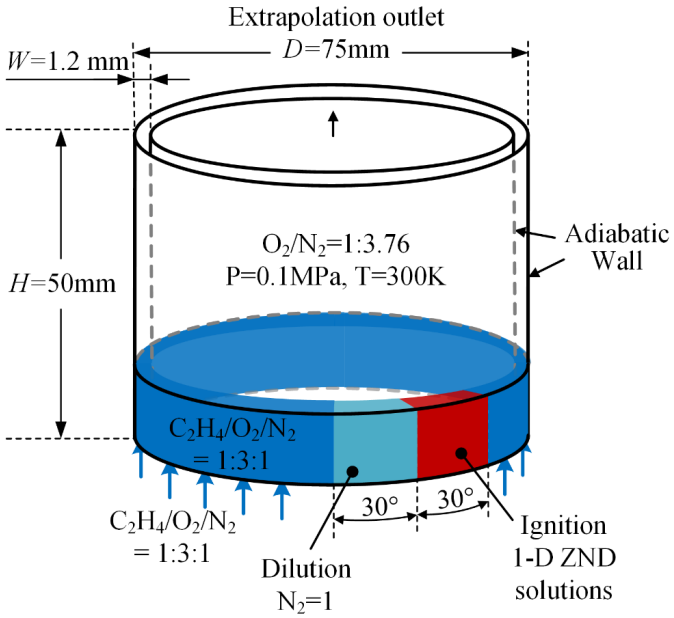

Figure 6.4 Configurations of 3D ethylene RDE simulations (E-3D-75).

6.1.3 Mesh dependency study

For the 2D ethylene RDE simulations (E-2D-75), three types of meshes are tested to simulate the stand-off detonation wave at 0.1 MPa and 300 K. The refinement factor is 2 for each level. The minimum mesh size is 0.0625 mm, 0.03125 mm and 0.015625 mm with 3, 4 and 5 refinement level, respectively. As shown in Figure 6.5, the detonation wave is located virtually at the same position when the mesh is refined. The temperature profiles are also convergent. Although a higher pressure peak can be obtained by increasing the mesh refinement level up to 5, the four-level refinement with a resolution of 0.03125 mm is considered a good trade-off between computational accuracy and cost.

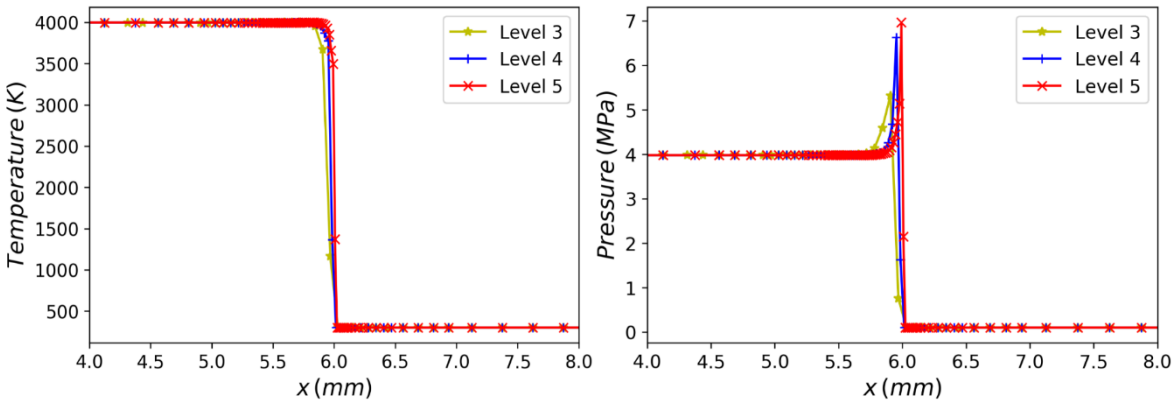

Figure 6.5 1D temperature and pressure profiles of ethylene/oxygen detonation front.

For the 3D ethylene RDE simulations (E-3D-75), a similar mesh resolution is challenging to achieve with current computational resources. Different coarse meshes are tested to study the effects of mesh resolution on 3D RDE simulations. The diluted mixture is injected at 300 K and 0.2 MPa. The inflow velocity is given as 200 m/s in this case. The average inlet mass flow rate is computed as 42.1 g/s. As shown in Figure 6.6, the ethylene RDE is simulated on three different mesh sizes with AMR and without AMR. The coarsest mesh gives three detonation waves at the end of the calculation, while the other three cases only have two waves. This means that using an insufficient mesh resolution may influence the number of waves in the 3D simulations.

The finest adaptive computation uses approximately 11.6 M to 12.3 M instead of 94.4 M cells in the uniform case. This calculation is performed on 480 cores (Intel Xeon E5-2670 2.0GHz). Typical run times for a simulated time of 1 ms were approximately 11 days wall clock time. The medium case uses a mesh at the size of 0.1 mm. The C-J velocity is computed based on the mixture state (0.2 MPa and 300 K). The difference in detonation velocity is small between the medium cases and the finest one. As shown in Table 6.1, the number of cells can be decreased by 76%, and the computational cost is reduced by 60% when using AMR. The mesh size of 0.1 mm is used in the following E-3D-75 cases considering the balance of computing accuracy and costs. The calculations are performed on 120 cores. Typical run times for a simulated time of 1 ms were approximately 4 to 5 days wall clock time.

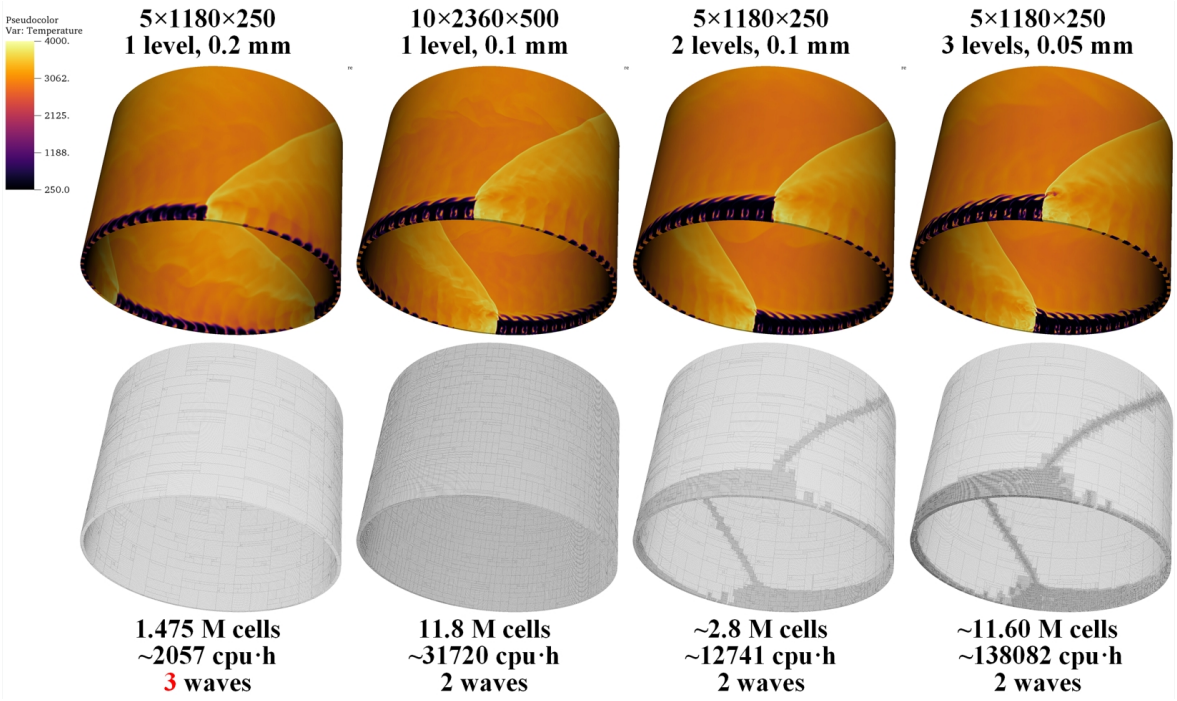

Figure 6.6 Pseudo-colour images of temperature and meshes of 3D RDEs (E-3D-75).

Table 6.1 The ethylene detonation velocity within different mesh resolution (E-3D-75).

Refinement level	Δ_{min} (mm)	Number of cells (M)	Run time (cpu·h)	Detonation velocity (m/s)	Theoretical C-J velocity (m/s)	$\%D_{C\text{-}J}$
1	0.2	1.475	2057	2175.42	2299.36	94.61%
1	0.1	11.8	31720	2187.38		95.13%
2	0.1	~2.8	12741	2179.52		94.79%
3	0.05	~11.6	138082	2189.41		95.22%

6.1.4 RDE initiation

To demonstrate the initiation process under the present configurations, a premixed ethylene RDE (E-2D-75) is tested with different inlet static pressure. The inflow pressure is given as 0.2 MPa and the temperature is 300K. The injection velocity is set to 200 m/s. The base cell size in the 2D calculations is 0.25 mm. The maximal refinement level is set to 4 with a uniform refinement factor of 2 on each level. The respective minimum cell size is 0.03125 mm in every direction. The refinement indicator threshold values for density and pressure are 0.1 kg/m^3 and 50 kPa, respectively. The CFL number in this case is set to 0.9.

Figure 6.7 shows the formation of two detonation waves in the chamber. A cycle is defined as the period of a detonation successfully propagating from the left boundary to the right boundary. In the

first two cycles after the ignition, only one detonation wave forms and travels in one direction. In the third cycle, self-ignition occurs behind the first detonation wave. The second ignition source finally develops into the second detonation wave in the chamber. After 6 to 7 cycles, a stable two-wave mode is observed. The average inlet mass flow rate per unit length is 30.6 kg/(m·s) in this case. To estimate the inlet area for the mass flow rate in the 2D simulation, the injection length perpendicular to the view plane is defined as 1.2 mm according to the experimental set-up. As a result, the mass flow rate is estimated to be 36.7 g/s under this condition.

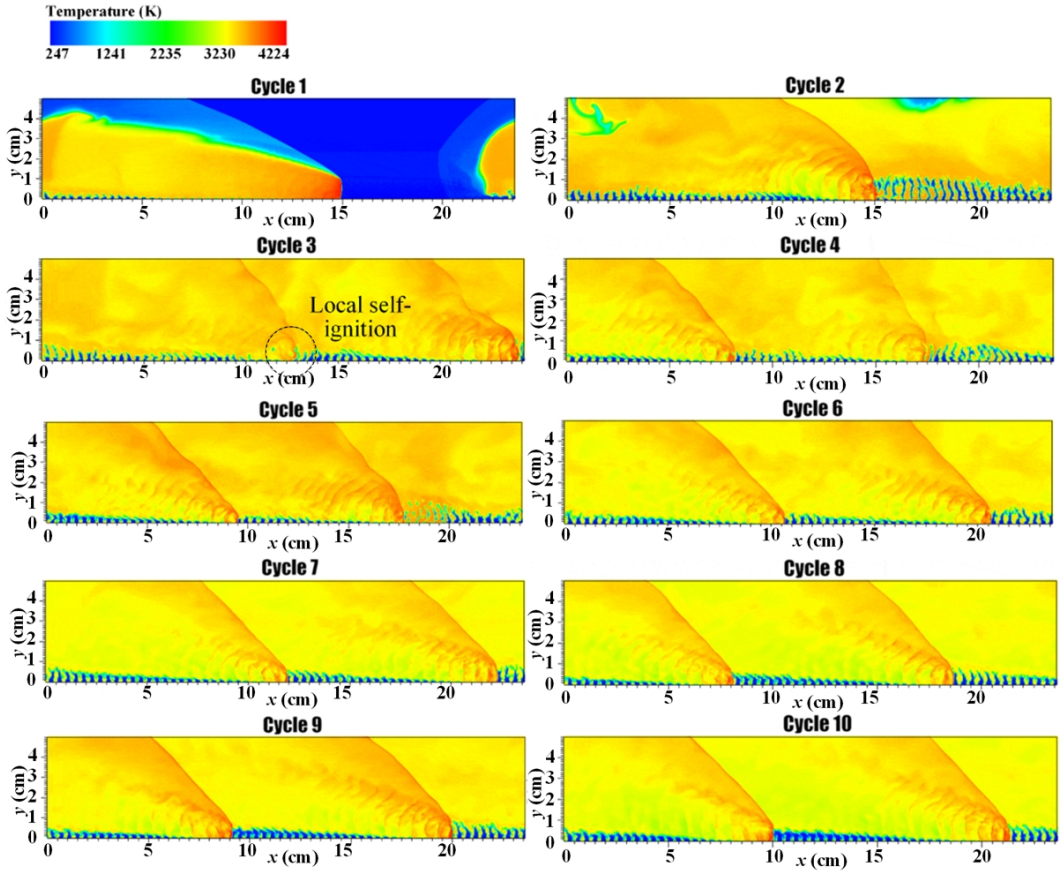

Figure 6.7 A stable double-wave mode in the 2D unwrapped RDE (E-2D-75) with the inlet mass flow rate at 36.7 g/s.

Some probes are also placed to monitor the pressure variations in the chamber. Figure 6.8 shows the pressure history of different locations. The numbers in the figure legend indicate the coordinates of the probe locations (unit: mm). The height of the detonation wave is estimated from Figure 6.7, which ranges from 7.2 mm to 7.8 mm. Hence, the first three probes, at 2 mm from the bottom wall, measure the pressure of detonation waves, and the other three probes measure the pressure of oblique shock waves.

As shown in Figure 6.8 (a), the initial pressure peak can be up to 8 MPa, which is higher than the C-J pressure, 6.81 MPa, computed by Cantera [198]. It means that the detonation is overdriven and unstable at the initial stage. When the detonation propagates at a stable two-wave mode, the observed maximum pressure declines to 4 MPa. The average horizontal flow velocity is computed by

calculating the interval of the cycle from the frequency of the pressure history. In this case, the frequency of the pressure is 19.49 kHz using the FFT analysis, and the velocity is estimated as 2300 m/s.

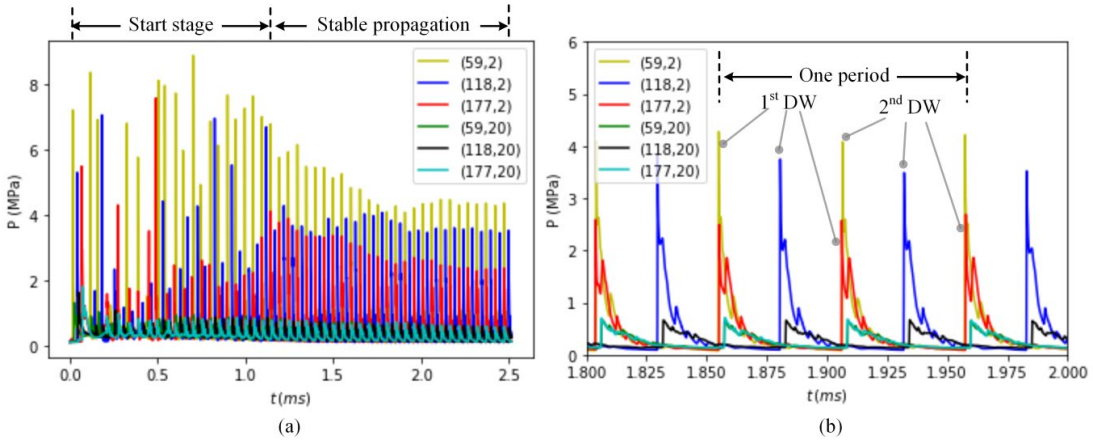

Figure 6.8 Static pressure records in the two-wave mode case (DW: detonation wave).

The position of the probes leads to the pressure peak variations in the chamber as illustrated in Figure 6.9. When the detonation wave propagates in a discontinuous mixture, the strength of detonation changes with the reactive mixture distribution. The detonation is strong on the central line of injectors and is weak on the central line of walls. The average peak pressure is also lower than the C-J pressure at the equilibrium state.

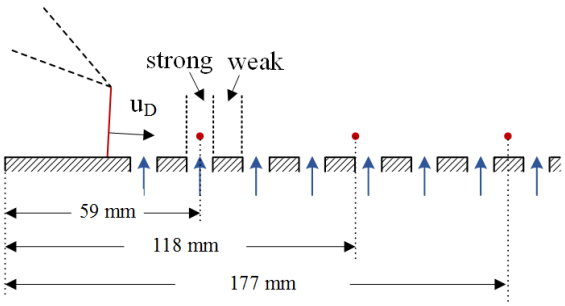

Figure 6.9 Schematic diagram of the probes at different circumferential locations.

When increasing the static pressure of the inflow mixture to 0.3 MPa, a three-wave mode is observed. The average inlet mass flow rate per unit length increases to 43.4 kg/(m·s), and the mass flow rate is estimated to be 52.1 g/s in this case. Figure 6.10 shows the process of the three-wave mode in the 2D RDE simulation. The self-ignition is also observed as the source of the subsequent detonation wave. The higher static pressure of the mixture leads to a shorter induction time. As a result, the fresh mixture is ignited by the burnt gas at a lower injection height. If the circumferential distance between any two detonation waves is not enough long, the injected fresh reactants will be not enough to sustain the propagation of the detonation behind. The decay is shown in the cycle 5 of Figure 6.10. The three-wave mode temporarily degenerates into a two-wave mode. Then, a self-ignition is observed resulting in a new detonation wave. Finally, the three detonation waves propagate in a stable manner.

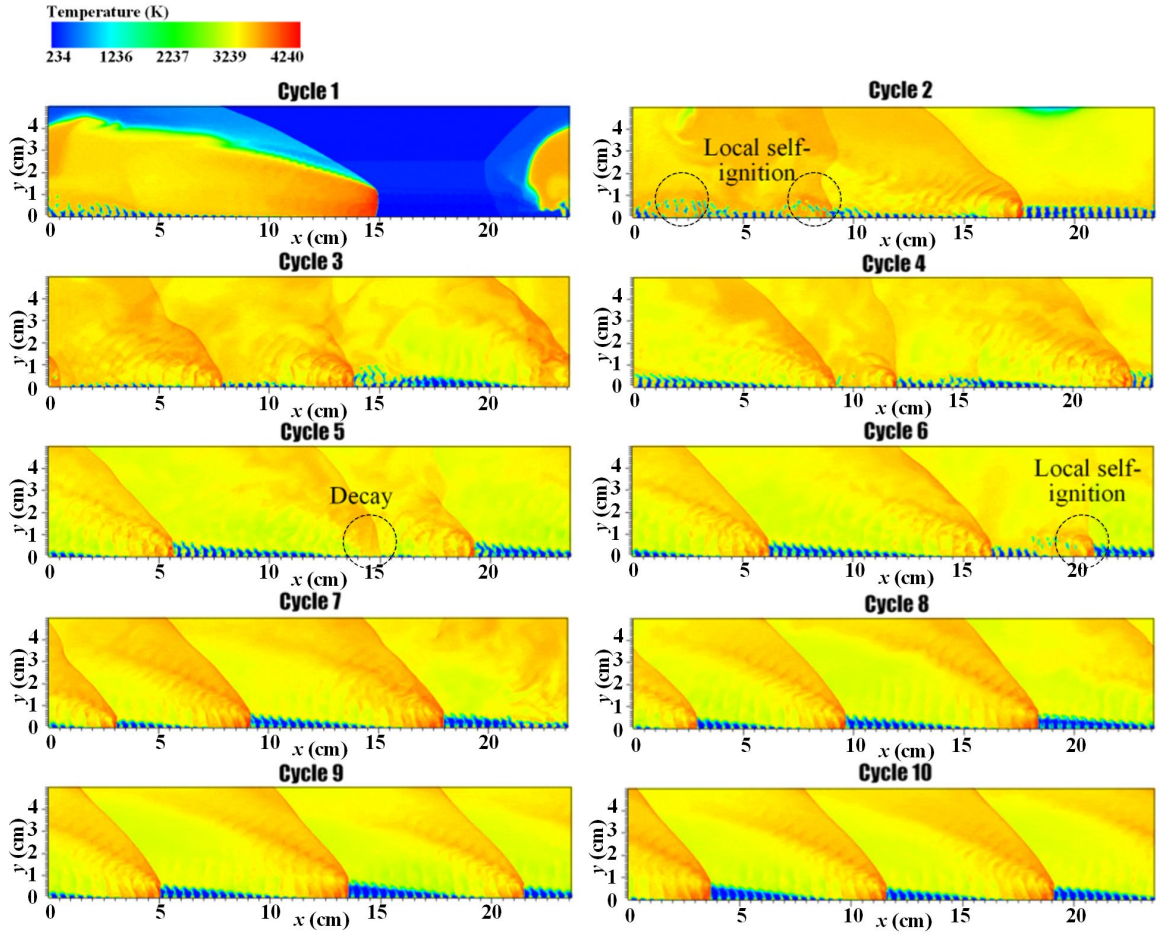

Figure 6.10 A stable three-wave mode in the 2D unwrapped RDE (E-2D-75) with the inlet mass flow rate at 52.1 g/s.

Figure 6.11 also shows an unstable start stage and a stable propagation stage in the pressure history. The same pressure declines are observed at different probes. In a similar way, the average flow velocity is computed as 2313.90 m/s. The inclination of detonation fronts is computed as 85.06°, and the corresponding detonation velocity is 2322.53 m/s.

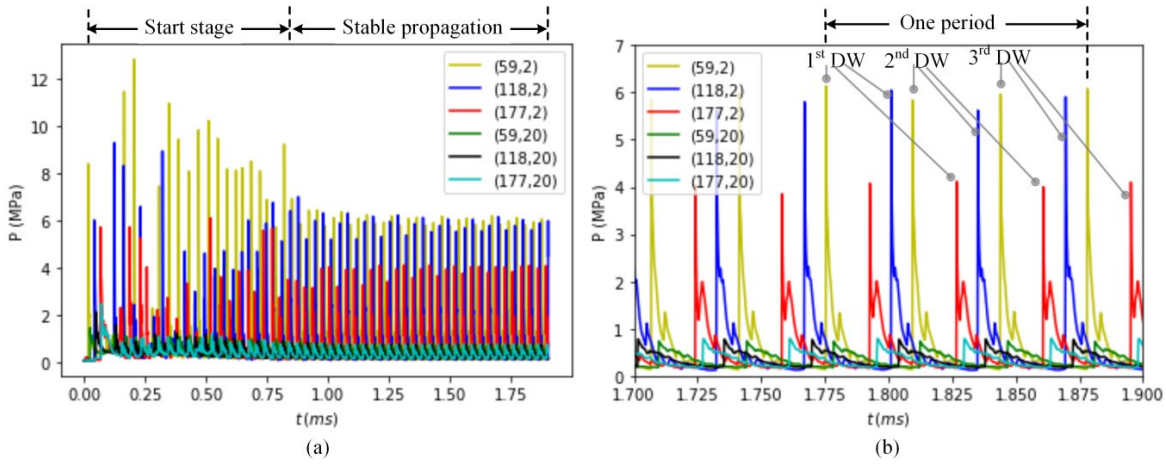

Figure 6.11 Static pressure records in the three-wave mode case (DW: detonation wave).

6.1.5 Comparison with experimental results

The detonation velocities under different mass flow rates are presented in Table 6.2. The mass flow rate is increased by increasing the injection pressure from 0.2 MPa to 0.3 MPa. There exists a difference in the detonation velocity deficit between the experiments and simulations. The deficit of detonation velocity is remarkable in the experiments with 26.5% or 37.8%. Similar velocity deficits ranging from 13% to 37% are also reported in some published RDE experiments [77,78,226,227], whereas the deficits in simulations are normally less than 15% [7,106,107,128]. There are many factors leading to the deficit of detonation velocity, such as the degree of mixing, the injection conditions and the boundary layer near the wall. The present inviscid simulation neglects those factors and estimates a detonation velocity that is close to the theoretical C-J velocity.

Table 6.2 Comparison of the detonation velocities (E-2D-75) between the experiment [222] and the present simulations.

Case	Mass flow rate (g/s)	Number of waves	Detonation velocity (m/s)	Theoretical C-J velocity (m/s)	$U_D/U_{C\text{-}J}$
Experiment	6.6	2	1770.00	2409.28	73.5%
2D Simulation	36.7	2	2308.68	2409.28	95.8%
3D Simulation with N_2 dilution	41.8	2	2179.52	2299.36	94.8%
Experiment	9.7	3	1510.00	2429.11	62.2%
2D Simulation	52.1	3	2322.53	2429.11	95.6%
3D Simulation with N_2 dilution	62.7	3	2219.84	2317.40	95.8%

Another apparent difference is that the experimental RDE operates at a low mass flow rate, whereas the simulations can only run at a relatively high mass flow rate. It should be pointed out that nitrogen is used to increase the computational stability in the 3D simulations. The dilution of 20% nitrogen in 3D simulation leads to the discrepancy in detonation velocities and mass flow rates. It is therefore difficult to make a quantitative comparison with the experimental results. However, some qualitative results are comparable.

Figure 6.12 displays the images of a comparison between the 3D numerical result and the micro ethylene/oxygen RDE experiments. The high-speed camera photographs also show the two-wave mode and three-wave mode at different inlet mass flow rates. The number of detonation waves increases at a higher mass flow rate, which is observed in both the experiments and simulations.

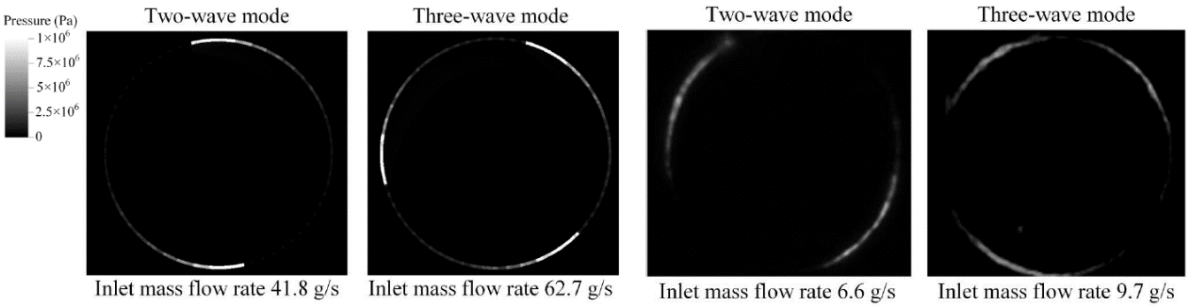

Figure 6.12 Photograph of 3D simulation (E-3D-75) result (left), and high-speed (right) from the outlet view.

When the mass flow rate is reduced to match the experimental value, detonation is not sustained in both the 2D and 3D simulations. In this scenario, the injection plane is entirely choked by the high-pressure burned gases in the chamber as the inlet velocity is relatively low. Despite that using small-scale geometry reduces the computational cost, the effects of wall fraction and heat loss become more obvious. The small mass flow rate brings uncertainties in the experimental mixing and detonation performance. As a result, it is challenging to ensure the operability of an ethylene/oxygen RDE at such low mass flow rates in the present simulations. As an alternative, subsequent simulations are conducted in a large-scale RDE. Numerical configurations of hydrogen RDE are introduced in the next sections.

6.2 Hydrogen/air RDE

6.2.1 2D unwrapped plane

A typical 2D unwrapped model for the hydrogen RDE is introduced first as shown in Figure 6.13. The length of the unwrapped domain is 280 mm and the axial height is set to 100 mm according to the domain size used in Ref. [228]. Dispersed injectors are simulated instead of using continuous injection. The injection slot width is 2 mm and the interval between adjacent injectors is 2 mm, resulting in 70 discrete injectors in total. A detailed hydrogen mechanism [229] is adopted for the hydrogen RDE, which consists of 9 species and 23 reactions.

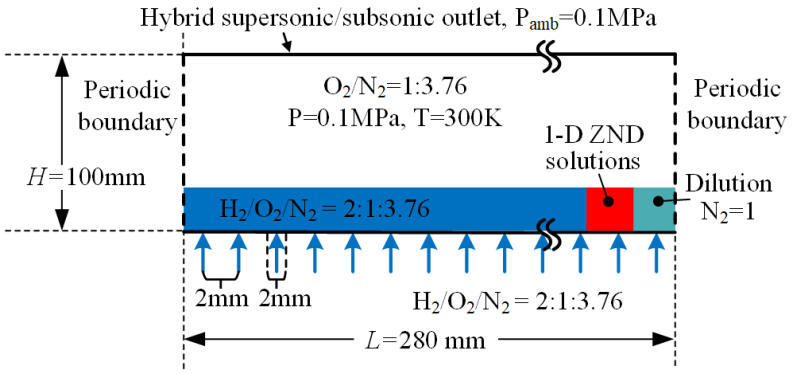

Figure 6.13 2D computational domain of the hydrogen RDE.

In the 2D unwrapped model, the domain is filled with air at 300 K and 0.1 MPa. A layer of stoichiometric hydrogen-air mixture is initialised from 0 to 280 mm with a height of 10 mm, which sustains the propagation of the detonation in the first cycle. A 10 mm × 10 mm patch of 1D ZND solutions is used to ignite the detonation. Another 10 mm × 10 mm patch of pure nitrogen is initialised adjacent to the ignition region to avoid the reverse propagation of detonation at the beginning. The alias for this baseline case is H-2D-89.

For the H-2D-89 unwrapped model, the left and right boundaries are periodic to simulate the circumferential detonation propagation. The top is set as a hybrid subsonic/supersonic outflow boundary condition, where the ambient pressure is 0.1 MPa. In this case, a pressure inlet is used, and the pressure P_w on the bottom wall is extrapolated from the interior domain as a reference pressure. A bottom boundary condition similar to Ref. [126] is chosen, where three situations are considered as follows:

Firstly, if $P_w > P_{jet}$, where P_{jet} is the stagnation pressure of injection, then the bottom boundary is blocked and considered as a reflecting wall.

Secondly, if $P_{cr} < P_w < P_{jet}$, where P_{cr} is the critical pressure defined as

$$P_{cr}=P_{jet}\left(\frac{2}{\gamma+1}\right)^{\frac{\gamma}{\gamma-1}}, \tag{6.1}$$

the pressure on the bottom boundary has $P = P_w$ and the inflow condition is subsonic. The normal velocity to the wall is derived as

$$v=\sqrt{\frac{2\gamma}{\gamma-1}\left[1-\left(\frac{P}{P_{jet}}\right)^{\frac{\gamma-1}{\gamma}}\right]}. \tag{6.2}$$

The temperature is updated by

$$T=T_{jet}\left(\frac{P}{P_{jet}}\right)^{\frac{\gamma-1}{\gamma}}, \tag{6.3}$$

where T_{jet} is the stagnation temperature of injection and the specific heat ratio γ in these equations is calculated by

$$\gamma=\frac{\mathrm{R_u}}{\bar{W}\bar{C}_p-\mathrm{R_u}}+1. \tag{6.4}$$

$\mathrm{R_u}$ is the universal ideal gas constant. The average specific heat at constant pressure $\bar{C}_p$ is dependent on the temperature and species of the mixture. The average molar mass of the mixture is calculated by

$$\bar{W} = \rho / \left(\sum_{i=1}^{Nsp} \frac{\rho_i Y_i}{W_i} \right). \tag{6.5}$$

Thirdly, if $P_w < P_{cr}$, the pressure on the bottom boundary is given as $P = P_{cr}$, and the inflow is injected with a sonic speed. The temperature can also be updated by Equation (6.3). The velocity normal to the wall is given by

$$v = \sqrt{\frac{2\gamma}{\gamma+1} \frac{R_u}{\bar{W}} T_{jet}}. \tag{6.6}$$

The implementation of this pressure boundary condition is conducted by adding the mass flux into the source term of the first layer interior mesh. In the present cases, the use of source terms is more numerically stable than prescribing the states in the ghost cells and then solving the Riemann problem on the interfaces. The stagnation pressure of injection is set to 0.4 MPa and the stagnation temperature is 300 K in the baseline case. The area ratio between walls and injectors is 0.5.

6.2.2 3D annulus

As discussed in Section 2.2, it is essential to be able to observe the detonation process in the channel. Most RDE experiments use a stainless steel chamber, which makes it difficult to observe the detailed flow structure inside. The experiment at AFRL (Air Force Research Laboratory) [77] uses both the optically and non-optically accessible RDE. For the optically accessible RDE, as shown in Figure 6.14, air is fed from a plenum into an annular detonation channel via a circumferential slot (123 mm in diameter). To alter the air injection area (3.46, 6.92, or 13.83 cm^2), the height of the air slot (0.89, 1.78, or 3.56 mm) is changed. A 134 mm-diameter circle, with holes uniformly placed around it, is located close to the inner edge of the annular detonation channel, and fuel is injected into it from a separate plenum through the holes.

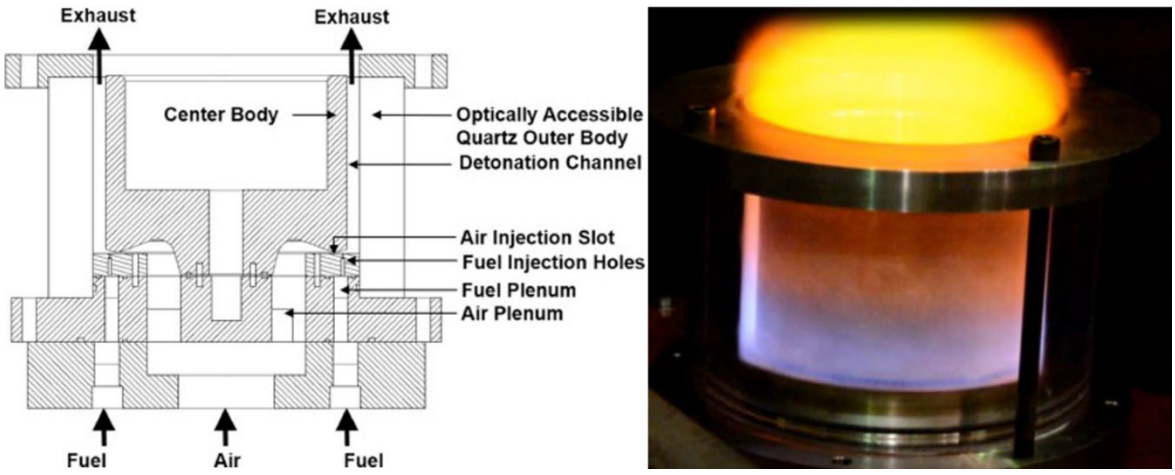

Figure 6.14 Schematic of the optically accessible AFRL rotating detonation engine [77].

The fuel injection area (0.48 or 0.75 cm^2) is altered by varying the fuel injection holes' diameter (0.71 or 0.89 mm) and number (120 or 80). The annular detonation channel has an inner and outer

diameter of 138.7 mm and 153.9 mm, respectively. This results in a 7.6 mm channel width. The annular detonation channel has a height of 101.6 mm. The outer body is a quartz tube that is 2.54 cm thick, allowing for optimal access to the annular detonation channel.

Figure 6.15 shows the schematic of the AFRL RDE. To simplify the computation, only a group of fixed geometry parameters is used. In addition, two similar injection schemes are tested. In simplified case 1, hydrogen and air are mixed before being injected into the chamber. The hydrogen and air plenums are replaced by using a specific inlet boundary condition applied to the wall. The de Laval nozzle is replaced by a nozzle with the same height of the throat. This simplified configuration fails in maintaining a continuous supply of mixture during operation. As a result, it is excluded in the following simulations.

In simplified case 2, hydrogen and air are injected using a jet in cross flow pattern. As the radial location of the air slot changes, the slot height is also varied for the same injection area. In the simulation, the air slot height is given as 1.6 mm instead of 1.5785 mm for simplification. This configuration successfully maintains the injection of both the fuel and oxidiser, resulting in continuous rotating detonation waves. Hence, the jet in cross flow pattern is used in the following 3D hydrogen RDE simulations.

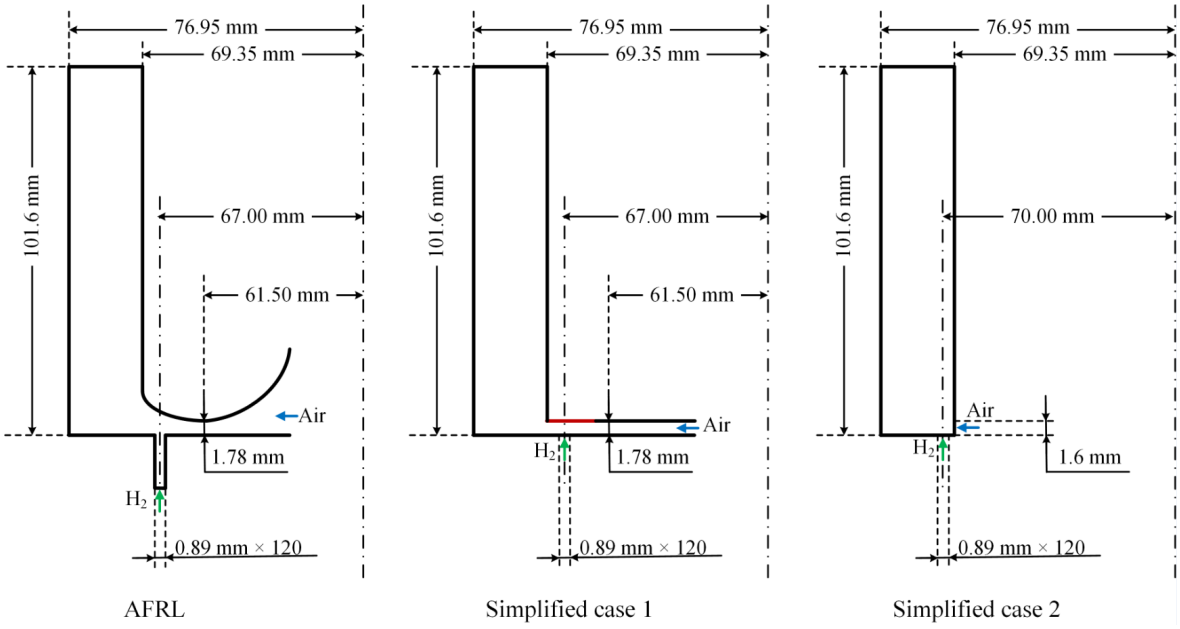

Figure 6.15 Schematic of the different injection schemes for the hydrogen RDE.

The 3D computational domain of hydrogen RDE is shown in Figure 6.16. The chamber is filled with air at atmospheric pressure and at a temperature of 295 K. The presence of nitrogen is assumed as inert and its chemical reactions are neglected. A layer of stoichiometric hydrogen-air mixture is initialised with a height of 10 mm. Patches of pure nitrogen and 1D ZND solutions are used to artificially generate a single stable detonation wave in the first cycle. Similarly, nitrogen is used to prevent the initial burned gas from inducing detonation in the reverse direction, which may occur in realistic ignition scenarios but is not considered in the present work.

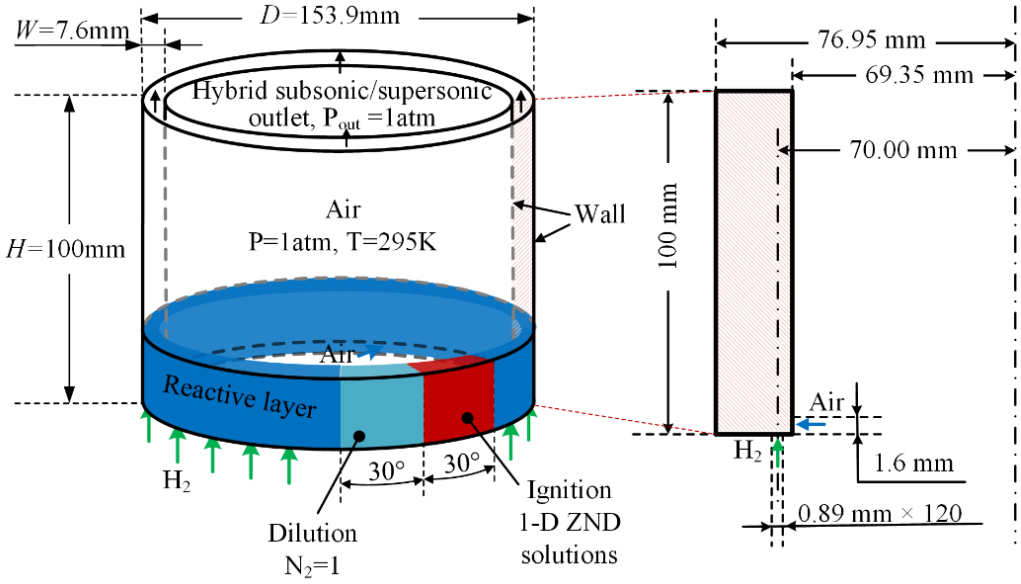

Figure 6.16 Computational domain of the hydrogen/air annular RDE model.

Fuel is injected from the head plane through 120 holes with a diameter of 0.89 mm, and air is injected through a 1.6 mm tall slit on the inner wall. A mass flow rate inlet is used for the injection. The 3D annular model's top side is set as a hybrid subsonic/supersonic outflow with atmospheric pressure as ambient pressure. Outflow variables are extrapolated if the local Mach number is greater than 1, otherwise a subsonic outlet is set based on ambient pressure. The mass flow inlet is used for both the hydrogen injection holes and the air slit. Other boundaries are considered slip walls, for which either adiabatic wall or isothermal wall boundary conditions are applied in various cases. This baseline configuration is named H-3D-154.

6.2.3 Mesh dependency study

In order to evaluate the required mesh size for hydrogen RDE simulations, different refinement levels are adopted with the same initial base mesh. In the 2D hydrogen RDE simulations (H-2D-89), all refinement factors are 2 and the respective mesh size is shown in Table 6.3. The detonation velocity is also calculated on different meshes. Table 6.3 gives a comparison between the theoretical C-J velocity and the numerical results. The C-J velocity is computed based on the mixture state (50 kPa and 300 K) ahead of the detonation. A small velocity deficit (up to 6.4%) is observed in all the cases. It has also been reported that the detonation velocity deficit is around 5% in hydrogen premixed simulations [7].

Figure 6.17 shows temperature and respective refinement level distribution on different meshes in the steady state. As shown in this figure, the slip line and continuous contact surface disappear when the mesh is refined. The use of a coarse mesh leads to more numerical mixing for the injection. The detonation propagates in a relatively uniform mixture, yielding an ideal rotating detonation structure. As a result, the detonation velocity deficit is the smallest in the coarsest case. When a finer mesh is

used, the burned gas in the mixture layer is captured and the cellular structure of detonation is observed. The non-uniform mixture layer yields a non-ideal detonation and unburned jets behind the detonation. The vortex-like structures on the contact surface also vanish. Instead, some unburned pockets exist in the products due to the uncompleted reactions. The results also show that the main features in the flow field, i.e., the detonation wave, the oblique shock and the mixture layer, are all dynamically captured by the finest meshes.

Table 6.3 The hydrogen detonation velocity within different mesh resolution (H-2D-89).

Refinement level	Δ_{min} (mm)	Number of cells (M)	Run time (cpu·h)	Detonation velocity (m/s)	Theoretical C-J velocity (m/s)	$\%D_{C\text{-}J}$
1	0.2	0.7	285.5	1877.46	1959.44	95.82%
2	0.1	~1.09	744.5	1854.04		94.62%
3	0.05	~2.19	4105.7	1852.65		94.55%
4	0.025	~4.07	7636.4	1853.55		94.60%

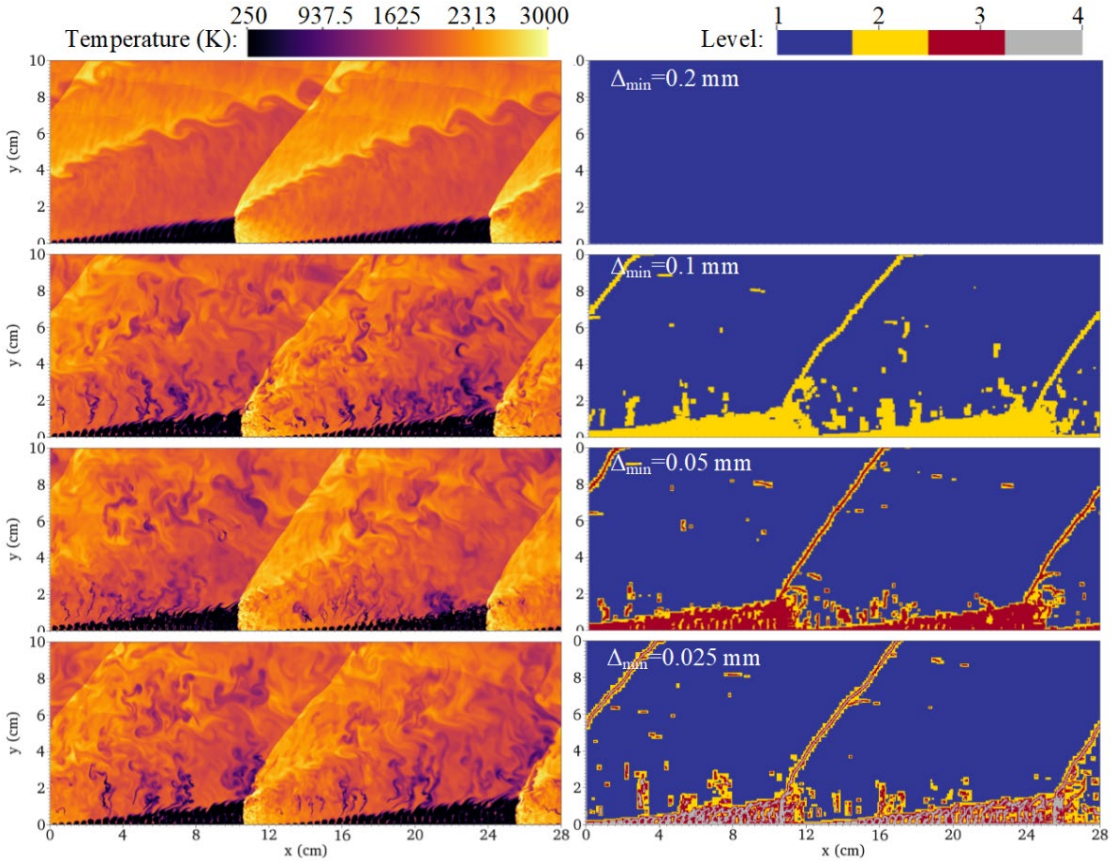

Figure 6.17 Pseudo-colour images of temperature and refinement levels of 2D premixed hydrogen RDEs (H-2D-89).

Three different meshes are tested in the 3D case (H-3D-154) to study the effects of mesh dependency as presented in Figure 6.18. The mass flow rates of hydrogen and air are given as 9.3 g/s and 320 g/s,

respectively. The slip adiabatic wall boundary condition is adopted in this case. The base mesh consists of 20 × 580 × 250 cells, and the first four cells near the walls are always flagged to be refined. The refinement criteria are given in terms of the temperature, density and pressure scaled gradient: ε_T = 500 K, ε_ρ = 0.15 kg/m^3 and ε_p = 50 kPa. The results demonstrate that the number of waves is independent of the chosen mesh. Table 6.4 shows the cell count, typical run times for 1 ms operation time, and the detonation velocity comparison in these cases. The detonation velocity is computed on the inner wall through the operation frequency. The results show that the difference in the ratio of detonation velocity to the C-J velocity is within 1% when the mesh is refined. The velocity deficit is 11.4%, 8.7% and 8.1% in these cases, respectively. Despite variations in the flow field when the cell is refined, the two-level mesh is considered a suitable balance between computational accuracy and cost. Hence, the following simulations based on H-3D-154 are conducted using this two-level mesh.

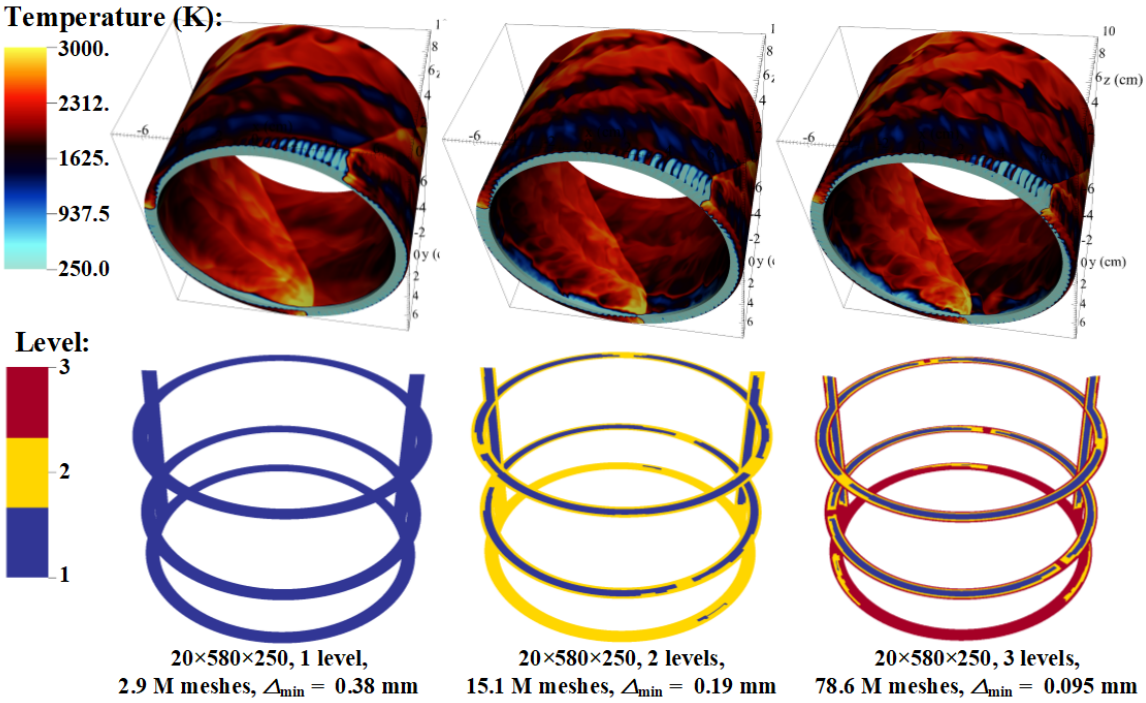

Figure 6.18 Pseudo-colour images of temperature and refinement levels of 3D non-premixed hydrogen RDEs (H-3D-154).

Table 6.4 The hydrogen detonation velocity within different mesh resolution (H-3D-154).

Refinement Level	Δ_{min} (mm)	Number of cells (M)	Run time (cpu·h)	Detonation velocity (m/s)	Theoretical C-J velocity (m/s)	$\%D_{C\text{-}J}$
1	0.38	2.9	4260	1751.67		88.6%
2	0.19	~15.1	27648	1803.96	1976.7	91.3%
3	0.095	~78.6	194246	1817.03		91.9%

6.2.4 Comparison with experimental results

Figure 6.19 shows a comparison of the mean static pressure distribution in published experiments [77], simulations [148] and the numerical results obtained by the present solver at different axial positions on the outer wall of the detonation channel. The numerical predictions are in good agreement with the experimental results at a relatively low mass flow rate. The present solver predicts a less fluctuating mean static pressure near the outlet. At the high mass flow rate, this discrepancy is mainly due to the injection simplification on the injectors. In experiments, a large pressure drop is observed in the chamber as an influence of the injector throat.

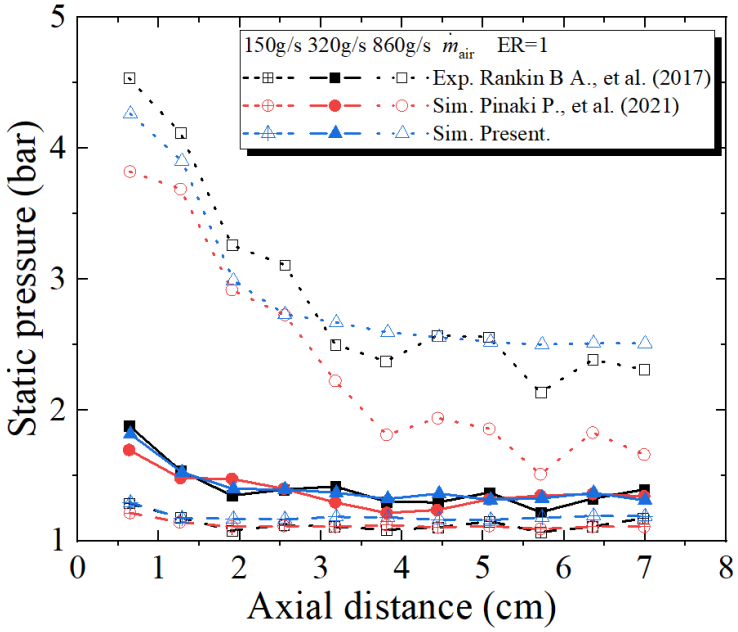

Figure 6.19 Comparison of measured and predicted mean axial static pressure distribution (H-3D-159).

Table 6.5 Comparison of the hydrogen detonation velocities (H-3D-159) between the experiment [77] and the present simulations.

Case	Air mass flow rate (g/s)	Number of detonation heads, n_{det}	Detonation head height H_{det}*n_{det} (cm)	Detonation velocity (m/s)	Theoretical C-J velocity (m/s)	$U_D/U_{C\text{-}J}$
Experiment	150	1	2.0-2.4	1370	1957.1	70.0%
Simulation	150	2	4.0-4.6	1615.72		82.6%
Experiment	320	1	3.8-4.0	1700	1976.7	86.0%
Simulation	320	3	4.5-5.1	1803.96		91.3%
Experiment	860	2	5.8-6.2	1690	1965.1	86.0%
Simulation	860	4	6.8-8.0	1647.09		83.8%

The respective detonation velocities are also compared as shown in Table 6.5. The detonation velocity is computed on the inner wall of the chamber. The simulation overestimates the detonation velocity over 12.6% and 5.3% of the C-J velocity at low mass flow rates, whereas it underestimates the velocity 2.2% at a high mass flow rate, indicating the errors of simulation are within a reasonable range compared to the experiments. The simulation overestimates the number of detonation heads under different mass flow rates. The number of heads increases with increasing mass flow rate in the simulation.

Several reasons can lead to this discrepancy between the experiment and the present simulation. One distinction arises from the simplification of the jet in cross flow configuration, which changes the local mixing near the injection plane. The local numerically enhanced mixing can lead to a bifurcation of detonation heads. Another possible explanation for the discrepancy is that the numerical initiation differs from the experimental ignition. The detonation diffraction at the pre-detonator exit is neglected. This may result in two counter-rotating detonation waves at the initial stage, consuming the mixture ahead of the detonation. Despite the discrepancy from several numerical simplifications, the number of heads is found to be independent of the chosen mesh resolution, and the pressure and detonation velocity are close to the experimental results at an air mass flow rate of 320 g/s. This configuration is regarded as an acceptable numerical set-up for further studies.

6.3 Detonation cellular structure in RDE

The numerical detonation cells are represented by the trajectories of triple points in the flow field. This is accomplished by monitoring the maximum pressure in the entire domain on the finest mesh. As presented in Section 5.2 and Section 5.3, a regular detonation cell is a closed “fish-scale” pattern formed between two triple point trajectories. Figure 6.20 shows the formed detonation cells in the 2D hydrogen RDE simulation (H-2D-89). The detonation cellular structures are irregular at various length scales due to the presence of mixture inhomogeneity ahead of the detonation, such as burned gases between the fresh mixture.

These structures may contain unburned pockets, leading to the formation of a large detonation cell. The heat release rate is also accumulated to show the intensity of reaction evolution. In the region where the maximum pressure is low and the cell size is large, the heat release is relatively slow.

In addition to the case with an injection stagnation pressure of 0.4 MPa, a simulation is conducted with a higher inlet pressure condition of 1 MPa. Other numerical set-ups remain unchanged. The simulation presented in this work shows three detonation heads in the high-pressure case as depicted in Figure 6.21. The cell size decreases near the injection plane due to triple point collisions [7]. The region between the reactant jets is characterized by relatively low pressure and a low heat release rate, in which the products exist, leading to a weakened detonation.

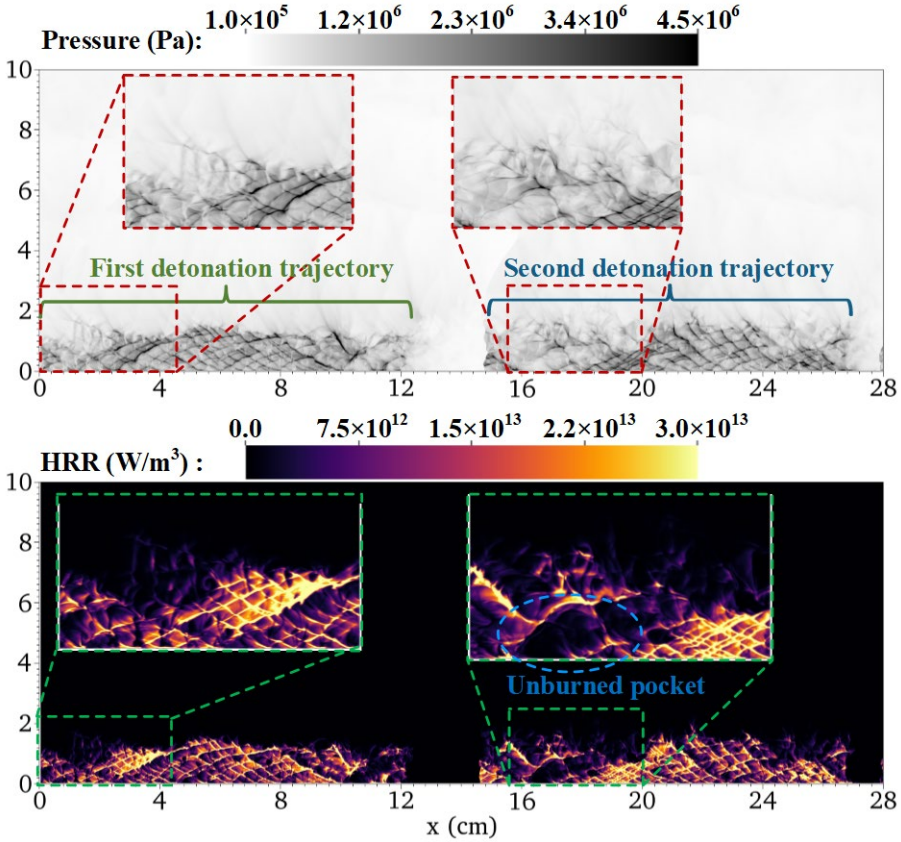

Figure 6.20 Trajectory of maximum pressure and heat release rate in 2D hydrogen RDE case (H-2D-89) with injection pressure at 0.4 MPa.

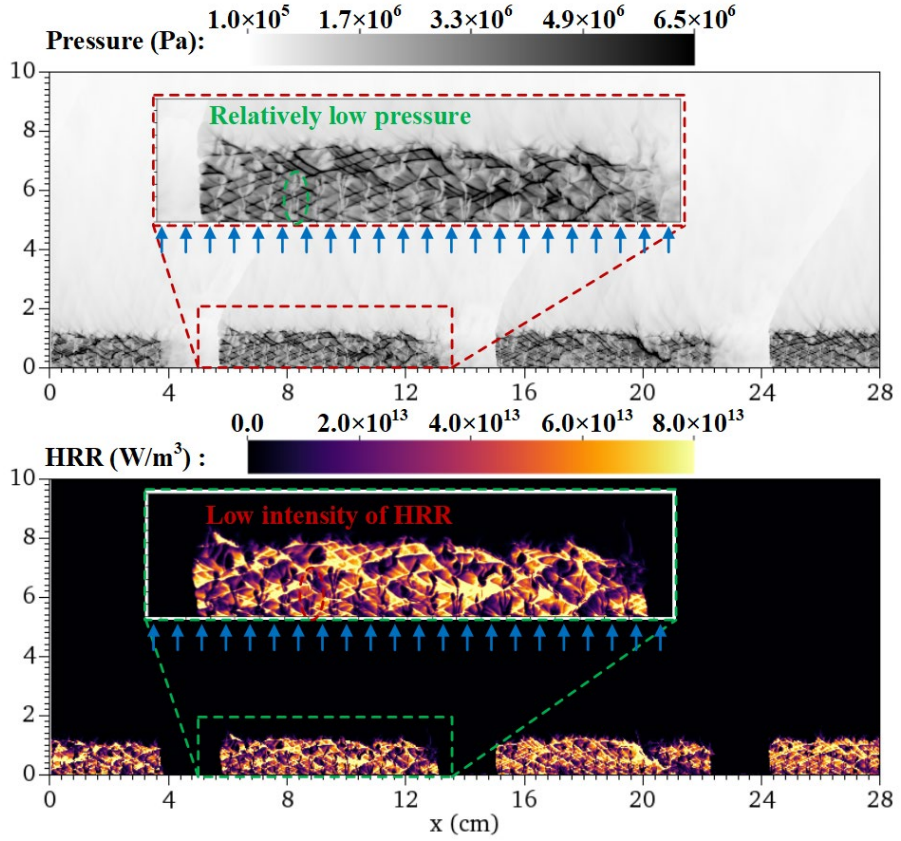

Figure 6.21 Trajectory of maximum pressure and heat release rate in 2D hydrogen RDE case (H-2D-89) with injection pressure at 1 MPa.

Figure 6.22 shows the distribution of accumulated maximum pressure and heat release rate over half of the detonation cycle. Discrete high-pressure regions are recorded, with corresponding high heat release rates. The heat release is found to be enhanced in jets of premixed reactants, with decay occurring in the region between these jets. The use of slip wall boundary conditions leads to the neglect of wall effects; hence, the cellular structure still remains on both the inner and outer surfaces.

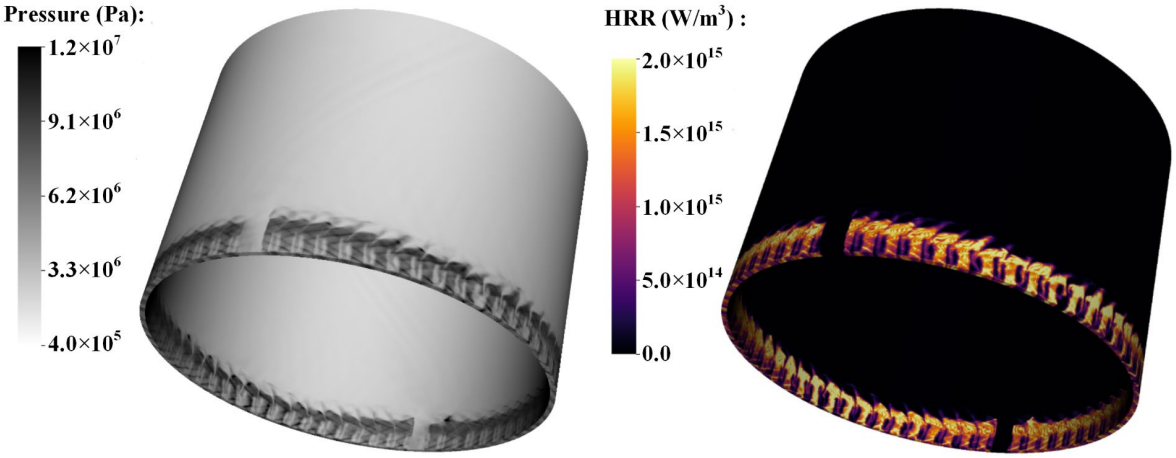

Figure 6.22 Trajectory of maximum pressure and heat release rate in 3D ethylene RDE case (E-3D-75) at a mass flow rate of 41.8 g/s.

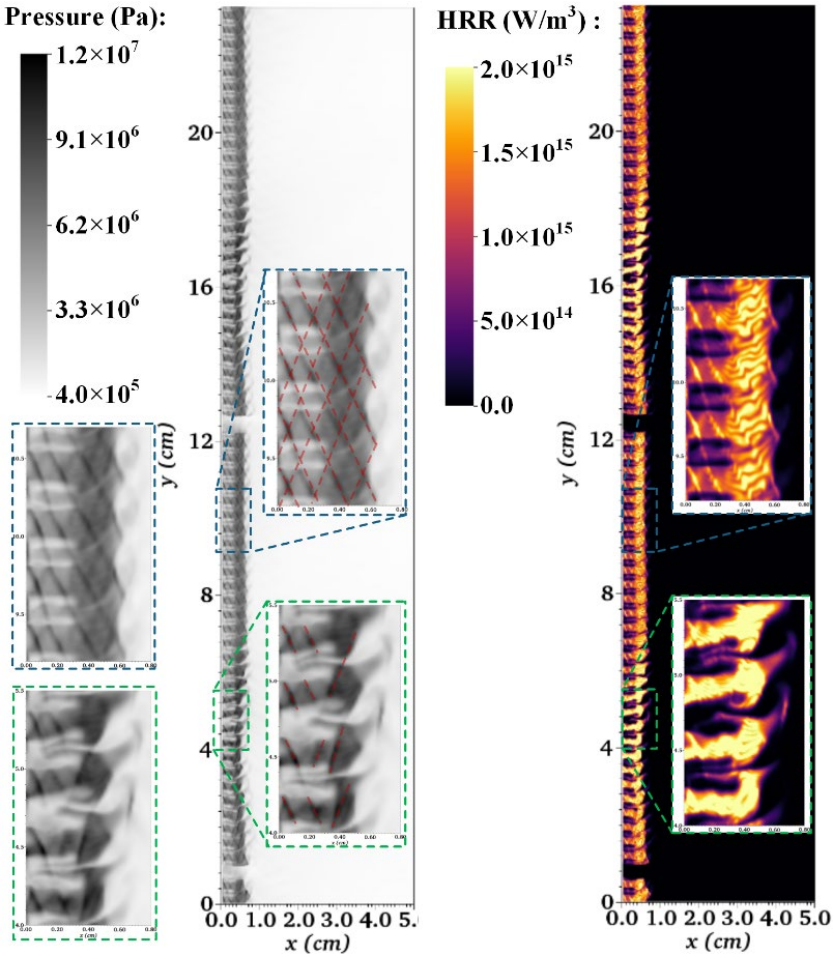

Figure 6.23 Unrolled slices of trajectory of the maximum pressure and heat release rate in 3D ethylene RDE case (E-3D-75).

Figure 6.23 demonstrates the unrolled plane in the middle of the channel. Two types of structures are captured during the detonation propagation process. The discrete injection leads to flow disturbances ahead of the detonation, and the mixing between the mixture jets and their interval determines the detonation strength locally. The reflected waves are enhanced in the region where the mixture exists. The detonation cell size is estimated at 1.5 mm. These numerical results offer a visual representation of the detonation wave structure. Weaker reflected waves are observed in regions where mixing is incomplete, which leads to the disappearance of the detonation cellular structure.

Despite the observation of detonation cellular structure, the detonation cells are not apparent even in the present 3D premixed simulation. It is challenging to resolve the 3D detonation cells of a highly reactive mixture at a high pressure, which requires an extremely fine mesh exceeding current computing power. There is no detonation cell observed in the present non-premixed simulations. This limitation is attributed to the discrete injection and the inadequate mesh resolution. As a result, the rotating detonation cells are not further discussed in this thesis.

6.4 RDE workload balancing and scaling test

In balanced parallel computing, workloads are distributed evenly among all processors in the whole process. This ensures that all processors are utilized to their maximum potential and no processor is idle while others are overloaded. To accomplish this objective, an appropriate partition is required at both the initiation and run time. When the base domain is initialized, the workload for the new grid hierarchy is estimated and projected onto the base level. Non-overlapping portions are then constructed until the work in each unit is homogeneous. Due to the frequent changes in workloads during RDE simulations, the workload and new tasks for each processor are recalculated at run time. The partition is refined based on the assigned workload at the specified redistribution frequency.

Figure 6.24 shows the processors distribution in the 2D hydrogen simulation. The mesh is adaptively refined on the fly in areas around detonation waves, oblique shock waves, and in the fresh mixture layer. More processors are utilized in regions where the workload is high and the mesh is refined to the highest level.

The density and processor distribution of the 3D annular ethylene RDE are displayed in Figure 6.25. From this figure, the mesh is adaptively refined at different times. Most processors are utilized in regions where the workload is high and the mesh has been refined to its highest level. The continuous redistribution, while the mesh is changing, ensures a balanced workload at run time.

Figure 6.26 shows the workload of the 2D hydrogen RDE simulation at different times. In the current solver, the imbalance is primarily due to the non-uniform computational cost of the chemical source terms on different meshes. To address this, processors are redistributed on the fly during the computing process, which helps mitigate the imbalance in computation as displayed in Figure 6.26.

As the simulation progresses, fewer processors are assigned workloads that deviate significantly from the ideal state, yielding a reduction of maximum waiting time to 5%. A similar result is observed in the 3D simulation as depicted in Figure 6.27. A more physically informed balancing strategy would be an improvement for present solvers.

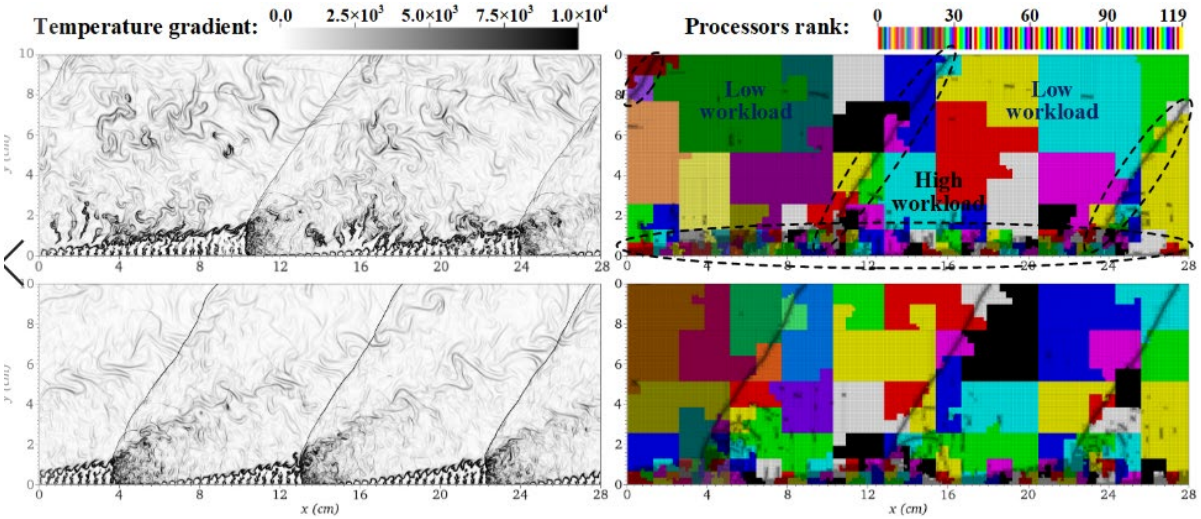

Figure 6.24 Processors distribution and temperature gradient contours of the 2D hydrogen RDE case (H-2D-89).

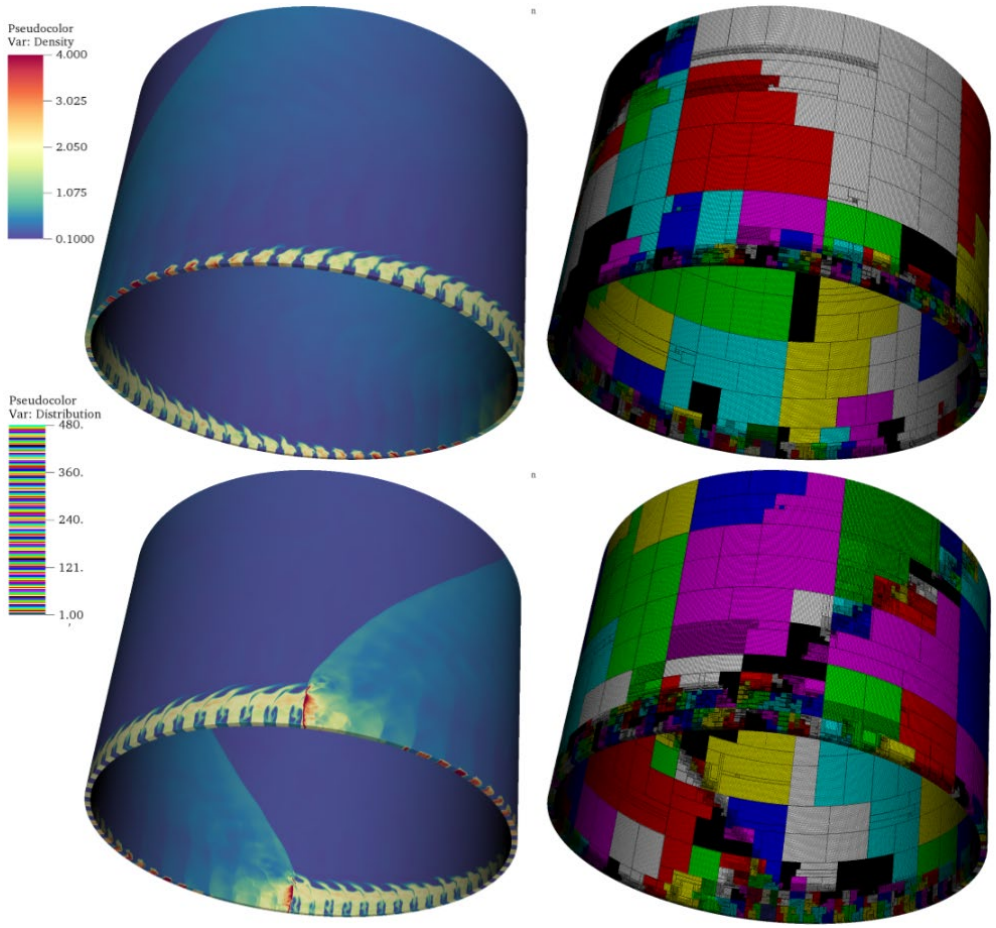

Figure 6.25 Density and processors distribution of the 3D ethylene RDE case (E-3D-75).

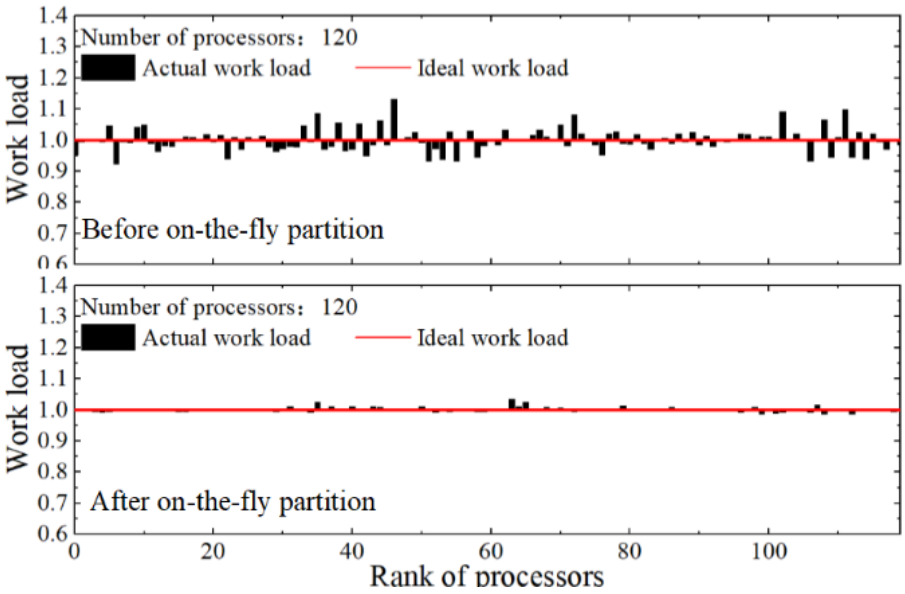

Figure 6.26 Workload of the 2D hydrogen RDE simulation (H-2D-89) on different processors at different times.

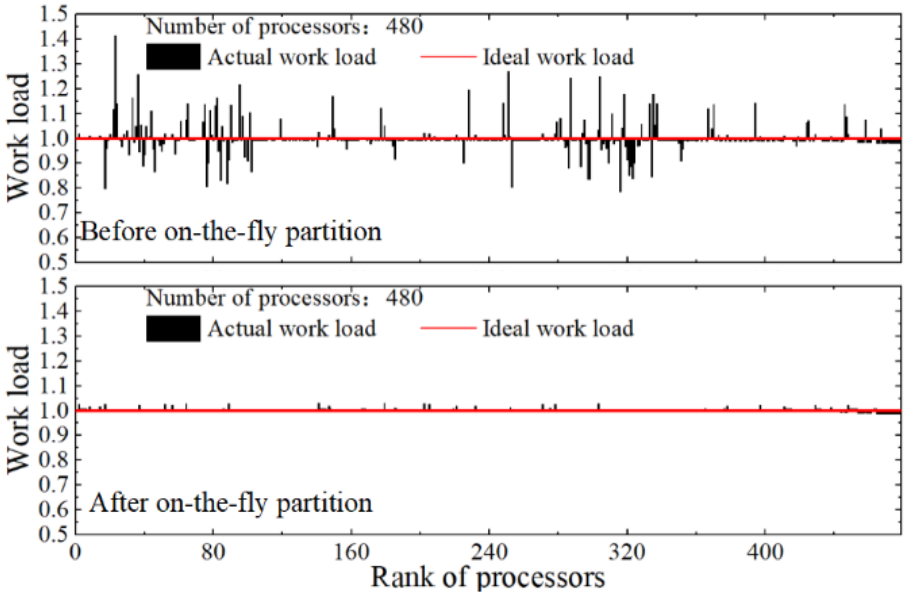

Figure 6.27 Workload of the 3D ethylene RDE simulation (E-3D-75) on different processors at different times.

The strong scalability of the present solvers in simulating rotating detonation is tested on different platforms. The problem size is fixed when using different numbers of processors. The scaling test is performed using a three-level mesh for both the 2D and 3D models. As shown in Figure 6.28, a linearly computational speedup is obtained by increasing the number of processors. Both solvers achieve an acceleration rate close to that in an ideally scaled state, indicating that they scale well when simulating the rotating detonation problems.

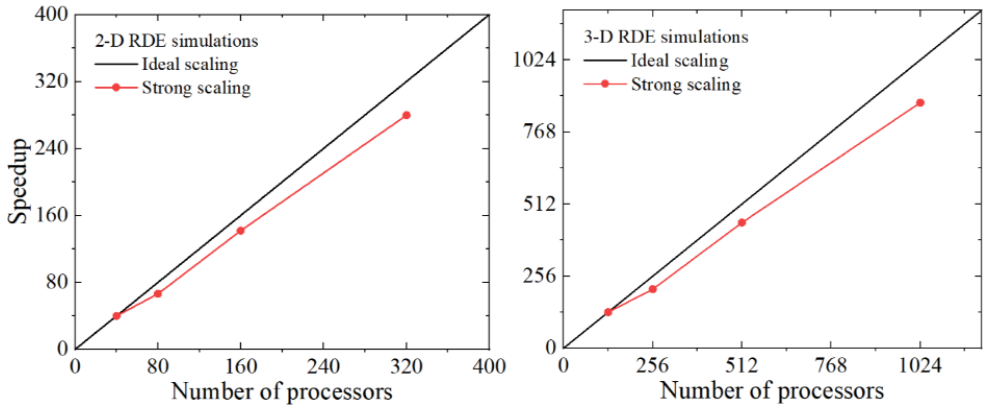

Figure 6.28 Strong scaling test of the 2D hydrogen RDE (H-2D-89) and 3D ethylene RDE (E-3D-75) simulation.

The weak scalability of the present solvers is not tested in this work due to the difficulty in ensuring a constant number of cells, or the load, on each processor during the dynamic adaptation process. The run times for both 2D and 3D RDE simulations are extracted over a short period of physical time, and the time spent on different modules is compared, as shown in Figure 6.29.

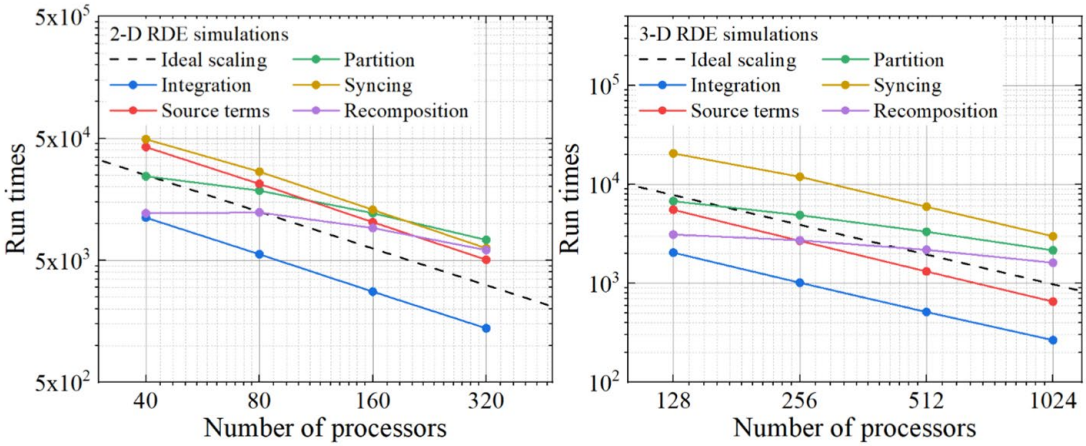

Figure 6.29 Comparison of partial run times for the 2D hydrogen RDE (H-2D-89) and 3D ethylene RDE (E-3D-75) simulation.

In the 2D simulations, the computation of fluid and chemistry linearly accelerates with the increasing computational resources. The synchronisation time also decreases linearly. The 3D simulations show a similar trend compared to the 2D case, with the synchronisation cost increasing as the number of state vectors increases. The 3D simulations also require more grids synchronisation during the run time. The partition and recomposition process in both cases does not scale well, resulting in a loss of acceleration rate overall, as shown in Figure 6.28.

6.5 Chapter summary

The numerical configurations of different RDEs have been detailed in this chapter. The respective 2D and 3D computational domain, initial conditions and boundary conditions were introduced. The alias was used to reference the introduced baseline configuration, as shown in Table 6.6.

Table 6.6 References of the baseline cases.

Alias	Simulating dimensions	Reference geometry	Fuel and oxidiser	Injection schemes	Inlet boundary conditions	Outlet boundary conditions
E-2D-75	2D	UoS RDE [222]	C_2H_4/O_2	Slot	Velocity inlet	Extrapolation
E-3D-75	3D	UoS RDE [222]	$C_2H_4/O_2/N_2$	Slot	Velocity inlet	Extrapolation
H-2D-89	2D	Zhao et al. [228]	H_2/air	Slot	Pressure inlet	Hybrid subsonic/ supersonic outlet
H-3D-159	3D	AFRL RDE [77]	H_2/air	Holes for H_2, slot for air	Mass flow inlet	Hybrid subsonic/ supersonic outlet

The mesh dependency studies were carried out. The multi-wave mode was analysed and the numerical results were compared with experiments. The results showed that the computational model could predict the RDE performance in a reasonable error range. The generated waves were captured by the adaptive meshes. The numerical simulations predicted a greater number of detonation heads while the number of heads observed increased with increasing mass flow rate. Finally, the workload balance and scalability of the present solver were tested in 2D and 3D RDE simulations.

Chapter 7 Premixed and non-premixed RDE

This chapter shows some results of premixed RDEs with different local equivalence ratios based on the 2D unrolled model and compared to a fully non-premixed case. 3D RDE simulations are then demonstrated to study the partially premixed RDE with different bypass flows. These 3D simulations are carried out using the developed solver by applying the adaptive meshes on curvilinear meshes. The results are analysed in terms of the detonation wave structures, temperature distribution, number of waves and the performance of RDE.

7.1 Comparison of 2D premixed and non-premixed RDE

In the RDE simulation field, some premixed simulations were conducted using hydrogen and hydrocarbon fuels. Yet, in realistic experimental tests, the premixed propellants may cause a backfire into the plenum if no specialised injectors are employed. It is hence necessary to conduct some simulations based on non-premixed injection. To simulate the non-premixed injection, the injectors for fuel and oxidizer have been individually simulated in some 3D simulations. However, the extreme thermodynamic conditions in an RDE make 3D simulations costly and challenging. The 2D unwrapped model is a good approach to simplifying the study. The 2D model (E-2D-75) has been used in simulations of RDEs as it decreases the computational costs without missing the main features of the flow field as introduced in Chapter 6. The geometry parameters, initial conditions and boundary conditions are detailed in Section 6.1.1.

In this section, the 2D unwrapped model (E-2D-75) is used with a modification of the width of injectors, as shown in Figure 7.1 The premixed ethylene/oxygen mixtures are injected from 1 mm wide slots on the bottom that are spaced 1 mm apart. The axial velocity, static pressure and temperature of the inflow are prescribed in the ghost cells.

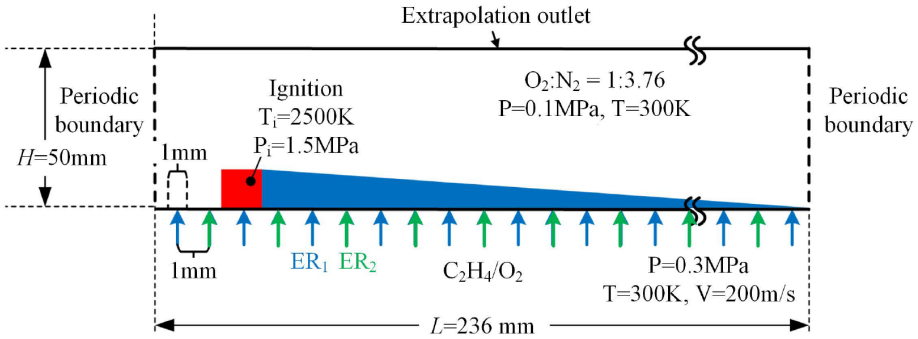

Figure 7.1 Numerical configurations for the 2D premixed and non-premixed RDE simulations.

For each case, the equivalence ratio (ER) of adjacent slots is indicated by ER_1 and ER_2, respectively. Table 7.1 shows the difference between ER_1 and ER_2 ranging from 0 to 1 in six cases. The seventh case is a fully non-premixed case, in which the velocities of ethylene and oxygen are adjusted to

make a nearly stochiometric condition. In the premixed cases, as the mixtures are injected at the same velocity, the volumetric flow rate is constant. Hence, the global equivalence ratio is uniform in the different cases.

Table 7.1 Local equivalence ratio arrangements in the investigated cases.

Case	ER_1	ER_2	ER difference (ERD)
1	1.0 (Stoichiometric)	1.0 (Stoichiometric)	0
2	0.9 (Lean)	1.1 (Rich)	0.2
3	0.8 (Lean)	1.2 (Rich)	0.4
4	0.7 (Lean)	1.3 (Rich)	0.6
5	0.6 (Lean)	1.4 (Rich)	0.8
6	0.5 (Lean)	1.5 (Rich)	1.0
7	Pure fuel (100m/s)	Pure oxygen (300m/s)	-

The 2D simulations were performed on the high-performance computing cluster Iridis 5 at the University of Southampton, where 120 cores (Intel Xeon E5-2670 2.0 GHz) were used. The total number of four-level cells is changed dynamically from 1.6 to 2.4 M in the premixed case and is changed from 4.2 to 4.7 M in the non-premixed case instead of 12.08 M cells in the uniform case. Typical run times for the premixed and non-premixed RDE operating time 1 ms were approximately 7 to 8 days and 12 days wall-clock time, respectively.

7.1.1 Number of detonation heads

Figure 7.2 shows the instantaneous local equivalence ratio distribution in different cases with fully developed detonation waves. In Case 1, the stoichiometric mixtures are injected, and the local equivalence ratio is uniform in the mixture layer ahead of the detonation wave. In other cases, the differences of mixture mole fractions result in non-uniform local equivalence ratios. The premixed mixtures are injected vertically from the bottom. As a result, the propellants are not mixed adequately before being consumed. It is noted that only in Case 4 a four-wave mode is observed. In this case, the height of the fresh mixture layer is lower than that in the other cases.

In addition, a non-premixed case is simulated and compared to the fully premixed case. The temperature and pressure gradient distribution are shown in Figure 7.3. In the premixed case, a stable three-wave mode is observed. The multiple detonation waves are each followed by an oblique shock wave. Some expansion waves are observed behind the detonation wave since the premixed gases are injected discretely. Each premixed jet is surrounded by a small amount of burned gas. In addition, the temperature gradient is large on the contact surface ahead of the detonation waves, where the premixed reactants are also consumed by the burned products.

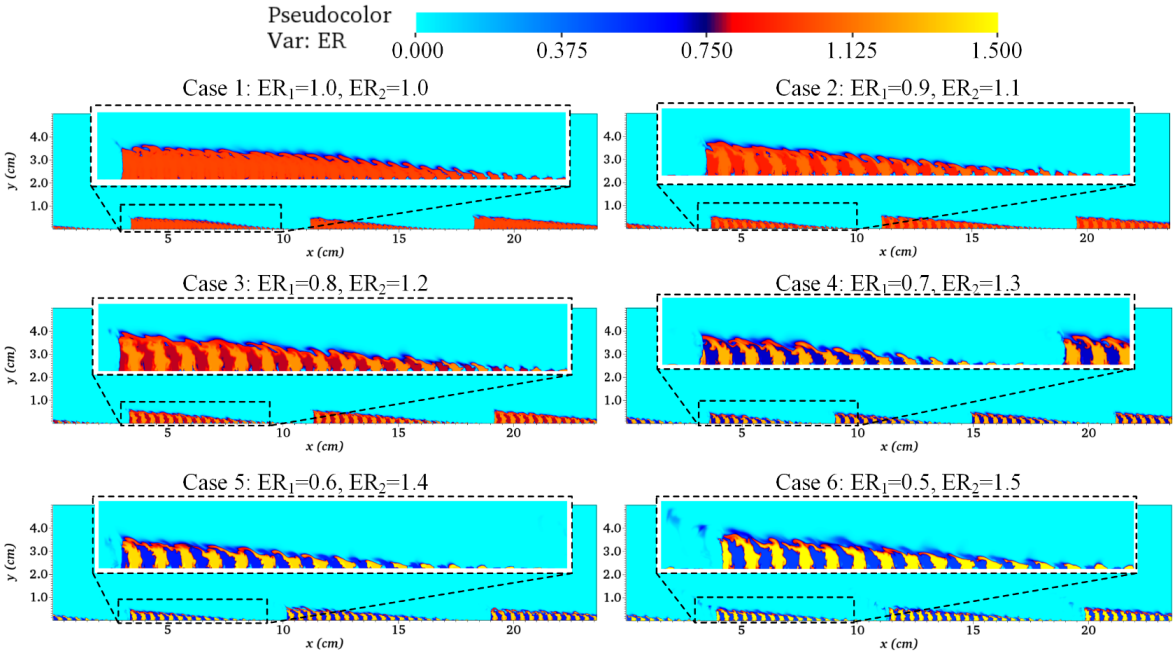

Figure 7.2 Pseudo-colour images of local equivalence ratio (ER) under different injection conditions.

In the non-premixed case, only a single detonation wave with a higher head propagates in the chamber. The average temperature is lower than that in the premixed case due to incomplete combustion. The results also show that the main features in the flow field, i.e., the detonation wave, the oblique shock and the mixture layer, are all captured by the finest meshes.

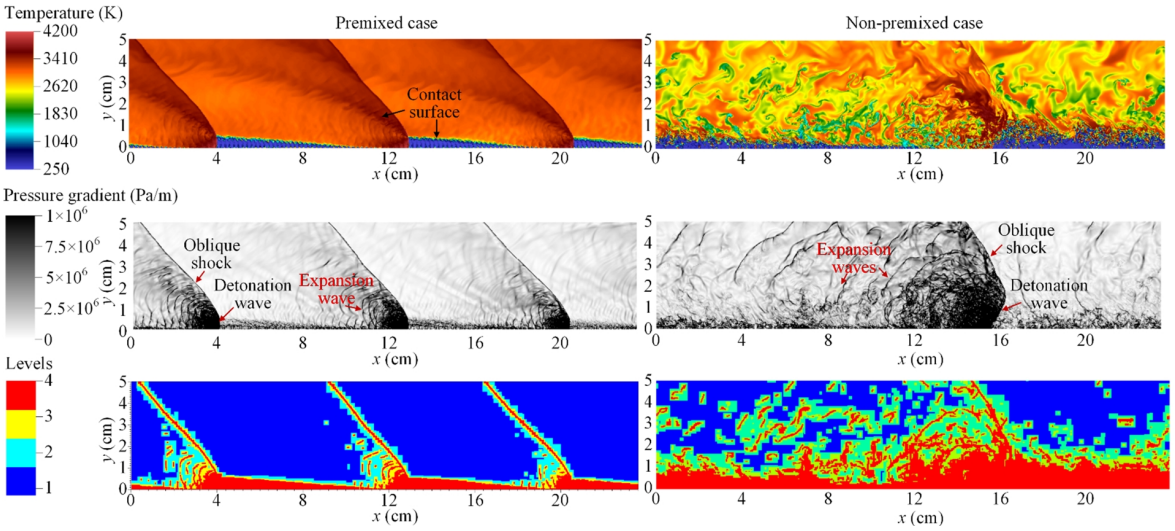

Figure 7.3 Pseudo-colour images of temperature, temperature gradient and refinement level distribution under different injection conditions.

7.1.2 Detonation velocity deficits

The flow velocity in the horizontal direction is computed by calculating the distance and time that the detonation wave requires to cross the probe. The average flow velocity can also be computed by calculating the interval of the cycle from the frequency of the pressure history as shown in Figure

7.4. The average detonation velocity is computed through the horizontal flow and vertical injection velocity, considering the inclination of the detonation wave.

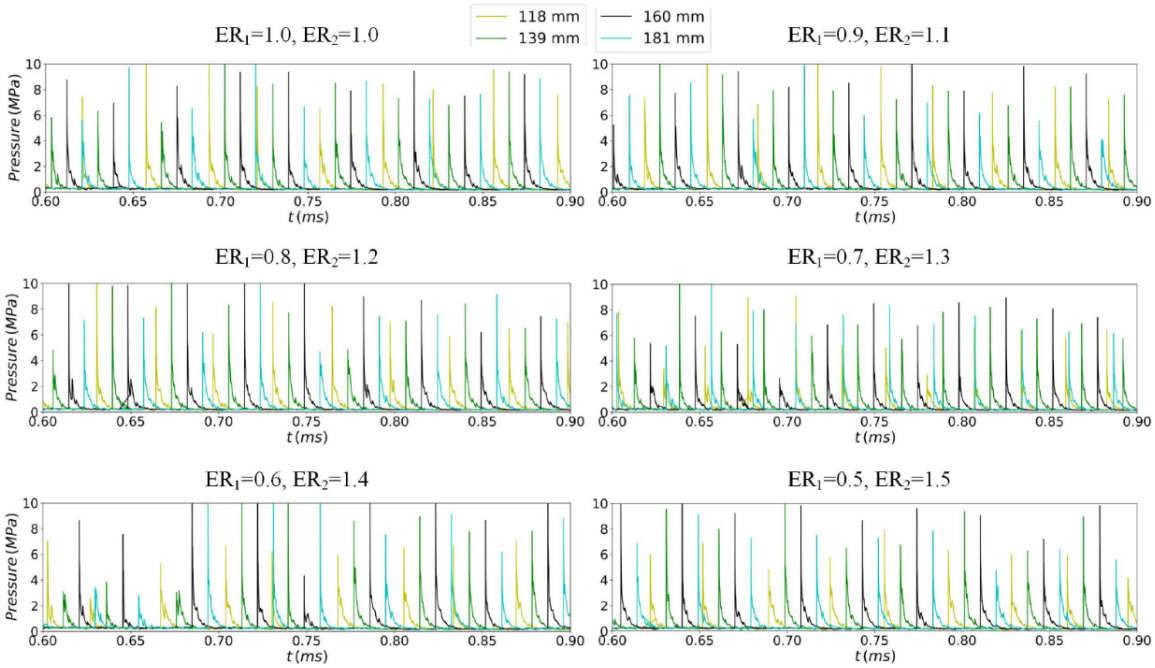

Figure 7.4 Pressure history from 0.6 ms to 0.9 ms.

As depicted in Figure 7.5, the average propagation velocity of detonation waves declines when the local equivalence ratio difference increases. For all the cases, the detonation velocity is lower than the C-J velocity of a stochiometric mixture. The detonation velocity of the four-wave mode is lower than the velocity in other three-wave cases, even when the ER difference gets larger. The detonation velocity deficit is up to 20% when a fully non-premixed injection is used.

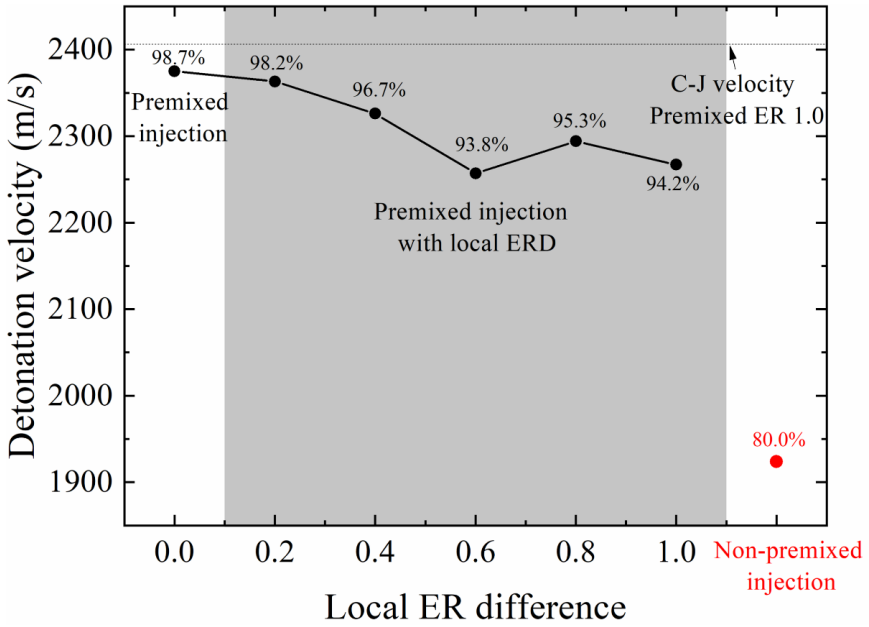

Figure 7.5 Average detonation velocity computed from the pressure profiles from 0.6 ms to 0.9 ms versus local equivalence difference.

7.1.3 RDE performance

The decreases in terms of specific thrust and specific impulse are also observed as shown in Figure 7.6 and Figure 7.7. When a premixed injection is used, the thrust slightly decreases with the increases in the local ER difference. The specific impulse also fluctuates within 4.2%.

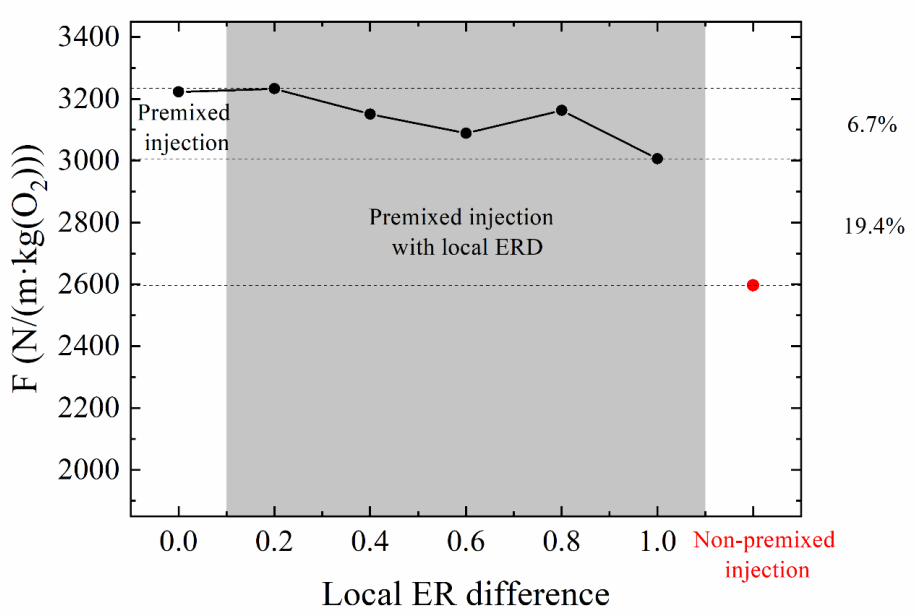

Figure 7.6 Specific thrust versus local equivalence difference.

When using non-premixed injection, the losses in RDE performance are more noticeable. The reduction reaches 52.5% in terms of specific impulse when the fully non-premixed injection is adopted. Using premixed injection, even with large local ER differences, has the potential to improve the performance of an RDE compared with the fully non-premixed configurations.

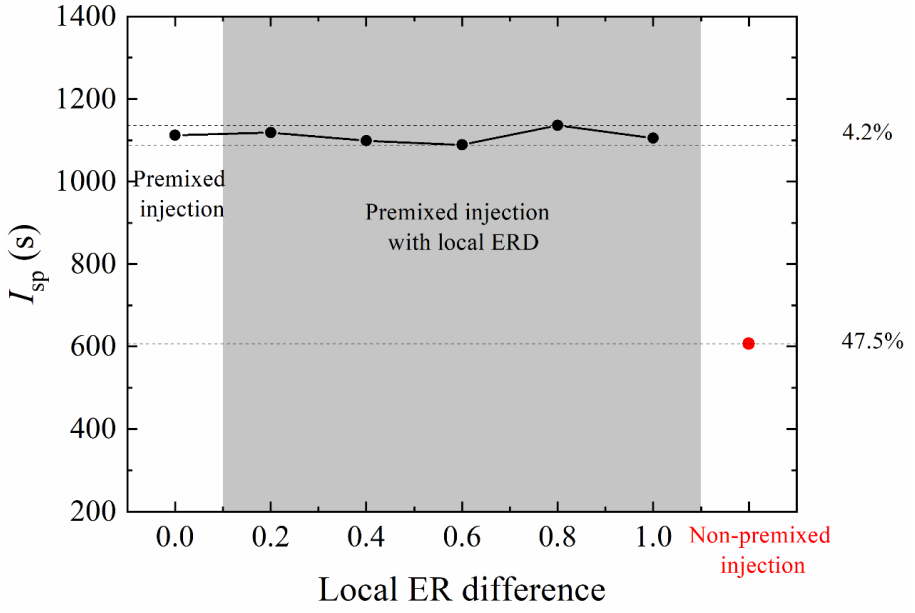

Figure 7.7 Specific impulse versus local equivalence difference.

7.2 3D Partially premixed RDE

Early numerical simulations of RDEs mainly focused on premixed injection, as it is easier to establish stable detonation waves. However, fully premixed injection can lead to flashback in the plenum, so experiments have focused on different non-premixed injection schemes. Improving the mixing degree in RDE has the potential to enhance performance, and researchers have recently turned their attention to RDEs with partially premixed injection. The bypass flow rate is defined in Ref. [19] as

$$\text{Bypass flow rate} = \frac{\dot{m}_b}{\dot{m}_f} \times 100\%, \tag{7.1}$$

where $\dot{m}_b$ denotes the hydrogen mass flow rate in the air flow, and $\dot{m}_f$ is the total hydrogen mass flow rate.

In this section, simulations are conducted with different bypass flow rates through the air slot. The initial configuration is referred to the model (H-3D-159) introduced in Section 6.2.2. The non-slip adiabatic wall boundary condition is used in the present partially premixed cases. A stretched mesh is used as presented in Equation (A.11). The base mesh uses 20 × 580 × 250 cells and is stretched in the radial and axial direction. The first two-layer cells near the wall are always flagged to be refined, as depicted in Figure 7.8. The refinement criteria for temperature, density and pressure are given as ε_T = 500 K, ε_ρ = 0.15 kg/m^3 and ε_p = 50 kPa, respectively. With the boundary refinement, the height of the first layer cell to the inner and outer walls is 0.0923 mm. The height of the first layer cell to the head plane is 0.08825 mm. The coarsest mesh is 0.272 mm in the radial direction and 0.288 mm in the axial direction.

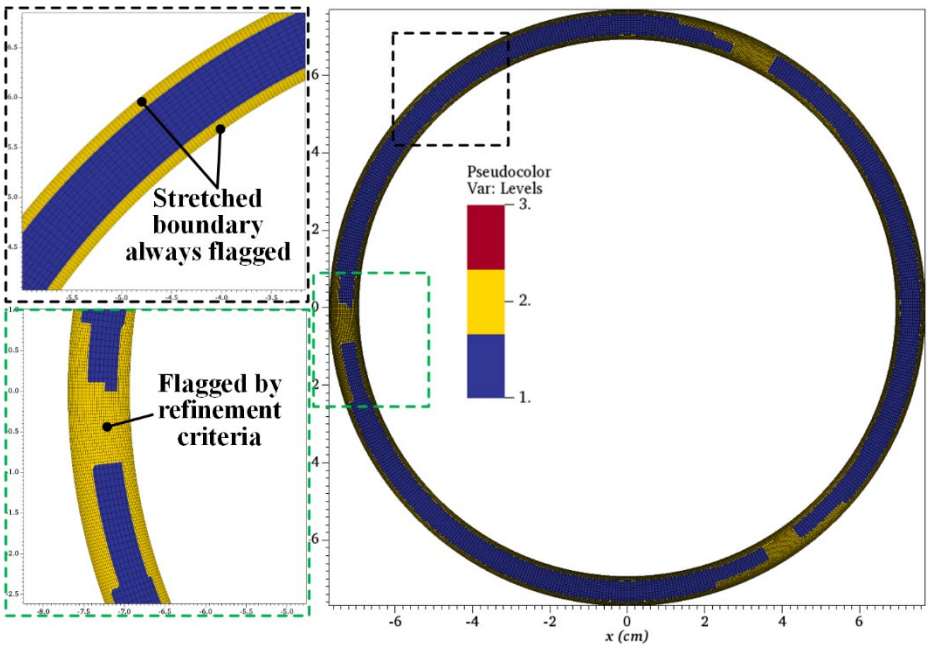

Figure 7.8 Pseudo-colour images of refinement level distribution slices on the z = 7 cm plane overlapped by the mesh.

The refinement criteria, as illustrated in Figure 7.8, play a dynamic role in identifying the region where there is a large gradient of physical variables, i.e., the detonation and oblique shock waves. The cross-sectional plane exhibits a three-wave mode, and the refined meshes effectively capture the oblique shock waves. The 2-level adaptive computation uses approximately 17.5 M to 18.3 M cells. The calculations are performed on 256 cores (AMD EPYC 7742 2.25 GHz). Typical run times for a simulated time of 3 ms were approximately 12 days wall clock time.

The total hydrogen mass flow rate remains constant at 9.3 g/s. In the partially premixed cases, hydrogen was injected not only via holes on the head plane, but also via the slot on the inner wall with air. Table 7.2 illustrates the bypass percentage configurations for a global equivalence ratio of one when varying the fuel premixing bypass proportion from 0 to 15%.

Table 7.2 Bypass flow conditions for all cases.

Case	Injection via holes		Injection via the slot on the inner wall		Global ER	Bypass flow rate
	Mass flow rate (g/s)	Flow component	Mass flow rate (g/s)	Flow component		
1	9.3	H_2=1	320	O_2/N_2=1:3.76	1	0%
2	8.835		320.465	$H_2/O_2/N_2$=1:9.94:37.3744		5%
3	8.37		320.93	$H_2/O_2/N_2$=1:4.97:18.6872		10%
4	7.905		321.395	$H_2/O_2/N_2$=1:3.313:12.4569		15%

7.2.1 Partially premixed flow field

Figure 7.9 displays the equivalence ratio distribution on the inner wall. The local equivalence ratio of the air slot rises from 0 to around 0.15 when the bypass flow rate is increased. The local zoomed-in figures show the penetration of the unburned mixture on the wall. As the air slot is injected in the direction perpendicular to the viewing plane, the penetration is regarded as the downstream recirculation zone of the air/bypass flow on the inner wall.

Figure 7.10 shows the 3D temperature distribution. The varying bypass flow rate does not change the number of detonation heads or the direction of rotation. All the cases have three co-rotating detonation waves in the annular channel. The refill zones of the fresh mixture are observed in front of the detonation. As the air is injected through the slot on the inner wall and hydrogen is injected through the holes on the bottom plane, the non-premixed rotating detonation leads to different structures in the radial direction. An obvious finding is that the detonation is enhanced near the inner wall due to the effects of a concave wall, as demonstrated in a higher temperature. To analyse the detonation structure, the temperature distribution is extracted at different radial locations.

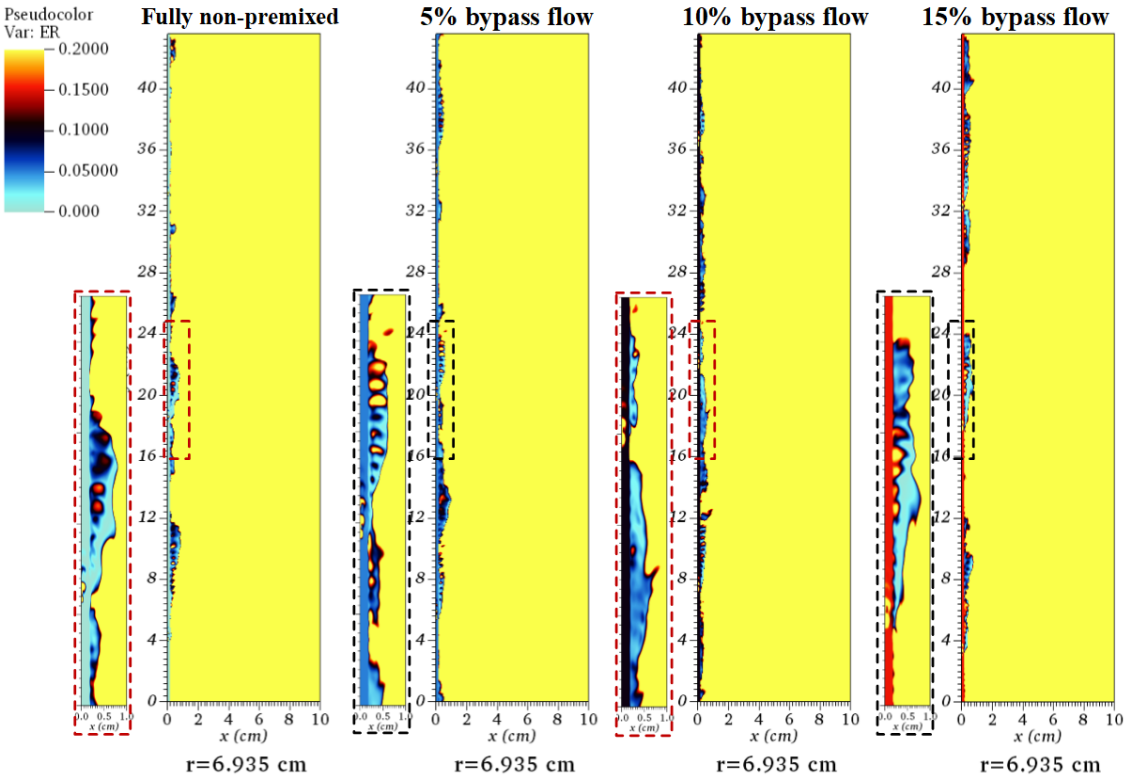

Figure 7.9 Pseudo-colour images of unrolled equivalence ratio on the inner wall.

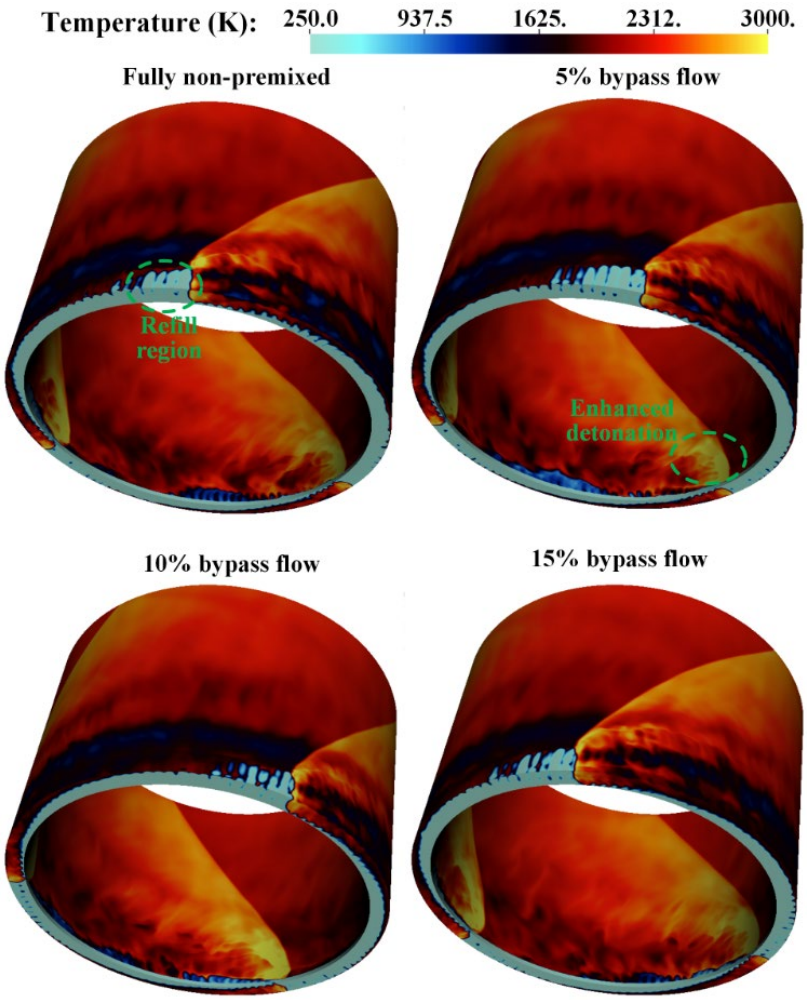

Figure 7.10 Pseudo-colour images of temperature distribution with different bypass flow.

Figure 7.11 presents the temperature distribution on the inner adiabatic wall. The air slot indicates the low-temperature air flow or air with bypass flow. As the adiabatic wall boundary conditions are used in these cases, both detonation and deflagration are observed near the inner wall. The difference in the main structure is small between these cases in terms of the oblique shock angles. Under the present jet in cross flow injection scheme, there is a recirculation zone in the vicinity of the inner wall when the reactants are refilled into the chamber. In the recirculation zone, the burned products are mixed with the gas injected from the air slot. The area of the relatively low-temperature recirculation zone decreases as the bypass flow rate increases. This suggests that more combustion occurs behind the detonation on the wall in these cases due to the premixing in the air slot.

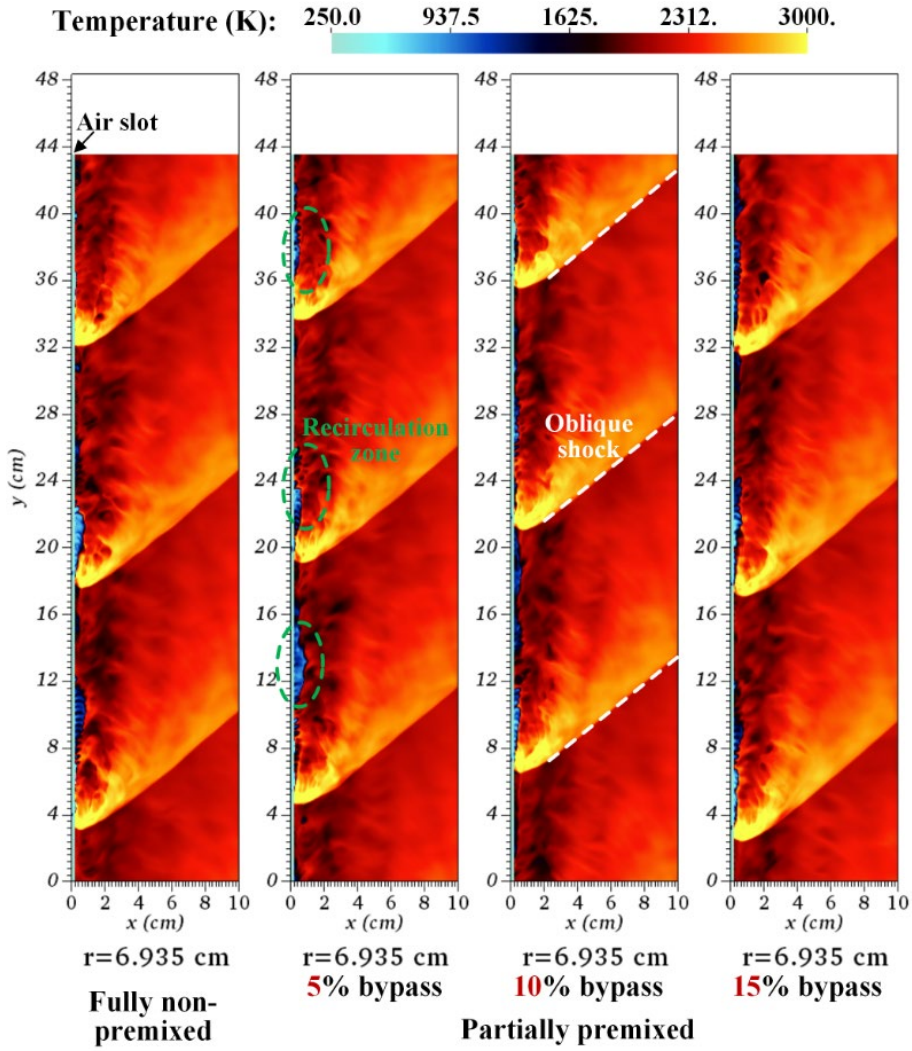

Figure 7.11 Pseudo-colour images of unrolled temperature on the inner wall.

Parasitic combustion is observed inside the chamber in all these cases, as shown in Figure 7.12. Parasitic combustion indicates combustion that takes place before the detonation waves [230,231]. Although the fully non-premixed case has a slightly larger amount of pre-burning gases, the typical rotating detonation macro structure remains qualitatively unchanged. Multiple detonation waves are followed by oblique shock waves, with slip lines on the contact surface being clearly visible. The buffer zone is also observed between the contact burning surface and parasitic combustion. The

differences in terms of the detonation height, the oblique shock angle and the buffer zone size are minor.

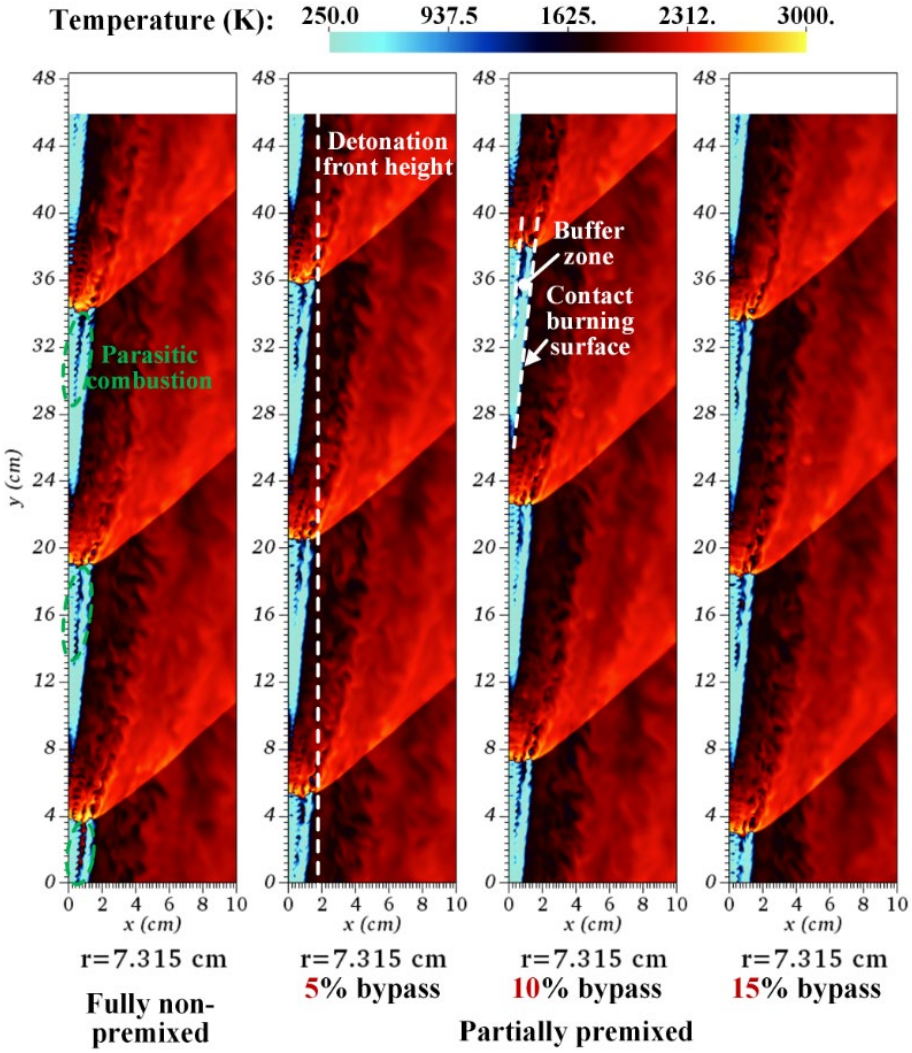

Figure 7.12 Pseudo-colour images of unrolled temperature on the middle plane.

On the outer wall, the temperature distribution shows a difference in the parasitic combustion region, as can be seen in Figure 7.13. Discrete parasitic combustion is observed when the fully non-premixed injection is adopted. With the increases in the premixing percentage, the separate parasitic combustion regions eventually combined into one continuous region. This phenomenon can be attributed to the partially premixed flow via the slot impinging on the outer wall and enhancing local mixing, which in turn strengthens parasitic deflagration on the wall. However, this enhanced combustion has a negative influence on the detonation performance. It should be noted that in this study, the observed temperature difference on the detonation front between non-premixed and partially premixed cases is not prominent. The temperature in the buffer zone increases slightly when the bypass flow rises to 15%. This is another result of the enhanced parasitic combustion near the head plane.

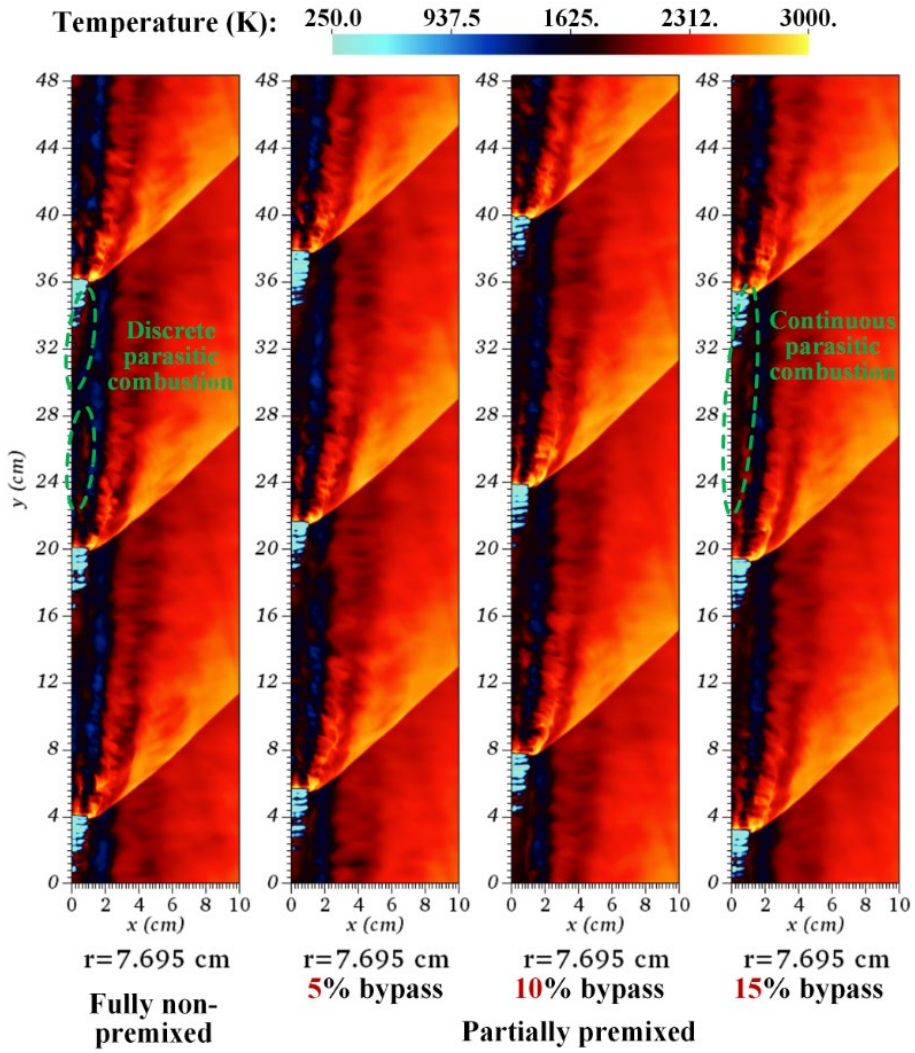

Figure 7.13 Pseudo-colour images of unrolled temperature on the outer wall.

7.2.2 Effects of premixing on heat release

To quantitatively study the effects of partial premixing on the RDE, the probability density function of the normalised flame index (NFI) is extracted. The normalised flame index is used as an indicator of the premixing degree in the flow field. It was defined to identify the premixing degree in the flow field. The equation reads

$$\mathrm{NFI} = \frac{\nabla Y_{\mathrm{F}} \cdot \nabla Y_{\mathrm{O}}}{\left|\nabla Y_{\mathrm{F}}\right|\left|\nabla Y_{\mathrm{O}}\right|}, \tag{7.2}$$

where the ∇Y_{F} and ∇Y_{O} denote the gradient of fuel and oxidiser, respectively. The normalised flame index indicates the direction of fuel and oxidiser gradient. When the normalised flame index is positive, it implies that fuel and oxidizer gradients are aligned, namely a premixed flow. Conversely, a negative normalised flame index presents a non-premixed flow. As the effects of reactions are not included in the normalised flame index, other reacting parameters are required to identify the premixed and non-premixed reactions.

The statistics of the 3D flow field are analysed through the entire chamber. A negative NFI indicates the local flow is non-premixed and a positive NFI represents a premixed flow. Figure 7.14 shows the probability density function of the normalised flame index. In all the cases, the fully non-premixed flow is dominated in the chamber with a portion of more than 56%. This portion drops from 61.1% to 56.8% with the increases in bypass flow percentage. Conversely, the proportion of fully premixed flow rises from 10.2% to 12.5%. The partially premixed flow slightly enhances the premixing degree in the chamber as only a small amount of hydrogen is added into the air slot. The NFI indeed shows the flow is still dominated by non-premixed flow even though the partially premixed injection is adopted.

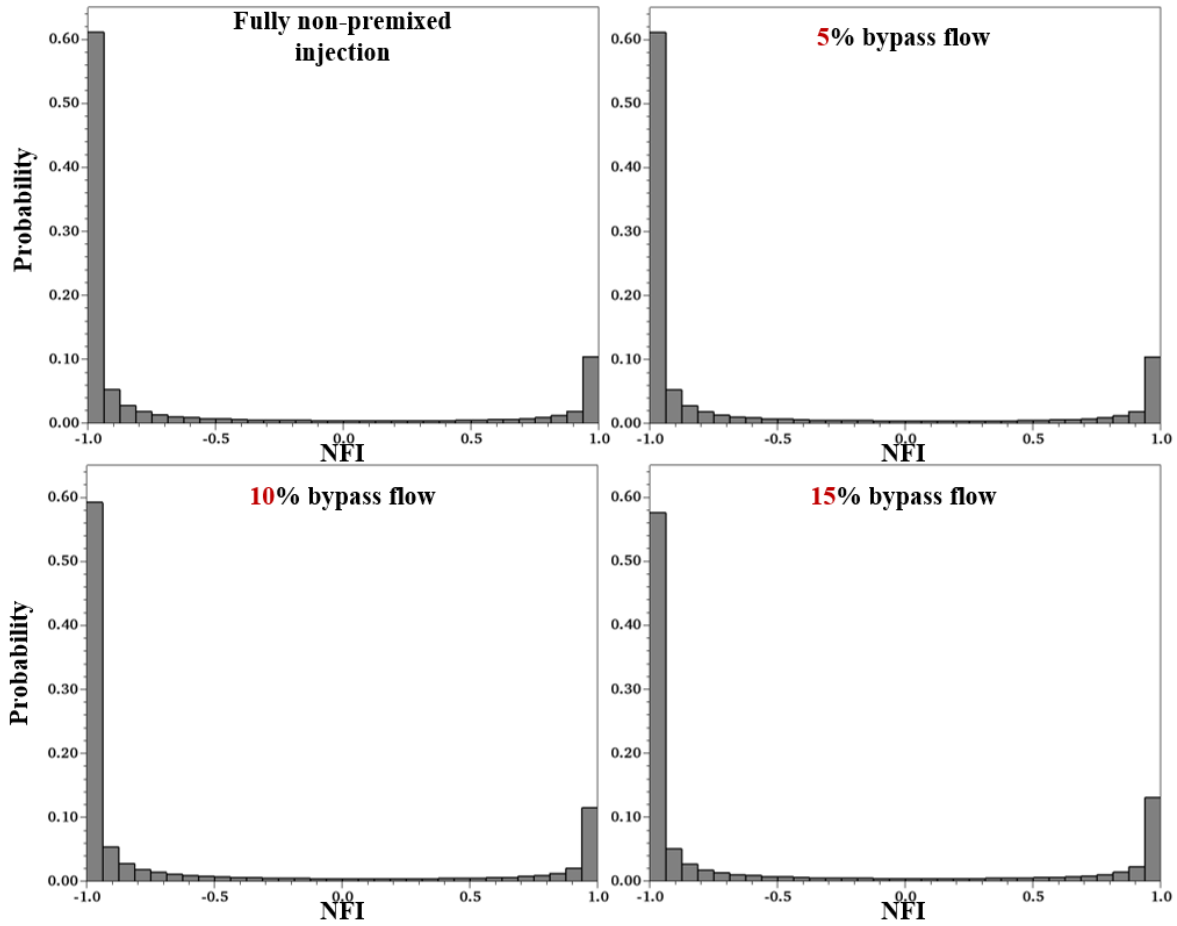

Figure 7.14 Probability density function of the normalised flame index.

To identify the part of reactions in the chamber, the thermicity distribution is analysed in combination with the NFI. Thermicity is a measure of heat release in reacting flows. It indicates the extent of chemical reactions in combustion and detonation problems. For an ideal gas, the thermicity is calculated by

$$\dot{\sigma} == \sum_{m=1}^{N_{sp}} \left(\frac{\bar{W}}{W_m} - \frac{h_m}{c_p T} \right) \frac{\mathrm{d}Y_m}{\mathrm{d}t}, \quad \frac{\mathrm{d}Y_m}{\mathrm{d}t} = \frac{W_m \dot{\omega}_m}{\rho} \quad \left(m = 1, \ldots, N_{sp} \right). \tag{7.3}$$

In AMROC, the species mass production rate $\dot{\omega}_m$ is calculated during several sub time steps when using the GRK4A solver and the exact mass production is not outputted explicitly. The term $\mathrm{d}Y_m / \mathrm{d}t$ is computed by the species differences in each flow time step as

$$\frac{\mathrm{d}Y_m}{\mathrm{d}t} = \frac{Y_m^{t+\Delta t} - Y_m^t}{\Delta t} \quad \left(m = 1, \ldots, N_{\mathrm{sp}}\right). \tag{7.4}$$

As shown in Figure 7.15, the majority of heat release comes from the premixed flow in all the cases. The heat release in fully non-premixed flow decreases from 12.8% to 3.9% when increasing the bypass flow rate. As compared to the probability density function in Figure 7.14, the proportion of heat release in non-premixed flow drops more obviously, indicating that the presence of partial premixing has a significant influence on the reacting flow compared to the downstream flows. In spite of decreases in fully non-premixed reactions, there has also been a fall in the fraction of heat release in fully premixed flow when NFI is equal to positive one. The ratio between them indicates that the heat release decreases in both the fully premixed and the non-premixed flow when a bypass flow is injected and the decline is relatively apparent in the non-premixed flow.

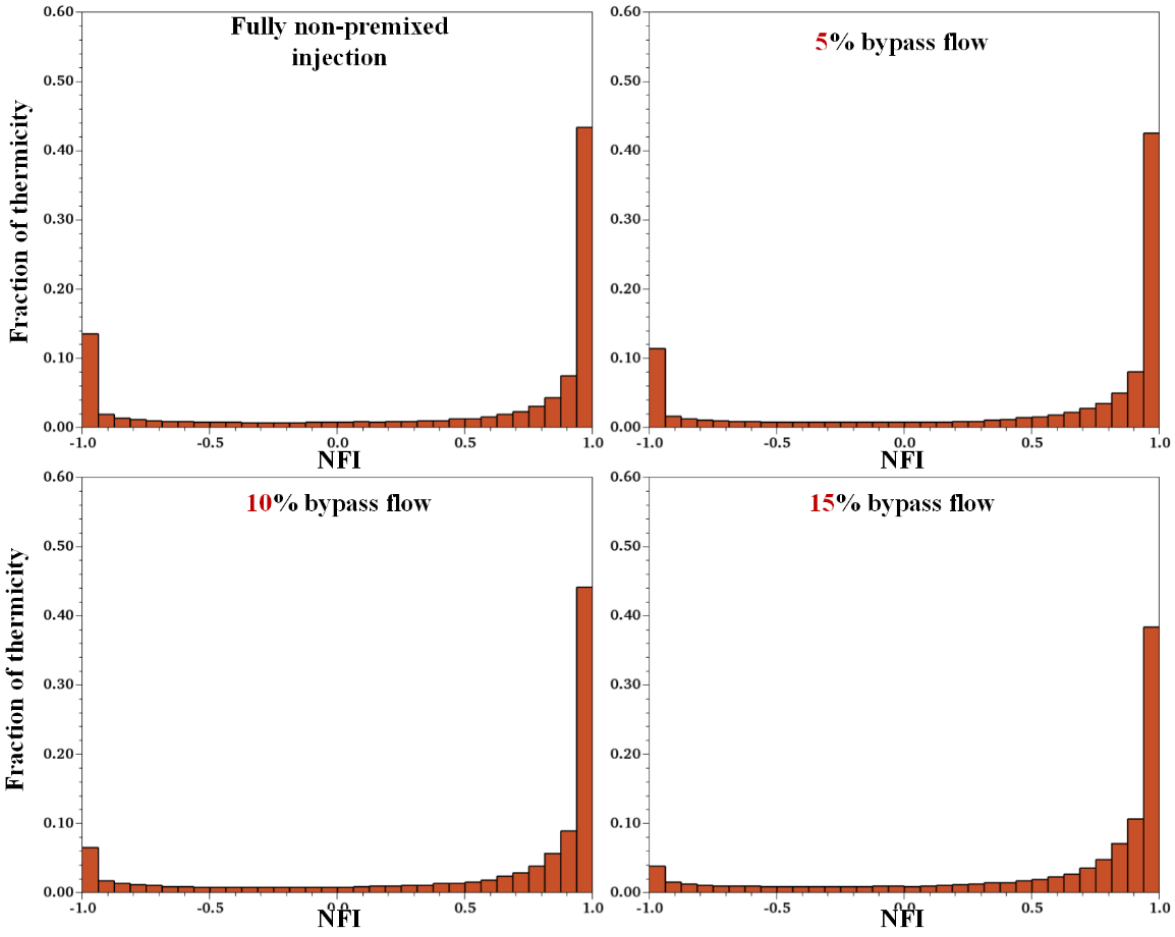

Figure 7.15 Fraction of thermicity as a function of the normalised flame index.

Figure 7.16 presents the heat release under different local equivalence ratios in the flow. The fuel-lean and fuel-rich regions are distinguished by different background colours in this figure. The results

show that all the cases operate at a dominant stoichiometric equivalence ratio as the global equivalence ratio is expected to be uniform according to the injection configurations. The highest value of heat release decreases from 10.4% to 8.7% in the ranges near the stoichiometric ratio when partial premixing is added. The heat release percentage in the flow of an equivalence ratio below one declines from 34.4% to 26.6% with increasing partial premixing. Another finding is that the increasing premixing flow results in a smoother gradient in the heat release varying from fuel-lean to fuel-rich regions. This suggests that the premixing leads to a more homogeneous heat release in the chamber and an enhanced local heat release in discrete fuel-rich regions.

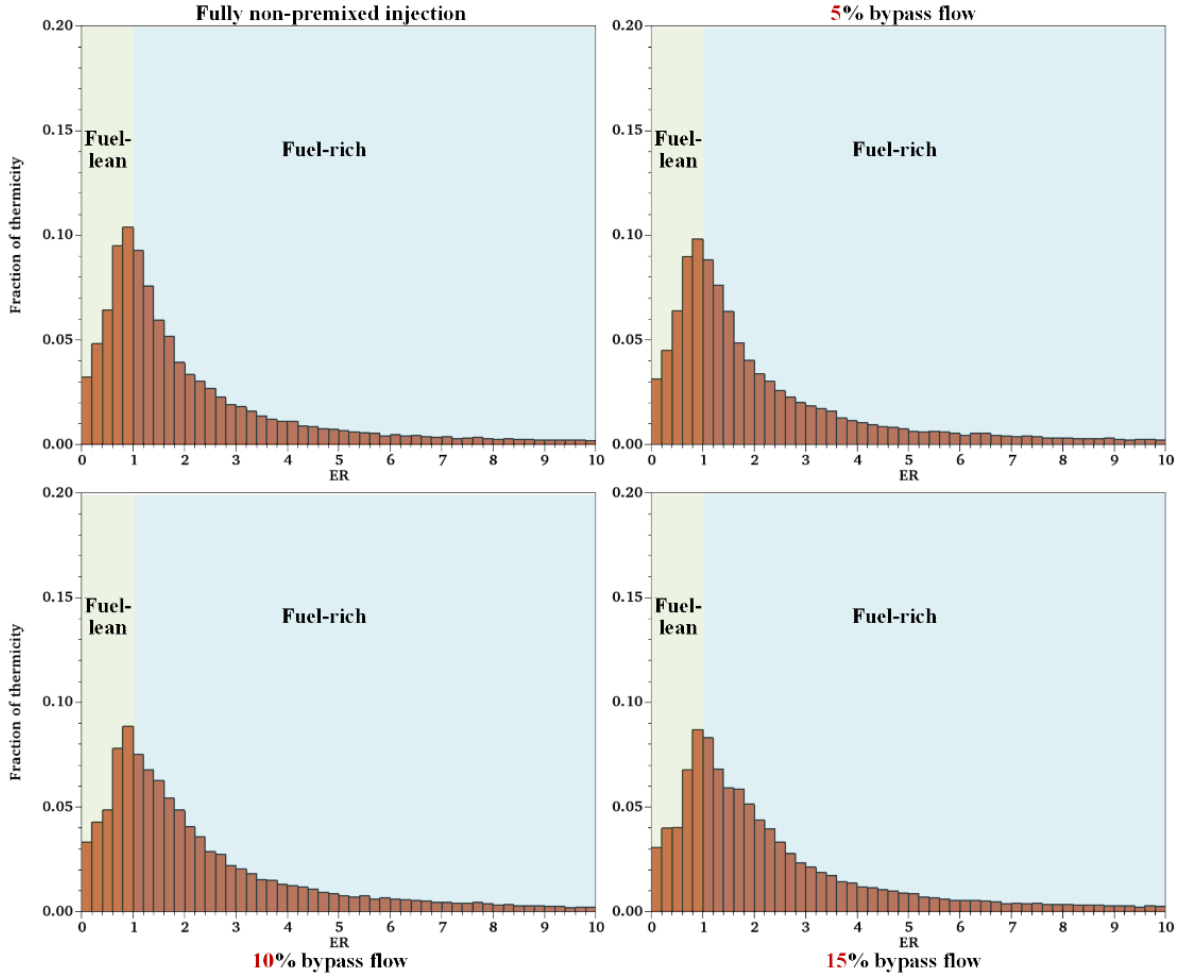

Figure 7.16 Fraction of thermicity as a function of the equivalence ratio.

The results of thermicity show a quantitative analysis of the heat release from reactions in the flow field. To further identify the source of the heat release, the thermicity is counted under different pressure ranges as shown in Figure 7.17. Around 21.1% of the total heat release occurs at a pressure from 0.1 MPa to 0.2 MPa, namely operating in a low-pressure region. This proportion drops to 18.6% when the bypass flow increases to 15%. As adiabatic boundary conditions are used in these four cases, the deflagration in the vicinity of walls leads to the large proportion of low-pressure heat release. This is also seen from the temperature slices in Section 7.2.1, where the high temperature on the walls also indicates the consumption of the reactants. The previous results show that parasitic

combustion is locally enhanced on the walls when increasing the premixing degree. An explanation for the decrease in total low-pressure deflagration is that the partial premixing reduces the amount of commensal combustion, which is defined as combustion occurring downstream of the detonation front [230,231]. In Figure 7.17, the presence of partial premixing decreases the low-pressure heat release, and consequently enhances the heat release at a pressure over 0.5 MPa. The suppression of low-pressure deflagration is beneficial as more reactants are consumed in a high-pressure region, namely a detonative mode. The increasing high-pressure heat release indicates that the RDE can take the performance advantages of detonation.

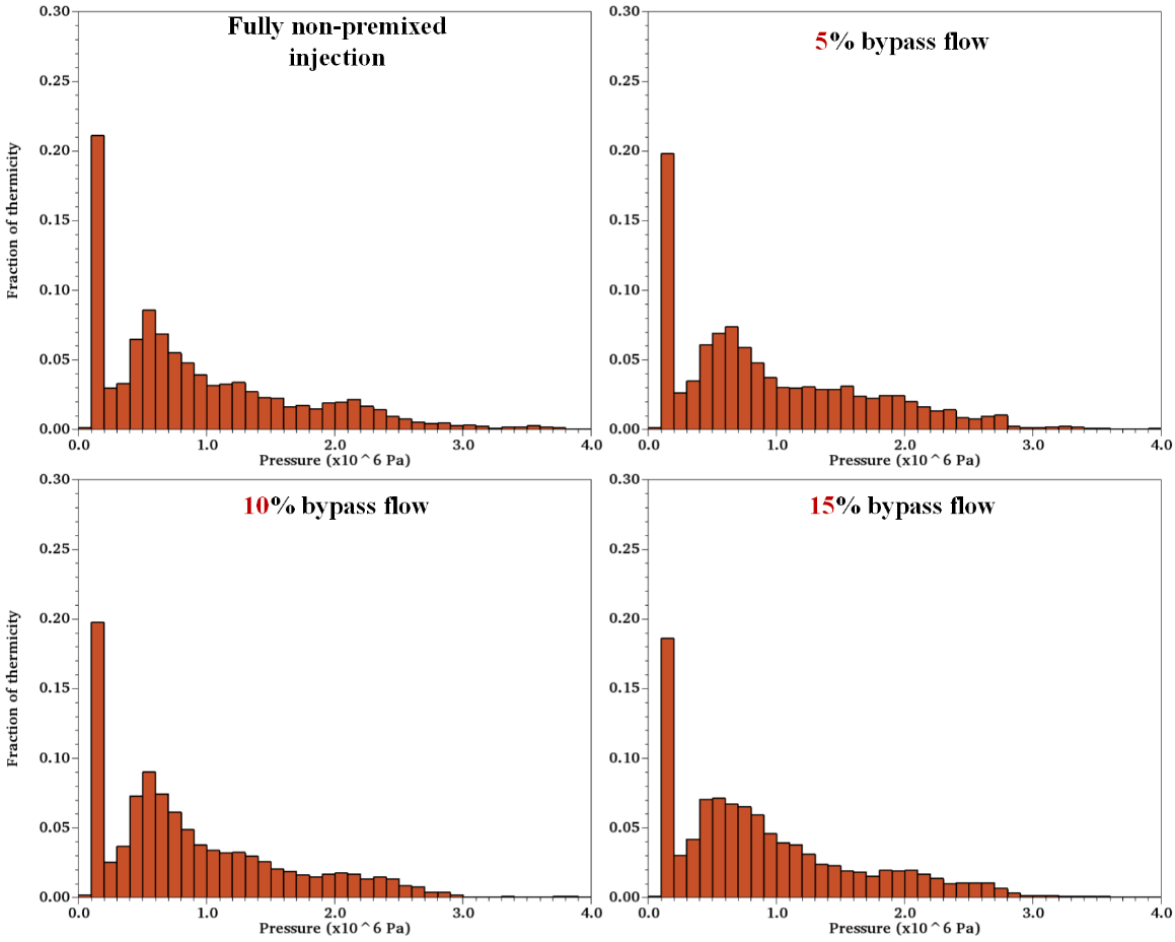

Figure 7.17 Fraction of thermicity as a function of the pressure.

7.2.3 RDE performance

Figure 7.18 displays the average detonation velocities obtained from pressure profiles. The results indicate that the detonation velocity increases as the hydrogen bypass flow rate increases in all four configurations. In the fully non-premixed case, the maximum detonation velocity deficit is observed as 8.2% on the inner wall. The detonation velocity in the middle channel is slightly lower than the ideal premixed C-J velocity, while the detonation waves on the outer wall are all overdriven according to the velocity.

The presence of premixing in the air flow increases detonation wave speeds. This finding is consistent with that in Ref. [19], in which the relative increase is around 1% of C-J velocity when the bypass flow rate is up to 15%.

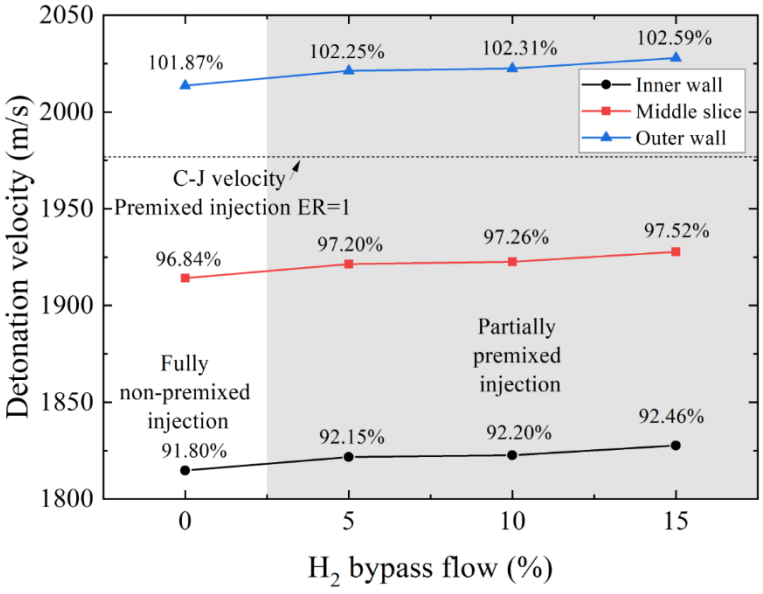

Figure 7.18 Average detonation velocities computed from the pressure profiles versus hydrogen bypass flow percentage.

In addition to the detonation velocities, the performance of the RDE is further analysed, which is not obtained in the partially premixed experiments. The average thrust and specific impulse are computed on the plane of the outlet. As shown in Figure 7.19 and Figure 7.20, the results indicate that the partially premixed cases have a higher average thrust and specific impulse compared to the fully non-premixed case. Figure 7.19 and Figure 7.20 reveal that there has been a gradual increase in the number of thrust and specific impulse, respectively. The performance benefit rises to 8.53% when increasing the bypass flow rate to 15%. This finding confirms the improvement of the partially premixed injection.

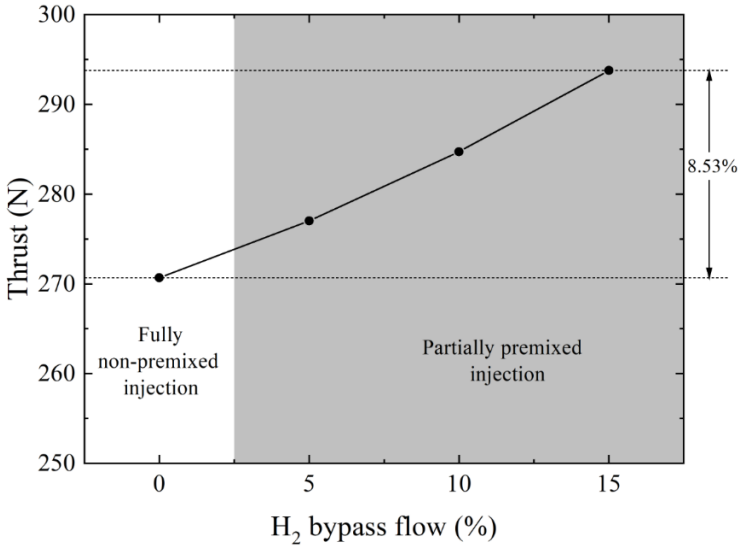

Figure 7.19 Average thrust versus hydrogen bypass flow percentage.

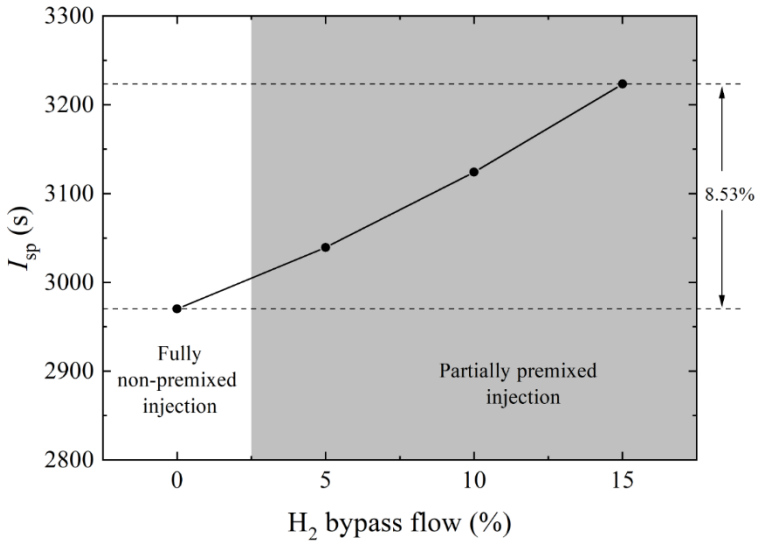

Figure 7.20 Average specific impulse versus hydrogen bypass flow percentage.

7.3 Chapter summary

In this chapter, the effects of premixing have been studied on the RDE flow field and performance. The main findings are drawn as follows:

- The numerical results of 2D ethylene RDE showed that the local equivalence ratio could have an influence on the number of detonation heads. Detonation velocity deficits were observed when increasing the local equivalence ratio difference. The non-premixing injection decreased the number of detonation heads, in terms of specific thrust by 19.4% and specific impulse by 47.5%.
- As partial premixing could enhance the local mixing and reduce the risk of flashback, the partially premixed injection has become a potential improvement on the RDE injection scheme. The temperature distribution of 3D hydrogen RDEs showed that the partial premixing enhanced parasitic combustion on the wall. The heat release was dominated by the premixed flow even though the majority of the flow was non-premixed. Partial premixing led to a more homogeneous heat release in the chamber and an enhanced local heat release in discrete fuel-rich regions.
- Thermicity of 3D hydrogen RDEs showed that the partial premixing decreased the total low-pressure heat release. It was deduced that partial premixing enhanced parasitic combustion on the wall but reduced commensal combustion in the chamber. The results also indicated that a small amount of partial premixing could increase the thrust and specific impulse by 8.53%. The relative detonation velocity increase was around 1% of the C-J velocity when the bypass flow rate was up to 15%, which was also confirmed in a published experimental work.

In summary, these findings enhanced the understanding of the RDE performance changes when using the widely used premixing assumption. The premixing changed the number of detonation heads in 2D computations while this phenomenon was not observed in 3D simulations due to the better mixing process. 3D simulations confirmed that adopting partially premixed injection could improve RDE performance in terms of detonation velocity, average thrust, and specific impulse. The numerical results provided additional evidence for the advantages of applying partial premixing to future RDE injection designs.

Chapter 8 Effects of the wall conditions on RDE

The effects of different wall boundary conditions are evaluated in this chapter adopting set-ups according to the 3D hydrogen RDE configuration (H-3D-159). The simulations are first conducted on varying wall temperatures of the RDE. The differences between the RDE with cooling walls and adiabatic walls are compared. The influence of non-slip boundary conditions on RDE is also studied. Further simulations of 3D RDE with different channel widths are presented at the end.

8.1 Comparison of adiabatic and isothermal walls

Most 3D numerical models of RDEs assume adiabatic walls for simplicity, despite the fact that RDEs typically operate for only a few seconds in experiments, making the adiabatic wall boundary condition potentially inadequate for simulating real-world processes. Some numerical simulations have been carried out to study the effects of isothermal walls on RDEs. Results showed that, in cases with adiabatic walls, the high wall temperature can cause deflagration, altering the detonation front shape and wave structures [129,125,133]. In a premixed simulation with continuous injection utilising isothermal walls, the detonation cellular structure vanished [129]. Furthermore, it has been reported that the use of a cooling wall from the start can lead to the subsequent quenching of detonation [132].

In this section, all the cases start with the adiabatic slip wall boundary conditions. The two-level mesh in Figure 6.18, as introduced in Section 6.2.3, is used for this case. The first four cells near the walls are always flagged to be refined. The 2-level adaptive computation uses approximately 10.4 M to 15.5 M cells. The calculations are performed on 256 cores (AMD EPYC 7742 2.25 GHz). Typical run times for a simulated time of 1 ms were approximately 4 to 5 days wall clock time.

As shown in Figure 8.1, a single detonation wave is ignited at the start, followed by multiple unstable cycles and a transition to a three-wave mode. At t = 1.8 ms, the wall temperature changes in each case. A phase difference appears when isothermal walls are used. In these cases with cooling walls, the pressure peaks drop to around 0.8 MPa and then recover to 1 MPa at the final stable stage. The wave frequency is estimated from 2.3 ms to 4.4 ms using a fast Fourier transform. The single wave frequency is 4.14 kHz, 4.03 kHz, 4.03 kHz and 4.05 kHz for the cases with adiabatic walls, and isothermal walls at 300 K, 600 K and 900 K, respectively. Compared to the ideal frequency of 4.3 kHz based on a premixed C-J detonation, the average detonation velocity deficit is 3.7% in the adiabatic case and ranges from 5.8% to 6.3% in the cases with isothermal walls.

Figure 8.2 shows the transient temperature distribution and its slice on the head plane when the different cases run in a stable mode. The use of a cooling wall does not change the number of detonation heads in the present simulations. All the cases still operate in a three-wave mode lasting

over 2 ms. The isothermal walls rapidly cool the burned gases, limiting high-temperature regions near the wall to only the area where the detonation exists.

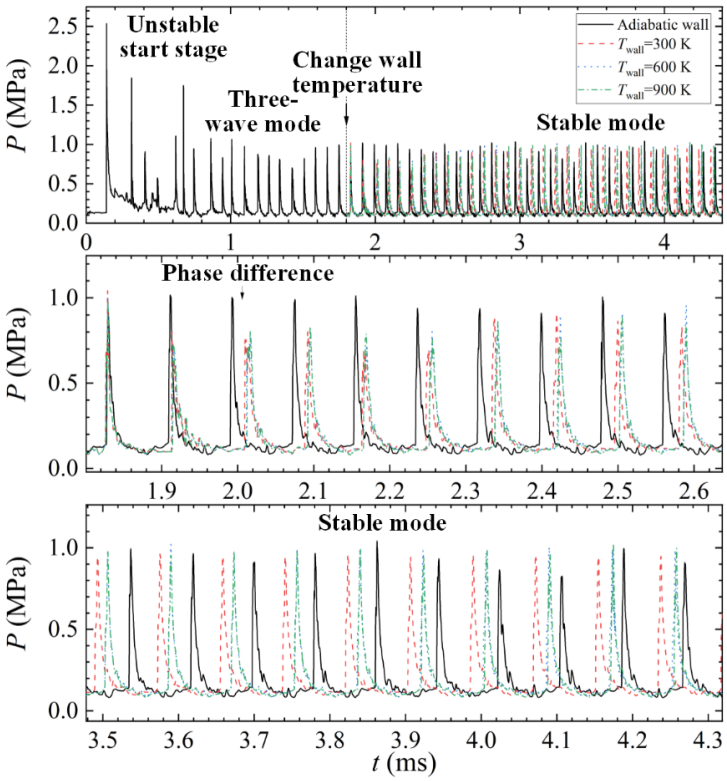

Figure 8.1 Pressure history in different cases, sensors at R = 73.15mm, H = 5mm.

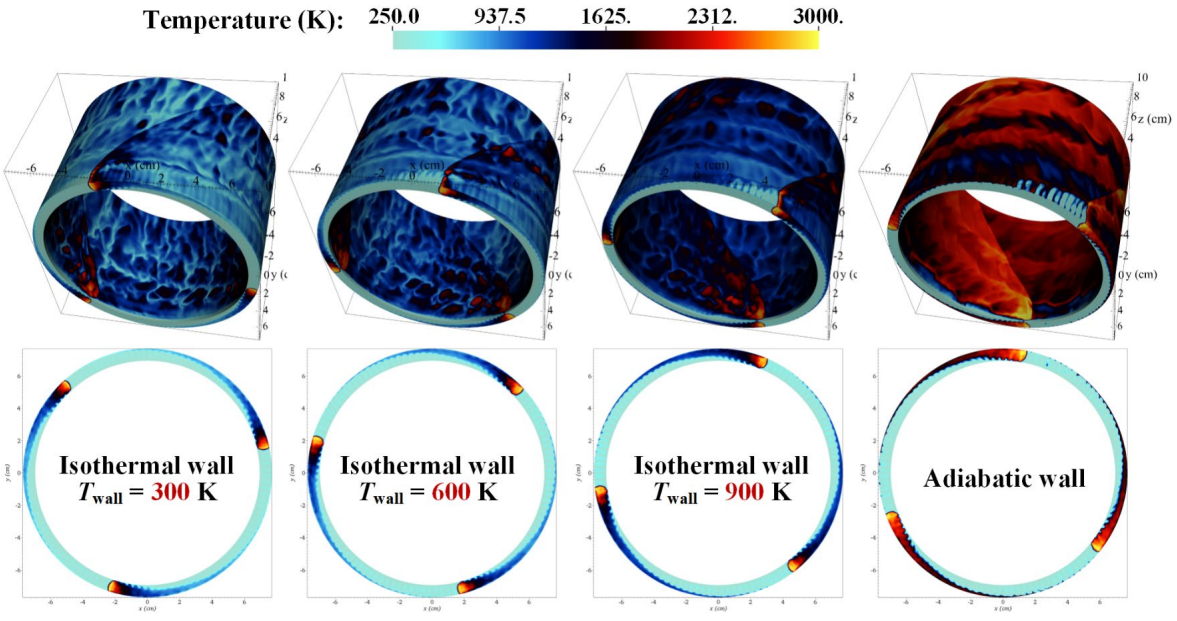

Figure 8.2 Pseudo-colour images of temperature distribution and its slices on the bottom plane.

The temperature distribution near the inner wall is depicted in Figure 8.3. The value indicates the central value of the first layer mesh from the wall. The detonation is observed to be detached from the bottom plane due to the presence of an air slot. The penetration height of the recirculation zone is seen to be low on the inner wall. Discrete high-temperature regions are also visible behind the detonation wave in cases with cooling walls. These regions indicate commensal combustion

occurring behind the detonation. Commensal combustion is suppressed when the temperature of the wall is lower. The detonation is also weakened as presented at a lower temperature peak. These weakened reactions are caused by the heat loss from the wall. Another phenomenon is that parasitic combustion near the wall is eliminated when a cooling wall is adopted. The suppression of the secondary deflagrative waves contributes more reactants to being consumed by the detonation.

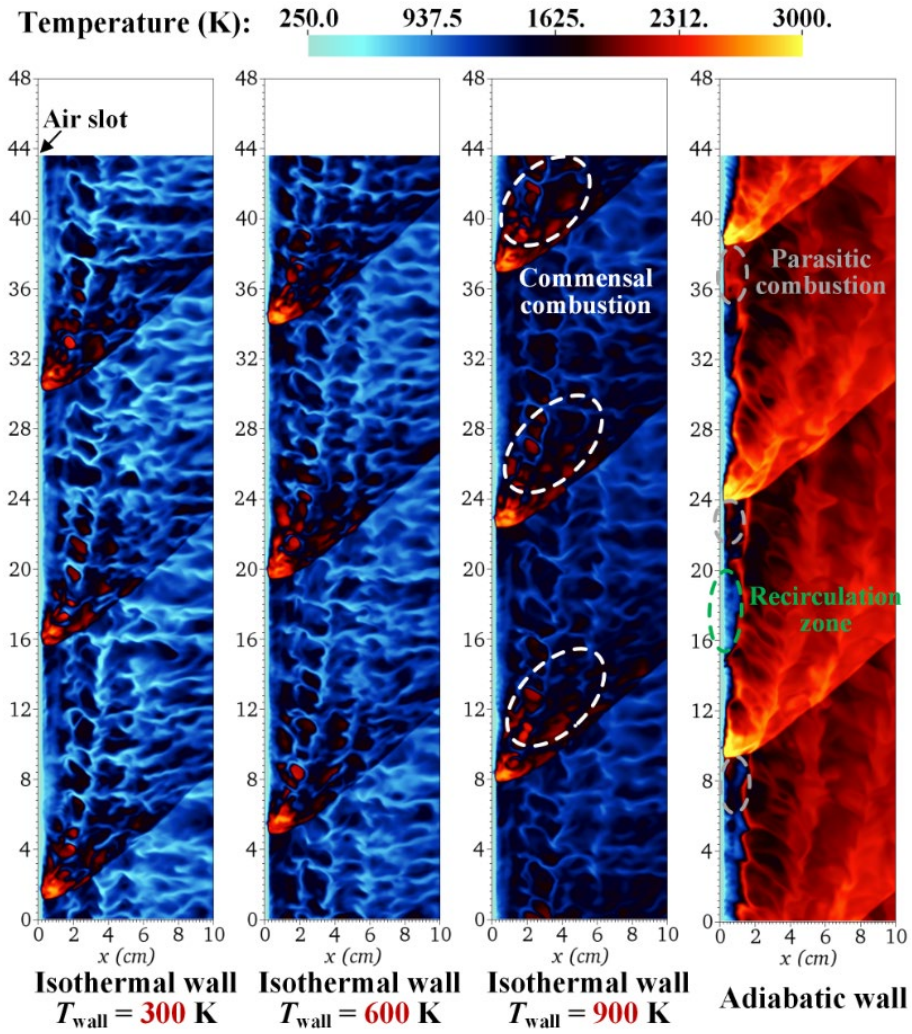

Figure 8.3 Pseudo-colour images of unrolled temperature slices on the inner wall.

Figure 8.4 shows the unwrapped slices of the outer wall. In the case using adiabatic walls, the typical rotating detonation structure is observed. The multiple detonation waves are each followed by an oblique shock wave. Irregular slip lines are captured on the contact surface. The stratification in the mixture layer is a result of non-premixed injection and incomplete mixing. As the wall temperature decreases, the temperature behind the detonation wave and oblique shock also decreases, but the detonation still sustains even at a wall temperature of 300 K.

The multiple-wave structure leads to the temperature stratification along the direction of slip lines near the outer wall, as given in Figure 8.5. Only one detonation wave is analysed with 100% opacity. In the mixture layer (region A), the low-temperature mixture is mixed with the burned products, resulting in local stratification. A small amount of parasitic combustion is observed in the refill

region. The contact surface burning occurs on the upper bound of region A. The symbols D and O indicate the detonation (D) and its attached oblique shock (O). Commensal combustion occurs in region E as the fuel is not completely consumed by the detonation. The first slip lines, depicted in the green dashed line, divide the products in region B and the product in region C from the previous detonation. In the three-wave mode, the product from the following detonation in region F is divided by another slip line (seen in the yellow dashed line). The different resident times of the products from different detonation waves lead to a varying expansion and a stratified temperature distribution in the axial direction.

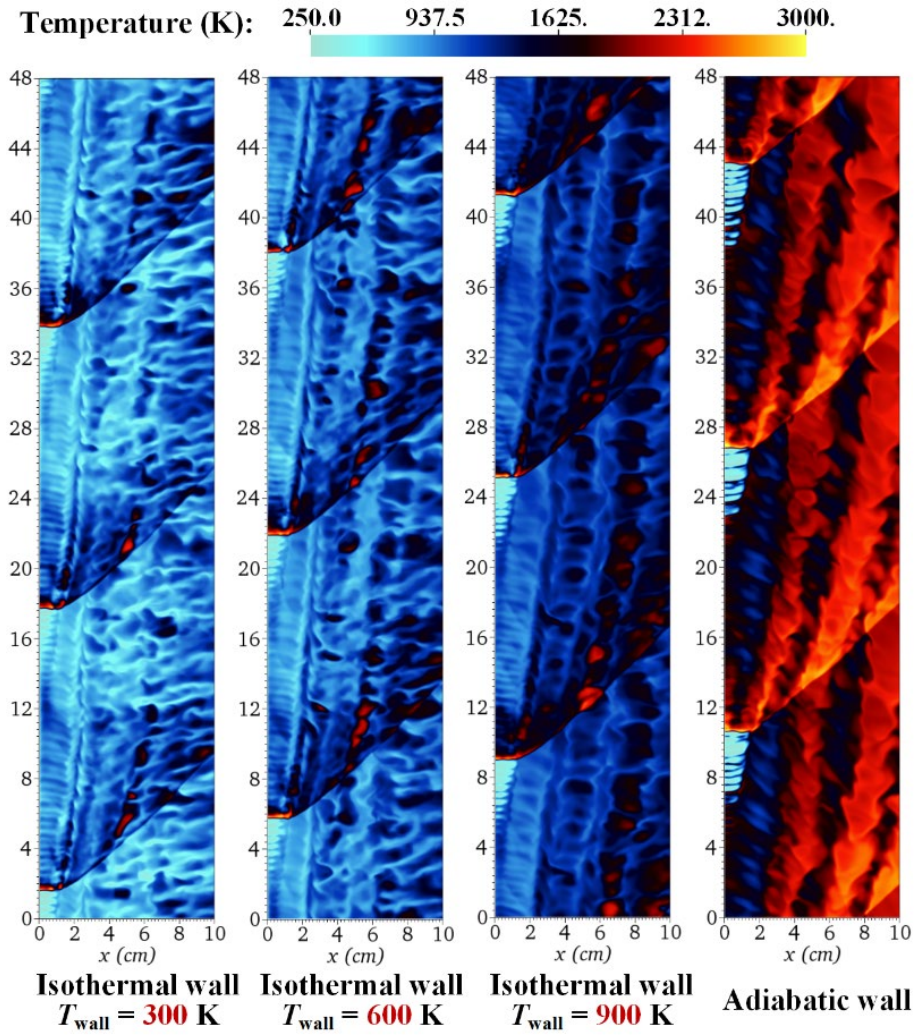

Figure 8.4 Pseudo-colour images of unrolled temperature slices on the outer wall.

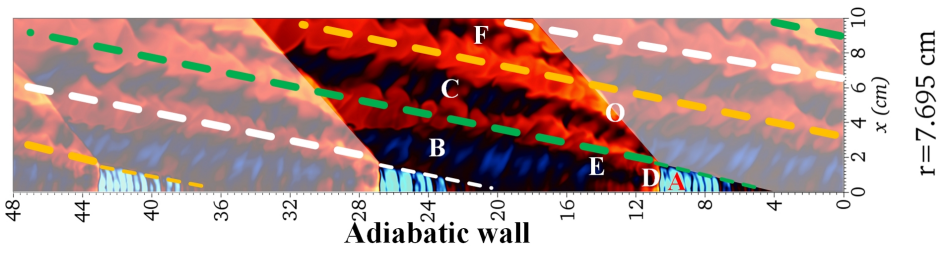

Figure 8.5 Schematic of temperature in different regions near the adiabatic outer wall.

When the cooling walls are adopted, parasitic combustion in the mixture layer is eliminated near the outer wall, as shown in Figure 8.4. The burned gases are cooled by the wall, and the temperature of the products in regions B, C and F decreases with the declines of the wall temperature. The gases close to the exit are at a slightly higher temperature in all cases. The oblique shock enhances the local burning, as a result, some hot pockets are observed downstream. These hot pockets are reduced by a low-temperature wall, as seen in the case with walls at 300 K. Commensal combustion in the post-detonation region is also suppressed by wall cooling.

Both the cooling inner and outer walls demonstrate a notable influence on the temperature distribution near the wall as shown in Figure 8.3 and Figure 8.4. Parasitic combustion is eliminated near the wall as the burned gas behind the detonation is cooled rapidly. Despite the stratification in the mixture layer, the temperature difference is relatively small between the cooled products and the fresh mixture. This reduces the probability that the secondary deflagration wave occurs. As a result, more reactants are utilised by the detonation in the chamber. The reduction of deflagration near the walls and the heat losses from the wall play a complex role in the RDE overall performance. To study the effects of the cooling wall on RDE, the temperature in the chamber is extracted and compared in these cases.

Figure 8.6 presents a comparison of the temperature in the middle of the channel and shows that parasitic combustion occurs in the mixture layer ahead of the detonation. The differences, observed among the varying cases, are relatively minor compared to those on the walls. The wall cooling has a limited influence on the detonation structure in terms of the detonation front height, oblique shock angle, the scale of parasitic combustion and the buffer zone size. The temperature in regions A and B in Figure 8.6 decreases with the decrease in the wall temperature.

To quantify the effects of isothermal walls in the RDEs, the thermicity is also analysed in combination with the local static pressure, as shown in Figure 8.7. The pressure of 0.5 MPa has been chosen as a rough threshold to identify the low-pressure and high-pressure heat release [130]. Due to the non-homogeneous flow field in the discrete non-premixed injection cases, it is difficult to determine the exact C-J pressure for the whole domain. In this section, the C-J pressure is calculated based on an initial temperature of 300 K and an initial pressure of 0.1 MPa. It is noted the C-J pressure is regarded as a reference value instead of a rigorous standard of detonation occurrence.

The percentage of low-pressure heat release drops obviously when the isothermal walls are introduced in the RDE. The thermicity fraction in the adiabatic case is 21.1% at a pressure ranging from 0.1 MPa to 0.2 MPa. As a comparison, this fraction ranges from 10.5% to 11.8% in the cases with isothermal walls. The result indicates that the use of isothermal walls can suppress the low-pressure deflagration near the walls and consequently enhance the high-pressure heat release above 0.5 MPa. Another interesting finding is that there has been a small amount of heat release in the region where the pressure is below 0.1 MPa when the wall temperature is high. The high-temperature

walls enhance the reactions of the incomplete burning products in the low-pressure expansion region after the detonation front.

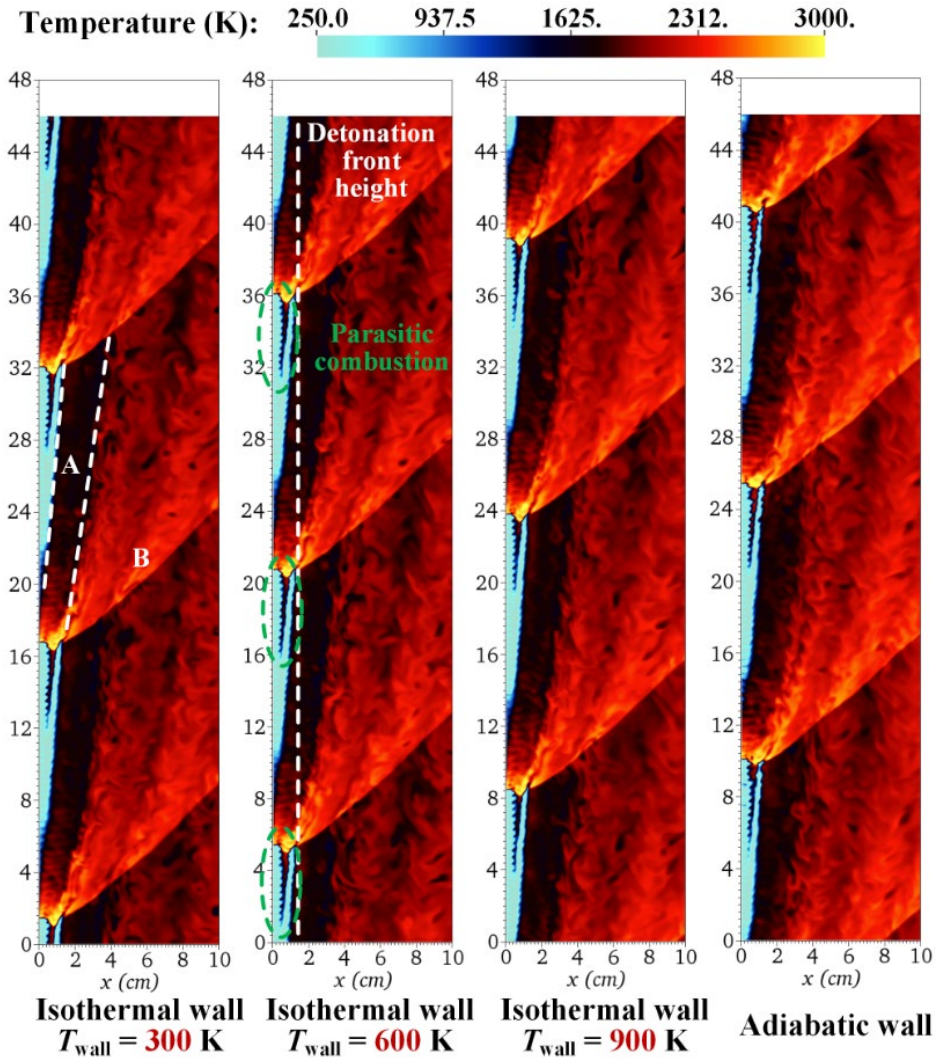

Figure 8.6 Pseudo-colour images of unrolled temperature slices on the outer wall.

The heat flux on the inner wall is extracted circumferentially at the maximum heat flux axial location, as shown in Figure 8.8. The heat flux peak is 7.84 MW/m^2 at z = 7.3 mm when the wall temperature is set to 300 K. The heat flux peak is lower in these cases with higher temperature walls. The heat flux peak is 7.11 MW/m^2 and 6.14 MW/m^2 in the case with walls of 600 K and walls of 900 K, respectively. The maximum heat flux is observed at z = 6.9 mm in both the cases with higher wall temperatures. The heat flux peak is corresponding to the detonation heads in the chamber. As the multiple detonation waves show a varying heat flux peak in the same period, this indicates that the temperature peaks are also varying in the multiple-wave mode. The averaged heat flux is 1.27 MW/m^2 on the inner wall of 300 K. This averaged heat flux drops to 1.01 MW/m^2 on the inner wall of 600 K and drops to 0.86 MW/m^2 on the inner wall of 900 K.

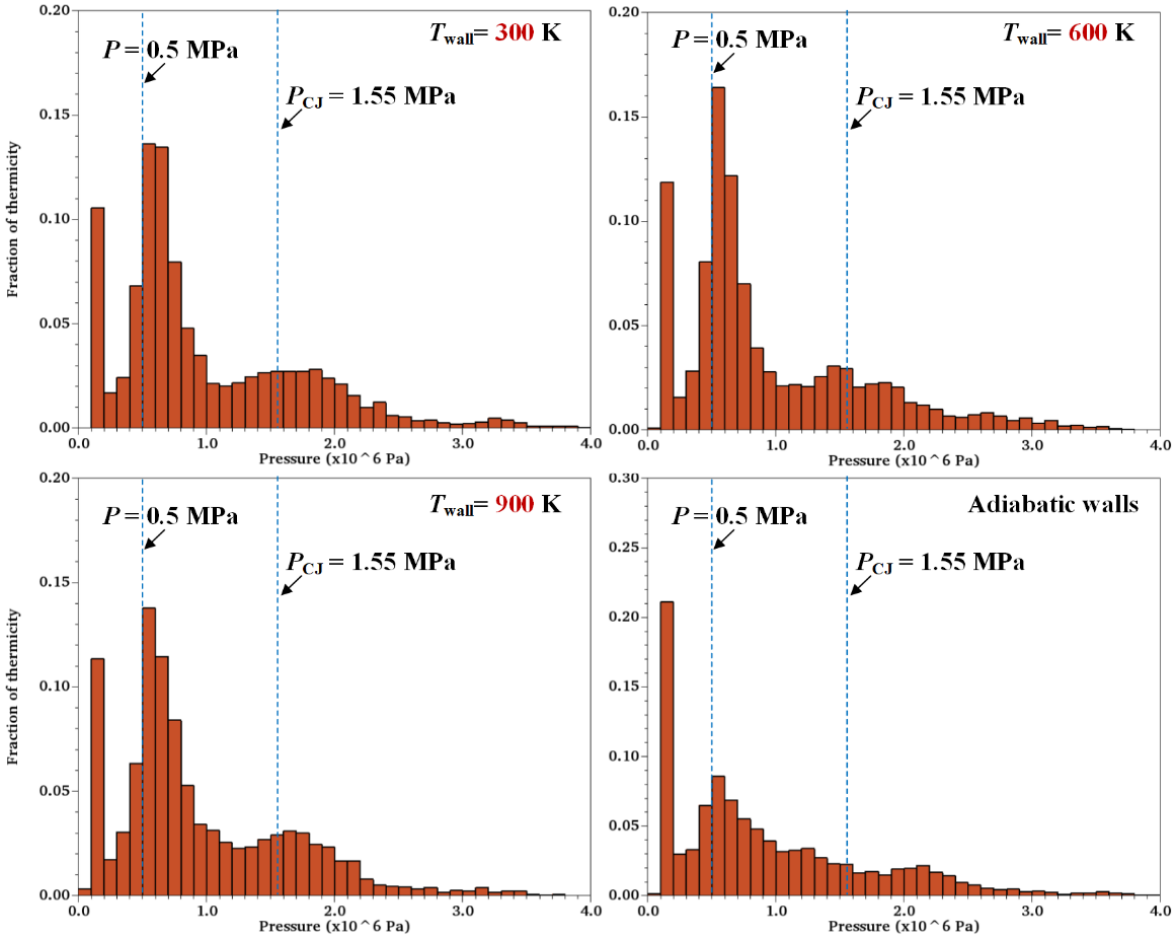

Figure 8.7 Fraction of thermicity as a function of pressure.

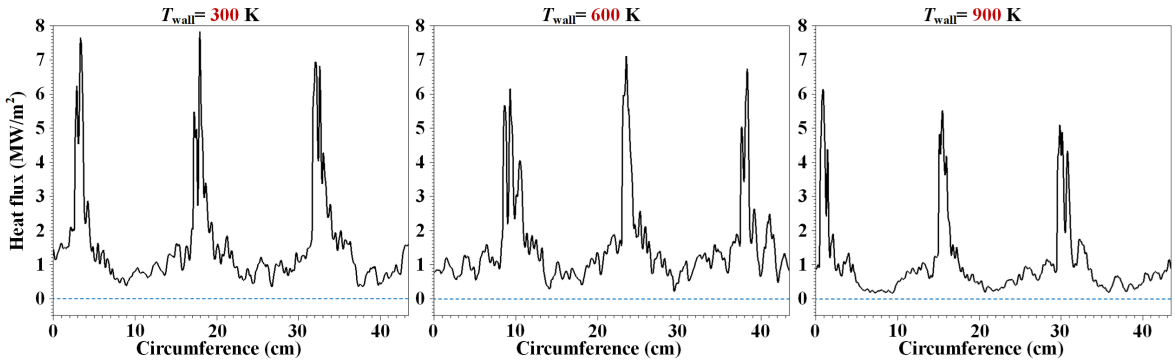

Figure 8.8 Profiles of heat flux on the inner wall in the circumferential direction.

Figure 8.9 shows the heat flux in the case with walls of 900 K at different axial positions. The heat flux is observed lower when the sample line is close to the air inlet on the inner wall (z = 0 to 1.6 mm). The negative heat flux at z = 2 mm represents the heat added from the wall into the internal flow field. The high-temperature wall heats the low-temperature unburned gases. The heat addition decreases downstream and there is no negative heat flux at the axial location (z = 6.9 mm) where maximum heat release occurs. The axial heat flux distribution implies a varying axial heat load in RDEs. This requires thermal management in future practical experimental designs.

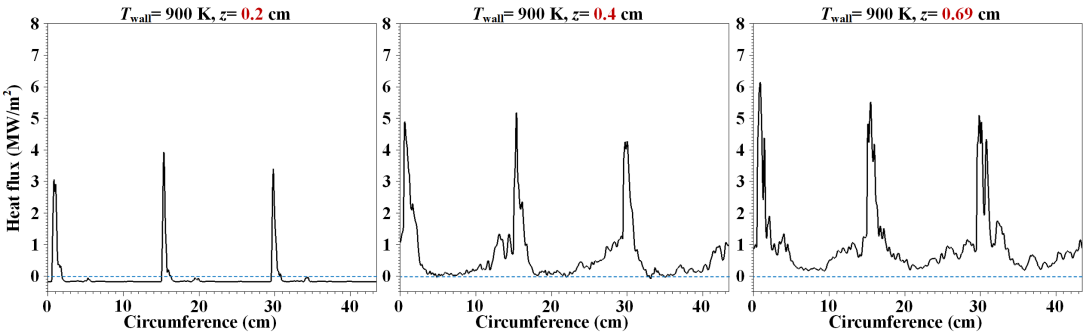

Figure 8.9 Profiles of heat flux on the inner wall at different axial locations.

The heat flux peak on the outer wall is lower than that on the inner wall, as shown in Figure 8.10. The heat flux peak is 5.89 MW/m^2, 4.85 MW/m^2 and 5.01 MW/m^2 when the wall is 300 K, 600 K and 900 K, respectively. As compared to the positive heat flux on the inner wall, a negative heat flux is observed in some regions of the outer wall at the axial location where the heat flux peak occurs. As the air is injected through the slots on the inner wall, the impact of the air and hydrogen jets results in the triangular mixture layer on the outer wall, as shown in the previous temperature slices. The low-temperature mixture absorbs the heat from high-temperature walls. The temperature on the inner wall is relatively higher due to the lack of the impact of low-temperature reactants and the existence of the recirculation zone downstream.

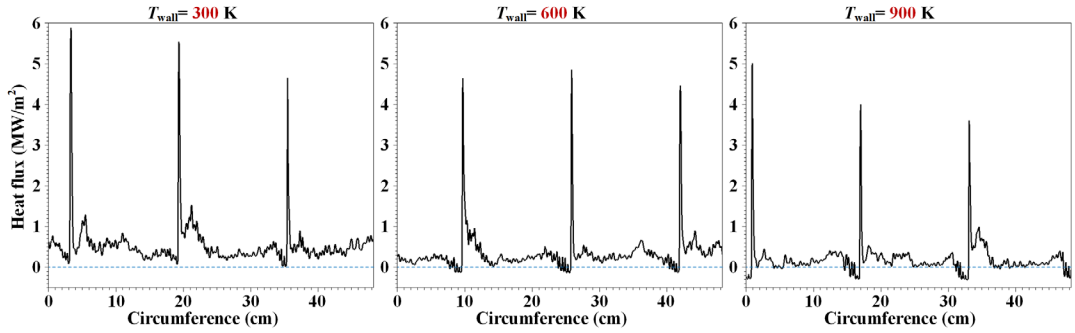

Figure 8.10 Profiles of heat flux on the outer wall in the circumferential direction.

Despite that the heat flux peak varies case by case when the temperature of walls increases, a monotonous decline is observed in terms of the averaged heat flux. The averaged heat flux over the respective wall is 0.61 MW/m^2, 0.57 MW/m^2, and 0.54 MW/m^2. Although the decline is comparable to that on the inner wall, the differences between the averaged heat flux on the outer wall are relatively small. This result indicates that the temperature gradient in the vicinity of the outer wall is more comparable. The temperature of the gases near the wall decreases with the decreasing temperature of walls, as shown in both Figure 8.3 and Figure 8.4. The cooling effects of the unburned mixture near the outer wall play a vital role in the total heat loss and lead to the relatively lower averaged heat flux and its discrepancy on the outer wall.

The effects of cooling walls on rotating detonation waves are studied by numerical simulations on 3D adaptive meshes. Non-premixed hydrogen/air mixtures are injected with a uniform global

equivalence ratio. The simulation starts with adiabatic walls until it reaches a stable multiple-wave mode, and then the wall temperature is varied. The results indicate that the number of detonation waves in a stable mode remains unchanged by the wall temperature within a short simulation duration. The average detonation velocity deficit rises from 3.7% to 6.3% when cooling walls are utilized. The phase differences and temperature variations are noticeable, but the wall temperature has a limited effect on the temperature distribution in the middle of the channel. Despite the heat losses from the cooling walls, the low-temperature walls suppress the deflagration near the wall and result in more heat release in the high-pressure detonative region. The heat flux distribution indicates that the inner wall faces a severer heat load due to the lack of internal cooling from reactants under the present jet in cross flow injection scheme. This numerical study demonstrates that wall cooling to enable RDEs with extended operation will have only limited effects on detonation efficiency.

8.2 Effects of the non-slip walls

This section aims to investigate the effects of non-slip wall boundary conditions on RDE simulations. The adiabatic Case 1 in Table 7.2 is further analysed. Figure 8.11 presents the pressure distribution on slices along the axial direction. The area of high-pressure regions decreases along the axial direction due to lateral expansion behind the detonation. The detonation waves rotate clockwise, accompanied by pressure waves reflected between the inner and outer walls. The leading front takes on a finger-like shape on the head plane. As depicted in Figure 8.11 on the z = 0.5 cm plane, the mainstream flow is slower than the flow near the inner wall, resulting in a leading wave curvature. The difference diminishes as the flow propagates towards the outlet.

Figure 8.12 illustrates the distribution of axial velocity on the slices. The region behind the detonation front is blocked, and the injection velocity of the hydrogen jet is nearly zero. An increase in axial velocity is observed behind the detonation, corresponding to the axial expansion of burned gases. The differences also decrease as the flow propagates towards the outlet. What stands out in this figure is the low-velocity regions close to the inner wall from z = 0.5 cm to z = 1.0 cm. These regions are the recirculation zone of the air slot on the inner wall.

As displayed in Figure 8.13, the detonation wave structure is represented near the head plane. The recirculation zone near the inner wall enhances the mixing between hydrogen and air. It leads to a faster propagating detonation. As a result, the detonation front changes from a finger-like shape in Figure 8.13 (a) to a structure with leading wave curvature in Figure 8.13 (b).

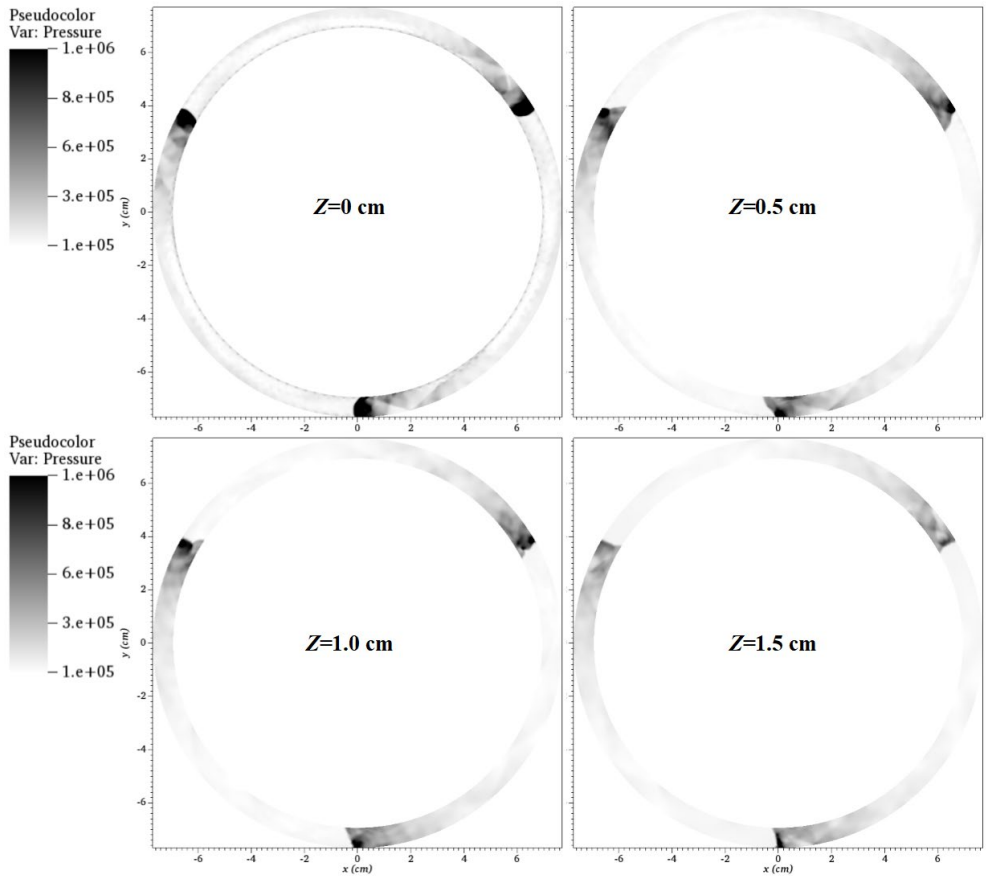

Figure 8.11 Pseudo-colour images of pressure distribution slices on the *z*-planes.

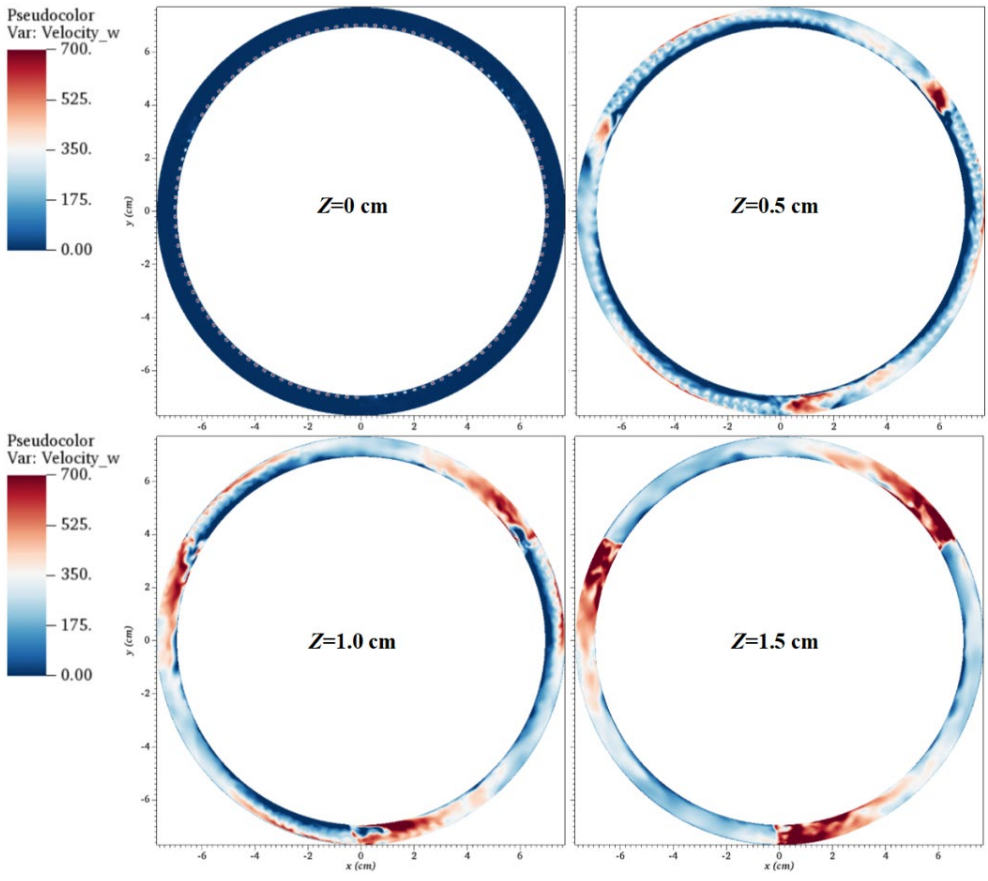

Figure 8.12 Pseudo-colour images of axial velocity distribution slices on the *z*-planes.

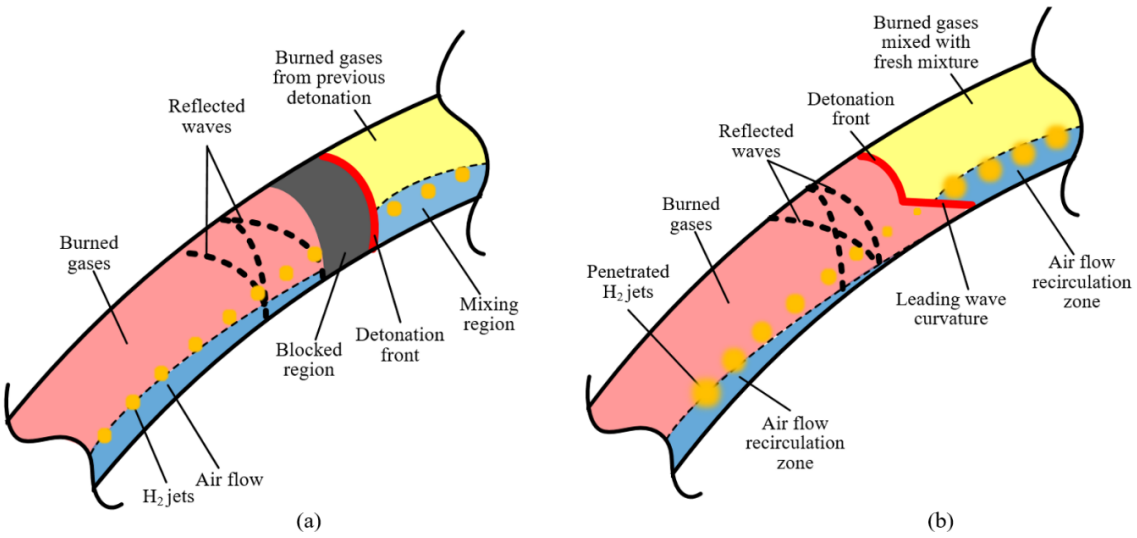

Figure 8.13 Schematic of the rotating detonation wave structures on the *z*-planes near the head of chamber.

The pressure and axial velocity distributions are further extracted on planes closer to the outlet. As shown in Figure 8.14 and Figure 8.15, the detonation front and oblique shock waves are flattened with different schemes in the boundary layer. The axial velocity increases and its changes become more uniform along the circumferential direction when the gases expand towards the outlet. Another observation from these figures is the increasingly prominent boundary layer flow. The non-slip boundary condition highlights the presence of low-velocity regions on both the inner and outer walls.

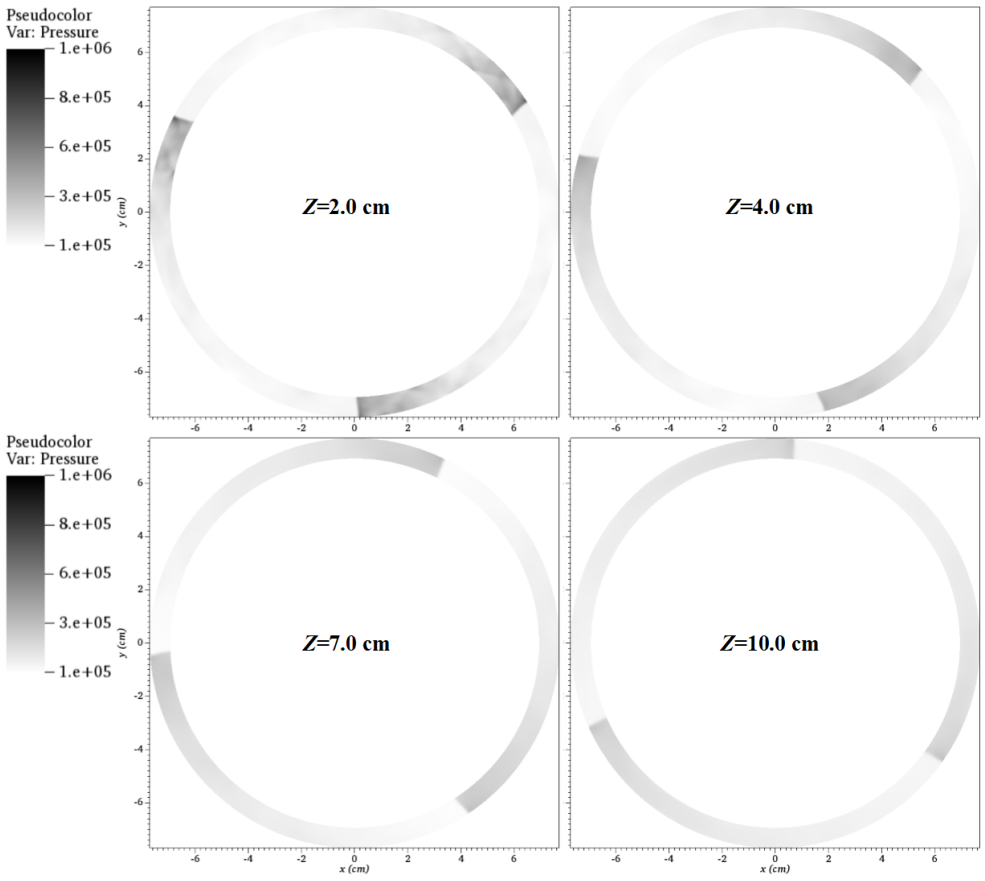

Figure 8.14 Pseudo-colour images of pressure distribution slices on the *z*-planes.

When extracting the planes where only the oblique shock waves exist, the reflected waves behind the detonation disappear. The low-velocity boundary layer results in different wave patterns, as depicted in Figure 8.16. For the detonation front, the extended deflagration [232] on the adiabatic walls increases the temperature ahead of the detonation. The mixing of burned gases and fresh mixture has a slightly lower temperature in the middle of the channel, resulting in higher velocity on the walls. On the other hand, for the non-reacting oblique shock wave, the burned gases flow slower in the near wall region due to the influences of the viscous walls, and the middle shock front leads. In both cases, the boundary layer is not thick enough compared to the channel width; hence, the influence of virtual contraction is limited and not discussed.

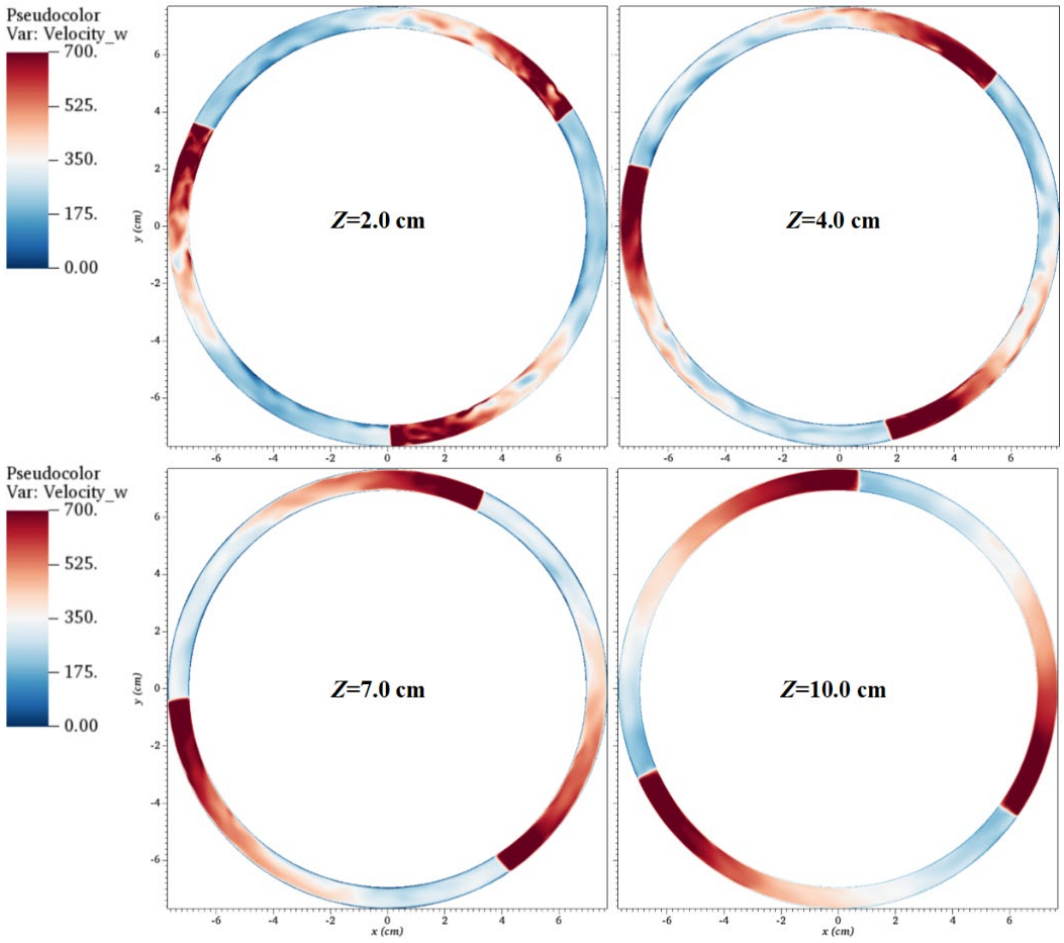

Figure 8.15 Pseudo-colour images of axial velocity distribution slices on the *z*-planes.

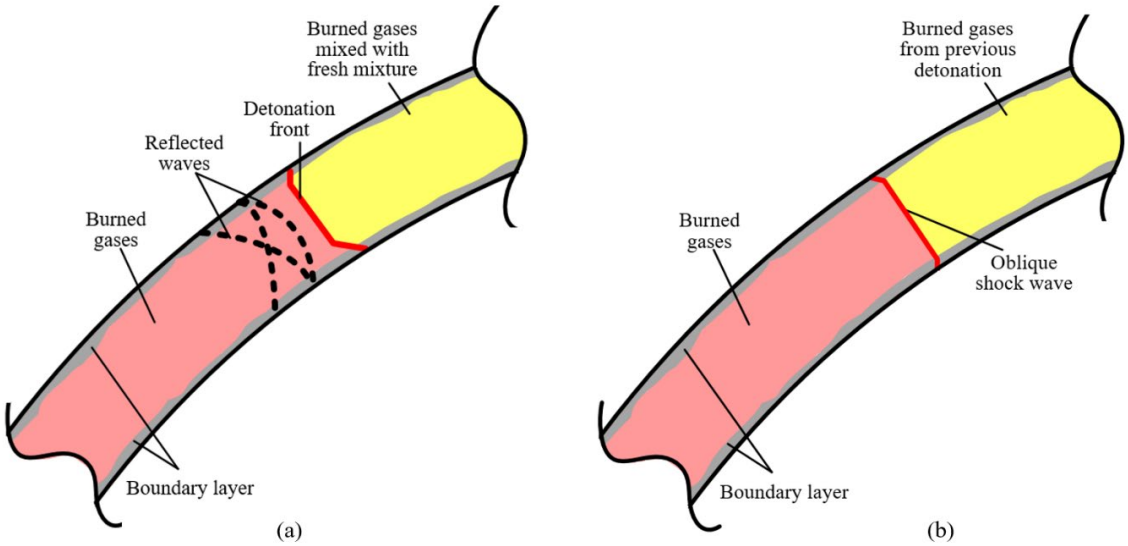

Figure 8.16 Schematic of the rotating detonation wave structures on the *z*-planes away from the head of chamber.

8.3 Effects of the channel width

In addition to the wall temperature and wall friction, the effects of the geometry can play a significant role when the channel width is not relatively negligible compared to the chamber radius. In this section, the effects of different channel widths are numerically studied. The baseline case simulated in this study is the hydrogen RDE (H-3D-159) with the stretched mesh, as introduced in Section 7.2. The total hydrogen mass flow rate remains constant at 9.3 g/s and the air mass flow rate is given as 320 g/s in the following computations. The outer diameter is fixed at 153.9 mm, while the inner diameter is varied. Table 8.1 presents the simulated cases with different channel widths, ranging from 3.8 mm to 15.2 mm, which corresponds to a ratio of width and outer radius from 4.938% to 19.753%. A non-slip isothermal wall boundary condition is employed and the wall temperature for all cases is set to 600 K.

Table 8.1 Configurations of cases with different channel widths.

Case	Inner radius (mm)	Air slot height (mm)	H_2 jets centre radial location (mm)	Outer radius (mm)	Channel width (mm)	w/R_{out}
1	73.15	1.52	73.8	76.95	3.8	4.938%
2	69.35	1.60	70.0	76.95	7.6	9.877%
3	61.75	1.80	62.4	76.95	15.2	19.753%

The 3D temperature distribution of the RDE is shown in Figure 8.17. All the cases run into a stable two-wave mode. In previous cases and the case with a channel width ratio of 4.938%, the detonation waves rotate in a clockwise direction when viewed from the outlet. However, an interesting finding is that the rotation of detonation changes to a counterclockwise direction when the channel width

increases. The number of detonation waves remains unchanged since the mass flow rate is kept constant. Figure 8.18 shows the temperature distribution on the inner walls. Discrete high-temperature regions are visible behind the detonation wave in all cases.

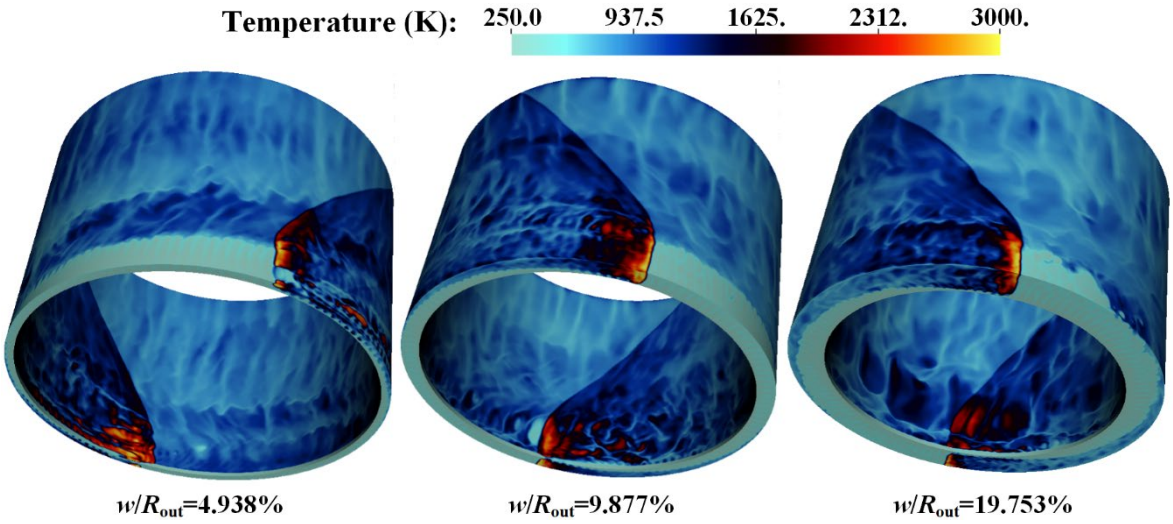

Figure 8.17 Pseudo-colour images of temperature distribution in cases with different channel widths.

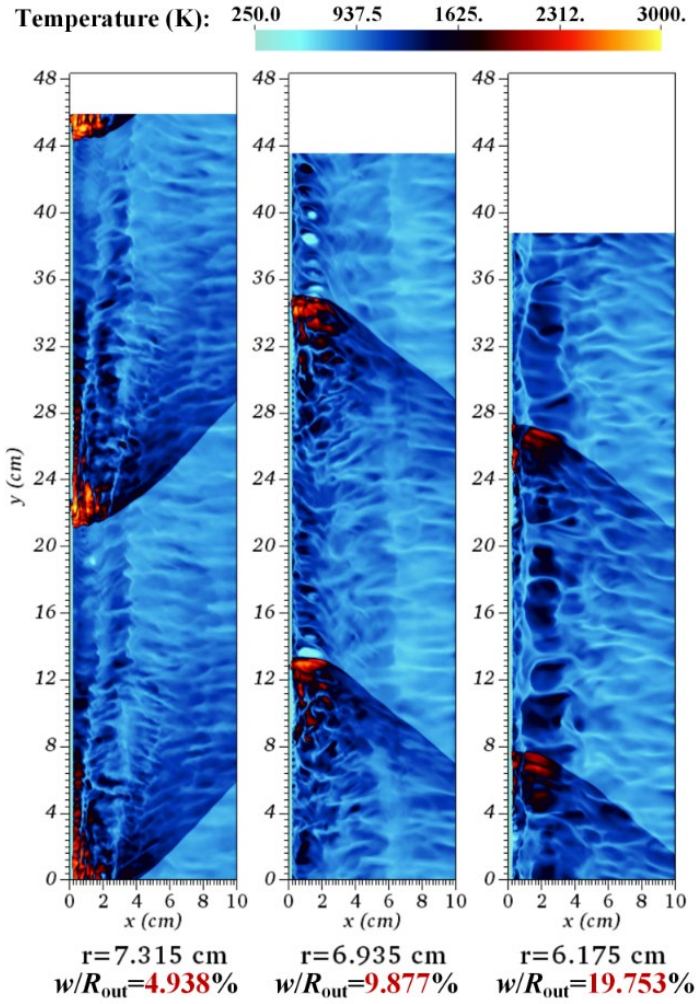

Figure 8.18 Pseudo-colour images of unrolled temperature slices on the inner wall.

Due to the cooling effect of the wall, the deflagration on the wall disappears. The highest temperature peak is observed in the case with the smallest channel width. The temperature stratification on the wall can be attributed to the non-uniform temperature flow field within the channel.

Figure 8.19 displays the temperature field on the middle plane. The slip lines on the contact surface become more irregular in the case with the largest channel width. More parasitic combustion is also observed in this case. Only a small amount of mixture is pre-burning when the channel width is small. Parasitic combustion ahead of the detonation is a result of the non-premixed injection and recirculation zones in the mixture layer. This finding indicates that the recirculation of the mixture in the channel is restricted when the channel width is small.

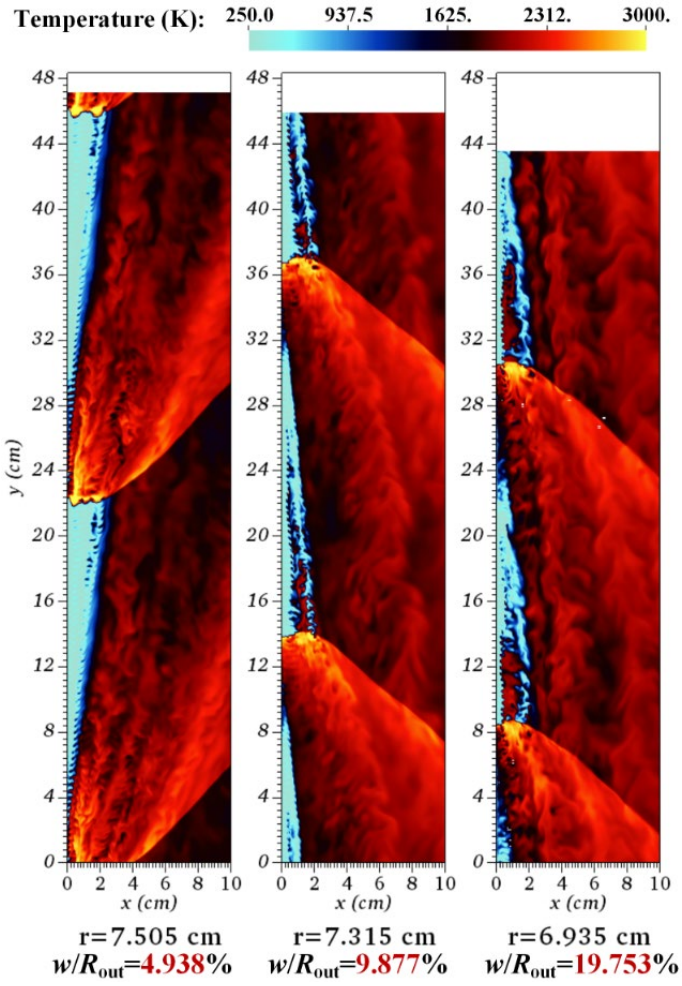

Figure 8.19 Pseudo-colour images of unrolled temperature slices on the middle plane.

An unburned pocket is found following the detonation in the case with the smallest channel width, as displayed in Figure 8.20. This unburned low-temperature region is located at a similar height to the air slot. It is caused by the incomplete mixing of air and hydrogen when there is not enough room for mixing in the radial direction. When the air is injected via the slot on the inner wall, the high-speed flow impinges on the outer wall quickly before being mixed with hydrogen jets. Besides, the contact surface is unstable when the channel width is large, indicating a fluctuating penetration height of the mixture.

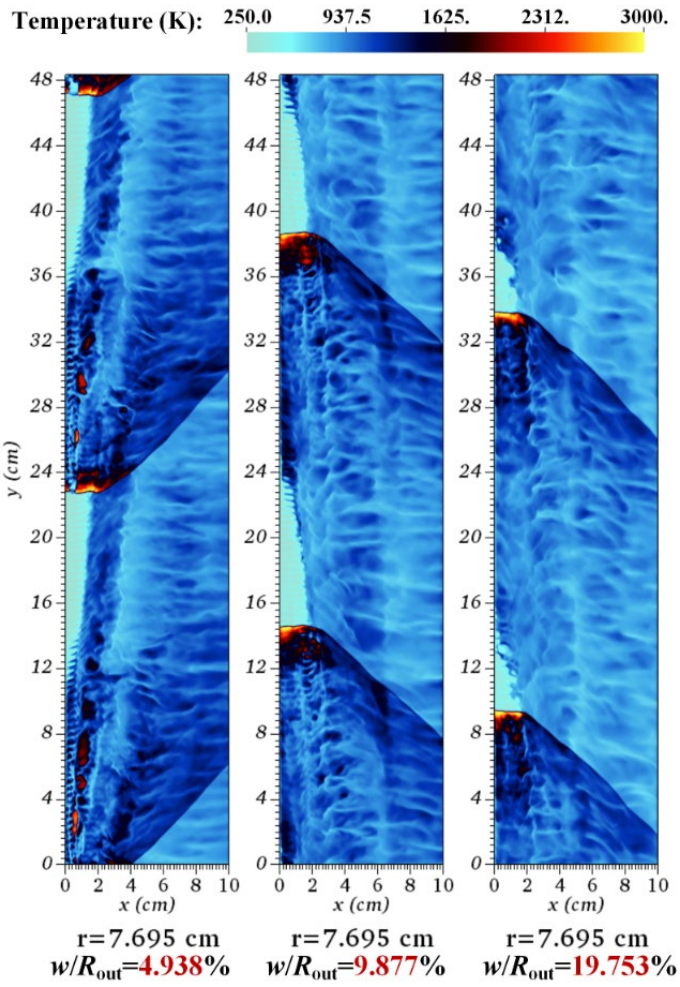

Figure 8.20 Pseudo-colour images of unrolled temperature slices on the outer wall.

Figure 8.21 shows the temperature gradient slices in the axial direction. This figure confirms the finding that the mixing is enhanced when the channel is wider. The air flow and hydrogen jets are injected as jets in cross flow. The wakes and vortexes downstream of the hydrogen jets form recirculation zones when the channel is wide enough. These recirculation zones strengthen the mixing and increase the probability of parasitic combustion occurrence.

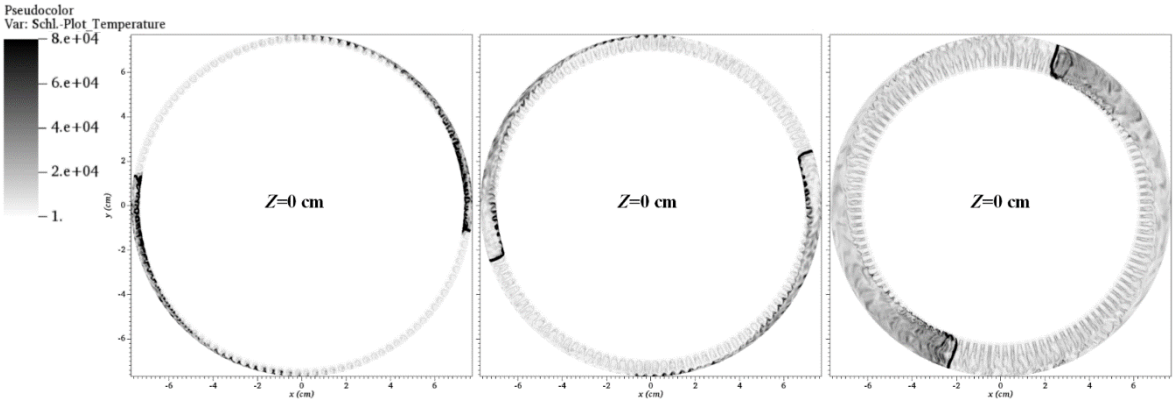

Figure 8.21 Pseudo-colour images of temperature gradient slices on the z = 0 cm planes.

The width of the chamber also has an influence on the detonation front structure. As shown in Figure 8.22, the slices are extracted below the detonation head height. The wave front is nearly oblique

when the channel width is small. The wave propagates faster near the inner wall (along the clockwise direction), whereas the detonation front can be divided into two parts when the channel width is large. The front close to the inner wall also flows fast (along the counterclockwise direction). The length of the wave ahead is large when increasing the channel width.

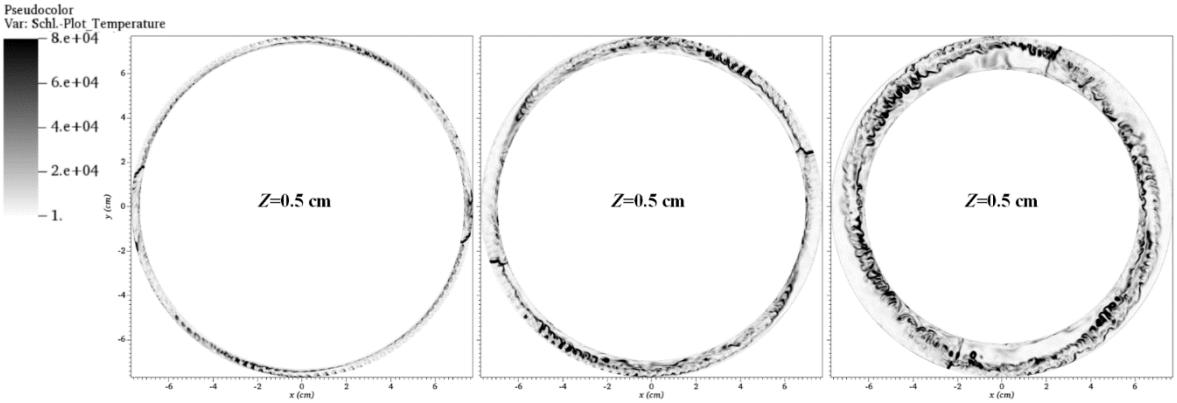

Figure 8.22 Pseudo-colour images of temperature gradient slices on the z = 0.5 cm planes.

Figure 8.23 shows the extracted temperature gradient slices at an axial height where oblique shock waves are captured. When the flow field is closer to the outlet, the shock front tends to be straight in the radial direction. The oblique shock front is still slightly curved when the channel curvature is large. This suggests that the expansion of the burned gas is more non-uniform in the radial direction, resulting in different pre-shock states. These non-uniform states lead to the curved shock wave.

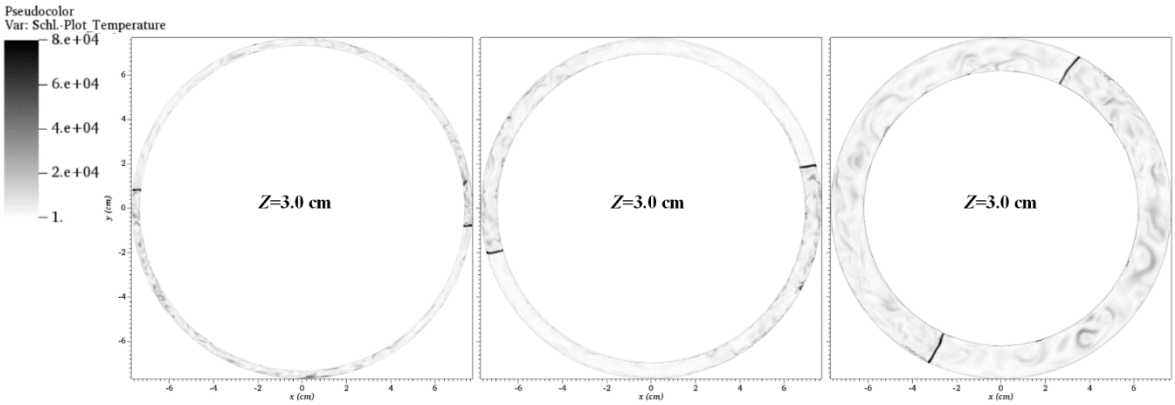

Figure 8.23 Pseudo-colour images of temperature gradient slices on the z = 3.0 cm planes.

Figure 8.24 presents the statistics of heat release in the radial direction. In the case with the smallest channel width, around 11.6% of the heat release occurs in the vicinity of the outer wall. Over 1% heat release occurs on the inner wall, which is also observed in Case 2. However, the heat release on the inner wall is less in Case 3 with the widest channel, which is due to the decreased area of the inner wall surface. The variation of the heat release distribution is also smoother when the channel width is large.

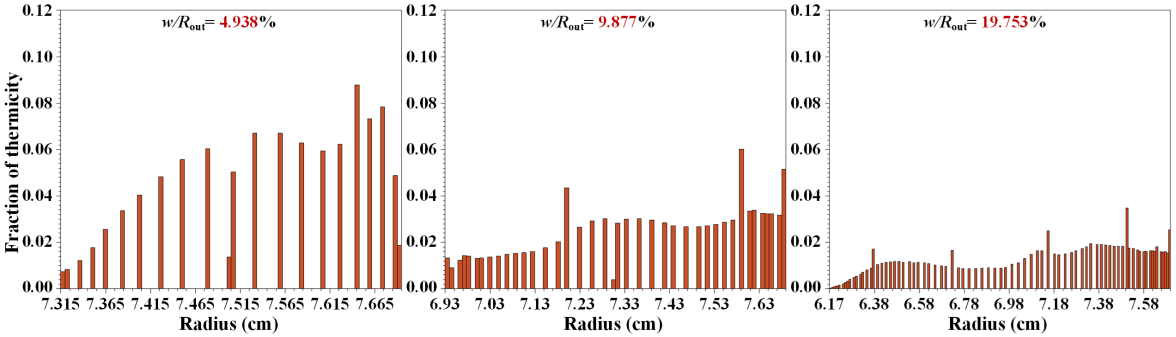

Figure 8.24 Distribution of thermicity in radial direction.

The heat flux profiles are extracted at their axial peak location on the inner wall, as shown in Figure 8.25. The peak flux heat is observed as 8.08 MW/m^2 when the channel width is smallest. A notable decrease is also recorded in terms of the heat flux peak when the channel width of the RDE is larger. The heat flux peak drops to 6.36 MW/m^2 and 3.82 MW/m^2 when the width-radius ratio is 9.877% and 19.753%, respectively. The axial location of the heat flux peak also varies in these cases. The maximum heat flux occurs at z = 8.41 mm and z = 13.72 mm when the width-radius ratio is 4.938% and 9.877%, whereas the heat flux peak occurs at z = 2.25 mm as this ratio increases to 19.753%. This indicates that the detonation strength varies in the axial direction when the channel width changes. As shown in the temperature slices of Figure 8.19, parasitic combustion weakens the local heat release on the detonation front, resulting in a stronger detonation front near the head plane when the channel width is the largest.

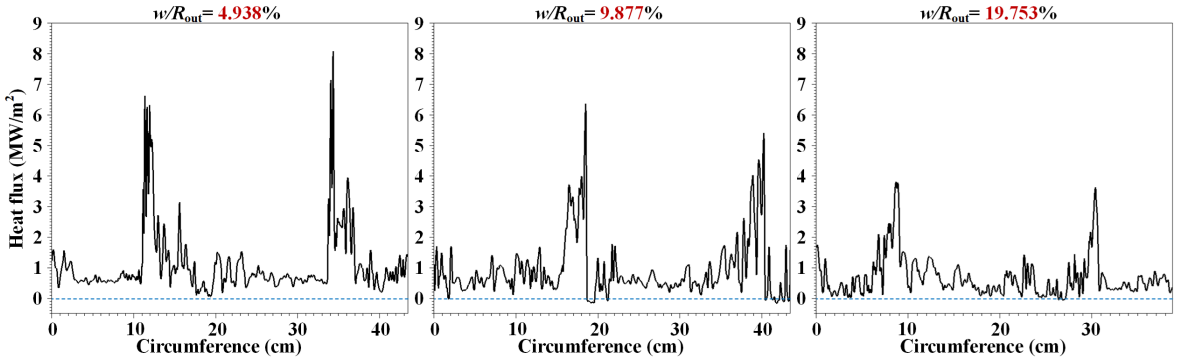

Figure 8.25 Profiles of heat flux on the inner wall.

The averaged heat flux on the inner wall is 0.60 MW/m^2, 0.52 MW/m^2 and 0.53 MW/m^2 when the width-radius ratio is 4.938%, 9.877% and 19.753%, respectively. The differences between the averaged heat flux are relatively minor compared to the heat spikes. Despite the high heat flux peak when the channel is narrow, the area of the inner wall is large, leading to a low area-averaged heat flux, and vice versa. The total heat load is higher on the wall when the channel width is small as the heat is released rapidly in the radial direction. The result shows that in a very thin annular RDE, the local extreme heat load is severe for thermal management. Considering the decreasing area of the inner wall when the channel width increases, the averaged heat flux on the wall also slightly increases.

The heat flux peak on the outer wall is presented in Figure 8.26 at the respective axial locations. The trend differs from that on the inner wall. The maximum heat flux slightly increases when increasing the width-radius ratio. The heat flux peak on the outer wall is 6.85 MW/m^2, 7.36 MW/m^2 and 7.41 MW/m^2 when the width-radius ratio is 4.938%, 9.877% and 19.753%, respectively. The axial location of the respective spike is 17.19 mm, 2.05 mm and 1.08 mm, and the maximum heat flux is close to the head plane when the channel is wider. Similarly, this difference in axial locations can also be explained by the weakened detonation front along the axial direction due to the existence of parasitic combustion. Another reason is that the local unburned pockets lead to the low-temperature regions near the head plane on the outer wall when the channel is relatively narrow.

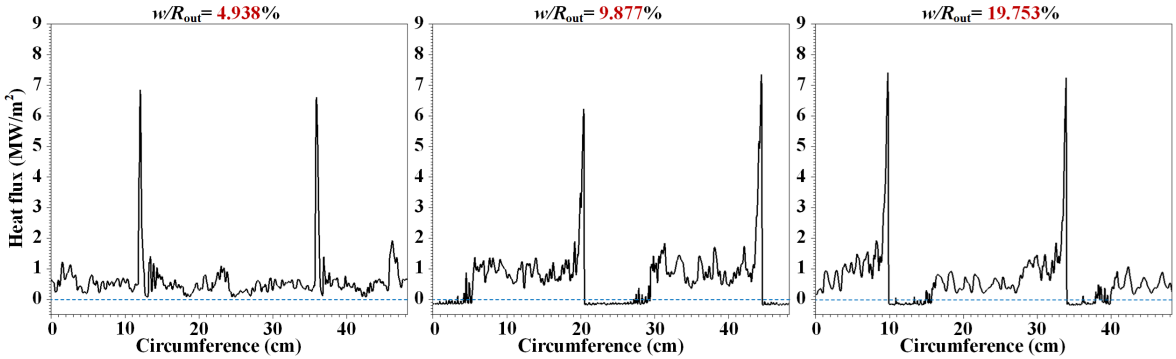

Figure 8.26 Profiles of heat flux on the outer wall.

The averaged heat flux on the outer wall is 0.47 MW/m^2, 0.40 MW/m^2 and 0.40 MW/m^2 when the width-radius ratio is 4.938%, 9.877% and 19.753%, respectively. As the outer radius remains unchanged in these cases, the area of the outer wall is the same. The difference between the total heat load on the outer wall is relatively small. On the one hand, the narrow channel requires that the temperature decreases in the vicinity of the walls quickly compared to the wider channel. On the other hand, the local insufficient mixing and the impact of unburned reactants in the narrow channel reduce the local heat release. As a result, the averaged heat flux on the outer wall varies not obviously when the width of the RDE changes.

In addition to the heat flux, the mixing is also influenced by the channel width of the annulus in a non-premixed RDE. Figure 8.27 shows the fraction of thermicity under different equivalence ratios in the whole chamber with different width-radius ratios. The fraction of the heat release in the fuel-lean region decreases when the channel is wider. The reactions in the chamber transition into a fuel-rich dominated operating condition.

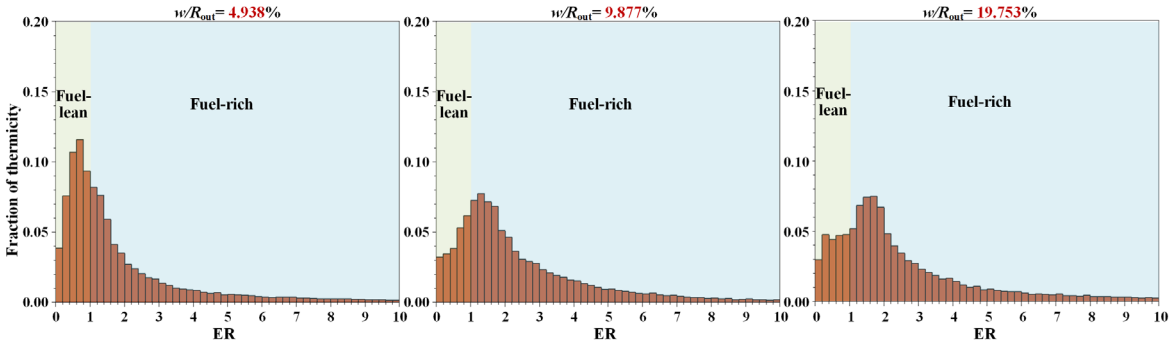

Figure 8.27 Fraction of thermicity as a function of equivalence ratio.

8.4 Chapter summary

This chapter was about the results of 3D RDE with different wall boundary conditions. Isothermal walls were firstly used in the computation to study the effects of cooling walls on the RDE performance. Then, the non-slip adiabatic wall conditions were tested with non-premixed injection. In addition, the influences of different channel widths were analysed using 3D models with different width-radius ratios. The main findings are drawn as follows:

- The effects of cooling walls were studied in the RDE operation process with multiple detonation heads. Non-premixed hydrogen/air mixtures were injected with a uniform global equivalence ratio. The simulation started with adiabatic walls until it reached a stable multiple-wave mode, and then the wall temperature was varied. The results indicated that the number of detonation waves in a stable mode remained unchanged by the wall temperature within a short simulation duration. The average detonation velocity deficit rose to 6.3% when cooling walls were utilized. The phase differences and temperature variations were noticeable, but the wall temperature had a limited effect on the temperature distribution in the mainstream.
- Cooling walls suppressed the secondary combustion wave, including parasitic combustion and commensal combustion. The cooling walls reduced the heat release below 0.5 MPa and enhanced the heat release between 0.5 MPa and 1 MPa compared to the adiabatic case. The high-pressure heat release below 1 MPa slightly decreased when cooling walls were used, indicating that the heat loss led to a weakened detonation. An unequal heat load was observed on the inner and outer wall of the RDE due to the jet in cross flow injection scheme and downstream burned zone. The low-temperature unburned mixture cooled the outer wall resulting in a lower averaged heat flux.
- The non-slip boundary had an influence on the RDE internal flow field along the axial direction, resulting in different leading shock front shapes. The leading front took on a finger-like shape on the head plane under the combined effect of the low-speed boundary layer on the outer wall and local dilution from the air slot on the inner wall. The recirculation zone of the air slot on the inner wall resulted in a structure with leading wave curvature. The

boundary layer flow was increasingly prominent along the circumferential direction when the gases expanded towards the outlet.

- The channel width of RDE had an influence on the detonation direction in the present simulations. The direction of detonation heads reversed when the chamber was wider. Combustion in the recirculation zones on the inner wall was suppressed when the channel width is increased. Unburned pockets were observed on the detonation heads when the channel was the narrowest. The mixture layer length decreased with increasing channel width and the contact surface was more fluctuating. The detonation structure was also varying on the middle plane. The small channel width suppressed parasitic combustion ahead of the detonation, leading to higher detonation heads.
- A higher heat flux peak was observed on the inner wall of RDE with the smallest channel width. The total heat release on both walls increased with a decreasing width-radius ratio. These results indicated a severe thermal condition when the annular channel was narrow. The heat flux peaks on both walls were close to the head plane in the widest case. This was attributed to the presence of parasitic combustion, which weakened the local heat release on the detonation heads in the axial direction. The changes in the annular width also varied the local mixing degree in the chamber. The unburned pockets and insufficient mixing in the narrowest RDE decreased the heat flux peak on the outer wall. The RDE transitioned from a fuel-lean dominated operation mode to a fuel-rich operation mode when increasing the channel width.

In summary, the computations of RDE with cooling walls contribute to existing knowledge of cooling walls in RDE by providing insight into the operation process and the multi-wave mode. This work contributes to the understanding of how the cooling system interacts with the internal flow field. It demonstrates that wall cooling to enable RDEs with extended operation will have only limited effects on detonation efficiency. However, the channel width has a more obvious influence on the RDE flow field. The detonation direction is observed to change when increasing the chamber width. The unburned pockets on the detonation heads and higher heat flux peaks on the inner wall are observed in the case with the smallest width. These findings indicate that the cooling wall plays an increasingly notable role in the RDE internal flow structure when the chamber channel is narrow. The consequential variations in mixing also influence parasitic combustion, the detonation strength and the local heat release.

Chapter 9 Conclusions

9.1 Summary and contributions

In this thesis, a detailed chemistry solver has been developed on adaptive curvilinear meshes within the AMROC framework. The primary objective of this solver was to enable the simulation of detonation problems, with a particular emphasis on rotating detonation with detailed chemistry. This achievement was accomplished by combining the adaptive mesh refinement technique with structured curvilinear meshes. Several essential extensions were made to the existing code in AMROC, including the application of coordinate transformation on multi-species equations, grid-aligned inviscid flux schemes, a second-order accurate MUSCL-Hancock scheme and a second-order accurate central difference method for viscous fluxes. The computation of geometry information was also designed for 3D meshes. Additionally, the operators for AMR level transfer were modified, along with the flux conservation correction on the coarse-fine interface.

The method of manufactured solution was used to verify the solver on different meshes. The results confirmed that the present solvers can achieve second-order accuracy when simulating a smoothly varying flow field on a hierarchically refined mapped mesh. The preservation of conservation across the level interface was also successfully verified in a freestream flow scenario. To further assess the accuracy of the developed solver, comprehensive benchmark tests were conducted. The solutions obtained by the solver were in good agreement with published numerical and experimental results. It demonstrated the solver's capability of handling multi-species reacting flows featuring discontinuities on the adaptive curvilinear mesh.

The numerical configurations of different RDEs were detailed including the 2D unwrapped and 3D annular model. The mesh dependency study showed that the chosen mesh adequately captured the characteristics in the flow field, while a high mesh resolution was required to resolve the cellular structure of the detonation front. In addition, a mass flow rate inlet was employed referring to a micro ethylene/oxygen RDE experiment. Stable two- and three-wave modes were obtained in the simulations. The numerical detonation velocities were in good agreement with the C-J velocities, but there were still some discrepancies between the numerical results and the experimental results. Despite these differences, the qualitative behaviour was similar and the number of waves increased with the increasing inflow mass flow rate. The 3D numerical results showed a comparable pressure distribution at different locations compared to the experimental results.

Premixed injection with varying equivalence ratio differences was simulated in a 2D ethylene unwrapped RDE as an initial approach to studying the influences of non-uniform premixing. The simulations of the partially premixed injection were conducted in a 3D hydrogen RDE. The effects of the hydrogen bypass flow on RDE performance were analysed. More 3D numerical studies on the

effects of wall conditions were explored in the last chapter. The wall temperature was varied during the operation to investigate the impact of cooling walls on rotating detonation. The wave structure evolution was also observed in the non-slip case. Finally, the hydrogen RDE was simulated with different channel widths. Thermicity was quantified in these cases to explore the influence of cooling walls and geometry on heat load and global heat release.

The first major contribution is concluded as the development work conducted within the AMROC framework. The numerical methods were extended to curvilinear meshes for a non-Cartesian geometry in AMROC. The entire mapping strategy in AMROC has been extended to be used in a multi-species and multi-step chemistry solver. These modifications have been implemented as a new submodule and the 3D extension including the geometry information computation have also been built up in AMROC. To the best of the author's knowledge, this study marked the first reported utilization of the method of manufactured solutions to verify the 3D adaptive solver's accuracy. The flux fix-up procedure was also tested to confirm the conservation across the level interface. Different benchmark cases were established to validate the solver's accuracy in terms of inviscid shock waves, viscous flows, boundary flows and shock-induced combustion problems. The source code has been implemented into the AMROC framework and these benchmark cases have also been added into the AMROC repository. The set-up of verification and validation cases is another contribution to this repository.

The developed solver was then adopted to demonstrate its capability for detonation simulations. The 3D cellular detonation propagation in a smooth pipe bend was simulated, successfully reproducing typical features observed in published experimental work. The solver's capabilities were further demonstrated through several typical cases, including detonation propagation in a smooth round tube and interaction with boundary layers in a channel. The dynamic adaption method reduced the total mesh scale from $O(10^8) \sim O(10^9)$ to $O(10^6) \sim O(10^7)$ in these 3D cases without losses of main characteristics, such as the structure of the detonation front.

The second major contribution of the present work is the application of the block-structured adaptive mesh refinement technique to rotating detonation simulation with a combination of detailed chemistry mechanisms. The premixed RDE was first simulated with 2D adaptive meshes to study the initiation process in an ethylene RDE and a hydrogen RDE, respectively. The simulations demonstrated that the initial configuration artificially generated one detonation head and then spontaneously transitioned to a stable multi-wave mode. The adaptive meshes were shown to dynamically capture the main features including the detonation heads, oblique shock and the mixture layer. The local equivalence ratio difference was studied as an approach to simulating the non-uniform premixing injection.

The influence of partially premixed injection in RDE was then explored using the 3D solver. Three cases with different premixing percentages were compared with the fully non-premixed case. The

flame index and thermicity in the RDE were extracted to quantify the reactions dominated by premixed flows. The results showed that the thrust and specific impulse increased by 8.53% when the bypass flow rate of hydrogen increased to 15%. The number of detonation heads remained unchanged with partially premixed injection. This study has confirmed the existing experimental findings which found that the RDE could benefit from the partial premixing but the detonation velocity increase was not noticeable. This work contributes to limited numerical studies of partially premixed RDE.

The solver was finally used to study the influences of cooling walls on the non-premixed RDE. It provided a novel approach to varying the wall temperature in the operation process. The flow field was qualitatively analysed to describe the evolution of the multi-wave structure in the process. The statistics of the thermicity presented the heat release according to different references, such as the local pressure and the equivalence ratio. This analysis quantified the reactions occurring in the detonation or deflagration regime. The internal flow structure led to unequal heat loads on the walls. The introduction of wall cooling had a limited influence on the temperature distribution in the middle of the channel. The numerical results highlight the potential usefulness of a cooling system in a long-duration operation with only limited effects on detonation efficiency. In addition, the influences of channel width on the heat release were studied. The results indicated that despite the unburned pockets and insufficient mixing, the narrow RDE faced a severe thermal condition. The presence of parasitic combustion in a wide RDE led to the heat flux spike near the head plane. These understandings can aid in the experimental thermal management of RDE.

9.2 Future work

The present solver shows a stable capability on rotating detonation simulations, while it still has some limitations. The solver can only deal with geometries through a single block mapping strategy. The extension of the mapping strategy to a multi-block hierarchy can improve the ability of the solver to simulate more complex geometry. Besides, the sub-grid turbulence chemistry is neglected in the present solver and a finite rate laminar chemistry is employed based on the CHEMKIN library. The influences of turbulence chemistry interactions on detonation are still unknown as most studies in this community still adopt the induction chemistry assumption. The absence of turbulence chemistry for detonation problems is due to the fact that general turbulence models are primarily developed for subsonic combustion scenarios. The detonation simulation has been considered as a convection-dominated problem; however, the secondary combustion waves play non-trivial roles in the RDE. If the adiabatic wall assumption is used, the low-pressure and low-velocity deflagration near the wall requires to be solved accurately. The influence of turbulence chemistry interactions will need to be studied for a non-ideal RDE simulation.

Another improvement on the present solver is in the aspect of computational efficiency when solving a chemistry involved problem. The load balance in the present solver adopts the same strategy as used in the original AMROC framework. The workload only considers the number of cells in each block and excludes the unbalanced computational cost of the chemistry part. The current method is conducting partition at a given time frequency on the coarsest level. As the mesh is refined at the location where the stiff chemistry is solved, this method can distribute more processors to these regions where the chemical reaction occurs. A more advanced dynamic load balancing method will be needed to tackle the load imbalance issues in a 3D rotating detonation simulation in the future.

In addition to the accuracy and efficiency, the stability of the present solver can also be further studied when solving non-premixed detonation problems. Although the double-flux and hybrid-flux schemes have been implemented in this work, they have not been used to simulate the rotating detonation problems due to numerical crashes. Alternatively, a more diffusive Riemann solver was adopted to simulate the non-premixed detonation and retain its conservation properties. The numerical instabilities in the flow field with a large specific heat ratio gradient can only be solved with a non-conservative or quasi-conservative approach. This is regarded as a compromise between the conservation and the numerical stability. These non-conservative schemes will need to be studied for their quantitative influences on rotating detonation before being used in RDE simulations.

Based on the present numerical results obtained from the partially premixed RDE and wall-cooled RDE simulations with cooling walls, further investigation is necessary to explore additional physical issues. The effects of partial premixing on different injection schemes remain unknown and the blending of different fuels into the air stream has not been numerically studied. Besides, neither the adiabatic wall nor the isothermal wall boundary condition predicts the experimental initiation process correctly. A more advanced heat flux boundary condition can be applied to the walls to study the initial responses from the wall on the internal detonation structure. The study of initial ignition and detonation quenching will benefit from a time-varying heat flux boundary in RDE simulations.

References

[1] Khandelwal, B., Karakurt, A., Sekaran, P.R., Sethi, V. and Singh, R., 2013. Hydrogen powered aircraft: The future of air transport. Progress in Aerospace Sciences, 60, pp.45-59.

[2] Momirlan, M. and Veziroglu, T.N., 2002. Current status of hydrogen energy. Renewable and sustainable energy reviews, 6(1-2), pp.141-179.

[3] Khosravi, A., Koury, R.N.N., Machado, L. and Pabon, J.J.G., 2018. Energy, exergy and economic analysis of a hybrid renewable energy with hydrogen storage system. Energy, 148, pp.1087-1102.

[4] Williams, F.A., 2018. Combustion theory. CRC Press, Boca Raton.

[5] Kailasanath, K., 2000. Review of propulsion applications of detonation waves. AIAA journal, 38(9), pp.1698-1708.

[6] Lee, J.H.S., 2014. The detonation phenomenon. Cambridge University Press, Cambridge.

[7] Hishida, M., Fujiwara, T. and Wolanski, P., 2009. Fundamentals of rotating detonations. Shock waves, 19(1), pp.1-10.

[8] Anand, V. and Gutmark, E., 2019. Rotating detonation combustors and their similarities to rocket instabilities. Progress in Energy and Combustion Science, 73, pp.182-234.

[9] Wolański, P., 2013. Detonative propulsion. Proceedings of the combustion Institute, 34(1), pp.125-158.

[10] Lu, F.K. and Braun, E.M., 2014. Rotating detonation wave propulsion: experimental challenges, modeling, and engine concepts. Journal of Propulsion and Power, 30(5), pp.1125-1142.

[11] Xie, Q., Ji, Z., Wen, H., Ren, Z., Wolanski, P. and Wang, B., 2020. Review on the Rotating Detonation Engine and It's Typical Problems. Transactions on Aerospace Research, 2020(4), pp.107-163.

[12] Lin, W., Zhou, J., Liu, S., Lin, Z. and Zhuang, F., 2015. Experimental study on propagation mode of H2/Air continuously rotating detonation wave. International Journal of Hydrogen Energy, 40(4), pp.1980-1993.

[13] Frolov, S.M., Aksenov, V.S., Ivanov, V.S. and Shamshin, I.O., 2015. Large-scale hydrogen–air continuous detonation combustor. International Journal of Hydrogen Energy, 40(3), pp.1616-1623.

[14] Wang, Y., Le, J., Wang, C. and Zheng, Y., 2018. A non-premixed rotating detonation engine using ethylene and air. Applied thermal engineering, 137, pp.749-757.

[15] Peng, H.Y., Liu, W.D., Liu, S.J., Zhang, H.L. and Jiang, L.X., 2020. Hydrogen-air, ethylene-air, and methane-air continuous rotating detonation in the hollow chamber. Energy, 211, p.118598.

[16] Thomas, L., Schauer, F., Hoke, J. and Naples, A., 2011, January. Buildup and operation of a rotating detonation engine. In 49th AIAA Aerospace Sciences Meeting including the New Horizons Forum and Aerospace Exposition (p. 602).

[17] Andrus, I.Q., Polanka, M.D., King, P.I., Schauer, F.R. and Hoke, J.L., 2017. Experimentation of premixed rotating detonation engine using variable slot feed plenum. Journal of Propulsion and Power, 33(6), pp.1448-1458.

[18] Dunn, I.B., Thurmond, K., Ahmed, K. and Vasu, S., 2019. Wave dynamics of a partially premixed rotating detonation engine. In AIAA Propulsion and Energy 2019 Forum (p. 4128).

[19] Burke, R., Rezzag, T., Dunn, I., Flores, W. and Ahmed, K., 2021. The effect of premixed stratification on the wave dynamics of a rotating detonation combustor. International Journal of Hydrogen Energy, 46(54), pp.27816-27826.

[20] Rankin, B.A., Fotia, M.L., Naples, A.G., Stevens, C.A., Hoke, J.L., Kaemming, T.A., Theuerkauf, S.W. and Schauer, F.R., 2017. Overview of performance, application, and analysis of rotating detonation engine technologies. Journal of Propulsion and Power, 33(1), pp.131-143.

[21] Ishihara, K., Nishimura, J., Goto, K., Nakagami, S., Matsuoka, K., Kasahara, J., Matsuo, A., Funaki, I., Moriai, H., Mukae, H. and Yasuda, K., 2017. Study on a long-time operation towards rotating detonation rocket engine flight demonstration. In 55th AIAA aerospace sciences meeting (p. 1062).

[22] Lim, D., Heister, S.D., Humble, J. and Harroun, A.J., 2021. Experimental investigation of wall heat flux in a rotating detonation rocket engine. Journal of Spacecraft and Rockets, 58(5), pp.1444-1452.

[23] Bykovskii, F.A. and Vedernikov, E.F., 2009. Heat fluxes to combustor walls during continuous spin detonation of fuel-air mixtures. Combustion, Explosion, and Shock Waves, 45, pp.70-77.

[24] Theuerkauf, S.W., Schauer, F., Anthony, R. and Hoke, J., 2014. Average and Instantaneous Heat Release to the Walls of an RDE. In 52nd Aerospace sciences meeting (p. 1503).

[25] Theuerkauf, S.W., Schauer, F., Anthony, R. and Hoke, J., 2015. Experimental characterization of high-frequency heat flux in a rotating detonation engine. In 53rd AIAA Aerospace sciences meeting (p. 1603).

[26] Stevens, C.A., Fotia, M., Hoke, J. and Schauer, F., 2019. An experimental comparison of the inner and outer wall heat flux in an RDE. In AIAA SciTech 2019 Forum (p. 1252).

[27] Zhou, R., Wu, D. and Wang, J., 2016. Progress of continuously rotating detonation engines. Chinese Journal of aeronautics, 29(1), pp.15-29.

[28] Berger, M.J. and Oliger, J., 1984. Adaptive mesh refinement for hyperbolic partial differential equations. Journal of Computational Physics, 53(3), pp.484-512.

[29] Berger, M.J. and Colella, P., 1989. Local adaptive mesh refinement for shock hydrodynamics. Journal of Computational Physics, 82(1), pp.64-84.

[30] Deiterding, R., 2003. Parallel adaptive simulation of multi-dimensional detonation structures. PhD thesis, Brandenburg University of Technology Cottbus–Senftenberg, Cottbus.

[31] Cai, X., Liang, J., Deiterding, R., Mahmoudi, Y. and Sun, M., 2018. Experimental and numerical investigations on propagating modes of detonations: Detonation wave/boundary layer interaction. Combustion and flame, 190, pp.201-215.

[32] Wang, Y., Han, W., Deiterding, R. and Chen, Z., 2018. Effects of disturbance on detonation initiation in H2/O2/N2 mixture. Physical Review Fluids, 3(12), p.123201.

[33] Ziegler, J.L., Deiterding, R., Shepherd, J.E. and Pullin, D.I., 2011. An adaptive high-order hybrid scheme for compressive, viscous flows with detailed chemistry. Journal of Computational Physics, 230(20), pp.7598-7630.

[34] LeVeque, R.J., 2002. Finite volume methods for hyperbolic problems. Cambridge university press, Cambridge.

[35] Deiterding, R., 2009. A parallel adaptive method for simulating shock-induced combustion with detailed chemical kinetics in complex domains. Computers & Structures, 87(11-12), pp.769-783.

[36] Deiterding, R., 2011. Block-structured adaptive mesh refinement-theory, implementation and application. In Esaim: Proceedings, pp. 97-150.

[37] Fedkiw, R.P., Aslam, T., Merriman, B. and Osher, S., 1999. A non-oscillatory Eulerian approach to interfaces in multimaterial flows (the ghost fluid method). Journal of computational physics, 152(2), pp.457-492.

[38] Sethian, J.A., 1999. Level set methods and fast marching methods. Cambridge University Press, Cambridge.

[39] Osher, S. and Fedkiw, R.P., 2005. Level set methods and dynamic implicit surfaces. Springer, New York.

[40] Ingram, D.M., Causon, D.M. and Mingham, C.G., 2003. Developments in Cartesian cut cell methods. Mathematics and Computers in Simulation, 61(3-6), pp.561-572.

[41] Ji, H., Lien, F.S. and Yee, E., 2008. A robust and efficient hybrid cut-cell/ghost-cell method with adaptive mesh refinement for moving boundaries on irregular domains. Computer methods in applied mechanics and engineering, 198(3-4), pp.432-448.

[42] Atkins, C.W.C., 2022. A two-dimensional strand/Cartesian Adaptive Mesh Refinement solver for automated mesh generation around hypersonic vehicles. PhD thesis, University of Southampton, Southampton.

[43] Chapman, D.L., 1899. VI. On the rate of explosion in gases. The London, Edinburgh, and Dublin Philosophical Magazine and Journal of Science, 47(284), pp.90-104.

[44] Jouguet, E., 1905. On the propagation of chemical reactions in gases. Journal de Mathématiques Pures et Appliquées, 1(2), pp.347-425.

[45] Law, C.K., 2010. Combustion physics. Cambridge university press, Cambridge.

[46] Zeldovich, Y.B., 1950. On the theory of the propagation of detonation in gaseous systems. National Advisory Committee for Aeronautics, Washington, D.C.

[47] Von Neuman, J., 1942. Theory of detonation waves. Institute for Advanced Study Princeton NJ, New Jersey.

[48] Döring, W., 1943. On detonation processes in gases. Annals of Physics, 43(9), pp.421-436.

[49] Pintgen, F., Eckett, C.A., Austin, J.M. and Shepherd, J.E., 2003. Direct observations of reaction zone structure in propagating detonations. Combustion and Flame, 133(3), pp.211-229.

[50] Kaneshige, M. and Shepherd, J.E., 1997. Detonation database. California Institute of Technology, Pasadena.

[51] Roy, G.D., Frolov, S.M., Borisov, A.A. and Netzer, D.W., 2004. Pulse detonation propulsion: challenges, current status, and future perspective. Progress in Energy and Combustion Science, 30(6), pp.545-672.

[52] Ashford, S.A. and Emanuel, G., 1996. Oblique detonation wave engine performance prediction. Journal of Propulsion and Power, 12(2), pp.322-327.

[53] Baptista, M., Rasheed, A., Badding, B., Velagandula, O. and Dean, A., 2006. Mechanical response in a multi-tube pulsed detonation combustor-turbine hybrid system. In 44th AIAA aerospace sciences meeting and exhibit (p. 1234).

[54] St. George, A.C., Driscoll, R.B., Munday, D.E. and Gutmark, E.J., 2015. Development of a rotating detonation engine facility at the University of Cincinnati. In 53rd AIAA Aerospace Sciences Meeting (p. 0635).

[55] Fan, W., Yan, C., Huang, X., Zhang, Q. and Zheng, L., 2003. Experimental investigation on two-phase pulse detonation engine. Combustion and flame, 133(4), pp.441-450.

[56] Peng, H., Huang, Y., Deiterding, R., Luan, Z., Xing, F. and You, Y., 2018. Effects of jet in crossflow on flame acceleration and deflagration to detonation transition in methane–oxygen mixture. Combustion and Flame, 198, pp.69-80.

[57] Rosato, D.A., Thornton, M., Sosa, J., Bachman, C., Goodwin, G.B. and Ahmed, K.A., 2021. Stabilized detonation for hypersonic propulsion. Proceedings of the national academy of sciences, 118(20), p.e2102244118.

[58] Zhang, Z., Wen, C., Yuan, C., Liu, Y., Han, G., Wang, C. and Jiang, Z., 2022. An experimental study of formation of stabilized oblique detonation waves in a combustor. Combustion and Flame, 237, p.111868.

[59] Braun, E., Dunn, N. and Lu, F., 2010, January. Testing of a continuous detonation wave engine with swirled injection. In 48th AIAA Aerospace Sciences Meeting Including the New Horizons Forum and Aerospace Exposition, (p. 146).

[60] Bykovskii, F.A., Zhdan, S.A. and Vedernikov, E.F., 2005. Continuous spin detonation in annular combustors. Combustion, Explosion and Shock Waves, 41(4), pp.449-459.

[61] Tang, X.M., Wang, J.P. and Shao, Y.T., 2015. Three-dimensional numerical investigations of the rotating detonation engine with a hollow combustor. Combustion and Flame, 162(4), pp.997-1008.

[62] Lin, W., Zhou, J., Liu, S. and Lin, Z., 2015. An experimental study on CH4/O2 continuously rotating detonation wave in a hollow combustion chamber. Experimental Thermal and Fluid Science, 62, pp.122-130.

[63] Higashi, J., Nakagami, S., Matsuoka, K., Kasahara, J., Matsuo, A., Funaki, I. and Moriai, H., 2017. Experimental study of the disk-shaped rotating detonation turbine engine. In 55th AIAA aerospace sciences meeting, (p. 1286).

[64] Nakagami, S., Matsuoka, K., Kasahara, J., Kumazawa, Y., Fujii, J., Matsuo, A. and Funaki, I., 2017. Experimental visualization of the structure of rotating detonation waves in a disk-shaped combustor. Journal of Propulsion and Power, 33(1), pp.80-88.

[65] Goto, K., Matsuoka, K., Matsuyama, K., Kawasaki, A., Watanabe, H., Itouyama, N., Ishihara, K., Buyakofu, V., Noda, T., Kasahara, J. and Matsuo, A., 2023. Space flight demonstration of rotating detonation engine using sounding rocket S-520-31. Journal of Spacecraft and Rockets, 60(1), pp.273-285.

[66] Voitsekhovskii, B.V., 1960. Maintained detonations. Doklady Physics 4, p.1207.

[67] Nicholls, J.A., Cullen, R.E. and Ragland, K.W., 1966. Feasibility studies of a rotating detonation wave rocket motor. Journal of Spacecraft and Rockets, 3(6), pp.893-898.

[68] Adamson T.C., Olsson G.R., 1967. Performance analysis of a rotating detonation wave rocket engine. Astronaut Acta, 13(4), pp.1038-1041.

[69] Bykovskii, F.A.E., Klopotov, I.D. and Mitrofanov, V.V., 1975. Spin detonation of gases in a cylindrical chamber. Proceedings of the USSR Academy of Sciences, 224, pp.1038-1041.

[70] Bykovskii, F.A. and Mitrofanov, V.V., 1980. Detonation combustion of a gas mixture in a cylindrical chamber. Combustion, Explosion and Shock Waves, 16(5), pp.570-578.

[71] Frolov, S.M., Aksenov, V.S. and Ivanov, V.S., 2015. Experimental proof of Zel'dovich cycle efficiency gain over cycle with constant pressure combustion for hydrogen–oxygen fuel mixture. International Journal of Hydrogen Energy, 40(21), pp.6970-6975.

[72] Frolov, S.M., Shamshin, I.O., Aksenov, V.S., Gusev, P.A., Zelensky, V.A., Evstratov, E.V. and Alymov, M.I., 2020. Rocket engine with continuously rotating liquid-film detonation. Combustion Science and Technology, 192(1), pp.144-165.

[73] Kindracki, J., 2015. Experimental research on rotating detonation in liquid fuel–gaseous air mixtures. Aerospace Science and Technology, 43, pp.445-453.

[74] Wolański, P., 2015. Application of the continuous rotating detonation to gas turbine. In Applied Mechanics and Materials, 782, pp. 3-12.

[75] Stechmann, D.P., 2017. Experimental study of high-pressure rotating detonation combustion in rocket environments. PhD thesis, Purdue University, West Lafayette.

[76] Athmanathan, V., Braun, J., Ayers, Z.M., Fugger, C.A., Webb, A.M., Slipchenko, M.N., Paniagua, G., Roy, S. and Meyer, T.R., 2022. On the effects of reactant stratification and wall curvature in non-premixed rotating detonation combustors. Combustion and Flame, 240, p.112013.

[77] Rankin, B.A., Richardson, D.R., Caswell, A.W., Naples, A.G., Hoke, J.L. and Schauer, F.R., 2017. Chemiluminescence imaging of an optically accessible non-premixed rotating detonation engine. Combustion and Flame, 176, pp.12-22.

[78] Rankin, B.A., Codoni, J.R., Cho, K.Y., Hoke, J.L. and Schauer, F.R., 2019. Investigation of the structure of detonation waves in a non-premixed hydrogen–air rotating detonation engine using mid-infrared imaging. Proceedings of the Combustion Institute, 37(3), pp.3479-3486.

[79] Anand, V., George, A.S., Driscoll, R. and Gutmark, E., 2015. Characterization of instabilities in a rotating detonation combustor. International Journal of Hydrogen Energy, 40(46), pp.16649-16659.

[80] Anand, V., George, A.S., Driscoll, R. and Gutmark, E., 2016. Investigation of rotating detonation combustor operation with H2-Air mixtures. International Journal of Hydrogen Energy, 41(2), pp.1281-1292.

[81] Anand, V., George, A.S., Driscoll, R. and Gutmark, E., 2016. Analysis of air inlet and fuel plenum behavior in a rotating detonation combustor. Experimental Thermal and Fluid Science, 70, pp.408-416.

[82] Suchocki, J., Yu, S.T., Hoke, J., Naples, A., Schauer, F. and Russo, R., 2012. Rotating detonation engine operation. In 50th AIAA aerospace sciences meeting including the new horizons forum and aerospace exposition, (p. 119).

[83] Lentsch, A., Bec, R., Serre, L., Falempin, F., Daniau, D., Piton, D., Prigent, A., Canteins, G., Zitoun, R., Desbordes, D. and Jouot, F., 2005. Overview of current French activities on PDRE and continuous detonation wave rocket engines. In AIAA/CIRA 13th International Space Planes and Hypersonics Systems and Technologies Conference, (p. 3232).

[84] Liu, S.J., Lin, Z.Y., Liu, W.D., Lin, W. and Zhuang, F.C., 2012. Experimental realization of H2/air continuous rotating detonation in a cylindrical combustor. Combustion Science and Technology, 184(9), pp.1302-1317.

[85] Peng, H., Liu, W. and Liu, S., 2019. Ethylene Continuous Rotating Detonation in optically accessible racetrack-like combustor. Combustion Science and Technology, 191(4), pp.676-695.

[86] Huang, S.Y., Zhou, J., Liu, S.J., Peng, H.Y. and Yuan, X.Q., 2022. Continuous rotating detonation engine fueled by ammonia. Energy, 252, p.123911.

[87] Wang, C., Liu, W., Liu, S., Jiang, L. and Lin, Z., 2015. Experimental verification of air-breathing continuous rotating detonation fueled by hydrogen. International Journal of Hydrogen Energy, 40(30), pp.9530-9538.

[88] Wang, G., Liu, W., Liu, S., Zhang, H., Peng, H. and Zhou, Y., 2021. Experimental verification of cylindrical air-breathing continuous rotating detonation engine fueled by non-premixed ethylene. Acta Astronautica, 189, pp.722-732.

[89] Peng, L., Wang, D., Wu, X., Ma, H. and Yang, C., 2015. Ignition experiment with automotive spark on rotating detonation engine. International Journal of Hydrogen Energy, 40(26), pp.8465-8474.

[90] Yang, C., Wu, X., Ma, H., Peng, L. and Gao, J., 2016. Experimental research on initiation characteristics of a rotating detonation engine. Experimental Thermal and Fluid Science, 71, pp.154-163.

[91] Deng, L., Ma, H., Xu, C., Liu, X. and Zhou, C., 2018. The feasibility of mode control in rotating detonation engine. Applied Thermal Engineering, 129, pp.1538-1550.

[92] Zhou, S., Ma, H., Li, S., Liu, D., Yan, Y. and Zhou, C., 2017. Effects of a turbine guide vane on hydrogen-air rotating detonation wave propagation characteristics. International Journal of Hydrogen Energy, 42(31), pp.20297-20305.

[93] Zhou, S., Ma, H., Ma, Y., Zhou, C. and Hu, N., 2021. Experimental investigation on detonation wave propagation mode in the start-up process of rotating detonation turbine engine. Aerospace Science and Technology, 111, p.106559.

[94] Wang, Y., Wang, J., Li, Y. and Li, Y., 2014. Induction for multiple rotating detonation waves in the hydrogen–oxygen mixture with tangential flow. International journal of hydrogen energy, 39(22), pp.11792-11797.

[95] Ma, Z., Zhang, S., Luan, M., Yao, S., Xia, Z. and Wang, J., 2018. Experimental research on ignition, quenching, reinitiation and the stabilization process in rotating detonation engine. International journal of hydrogen energy, 43(39), pp.18521-18529.

[96] Xie, Q., Wen, H., Li, W., Ji, Z., Wang, B. and Wolanski, P., 2018. Analysis of operating diagram for H2/Air rotating detonation combustors under lean fuel condition. Energy, 151, pp.408-419.

[97] Xie, Q., Wang, B., Wen, H., He, W. and Wolanski, P., 2019. Enhancement of continuously rotating detonation in hydrogen and oxygen-enriched air. Proceedings of the Combustion Institute, 37(3), pp.3425-3432.

[98] Xie, Q., Wang, B., Wen, H. and He, W., 2019. Thermoacoustic instabilities in an annular rotating detonation combustor under off-design condition. Journal of Propulsion and Power, 35(1), pp.141-151.

[99] Teasley, T.W., Fedotowsky, T.M., Gradl, P.R., Austin, B.L. and Heister, S.D., 2023. Current State of NASA Continuously Rotating Detonation Cycle Engine Development. In AIAA SCITECH 2023 Forum (p. 1873).

[100] St. George, A.C., Driscoll, R.B., Anand, V., Munday, D.E. and Gutmark, E.J., 2015. Fuel blending as a means to achieve initiation in a rotating detonation engine. In 53rd AIAA aerospace sciences meeting (p. 0633).

[101] Li, J.M., Chang, P.H., Li, L., Yang, Y., Teo, C.J. and Khoo, B.C., 2018. Investigation of injection strategy for liquid-fuel rotating detonation engine. In 2018 AIAA aerospace sciences meeting (p. 0403).

[102] Ayers, Z., Athmanathan, V., Paxson, D.E. and Meyer, T.R., 2022. Design and Operability of a Variably Premixed Rotating Detonation Engine for the Evaluation of Mixing Effects. In AIAA SCITECH 2022 Forum (p. 1261).

[103] Fiorino, N.T., Schauer, F.R., Polanka, M.D., Schumaker, S.A. and Sell, B.C., 2021. Use of a Partially Pre-Mixed Injection Scheme and Pre-Detonator in a Small Scale Rotating Detonation Engine. In AIAA Propulsion and Energy 2021 Forum (p. 3656).

[104] Xu, S., Song, F., Wu, Y., Zhou, J., Cheng, P., Yang, X. and Chen, X., 2022. Experimental investigation on combustion efficiency of a partially premixed kerosene-air rotating detonation combustor. Fuel, 329, p.125418.

[105] Stevens, C.A., Fotia, M., Hoke, J. and Schauer, F., 2018. Quasi Steady Heat Transfer Measuments in an RDE. In 2018 AIAA Aerospace sciences meeting (p. 1884).

[106] Schwer, D. and Kailasanath, K., 2010. Numerical investigation of rotating detonation engines. In 46th AIAA/ASME/SAE/ASEE joint propulsion conference & exhibit, (p. 6880).

[107] Schwer, D. and Kailasanath, K., 2013. Fluid dynamics of rotating detonation engines with hydrogen and hydrocarbon fuels. Proceedings of the Combustion Institute, 34(2), pp.1991-1998.

[108] Schwer, D., Corrigan, A., Taylor, B. and Kailasanath, K., 2013. On reducing feedback pressure in rotating detonation engines. In 51st AIAA Aerospace Sciences Meeting including the New Horizons Forum and Aerospace Exposition, (p. 1178).

[109] Nordeen, C.A., Schwer, D., Schauer, F., Hoke, J., Barber, T. and Cetegen, B.M., 2016. Role of inlet reactant mixedness on the thermodynamic performance of a rotating detonation engine. Shock Waves, 26, pp.417-428.

[110] Schwer, D. and Kailasanath, K., 2011. Numerical investigation of the physics of rotating-detonation-engines. Proceedings of the Combustion Institute, 33(2), pp.2195-2202.

[111] Kindracki, J., Kobiera, A., Wolański, P., Gut, Z., Folusiak, M. and Swiderski, K., 2011. Experimental and numerical study of the rotating detonation engine in hydrogen-air mixtures. Progress in propulsion physics, 2, pp.555-582.

[112] Zhou, R. and Wang, J.P., 2012. Numerical investigation of flow particle paths and thermodynamic performance of continuously rotating detonation engines. Combustion and Flame, 159(12), pp.3632-3645.

[113] Subramanian, S. and Meadows, J., 2020. Novel approach for computational modeling of a non-premixed rotating detonation engine. Journal of Propulsion and Power, 36(4), pp.617-631.

[114] Fujii, J., Kumazawa, Y., Matsuo, A., Nakagami, S., Matsuoka, K. and Kasahara, J., 2017. Numerical investigation on detonation velocity in rotating detonation engine chamber. Proceedings of the combustion Institute, 36(2), pp.2665-2672.

[115] Liu, Y., Zhou, W., Yang, Y., Liu, Z. and Wang, J., 2018. Numerical study on the instabilities in H2-air rotating detonation engines. Physics of Fluids, 30(4), p.046106.

[116] Pan, Z., Fan, B., Zhang, X., Gui, M. and Dong, G., 2011. Wavelet pattern and self-sustained mechanism of gaseous detonation rotating in a coaxial cylinder. Combustion and Flame, 158(11), pp.2220-2228.

[117] Schwer, D. and Kailasanath, K., 2011. Effect of inlet on fill region and performance of rotating detonation engines. In 47th AIAA/ASME/SAE/ASEE joint propulsion conference & exhibit, (p. 6044).

[118] Tsuboi, N., Watanabe, Y., Kojima, T. and Hayashi, A.K., 2015. Numerical estimation of the thrust performance on a rotating detonation engine for a hydrogen–oxygen mixture. Proceedings of the Combustion Institute, 35(2), pp.2005-2013.

[119] Uemura, Y., Hayashi, A.K., Asahara, M., Tsuboi, N. and Yamada, E., 2013. Transverse wave generation mechanism in rotating detonation. Proceedings of the combustion institute, 34(2), pp.1981-1989.

[120] Sun, J., Zhou, J., Liu, S. and Lin, Z., 2018. Numerical investigation of a rotating detonation engine under premixed/non-premixed conditions. Acta Astronautica, 152, pp.630-638.

[121] Sun, J., Zhou, J., Liu, S., Lin, Z. and Lin, W., 2019. Effects of air injection throat width on a non-premixed rotating detonation engine. Acta Astronautica, 159, pp.189-198.

[122] Sun, J., Zhou, J., Liu, S. and Lin, Z., 2019. Interaction between rotating detonation wave propagation and reactant mixing. Acta Astronautica, 164, pp.197-203.

[123] Katta, V.R., Cho, K.Y., Hoke, J.L., Codoni, J.R., Schauer, F.R. and Roquemore, W.M., 2019. Effect of increasing channel width on the structure of rotating detonation wave. Proceedings of the Combustion Institute, 37(3), pp.3575-3583.

[124] Sato, T., Voelkel, S. and Raman, V., 2018. Analysis of detonation structures with hydrocarbon fuels for application towards rotating detonation engines. In 2018 joint propulsion conference, (p. 4965).

[125] Wang, Y., Wang, J. and Qiao, W., 2016. Effects of thermal wall conditions on rotating detonation. Computers & fluids, 140, pp.59-71.

[126] Li, Q., Liu, P. and Zhang, H., 2018. Further investigations on the interface instability between fresh injections and burnt products in 2D rotating detonation. Computers & Fluids, 170, pp.261-272.

[127] Zhao, M. and Zhang, H., 2020. Origin and chaotic propagation of multiple rotating detonation waves in hydrogen/air mixtures. Fuel, 275, p.117986.

[128] Raj, P. and Meadows, J.W., 2020. Influence of Fuel Inhomogeneity and Stratification Length Scales on Rotating Detonation Combustor (RDC) Performance. In AIAA Propulsion and Energy 2020 Forum, (p. 3875).

[129] Cocks, P.A., Holley, A.T., Greene, C.B. and Haas, M., 2015. Development of a high fidelity RDE simulation capability. In 53rd AIAA Aerospace Sciences Meeting (p. 1823).

[130] Cocks, P.A., Holley, A.T. and Rankin, B.A., 2016. High fidelity simulations of a non-premixed rotating detonation engine. In 54th AIAA aerospace sciences meeting, (p. 0125).

[131] Strakey, P., Ferguson, D., Sisler, A. and Nix, A., 2016. Computationally quantifying loss mechanisms in a rotating detonation engine. In 54th AIAA Aerospace sciences meeting (p. 0900).

[132] Wu, K., Zhang, L., Luan, M.Y. and Wang, J.P., 2021. Effects of isothermal wall boundary conditions on rotating detonation engine. Combustion Science and Technology, 193(2), pp.211-224.

[133] Liu, P., Li, C., Sun, D., Guo, Q. and Zhao, W., 2021, February. The effect of wall temperature on three-dimensional rotating detonation wave. In Journal of Physics: Conference Series, 1786 (1), p. 012045.

[134] Berti, G., 2001, June. A generic toolbox for the grid craftsman. In Proceedings of the 17th GAMM-Seminar Leipzig, pp. 1-28.

[135] Norton, C.D., Lou, J.Z. and Cwik, T.A., 2001. Status and directions for the PYRAMID parallel unstructured AMR library. In Parallel and Distributed Processing Symposium, (p. 30120b).

[136] Lawlor, O.S., Chakravorty, S., Wilmarth, T.L., Choudhury, N., Dooley, I., Zheng, G. and Kale, L.V., 2006. ParFUM: a parallel framework for unstructured meshes for scalable dynamic physics applications. Engineering with Computers, 22, pp.215-235.

[137] MacNeice, P., Olson, K.M., Mobarry, C., De Fainchtein, R. and Packer, C., 2000. PARAMESH: A parallel adaptive mesh refinement community toolkit. Computer physics communications, 126(3), pp.330-354.

[138] Stone, J.M., Tomida, K., White, C.J. and Felker, K.G., 2020. The Athena++ adaptive mesh refinement framework: design and magnetohydrodynamic solvers. The Astrophysical Journal Supplement Series, 249(1), p.4.

[139] Colella, P., Graves, D.T., Ligocki, T.J., Martin, D.F., Modiano, D., Serafini, D.B. and Van Straalen, B., 2012. Chombo software package for AMR applications design document. Lawrence Berkeley National Laboratory, Berkeley.

[140] Zhang, W., Almgren, A., Beckner, V., Bell, J., Blaschke, J., Chan, C., Day, M., Friesen, B., Gott, K., Graves, D. and Katz, M., 2019. AMReX: a framework for block-structured adaptive mesh refinement. The Journal of Open Source Software, 4(37), p.1370.

[141] Yi, T.H., Turangan, C., Lou, J., Wolanski, P. and Kindracki, J., 2009, May. A three-dimensional numerical study of rotational detonation in an annular chamber. In 47th AIAA aerospace sciences meeting including the new horizons forum and aerospace exposition, (p. 634).

[142] Yi, T.H., Lou, J., Turangan, C.K. and Wolanski, P., 2020. Numerical study of detonation processes in rotating detonation engine and its propulsive performance. Transactions on Aerospace Research, 2020(3), pp.30-48.

[143] Swiderski, K., Folusiak, M., Lukasik, B., Kobiera, A., Kindracki, J. and Wolanski, P., 2013. Three-dimensional numerical study of the propulsion system based on rotating detonation using Adaptive Mesh Refinement. In Proceedings of the 24th International Colloquium on the Dynamics of Explosion and Reactive Systems, (p. 133).

[144] Swiderski, K., Folusiak, M., Kobiera, A., Lukasik, B. and Wolanski, P., 2013. Numerical tools for three dimensional simulations of the rotating detonation engine in complex geometries. Journal of KONES, p. 20.

[145] Sato, T., Voelkel, S. and Raman, V., 2018. Detailed chemical kinetics-based simulation of detonation-containing flows. In Turbo Expo: Power for Land, Sea, and Air, (p. V04AT04A063).

[146] Pal, P., Kumar, G., Drennan, S., Rankin, B.A. and Som, S., 2019. Numerical modeling of supersonic combustion in a non-premixed rotating detonation engine. In 11th U. S. National Combustion Meeting.

[147] Pal, P., Xu, C., Kumar, G., Drennan, S.A., Rankin, B.A. and Som, S., 2020. Large-eddy simulations and mode analysis of ethylene/air combustion in a non-premixed rotating detonation engine. In AIAA Propulsion and Energy 2020 Forum (p. 3876).

[148] Pal, P., Kumar, G., Drennan, S.A., Rankin, B.A. and Som, S., 2021. Multidimensional numerical modeling of combustion dynamics in a non-premixed rotating detonation engine with adaptive mesh refinement. Journal of Energy Resources Technology, 143(11).

[149] Pal, P., Demir, S. and Som, S., 2023. Numerical Analysis of Combustion Dynamics in a Full-Scale Rotating Detonation Rocket Engine Using Large Eddy Simulations. Journal of Energy Resources Technology, 145(2), p.021702.

[150] Eude, Y., Davidenko, D., Falempin, F. and Gökalp, I., 2011, April. Use of the adaptive mesh refinement for 3D simulations of a CDWRE (continuous detonation wave rocket engine). In 17th AIAA international space planes and hypersonic systems and technologies conference, (p. 2236).

[151] Luan, Z., Huang, Y., Gao, S. and You, Y., 2022. Formation of multiple detonation waves in rotating detonation engines with inhomogeneous methane/oxygen mixtures under different equivalence ratios. Combustion and Flame, 241, p.112091.

[152] Nadakkal Appukuttan, S., Sitaraman, H., Yellapantula, S., Henry de Frahan, M. and Day, M., 2022. Computational Study of Variable Fuel-Air Ratio and Hydrogen Doping in a Rotating Detonation Engine. National Renewable Energy Lab. (NREL), Golden.

[153] Henry de Frahan, M.T., Rood, J.S., Day, M.S., Sitaraman, H., Yellapantula, S., Perry, B.A., Grout, R.W., Almgren, A., Zhang, W., Bell, J.B. and Chen, J.H., 2023. PeleC: An adaptive mesh refinement solver for compressible reacting flows. The International Journal of High Performance Computing Applications, 37(2), pp.115-131.

[154] Reyes Barraza, J., 2021. A generalised lattice Boltzmann method with block-structured adaptive mesh refinement. PhD thesis, University of Southampton, Southampton.

[155] Kee, R.J., Rupley, F.M. and Miller, J.A., Chemkin-II: A fortran chemical kinetics package for the analysis of gas-phase chemical kinetics, Sandia National Laboratories, Livermore.

[156] LeVeque, R.J., 2002. Finite volume methods for hyperbolic problems. Cambridge university press, Cambridge.

[157] Anderson, J.D. and Wendt, J., 1995. Computational fluid dynamics. McGraw-Hill, New York.

[158] Atkins, C. and Deiterding, R., 2020. Towards a Strand-Cartesian Solver for Modelling Hypersonic Flows in Thermochemical Non-Equilibrium. In 23rd AIAA International Space Planes and Hypersonic Systems and Technologies Conference, (p.2404).

[159] Liou, M.S. and Steffen Jr, C.J., 1993. A new flux splitting scheme. Journal of Computational physics, 107(1), pp.23-39.

[160] Sanders, R., Morano, E. and Druguet, M.C., 1998. Multidimensional dissipation for upwind schemes: stability and applications to gas dynamics. Journal of Computational Physics, 145(2), pp.511-537.

[161] Larrouturou, B., 1991. How to preserve the mass fractions positivity when computing compressible multi-component flows. Journal of computational physics, 95(1), pp.59-84.

[162] Toro, E.F., 2013. Riemann solvers and numerical methods for fluid dynamics: a practical introduction. Springer, Berlin.

[163] Van Leer, B., 1984. On the relation between the upwind-differencing schemes of Godunov, Engquist–Osher and Roe. SIAM Journal on Scientific and Statistical Computing, 5(1), pp.1-20.

[164] Abgrall, R. and Karni, S., 2001. Computations of compressible multifluids. Journal of computational physics, 169(2), pp.594-623.

[165] Billet, G. and Abgrall, R., 2003. An adaptive shock-capturing algorithm for solving unsteady reactive flows. Computers & fluids, 32(10), pp.1473-1495.

[166] Houim, R.W. and Kuo, K.K., 2011. A low-dissipation and time-accurate method for compressible multi-component flow with variable specific heat ratios. Journal of Computational Physics, 230(23), pp.8527-8553.

[167] Lv, Y. and Ihme, M., 2014. Discontinuous Galerkin method for multicomponent chemically reacting flows and combustion. Journal of Computational Physics, 270, pp.105-137.

[168] Ma, P.C., Lv, Y. and Ihme, M., 2017. An entropy-stable hybrid scheme for simulations of transcritical real-fluid flows. Journal of Computational Physics, 340, pp.330-357.

[169] Boyd, B. and Jarrahbashi, D., 2021. A diffuse-interface method for reducing spurious pressure oscillations in multicomponent transcritical flow simulations. Computers & Fluids, 222, p.104924.

[170] Oran, E.S. and Boris, J.P., 2005. Numerical simulation of reactive flow. Cambridge university press, Cambridge.

[171] Berger, M.J. and Leveque, R.J., 1998. Adaptive mesh refinement using wave-propagation algorithms for hyperbolic systems. SIAM Journal on Numerical Analysis, 35(6), pp.2298-2316.

[172] Calhoun, D. and LeVeque, R.J., 2005. An accuracy study of mesh refinement on mapped grids. In Adaptive Mesh Refinement-Theory and Applications: Proceedings of the Chicago Workshop on Adaptive Mesh Refinement Methods, (pp. 91-101).

[173] Press, W.H., William, H., Teukolsky, S.A., Vetterling, W.T., Saul, A. and Flannery, B.P., 2007. Numerical recipes 3rd edition: The art of scientific computing. Cambridge university press, Cambridge.

[174] Moukalled, F., Mangani, L. and Darwish, M., 2016. The finite volume method in computational fluid dynamics. Springer, Berlin.

[175] Economon, T.D., Palacios, F., Copeland, S.R., Lukaczyk, T.W. and Alonso, J.J., 2016. SU2: An open-source suite for multiphysics simulation and design. AIAA Journal, 54(3), pp.828-846.

[176] Salari, K. and Knupp, P., 2000. Code verification by the method of manufactured solutions. Sandia National Laboratories, New Mexico.

[177] Roy, C.J., Nelson, C.C., Smith, T.M. and Ober, C.C., 2004. Verification of Euler/Navier–Stokes codes using the method of manufactured solutions. International Journal for Numerical Methods in Fluids, 44(6), pp.599-620.

[178] Hoffmann, K.A. and Chiang, S.T., 2000. Computational fluid dynamics volume I. Engineering Education System, Kansas.

[179] Persson, P.O., Bonet, J. and Peraire, J., 2009. Discontinuous Galerkin solution of the Navier–Stokes equations on deformable domains. Computer Methods in Applied Mechanics and Engineering, 198(17-20), pp.1585-1595.

[180] Fedkiw, R.P., 1997. A survey of chemically reacting, compressible flows. PhD thesis, Purdue University of California Los Angeles, California.

[181] Ferrer, P.J.M., Buttay, R., Lehnasch, G. and Mura, A., 2014. A detailed verification procedure for compressible reactive multicomponent Navier–Stokes solvers. Computers & Fluids, 89, pp.88-110.

[182] Owen, L.D., Guzik, S.M. and Gao, X., 2018. A high-order adaptive algorithm for multispecies gaseous flows on mapped domains. Computers & Fluids, 170, pp.249-260.

[183] Ghia, U.K.N.G., Ghia, K.N. and Shin, C.T., 1982. High-Re solutions for incompressible flow using the Navier-Stokes equations and a multigrid method. Journal of computational physics, 48(3), pp.387-411.

[184] Evans, M.J., Medwell, P.R., Tian, Z.F., Ye, J., Frassoldati, A. and Cuoci, A., 2017. Effects of oxidant stream composition on non-premixed laminar flames with heated and diluted coflows. Combustion and Flame, 178, pp.297-310.

[185] Gregory P. Smith, David M. Golden, Michael Frenklach, Nigel W. Moriarty, Boris Eiteneer, Mikhail Goldenberg, C. Thomas Bowman, Ronald K. Hanson, Soonho Song, William C. Gardiner, Jr., Vitali V. Lissianski, and Zhiwei Qin. GRI-Mech 3.0. Available from: http://www.me.berkeley.edu/gri_mech/, accessed on: 12 March 2021.

[186] Billet, G., Giovangigli, V. and De Gassowski, G., 2008. Impact of volume viscosity on a shock–hydrogen-bubble interaction. Combustion Theory and Modelling, 12(2), pp.221-248.

[187] Jachimowski, C.J., 1988. An analytical study of the hydrogen-air reaction mechanism with application to scramjet combustion. National Aeronautics and Space Administration.

[188] Attal, N., Ramaprabhu, P., Hossain, J., Karkhanis, V., Uddin, M., Gord, J.R. and Roy, S., 2015. Development and validation of a chemical reaction solver coupled to the FLASH code for combustion applications. Computers & Fluids, 107, pp.59-76.

[189] Owen, L., 2019. Fourth-order solution-adaptive finite-volume algorithm for compressible reacting flows on mapped domains. PhD thesis, Colorado State University, Colorado.

[190] Choi, J.Y., Jeung, I.S. and Yoon, Y., 2000. Computational fluid dynamics algorithms for unsteady shock-induced combustion, part 1: validation. AIAA journal, 38(7), pp.1179-1187.

[191] Axdahl, E., Kumar, A. and Wilhite, A., 2011, July. Study of unsteady, sphere-driven, shock-induced combustion for application to hypervelocity airbreathing propulsion. In 47th AIAA/ASME/SAE/ASEE Joint Propulsion Conference & Exhibit, (p. 5790).

[192] Lehr, H.F., 1972. Experiments on shock-induced combustion. Astronautica Acta, 17, pp.589-597.

[193] Yu, S.T., 1993. Convenient method to convert two-dimensional CFD codes into axisymmetric ones. Journal of Propulsion and Power, 9(3), pp.493-495.

[194] Chemical-Kinetic Mechanisms for Combustion Applications. 2016. San Diego Mechanism, Mechanical and Aerospace Engineering (Combustion Research), University of California at San Diego, http://web.eng.ucsd.edu/mae/groups/combustion/mechanism.html.

[195] Kumar, P.P., Kim, K.S., Oh, S. and Choi, J.Y., 2015. Numerical comparison of hydrogen-air reaction mechanisms for unsteady shock-induced combustion applications. Journal of Mechanical Science and Technology, 29(3), pp.893-898.

[196] Pavalavanni, P.K., Sohn, C.H., Lee, B.J. and Choi, J.Y., 2019. Revisiting unsteady shock-induced combustion with modern analysis techniques. Proceedings of the Combustion Institute, 37(3), pp.3637-3644.

[197] Westbrook, C.K., 1982. Chemical kinetics of hydrocarbon oxidation in gaseous detonations. Combustion and Flame, 46, pp.191-210.

[198] Goodwin, D.G., Moffat, H.K. and Speth, R.L., 2009. Cantera: An object-oriented software toolkit for chemical kinetics, thermodynamics, and transport processes. Available from: http://www.cantera.org, accessed on: 20 May 2020.

[199] Browne, S., Ziegler, J. and Shepherd, J.E., 2008. Numerical solution methods for shock and detonation jump conditions. GALCIT report FM2006, 6, p.90.

[200] Gavrikov, A.I., Efimenko, A.A. and Dorofeev, S.B., 2000. A model for detonation cell size prediction from chemical kinetics. Combustion and flame, 120(1-2), pp.19-33.

[201] Kaneshige, M. and Shepherd, J.E., 1997. Detonation database. GALCIT report FM97-8.

[202] Oran, E.S., Weber Jr, J.W., Stefaniw, E.I., Lefebvre, M.H. and Anderson Jr, J.D., 1998. A numerical study of a two-dimensional H2-O2-Ar detonation using a detailed chemical reaction model. Combustion and Flame, 113(1-2), pp.147-163.

[203] Hu, X.Y., Zhang, D.L., Khoo, B.C. and Jiang, Z.L., 2005. The structure and evolution of a two-dimensional H2/O2/Ar cellular detonation. Shock Waves, 14(1), pp.37-44.

[204] Fickett, W. and Davis, W.C., 2000. Detonation: theory and experiment. Courier Corporation, Massachusetts.

[205] Yuan, X., Zhou, J., Lin, Z. and Cai, X., 2016. Adaptive simulations of detonation propagation in 90-degree bent tubes. International Journal of Hydrogen Energy, 41(40), pp.18259-18272.

[206] Williams, D.N., Bauwens, L. and Oran, E.S., 1996, January. Detailed structure and propagation of three-dimensional detonations. In Symposium (International) on Combustion, 26(2) pp. 2991-2998.

[207] Hanana, M. and Lefebvre, M.H., 2001. Pressure profiles in detonation cells with rectangular and diagonal structures. Shock Waves, 11, pp.77-88.

[208] Tsuboi, N., Katoh, S. and Hayashi, A.K., 2002. Three-dimensional numerical simulation for hydrogen/air detonation: Rectangular and diagonal structures. Proceedings of the Combustion Institute, 29(2), pp.2783-2788.

[209] Huang, Y., Ji, H., Lien, F. and Tang, H., 2014. Numerical study of three-dimensional detonation structure transformations in a narrow square tube: from rectangular and diagonal modes into spinning modes. Shock Waves, 24(4), pp.375-392.

[210] Monnier, V., Rodriguez, V., Vidal, P. and Zitoun, R., 2022. An analysis of three-dimensional patterns of experimental detonation cells. Combustion and Flame, 245, p.112310.

[211] Crane, J., Lipkowicz, J.T., Shi, X., Wlokas, I., Kempf, A.M. and Wang, H., 2023. Three-dimensional detonation structure and its response to confinement. Proceedings of the Combustion Institute, 39(3), pp.2915-2923.

[212] Schott, G.L., 1965. Observations of the structure of spinning detonation. The Physics of Fluids, 8(5), pp.850-865.

[213] Wu, Y. and Lee, J.H., 2015. Stability of spinning detonation waves. Combustion and Flame, 162(6), pp.2660-2669.

[214] Zhang, B., Shen, X., Pang, L. and Gao, Y., 2016. Methane–oxygen detonation characteristics near their propagation limits in ducts. Fuel, 177, pp.1-7.

[215] Tsuboi, N., Eto, K. and Hayashi, A.K., 2007. Detailed structure of spinning detonation in a circular tube. Combustion and Flame, 149(1-2), pp.144-161.

[216] Tsuboi, N., Daimon, Y. and Hayashi, A.K., 2008. Three-dimensional numerical simulation of detonations in coaxial tubes. Shock Waves, 18(5), pp.379-392.

[217] Cho, D.R., Won, S.H., Shin, J.R. and Choi, J.Y., 2013. Numerical study of three-dimensional detonation wave dynamics in a circular tube. Proceedings of the Combustion Institute, 34(2), pp.1929-1937.

[218] Chen, W., Liang, J., Cai, X. and Mahmoudi, Y., 2020. Three-dimensional simulations of detonation propagation in circular tubes: Effects of jet initiation and wall reflection. Physics of Fluids, 32(4), p. 046104.

[219] Calhoun, D.A., Helzel, C. and LeVeque, R.J., 2008. Logically rectangular grids and finite volume methods for PDEs in circular and spherical domains. SIAM review, 50(4), pp.723-752.

[220] Oran, E.S. and Gamezo, V.N., 2007. Origins of the deflagration-to-detonation transition in gas-phase combustion. Combustion and flame, 148(1-2), pp.4-47.

[221] Gamezo, V.N., Oran, E.S. and Khokhlov, A.M., 2005. Three-dimensional reactive shock bifurcations. Proceedings of the Combustion Institute, 30(2), pp.1841-1847.

[222] Law, H., Baxter, T., Ryan, C.N. and Deiterding, R., 2021. Design and testing of a small-scale laboratory rotating detonation engine running on ethylene-oxygen. In AIAA Propulsion and Energy 2021 Forum, (p.3658).

[223] Singh, D.J. and Jachimowski, C.J., 1994. Quasiglobal reaction model for ethylene combustion. AIAA journal, 32(1), pp.213-216.

[224] Yao, S. and Wang, J., 2016. Multiple ignitions and the stability of rotating detonation waves. Applied Thermal Engineering, 108, pp.927-936.

[225] Zhang, P., Meagher, P.A. and Zhao, X., 2021. Multiplicity for idealized rotational detonation waves. Physics of Fluids, 33(10), p.106102.

[226] Deng, L., Ma, H., Xu, C., Zhou, C. and Liu, X., 2017. Investigation on the propagation process of rotating detonation wave. Acta Astronautica, 139, pp.278-287.

[227] Cho, K.Y., Codoni, J.R., Rankin, B.A., Hoke, J. and Schauer, F., 2017. Effects of lateral relief of detonation in a thin channel. In 55th AIAA Aerospace sciences meeting, p. 0373.

[228] Zhao, M., Cleary, M.J. and Zhang, H., 2021. Combustion mode and wave multiplicity in rotating detonative combustion with separate reactant injection. Combustion and Flame, 225, pp.291-304.

[229] Burke, M.P., Chaos, M., Ju, Y., Dryer, F.L. and Klippenstein, S.J., 2012. Comprehensive H2/O2 kinetic model for high-pressure combustion. International Journal of Chemical Kinetics, 44(7), pp.444-474.

[230] Chacon, F. and Gamba, M., 2019. Study of parasitic combustion in an optically accessible continuous wave rotating detonation engine. In AIAA Scitech 2019 Forum, (p. 0473).

[231] Raman, V., Prakash, S. and Gamba, M., 2023. Nonidealities in rotating detonation engines. Annual Review of Fluid Mechanics, 55, pp.639-674.

[232] Liu, P., Guo, Q., Sun, D., Li, C. and Zhang, H., 2020. Wall effect on the flow structures of three-dimensional rotating detonation wave. International Journal of Hydrogen Energy, 45(53), pp.29546-29559.

Appendix A Mapping functions used for the mesh generation

In this appendix, the mapping functions used in this thesis are introduced as follows. The 3D stretched mesh is generated by a clustering function as

$$\begin{cases} y = r_d * L_{\mathrm{y}}\left[1+\dfrac{\sinh\left[\beta\left(\eta-A\right)\right]}{\sinh(\beta A)}\right], \quad A=\dfrac{1}{2\beta}\ln\left(\dfrac{1+\left(e^{\beta}-1\right)r_d}{1+\left(e^{-\beta}-1\right)r_d}\right) \\ x = \xi * L_{\mathrm{x}} \\ z = r_d * L_{\mathrm{z}}\left[1+\dfrac{\sinh\left[\beta\left(\zeta-A\right)\right]}{\sinh(\beta A)}\right], \quad A=\dfrac{1}{2\beta}\ln\left(\dfrac{1+\left(e^{\beta}-1\right)r_d}{1+\left(e^{-\beta}-1\right)r_d}\right) \end{cases}, \tag{A.1}$$

where the clustering factor β is 6. The factor r_{d} is set to 0.5 for the stretched mesh distributed in the domain centre. L_{x}, L_{y} and L_{z} are the total length of the domain in the x-, y- and z-direction, respectively. This stretched mesh is used for the cases in Section 4.1.4 and Section 4.1.5.

The following function is used to generate the skewed mesh in Section 4.1.4,

$$\begin{cases} x = \xi + \eta\tan\left(\dfrac{\pi}{12}\right) - 0.5 \\ y = 2\times\left(\eta + \zeta\tan\left(\dfrac{\pi}{12}\right)\right) \\ z = \zeta + \xi\tan\left(\dfrac{\pi}{12}\right) - 0.5 \end{cases}. \tag{A.2}$$

The mapping function for the 3D distorted mesh is given as

$$\begin{cases} x = \xi + L_{\mathrm{x}}S_{\mathrm{x}}\sin\left(\dfrac{2\pi\xi}{L_{\mathrm{x}}}\right)\sin\left(\dfrac{2\pi\eta}{L_{\mathrm{y}}}\right) \\ z = \zeta \\ y = \eta + L_{\mathrm{y}}S_{\mathrm{y}}\sin\left(\dfrac{2\pi\xi}{L_{\mathrm{x}}}\right)\sin\left(\dfrac{2\pi\eta}{L_{\mathrm{y}}}\right) \end{cases}, \tag{A.3}$$

where the subscripts x and y denote the respective direction. L is the total length of the domain and S is the scaling factor in the respective direction. The scaling factor S is set to 0.075 for each direction. Both of these factors satisfy the constraint $0 \le 2\pi S \le 1$ to ensure that the mesh does not tangle. The same distorted mapping is used in Section 4.1.4, Section 4.1.5, Section 4.1.6 and Section 4.2.1. The different computational domains in these cases result in different physical domains. The use of negative computational coordinates leads to a distorted boundary as shown in Figure 4.7, which is beneficial for verification. The non-negative computational coordinates hold the Cartesian boundary and distort the mesh in the centre as shown in Figure 4.11, which can be applied to a periodic boundary, i.e. in Section 4.1.6.

Appendix A

The mapping function for the skewed mesh in Section 4.1.5 is given as

$$\begin{cases} x = \xi + \eta \tan(\pi/12) \\ y = \eta + \zeta \tan(\pi/12) \\ z = \zeta + \xi \tan(\pi/12) \end{cases}. \tag{A.4}$$

For the 2D lid-driven cavity case in Section 4.2.3, the mesh is stretched near the boundaries in both directions by using

$$\begin{cases} x = L_{\mathrm{x}} \dfrac{(\beta+1)\left[(\beta+1)/(\beta-1)\right]^{2\xi-1} + 1 - \beta}{2 + 2\left[(\beta+1)/(\beta-1)\right]^{2\xi-1}} \\ y = L_{\mathrm{y}} \dfrac{(\beta+1)\left[(\beta+1)/(\beta-1)\right]^{2\eta-1} + 1 - \beta}{2 + 2\left[(\beta+1)/(\beta-1)\right]^{2\eta-1}} \end{cases}. \tag{A.5}$$

L_{x} and L_{y} are the domain length in the x- and y-direction, respectively. The computational space is set to [0, 1] × [0, 1]. The clustering parameter β is set to 1.2 in this case.

For the 3D laminar boundary flow case in Section 4.2.4 and the 3D detonation/boundary flow case in Section 5.5, the mesh is only stretched in the y-direction with β as 1.05,

$$\begin{cases} x = \xi \\ y = L_{\mathrm{y}} \dfrac{(\beta+1) - (\beta-1)\left\{\left[(\beta+1)/(\beta-1)\right]^{1-\eta}\right\}}{\left[(\beta+1)/(\beta-1)\right]^{1-\eta} + 1} \\ z = \zeta \end{cases}. \tag{A.6}$$

For the 2D unsteady shock-induced combustion case in Section 5.1, the mesh is generated through the function described in Ref. [168],

$$\begin{cases} x = -\left((r_{\mathrm{o}} - r_{\mathrm{in}}) * (1-\xi) + r_{\mathrm{in}}\right) * \cos(0.5\eta\pi) \\ y = \left((r_{\mathrm{o}} - r_{\mathrm{in}}) * (1-\xi) + r_{\mathrm{in}}\right) * \sin(0.5\eta\pi) \\ r_{\mathrm{o}} = \sqrt{\left(r_{\mathrm{a}} * \cos(0.5\eta\pi)\right)^2 + \left(r_{\mathrm{b}} * \sin(0.5\eta\pi)\right)^2} \end{cases}, \tag{A.7}$$

where the inner radius r_{in} is 7.5 mm. The outer radius r_{a} is 11 mm in the x-direction and r_{b} is 15 mm in the y-direction. The computational domain is given as [0, 1] × [0, 1].

In Section 5.3, the pipe bend with a straight channel is constructed based on a piecewise function as

$$
\begin{aligned}
x &= \begin{cases} L_{\mathrm{x},1} + L_{\mathrm{x},1}\left(\eta - L_{\mathrm{y},1}\right)/L_{\mathrm{y},1}, & \text{if } \eta \le L_{\mathrm{y},1} \\ L_{\mathrm{x},1} + \left(r_{\mathrm{in}} + \xi W\right)\cos\left(0.5\pi\dfrac{\eta - L_{\mathrm{y},1}}{L_{\mathrm{y},1}} - 0.5\pi\right), & \text{if } L_{\mathrm{y},1} < \eta \le L_{\mathrm{y},2} \\ L_{\mathrm{x},1} + r_{\mathrm{in}} + \xi W, & \text{otherwise} \end{cases} \\
y &= \begin{cases} \left(1-\xi\right)W, & \text{if } \eta \le L_{\mathrm{y},1} \\ r_{\mathrm{out}} + \left(r_{\mathrm{in}} + \xi W\right)\sin\left(0.5\pi\dfrac{\eta - L_{\mathrm{y},1}}{L_{\mathrm{y},2} - L_{\mathrm{y},1}} - 0.5\pi\right), & \text{if } L_{\mathrm{y},1} < \eta \le L_{\mathrm{y},2} \\ r_{\mathrm{out}} + L_{\mathrm{x},2}\dfrac{\eta - L_{\mathrm{y},2}}{1 - L_{\mathrm{y},2}}, & \text{otherwise} \end{cases} \\
z &= \zeta,
\end{aligned}
\tag{A.8}
$$

where $L_{\mathrm{y},1} = 0.56$ and $L_{\mathrm{y},2} = 0.83$ are the bounds of the straight part of the pipe. The length of the horizontal straight pipe $L_{\mathrm{x},1}$ is 13 cm and that of the vertical straight pipe $L_{\mathrm{x},2}$ is 4 cm in this case. r_{in} and r_{out} are the inner (2 cm) and outer radius (6 cm) of the pipe bend. W is the pipe width (4 cm). The computational space is set to [0, 1] × [0, 1] × [0, 1.6].

In Section 5.4, a convex combination mapping strategy [209] is used that reads

$$
\begin{aligned}
d &= \max\left(|\eta|,\ |\zeta|\right), \\
r &= \max\left(\sqrt{\eta^2 + \zeta^2},\ 1\times10^{-10}\right), \\
&\begin{cases} x = \xi \\ y = \left[d^3\eta/r + \left(1-d^2\right)\eta\sqrt{2}\right]r_1 \\ z = \left[d^3\zeta/r + \left(1-d^2\right)\zeta\sqrt{2}\right]r_1 \end{cases}.
\end{aligned}
\tag{A.9}
$$

r_1 denotes the radius of the mapped cylinder. The computational space is set to [0, 3] × [−1, 1] × [−1, 1].

In Section 6.1.2, Section 6.2.2 and Section 8.1, the cylindrical mapping is used for the annular RDE chamber as

$$
\begin{cases} x = \xi * \cos\left(\eta\right) \\ y = \xi * \sin\left(\eta\right) \\ z = \zeta \end{cases}.
\tag{A.10}
$$

ξ is bounded by the inner and outer radius for the specific case and η ranges from 0 to 2π. A periodic boundary condition is used to connect the domain in the η direction. ζ is the axial length of the chamber. In Section 7.2, Section 8.2 and Section 8.2, the boundary meshes are stretched by using the mapping,

$$
r = r_{\mathrm{in}} + W\frac{\left(\beta+1\right)\left[\left(\beta+1\right)/\left(\beta-1\right)\right]^{2\xi-1} + 1 - \beta}{2 + 2\left[\left(\beta+1\right)/\left(\beta-1\right)\right]^{2\xi-1}},
\tag{A.11}
$$

Appendix A

$$\begin{cases} x = r * \cos(\eta) \\ z = L_z \dfrac{(\beta+1)-(\beta-1)\left\{\left[(\beta+1)/(\beta-1)\right]^{1-\zeta}\right\}}{\left[(\beta+1)/(\beta-1)\right]^{1-\zeta}+1} \\ y = r * \sin(\eta) \end{cases}.$$

r_{in} denotes the inner radius of the cylinder and W is the channel width. ξ and ζ both range between 0 and 1. L_z is the axial length. The mesh is stretched near both the inner wall and outer wall. The mesh is also stretched in the axial direction with β as 1.2.